EPFL

Thèse n° 10 139

Assessing sublimation during snow transport and sublimation effects on the isotopic composition of water vapor

Présentée le 3 novembre 2023

Faculté de l'environnement naturel, architectural et construit
Laboratoire des sciences cryosphériques
Programme doctoral en génie civil et environnement

pour l'obtention du grade de Docteur ès Sciences

par

Armin SIGMUND

Acceptée sur proposition du jury

Prof. D. Tuia, président du jury
Prof. M. Lehning, directeur de thèse
Prof. X. Fettweis, rapporteur
Prof. J. D. Lundquist, rapporteuse
Prof. A. Nenes, rapporteur

École polytechnique fédérale de Lausanne

2023

The blue ice around it was so clear
we could see glaciers 50 or 60 miles away.
— Richard E Byrd.

To my parents, my sister, and my brother, who helped me to develop many valuable skills for my life.

Acknowledgements

I thank my supervisor Michael Lehning for offering this exciting PhD project and for regular fruitful discussions. I thank the jury members for their interest in my work and for taking the time to assess it. The Swiss National Science Foundation (SNSF) is acknowledged for providing funding for this work (grant number 179130). The Swiss National Supercomputing Centre (CSCS) is acknowledged for providing computing resources for the projects s873, s1031, and s1115. I thank Jérôme Dujardin for performing the field measurements presented in this thesis. Support for these measurements was provided by the team of the Japanese Antarctic Research Expedition. I thank Daniela Brito Melo for her contribution in further developing the LES-LSM model and regular and valuable discussions on snow transport. I thank Riqo Chaar for exploring the field of stable water isotopes and contributing to the publication presented in Chapter 3. I thank Iris Thurnherr, Franziska Aemisegger, and Sonja Wahl who provided inspiration and feedback for the study on stable water isotopes. I thank Varun Sharma and Franziska Gerber for helpful discussions about the simulations and data analysis. I thank Hendrik Huwald for technical support for my field work at Pincess Elisabeth Station, Antarctica, which gave me useful and fascinating insights in measurement techniques and the world of snow and ice and provided data for related projects of colleagues and master students. I am thankful for many nice group activities and excursions with all colleagues in the CRYOS laboratory and the snow processes group. Four anonymous reviewers are acknowledged for constructive comments, which helped to improve the publications presented in Chapters 1 and 3.

Sion, October 4, 2023 Armin Sigmund

Abstract

Sublimation influences the water storage in snow covers and glaciers, which is important for water use and projections of the sea level rise. Yet, it is challenging to quantify sublimation for large areas or in conditions of snow transport. In-situ measurements only provide local information and can be affected by errors in conditions of snow transport. Therefore, models are crucial. Large-scale models suggest that sublimation of drifting and blowing snow is a relevant term in the surface mass balance of the Antarctic Ice Sheet but the uncertainties are large because the underlying processes are strongly simplified. On the contrary, small-scale models such as large-eddy simulation (LES) with Lagrangian particles represent these processes with a high level of detail and provide unique insights. Indirect information on sublimation can be obtained by measuring stable water isotopes (SWIs) as their relative abundance is influenced by phase changes. Yet, SWIs have so far only provided qualitative insights in the sublimation process because the effects of snow processes on SWIs are still incompletely understood. The goals of this work are to (a) better understand the moisture transport through the near-surface atmosphere in conditions of snow transport using unique measurements and LES simulations, (b) leverage the LES simulations to improve the parameterization approach of large-scale models, and (c) better understand the effect of sublimation and other drivers on SWIs in air masses sampled at the coast of Antarctica. We compare sublimation assessments based on the Monin–Obukhov bulk parameterization and eddy-covariance measurements during a snow transport event at the S17 site, Antarctica. For specific situations, the vertical profiles of the vapor and heat fluxes are modeled using LES simulations and a simple one-dimensional model inspired by large-scale models. It is shown that snow transport violates an assumption of the Monin–Obukhov bulk measurements, leading to a significant underestimation of the vapor and heat fluxes in absolute magnitude. More reliable fluxes are obtained with the eddy-covariance technique after removing blowing-snow-induced artifacts from the raw data. To improve large-scale models, we propose to use (a) a high vertical resolution near the surface with at least one grid level in the lowest ~ 0.1 m of the atmosphere; (b) prognostic profiles of near-surface humidity and temperature; (c) an empirical correction for the sublimation of drifting and blowing snow in the lowest 0.3 m of the atmosphere, which should be further validated in other weather conditions; and (d) increased particle sizes at the top of the saltation layer as long as the height of this layer is underestimated. To explain SWI variations in water vapor, we develop a simple model for the isotopic composition along backward trajectories. Apart from ocean evaporation and isotopic distillation during cloud formation, sublimation of surface snow can be an important driver of the vapor isotopic composition, especially

for marine air masses arriving at the ice sheet or free-tropospheric air masses descending towards the surface. Further work is needed to address remaining questions concerning for example the effect of snow transport on SWIs or the impact of improved parameterizations on large-scale estimates of sublimation.

Keywords Backward trajectories, Eddy-covariance technique, Isotopic fractionation, Large-eddy simulations, Latent heat flux, Monin–Obukhov similarity theory, Snow transport, Stable water isotopes.

Zusammenfassung

Die Sublimation beeinflusst die Wasserspeicherung in Schneedecken und Gletschern, die für die Wassernutzung und Prognosen des Meeresspiegelanstiegs wichtig ist. Allerdings ist es schwierig, die Sublimation für große Gebiete oder bei Schneeverfrachtung zu bestimmen. In-situ-Messungen liefern nur lokale Informationen und können bei Schneeverfrachtung fehlerbehaftet sein. Daher sind Modelle wichtig. Großräumige Modelle legen nahe, dass die Sublimation von Triebschnee ein relevanter Term in der Oberflächenmassenbilanz des antarktischen Eisschildes ist, aber die Unsicherheiten sind groß, weil die zugrunde liegenden Prozesse stark vereinfacht werden. Dagegen stellen kleinräumige Modelle wie die Large-Eddy-Simulation (LES) mit Lagrangeschen Partikeln diese Prozesse sehr detailliert dar und liefern einzigartige Erkenntnisse. Indirekte Informationen zur Sublimation können durch die Messung stabiler Wasserisotope (SWI) gewonnen werden, da deren relative Häufigkeit durch Phasenänderungen beeinflusst wird. Allerdings haben SWI bisher nur qualitative Erkenntnisse zur Sublimation geliefert, da die Effekte von Schneeprozessen auf SWI nur teilweise verstanden sind. Diese Arbeit hat zum Ziel (a) den Feuchtetransport durch die oberflächennahe Atmosphäre bei Schneeverfrachtung mithilfe einzigartiger Messungen und LES-Simulationen besser zu verstehen, (b) die LES-Simulationen zur Verbesserung des Parametrisierungsansatzes großräumiger Modelle zu nutzen und (c) die Effekte der Sublimation und anderer Faktoren auf SWI in Luftmassen besser zu verstehen, die an der Küste der Antarktis beprobt wurden. Wir vergleichen Sublimationsraten, die auf der Monin-Obukhov-Parametrisierung und Eddy-Kovarianz-Messungen während eines Triebschneeereignisses am Standort S17 in der Antarktis beruhen. Für bestimmte Situationen werden die vertikalen Profile der Wasserdampf- und Wärmeströme mit LES-Simulationen und einem einfachen eindimensionalen Modell simuliert, das großräumigen Modellen ähnelt. Es wird gezeigt, dass die Schneeverfrachtung eine Annahme der Monin-Obukhov-Methode verletzt, was zu einer deutlichen Unterschätzung der absoluten Wasserdampf- und Wärmeströme führt. Die Eddy-Kovarianz-Methode liefert zuverlässigere Flüsse, nachdem Triebschnee-Artefakte aus den Rohdaten entfernt wurden. Zur Verbesserung großräumiger Modelle wird Folgendes empfohlen: (a) eine hohe vertikale Auflösung nahe der Oberfläche und mindestens eine Gitterebene in den untersten $\sim 0,1$ m der Atmosphäre; (b) prognostische Profile der oberflächennahen Feuchte und Temperatur; (c) eine empirische Korrektur der Sublimation von Triebschnee in den untersten 0,3 m der Atmosphäre, die unter anderen Wetterbedingungen weiter validiert werden sollte und (d) erhöhte Partikelgrößen an der Oberseite der Saltationsschicht, solange die Höhe dieser Schicht unterschätzt wird. Um SWI-Variationen im Wasserdampf zu erklären, wird ein einfaches

Zusammenfassung

Modell entwickelt, das die Isotopenzusammensetzung entlang von Rückwärtstrajektorien berechnet. Neben Ozeanverdunstung und Wolkenbildung kann die Oberflächensublimation ein wichtiger Faktor für die Isotopenzusammensetzung des Wasserdampfs sein, insbesondere wenn marine Luftmassen den Eisschild erreichen oder Luftmassen aus der freien Troposphäre zur Oberfläche hin absinken. Weitere Studien sind nötig, um z.B. zu klären, wie sich die Schneeverfrachtung auf SWI auswirkt oder wie verbesserte Parametrisierungen großräumige Schätzungen der Sublimation beeinflussen.

Schlüsselwörter Rückwärtstrajektorien, Eddy-Kovarianz-Methode, Isotopenfraktionierung, Large-Eddy-Simulation, Latenter Wärmestrom, Monin–Obukhov-Ähnlichkeitstheorie, Schneeverfrachtung, Stabile Wasserisotope.

Contents

General Introduction

Motivation and Current State of Research

The mass balance of ice sheets and mountain glaciers controls the sea level and influences the water availability in many areas of the world. Global warming is generally reducing the water storage in the ice sheets, glaciers, and snow covers with increasingly severe consequences for people living in coastal areas or benefiting from meltwater in mountains. Current and future assessments of the mass balance of snow and ice are challenging because this balance is the net effect of multiple processes, which depend on each other through feedback effects and are difficult to model for large areas. Apart from glacier movement and calving, it is important to quantify the surface mass balance (SMB), which represents the net mass change due to snowfall, sublimation, erosion by wind, deposition of drifting and blowing snow, and meltwater run-off (e.g., Agosta et al., 2019). In SMB studies, the sublimation term typically refers to the net effect of sublimation and vapor deposition. This term can be divided into the contributions of surface snow and particles of drifting and blowing snow. Additionally, falling snowflakes can be affected by sublimation, which reduces the amount of snowfall reaching the ground (Grazioli et al., 2017). The term drifting snow is typically used for wind-induced particle transport near the surface while blowing snow refers to particles transported above a certain height. In this study, drifting snow refers to the saltation layer, i.e., approximately the lowest 0.1 m of the atmosphere where the particles move along ballistic trajectories. We define blowing snow as particles lifted from the snow surface and transported in suspension. The sum of drifting and blowing snow is called snow transport.

For the whole Antarctic Ice Sheet, current large-scale atmospheric models suggest that sublimation of drifting and blowing snow amounts on average to approximately 100 Gt yr^{-1}, corresponding to 3.7%–4.6% of the SMB depending on the model (Van Wessem et al., 2018; Gerber et al., 2023). This amount is relevant because it is comparable to the average total mass balance of the Antarctic Ice Sheet between 1992 and 2017 (109 $\pm$56 Gt yr^{-1}) (The IMBIE team, 2018). It is unclear whether large-scale estimates of the sublimation of drifting and blowing snow are reliable as large-scale models strongly simplify particle-atmosphere interactions and require assumptions on uncertain parameters such as the surface roughness, interparticle cohesion of surface snow, and size and temperature of the snow particles. Additionally, current large-scale models yield conflicting results with respect to the relative importance of surface

sublimation and drifting/blowing snow sublimation (Van Wessem et al., 2018; Gerber et al., 2023).

While surface sublimation is a bit better understood, at least in the absence of snow transport, it is difficult to quantify sublimation in conditions of snow transport. This challenge is related to the fact that in-situ measurements suffer from increased uncertainties in these conditions and cannot resolve the vertical divergence of the moisture flux induced by sublimation of drifting and blowing snow. Intense blowing snow events are expected to cause measurement errors for both the eddy-covariance technique and the Monin–Obukhov bulk parameterization. While the former method can be affected by technical limitations (LI-COR, 2004; Campbell Scientific, 2017), the latter method is affected by a theory-related error because the turbulent moisture flux is incorrectly assumed to remain constant with height (Monin and Obukhov, 1954; Bintanja, 2001b). So far, it has not been possible to quantify these errors.

More detailed insights in the particle-atmosphere exchange can be obtained with large-eddy simulations coupled to a Lagrangian stochastic model (LES-LSM), representing turbulence effects and particle trajectories with high temporal and spatial resolutions. Yet, these simulations still require some assumptions, which are not fully realistic or difficult to verify. For example, the snow particles are modeled as spherical particles with the density of ice and the surface fluxes of moisture and heat have so far been neglected in the simulations (Sharma et al., 2018; Wang et al., 2019). Moreover, the high computational effort of LES-LSM simulations necessitates small model domains and short periods. In the present work, we use a combination of measurements and LES-LSM simulations to constrain moisture fluxes in conditions of snow transport.

As both measurements and simulations of drifting/blowing snow sublimation are challenging, it may be useful to explore further methods, which provide additional information about the sublimation process. Measurements of stable water isotopes (SWIs) seem to be a promising approach because phase changes of water are associated with isotopic fractionation (e.g. Beria et al., 2018). In other words, the heavy isotopologues ($H_2{}^{18}O$ and HDO) are preferentially transferred to the denser phase while the lighter isotopologue ($H_2{}^{16}O$) is preferentially transferred to the less dense phase. Consequently, SWI data offer the potential to draw conclusions about phase changes in the hydrologic cycle, which have influenced a water sample most recently (e.g. Kurita et al., 2016a; Thurnherr et al., 2020b).

In the interior of the ice sheets, the isotopic composition of snowfall is largely driven by isotopic distillation, i.e., the preferential removal of heavy isotopologues from the vapor phase with progressing cloud formation. As the extent of cloud formation is determined by the cooling of an air mass, the isotopic composition stored in ice cores can be used to reconstruct the temperature evolution for the past $\sim 700,000$ years (e.g. EPICA community members, 2004). In recent years, progress has been made in understanding the influence of weather conditions on short-term SWI variations in water vapor and snow (e.g., Bréant et al., 2019; Akers et al., 2020; Wahl et al., 2022; Aemisegger et al., 2022). This progress was, to a large

degree, possible due to advances in measurement technology, allowing for a continuous monitoring of the isotopic composition of water vapor with a high temporal resolution. Yet, the knowledge on isotopic fractionation in the process of snow sublimation is still limited. Although measurements provide empirical evidence of isotopic fractionation as a result of sublimation (e.g., Hughes et al., 2021; Wahl et al., 2021), debate continues about the theoretical explanation and appropriate representation in models. Additionally, the literature has not yet addressed the question of how sublimation of drifting and blowing snow affects the isotopic composition. Therefore, SWI analyses can currently not play an important role in quantitative assessments of snow sublimation. Nevertheless, ongoing research efforts may on the long term make it possible to leverage SWI data to improve models of the water cycle and SMB in snow-covered regions.

To harness the full potential of vapor isotopic measurements, it is necessary to develop a complete understanding of all relevant drivers. The present work contributes towards this goal by explaining a vapor isotopic time series measured at the outlet of the Mertz glacier, East Antarctica, which is difficult to reproduce with current isotope-enabled atmospheric models. While similar previous studies have largely focused on the influences of ocean evaporation and cloud formation (Helsen et al., 2006; Thurnherr et al., 2021), we pay special attention to the effect of surface snow sublimation on the isotopic composition of air masses.

Objectives and Structure of the Thesis

This work is part of the SNSF-funded project *From Cloud to Ground: Snow Accumulation in Extreme Environments*, which aims to improve the basic understanding and model representation of the SMB terms in extreme environments, especially the effects caused by snow transport. In this thesis, we focus on the sublimation component. The first goal is to assess the reliability and plausibility of sublimation measurements based on the Monin–Obukhov bulk parameterization and the eddy-covariance technique in conditions of snow transport. In particular, we aim to estimate the theory-related error of the Monin–Obukhov bulk parameterization induced by snow transport. For this purpose, we need insights in the vertical profile of the moisture flux, which can be obtained from LES-LSM simulations. Chapter 1 addresses this first goal and presents an analysis of a snow transport event at the S17 site, Queen Maud Land, coastal East Antarctica, in austral summer 2019 (Fig. 1).

The second goal is to verify the plausibility of a few LES-LSM simulations using sublimation measurements from an eddy-covariance system and snow transport measurements from snow particle counters during the same event at the S17 site. The third goal is to use the insights from these LES-LSM simulations to propose an improved parameterization approach for sublimation and snow transport in large-scale models. Both goals are addressed in Chapter 2. Various parameterization options are tested in a simple one-dimensional model, which resembles the snow transport scheme of the CRYOWRF model and can easily be compared to the LES-LSM simulations.

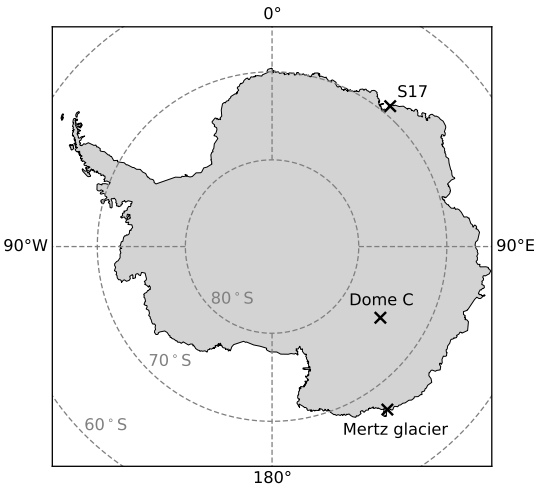

Figure 1: Map of Antarctica with sites studied in this thesis.

The fourth goal is to contribute to a better understandiong of SWI variations in water vapor by assessing the role of surface sublimation and other drivers in shaping the vapor isotopic composition measured on a ship at the outlet of the Mertz glacier, East Antarctica. This assessment is presented in Chapter 3. For this case study, we develop a simple model computing the isotopic composition of air parcels along backward trajectories under the influences of cloud formation and moisture fluxes at the Earth's surface. An important component of the model is the isotopic composition of surface snow, which is validated against measurements at Dome C, East Antarctica (Fig. 1).

The thesis is based on two published articles (Chapters 1 and 3) and one article draft (Chapter 2). The manuscript has been slightly modified, compared to the published articles, to harmonize the spelling and present important definitions in the general introduction instead of the first section of each chapter. The work published as supplementary material is included in the appendix.

1 Evidence of Strong Flux Underestimation by Bulk Parameterizations During Drifting and Blowing Snow

This chapter corresponds to the postprint version of the article published as

Sigmund, A., Dujardin, J., Comola, F., Sharma, V., Huwald, H., Melo, D. B., Hirasawa, N., Nishimura, K., and Lehning, M.: Evidence of Strong Flux Underestimation by Bulk Parametrizations During Drifting and Blowing Snow, *Boundary-Layer Meteorology*, 182, 119–146, https://doi.org/10.1007/s10546-021-00653-x, 2022,

As drifting snow and blowing snow are defined in the general introduction chapter, this definition is omitted in the introduction of the current chapter. AS co-designed the simulations, performed the data analysis, and wrote the first draft of the article.

Abstract

The influence of drifting and blowing snow on surface mass and energy exchange is difficult to quantify due to limitations in both measurements and models, but is still potentially very important over large areas with seasonal or perennial snow cover. We present a unique set of measurements that make possible the calculation of turbulent moisture, heat, and momentum fluxes during conditions of drifting and blowing snow. From the data, Monin–Obukhov estimation of bulk fluxes is compared to eddy-covariance-derived fluxes. In addition, large-eddy simulations with sublimating particles are used to more completely understand the vertical profiles of the fluxes. For a storm period at the Syowa S17 station in East Antarctica, the bulk parameterization severely underestimates near-surface heat and moisture fluxes. The large-eddy simulations agree with the eddy-covariance fluxes when the measurements are minimally disturbed by the snow particles. We conclude that overall exchange over snow surfaces is much more intense than current models suggest, which has implications for the total mass balance of the Antarctic ice sheet and the cryosphere.

1.1 Introduction

Sublimation of snow and ice is a significant component of the surface mass balance of the Antarctic ice sheet, which is an important driver of sea-level rise. However, current sublimation estimates from large-scale atmospheric models are uncertain because snow transport by wind can strongly amplify sublimation rates, and this effect is not or inaccurately represented in large-scale models (Van Wessem et al., 2018; Agosta et al., 2019).

Even on a local scale, drifting and blowing snow can make the quantification of sublimation challenging. In situ measurements of sublimation and evaporation often apply the eddy-covariance (EC) method or the bulk parameterization of Monin–Obukhov similarity theory (MOST). These measurements are not able to capture the part of blowing-snow sublimation that occurs above the measurement height during intense storms. Additionally, snow transport increases the uncertainties of the EC method and the MOST parameterization due to technical and theoretical limitations, respectively. The EC method is affected by advected or falling snow particles or rain droplets which pass through the measurement volume of open-path instruments perturbing the measurement signal (Pomeroy and Essery, 1999; Bintanja, 2001a; LI-COR, 2004; Campbell Scientific, 2017). This problem is typically visible from spikes in the raw data and sometimes indicated by diagnostic values provided by the instruments. During intense blowing-snow or precipitation periods, the transducer pathways of the sonic anemometer may become obscured, resulting in spurious data or data gaps. While a couple studies used the EC method at snow-covered sites for validating sublimation estimates or associated parameters (e.g., King and Anderson, 1994; Box and Steffen, 2001; Stössel et al., 2010; Reba et al., 2012), a few studies discussed the limitations of this technique associated with blowing-snow events. For example, Pomeroy and Essery (1999) mentioned that precipitation and blowing-snow particles near sensor heads perturb the measurements of the sonic anemometer. Nevertheless, they trusted the EC method because the diagnostic values of the sonic anemometer were acceptable. Bintanja (2001a) presented EC measurements during a storm at Svea Station, Drauning Maud Land, Antarctica. Although the diagnostic value of the sonic anemometer frequently indicated a reduced data quality, turbulence characteristics and spectra were in line with standard surface-layer theory and averaged measurement values were consistent with reference measurements. High sublimation rates with a maximum of 100 W m^{-2} were measured at a height of 2 m during the storm. Nowadays, statistical spike removal is used to minimize the influence of data records affected by precipitation or blowing snow (Vickers and Mahrt, 1997; Mauder et al., 2013).

Furthermore, the accuracy of the EC method depends on the validity of a few general assumptions. The method yields the vertical turbulent flux at the measurement height. This flux is only equal to the sum of all sources and sinks of the considered quantity in a representative volume of air between the surface and the measurement height if (i) the mean vertical velocity component is zero (i.e., vertical advection is negligible), (ii) the divergence of horizontal advection of moisture, heat, etc. is zero, (iii) the divergence of the horizontal turbulent flux is zero, and (iv) the conditions are stationary during the averaging period. These assumptions

generally require flat and horizontally homogeneous terrain to be fulfilled (Mauder et al., 2010). A violation of these assumptions can lead to a bias in the surface exchange. In sloped terrain, cold-air drainage can result in significant horizontal and vertical advection terms (Leuning et al., 2008). Several studies have indirectly evaluated the assumptions of the EC method by checking the closure of the surface energy balance using additional measurements of the radiation fluxes, the ground heat flux, and changes in heat storage in the volume between the surface and the height of the EC measurements. Wilson et al. (2002) found a general lack of energy-balance closure at many sites in different climates. The terrain at these sites was flat to hilly and, on average, the EC-based exchange of sensible and latent heat was approximately 20% lower than the available energy, i.e., net radiation minus ground heat flux and change in heat storage. Although the imbalance can also be influenced by uncertainties in the radiation fluxes and the ground heat flux or by a mismatch between the footprint areas of different energy fluxes, the frequent lack of energy-balance closure at many sites has caused some concerns regarding limitations of the EC method. For a flat and heterogeneous site, Mauder et al. (2010) identified buoyancy-driven quasi-stationary circulations as a likely reason for an energy imbalance during daytime. In mountainous terrain, a strong violation of the assumptions of the EC method is expected and a pronounced lack of energy-balance closure can be observed (Stiperski and Rotach, 2016). Additionally, the EC fluxes can be affected by a loss of high-frequency and low-frequency contributions, although correction procedures exist (Massman, 2000; Moncrieff et al., 2004).

The MOST parameterization is based on the same assumptions and additionally assumes that turbulent fluxes are constant with height in the surface layer of the atmosphere (Monin and Obukhov, 1954). The latter implies that the exchange of moisture, heat, and momentum between the air and solid or liquid media only occurs at the surface and not within the atmosphere. Snow transport violates this assumption because a significant part of the exchange happens at the surface of drifting/blowing-snow particles. For example, the latent heat flux (LE) increases with height in the layer of drifting and blowing snow if the snow particles are net moisture sources at all heights of this layer. In these conditions, the MOST parameterization is expected to underestimate the sum of surface and drifting/blowing-snow sublimation because the parameterization does not account for the large surface area and the strong ventilation of the particle–air interface (Schmidt, 1982).

Thiery et al. (2012) and Barral et al. (2014) investigated snow sublimation at Antarctic sites and assumed that the MOST parameterization is still a good estimate of surface sublimation only (i.e., the part of the phase change that happens at the snowpack surface) during periods of drifting snow. However, the MOST parameterization may overestimate surface sublimation but underestimate total sublimation during drifting-snow events if drifting snow represents a net moisture source and a net momentum sink. The former reduces the vertical humidity gradient at the surface and the latter reduces turbulence near the surface, resulting in lower rates of surface sublimation. To properly account for these effects, the local gradients at the surface would be needed, but these are typically not available. If turbulent fluxes vary with height, the result of the MOST parameterization depends on the upper measurement height.

In drifting-snow conditions, the MOST parameterization rather reflects a case without drifting snow and with the same humidity and wind velocity values at the considered heights as in the real drifting-snow case, at least if a constant roughness length is used.

Due to the challenges described above, the current knowledge on the sublimation of blowing snow is largely based on models. On local scales, large-eddy simulations coupled with a Lagrangian stochastic model (LES–LSM) have become a valuable tool for studying the thermodynamic interactions between particles and the air and to test assumptions made in simpler or larger-scale models (Sharma et al., 2018; Wang et al., 2019). A first quantitative comparison between in situ field measurements and LES–LSM results with respect to the sublimation of drifting and blowing snow was presented by Wang et al. (2019). However, these simulations assumed zero surface fluxes of latent and sensible heat at the lower domain boundary and the comparison did not involve direct turbulence measurements but a parameterization of the sublimation of drifting and blowing snow based on mean wind speed, humidity, and air temperature measurements at several heights (Bintanja, 2001a). Therefore, further comparisons between sublimation measurements and state-of-the-art numerical models are necessary to constrain sublimation rates in conditions of drifting and blowing snow.

The overarching objective of this study is to explain differences between the sublimation rates measured using two common in situ methods during snow-transport events. The following hypotheses are tested: (i) the MOST parameterization results in significant errors in turbulent fluxes during snow-transport events due to the false assumption of height-constant fluxes (theory-related errors); (ii) the EC method provides more reliable estimates for turbulent fluxes during snow-transport events, at least if the snow is mainly transported below the measurement height and snowfall is absent. Although the focus is on the latent heat flux (LE), the sensible heat flux (H), and the momentum flux (τ) are also compared between the measurement techniques. A drifting/blowing-snow event at the S17 site, Queen Maud Land, Antarctica, is discussed in detail. Using a case study with saltation-dominated snow transport and a case study with negligible snow transport, the coherence between the measurements and LES–LSM results is examined and the uncertainties of the MOST parameterization are estimated.

1.2 Methods

1.2.1 Measurement Site and Instrumentation

The S17 site (69°01′28″S, 40°05′14″E, 600 m above sea level) is located near the Japanese research station Syowa. The surrounding terrain is flat and homogeneous with a slight slope of less than 2° towards the coast, which is approximately 15 km west of the S17 site. Apart from some uncovered hills and rocks at the coast, the area is covered by snow throughout the year. During a field trip in January 2019, the wind direction was dominated by north-easterly to south-easterly directions with an unobstructed fetch of hundreds of kilometres over a homo-

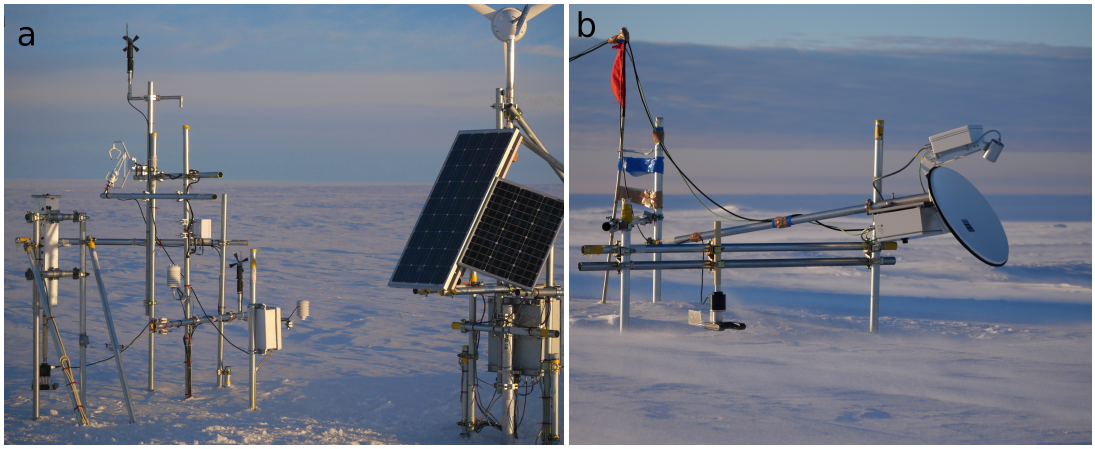

Figure 1.1: Measurement set-up at the S17 site: (a) micrometeorological station and (b) the MRR and SPC devices.

geneous snow surface. This study investigates the period from 10 to 13 January 2019, which includes an intense blowing-snow event. A micrometeorological station was equipped with a three-dimensional ultrasonic anemometer, an open-path infrared gas analyzer, a snow particle counter (SPC), an infrared radiometer for surface-temperature measurements, and standard meteorological sensors (Fig. 1.1a). Instruments, manufacturers, measurement heights, and data-acquisition intervals are specified in Table 1.1. Turbulent fluxes were computed using both the EC method and the MOST parameterization. From the ultrasonic anemometer (CSAT3, Campbell Scientific, Logan, USA), the digital output was used, which has a higher resolution than the analogue output.

In addition to the micrometeorological station, a Micro Rain Radar, MRR (MRR-Pro, METEK, Elmshorn, Germany), was installed at a horizontal distance of approximately 500 m. Although this instrument is usually deployed as a vertically pointing radar for precipitation measurements (Peters et al., 2002; Maahn and Kollias, 2012), a tilted configuration with an elevation angle of 7° was tested to observe the blowing-snow layer. Recently, Walter et al. (2020) demonstrated that a horizontally pointing radar can provide valuable data on blowing snow off a mountain ridge. In the present study, MRR measurements were used to estimate the depth of the blowing-snow layer and to assist in data interpretation. The offset parabolic antenna was installed such that its centre was at a height of 0.8 m and it was facing the dominant wind direction. With a range-gate length of 10 m, the vertical spacing between the range gates was 1.22 m and the measurements ranged up to a height of 39 m. The Doppler spectrum covered radial velocity components between 0 and 48 m s^{-1}. The time interval for internal averaging was initially 32 s and was conditionally reduced to 1 s when snow transport became intense. At the location of the MRR, an additional SPC was installed at a height of approximately 0.1 m above the surface.

Table 1.1: Instruments, variables, measurement heights (z), and data-acquisition interval (Δt) for the micrometeorological station.

Instrument	Instrument model	Variables	z (m)	Δt (s)
Ultrasonic anemometer	CSAT3, Campbell Scientific, Logan, USA	Wind velocity components, sonic temperature	1.9	0.05
Infrared gas analyzer	LI-7500, LI-COR, Lincoln, USA	Water-vapor molar density, air pressure	1.9	0.05
Propeller anemometer	Wind monitor 05108-45, Young, Traverse City, USA	Wind speed and direction	1.0, 3.0	30
Temperature/humidity probe	CS215, Campbell Scientific, Logan, USA	Air temperature, relative humidity	1.0	30
Infrared radiometer	SI-111, Campbell Scientific, Logan, USA	Surface temperature	0[a]	30
Snow particle counter	SPC-95, Niigata Electric, Japan	Particle number per size class	0.15	1

[a] Nominal height in contrast to the installation height of the radiometer of $z = 0.5$ m

1.2.2 Processing of Measurement Data

All measurements were aggregated into 10-min intervals. This time scale was chosen to avoid a significant influence of non-turbulent motions such as gravity waves on the EC turbulent fluxes.

Because a naturally ventilated radiation shield was used with the temperature and relative humidity probe, periods with low wind speeds resulted in an overestimation of the air temperature due to solar heating. This problem was evident from a comparison with the sonic temperature (not shown). Therefore, the air temperature was discarded if the wind speed was below 1 m s^{-1}.

Eddy-Covariance Method

The EC method enables a direct quantification of vertical turbulent fluxes by means of high-frequency measurements of the respective covariance components. For example, the latent heat flux (W m^{-2}) is given by

$$LE = L\,\overline{w'\rho_v'}\,, \tag{1.1}$$

where $\overline{w'\rho_v'}$ (kg m^{-2} s^{-1}) is the covariance between the vertical velocity component, w (m s^{-1}), and water-vapor density, ρ_v (kg m^{-3}), and L (J kg^{-1}) is the latent heat of sublimation. A positive LE indicates an upward flux (sublimation) while a negative LE indicates a downward flux (vapor deposition). The same sign convention applies to other turbulent fluxes.

The data post-processing included the removal of artifacts and spikes, a bias correction for vapor density, and common corrections for time lags, for the difference between sonic temperature and air temperature, for density fluctuations, and for spectral losses. Details on these procedures are presented in Appendix A. Block averaging was used to calculate the fluctuations (the 'prime' quantities). A large part of the post-processing was performed using the EddyPro® Software (LI-COR Biosciences, 2019). Finally, a quality-control procedure similar to that in Mauder et al. (2013) was applied. The EddyPro® output includes quality-control results of the tests on steady state and well-developed turbulence described by Foken et al. (2004). Each test yielded a flag of 0, 1, or 2, indicating good, intermediate, or bad quality, respectively. Additionally, a test on missing data (not a number test, NaN test) was introduced, yielding a flag of 0, 1, or 2 if the fraction of missing data was ≤ 10%, between 10% and 25%, or > 25%, respectively. The flags of the three tests were summed and values higher than 2 were set to 2 to continue the concept of three quality classes. Taking into account that the variables LE and H depend on each other due to the correction for the difference between the sonic temperature and air temperature and the correction for density fluctuations, the flag of one of these fluxes was increased by +1 if the quality of the other flux was bad (Mauder et al., 2013).

Monin–Obukhov Bulk Parameterization

According to MOST, the latent heat flux (W m^{-2}) can be expressed as (e.g., Monin and Obukhov, 1954; King et al., 2001)

$$LE = -\rho\, L\, C_q\, \bar{u}\, (\bar{q}_z - \bar{q}_0)\,, \tag{1.2}$$

where $\bar{q}_z$ and $\bar{q}_0$ (kg kg^{-1}) are average specific humidity at height z (m) and at the surface, respectively, $\bar{u}$ (m s^{-1}) is average wind speed at height z, and ρ (kg m^{-3}) is air density. The specific humidity at the surface was calculated from the measured surface temperature assuming saturation. Although the radiometer measurements of surface temperature are influenced by the temperature of drifting and blowing snow, the resulting bias is expected to be small because the concentration of particles quickly decreases with height and saltating particles are not expected to reach a thermal equilibrium with the air due to their short residence time in the air (Sharma et al., 2018). The dimensionless exchange coefficient for moisture, C_q, is given by

$$C_q = \frac{\kappa^2}{\left[\ln\left(\frac{z}{z_{0q}}\right) - \Psi_q(\frac{z}{L})\right]\left[\ln\left(\frac{z}{z_0}\right) - \Psi_m(\frac{z}{L})\right]}\,, \tag{1.3}$$

where $\kappa = 0.4$ is the von Kármán constant, z_{0q} and z_0 (m) are the roughness lengths for humidity and momentum, respectively, Ψ_q and Ψ_m are the stability corrections for latent heat and momentum, respectively, z (m) is the sampling height, and L (m) is the Obukhov length. The momentum and sensible heat fluxes are parameterized using analogue equations (e.g., King et al., 2001).

Based on the friction velocity measured by the ultrasonic anemometer in neutral conditions, z_0 was estimated to be 10^{-4} m, a typical value for rather flat snow surfaces. This value was assumed to remain constant with varying friction velocity. This assumption is supported by Andreas et al. (2010), at least for friction velocities larger than 0.15 m s^{-1}. Friction velocities below this value are very rare in the present dataset. The roughness lengths for humidity and temperature were calculated as a function of the friction velocity and z_0 according to the parameterization of Andreas (1987). Although measurement uncertainties make it difficult to validate this parameterization, a couple of studies support the plausibility of the parameterization at snow-covered sites with $z_0 < 10^{-3}$ m (Smeets and van den Broeke, 2008; Andreas et al., 2010; Park et al., 2010; Vignon et al., 2017; Liu et al., 2020).

The Monin–Obukhov stability parameter, $z\,L^{-1}$, was calculated iteratively, starting with a value of zero. For stable and neutral conditions ($z\,L^{-1} \geq 0$), the stability correction of Stearns and Weidner (1993) was used and for unstable conditions ($z\,L^{-1} < 0$), the stability correction of Businger et al. (1971) with the modifications of Högström (1988) was used. In the study of Schlögl et al. (2017), the MOST parameterization showed a low sensitivity to the choice of the stability correction functions, when applied to stable conditions at alpine and polar sites.

Drifting-Snow Mass Flux

The SPC optically detects snow particles in a volume (width × height × depth) of 25 × 2 × 0.5 mm^3 (Sugiura et al., 1998). The instrument aligns itself with the wind direction by means of a wind vane. The measurement output includes particle numbers for 64 size classes with mean diameters from 36 μm to 490 μm and time intervals of 1 s. The recorded particle diameters are equivalent diameters based on the assumption of a spherical shape. Because the measurement volume is limited by a depth of 500 μm, particles with larger diameters are assigned to the largest size class. The SPC cannot distinguish between particles lifted from the surface and snowfall particles but snowfall can be ruled out if the MRR only detects particles below a certain height.

Because the measured particle diameters depend on temperature, the SPC also records the temperature to enable a correction for the difference between the observed temperature and the reference temperature during factory calibration. This temperature correction was performed using the post-processing software of the manufacturer and increased the particle sizes because the observed temperatures were higher than the reference temperature. The horizontal mass flux of drifting or blowing snow (kg m^{-2} min^{-1}) was calculated as described by Sugiura et al. (1998), assuming spherical snow particles with the density of ice, 918.4 kg m^{-3}.

Estimating the Depth of the Blowing-Snow Layer

The depth of the blowing-snow layer was estimated using two standard products provided by the MRR instrument: the signal-to-noise ratio (*SNR*) and the radial velocity component. The signal-to-noise ratio (dB) is defined by

$$SNR = 10 \log \frac{S}{N} = 10 \log \frac{\int_{v_{r1}}^{v_{r2}} (s(v) - s_n) \mathrm{d}v_r}{s_n (v_{r2} - v_{r1})} , \tag{1.4}$$

where S and N are signal power and noise power, respectively, s is the spectral signal power of the raw Doppler spectrum, s_n is the value for the noise level, and v_{r1} and v_{r2} are the radial velocity components limiting the spectral peak. With the tilted MRR configuration, the horizontal projection of the radial velocity component (m s^{-1}),

$$u_{MRR} = \cos(\beta)\ v_r , \tag{1.5}$$

is a measure of the mean velocity of blowing-snow particles, which is close to the wind speed. Here, $\beta = 7°$ is the elevation angle of the radar beam and v_r (m s^{-1}) is the radial velocity component.

The raw Doppler spectra of the MRR frequently contained artifacts, characterized by a high spectral signal power at radial speeds close to the minimum (0 m s^{-1}) and maximum (48 m s^{-1}) values and mainly in the lowest few range gates (Fig. 1.2a). Possible reasons are ground clutter and enhanced turbulence around the offset parabolic dish resulting in radial speeds around

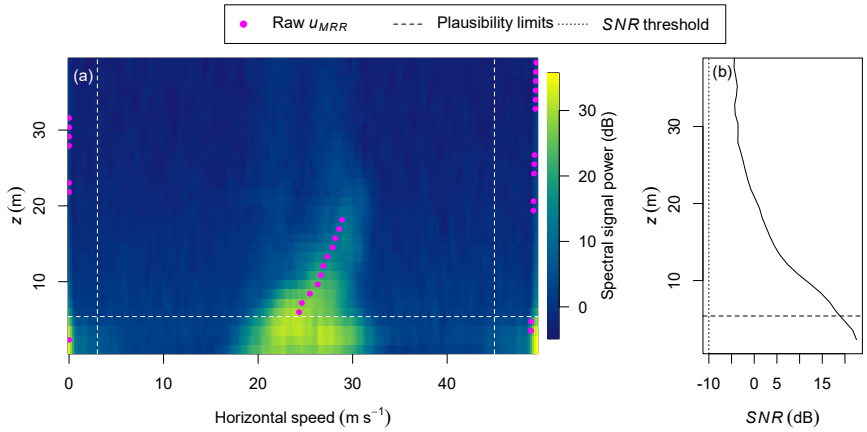

Figure 1.2: Example raw data of the Micro Rain Radar (2-s averages, 11 January 2019, 13:01 UTC): (a) Doppler spectrum and horizontal projection of the radial velocity component (u_{MRR}), (b) signal-to-noise ratio (SNR) as a function of height (z).

zero, which partly appear at the upper edge of the velocity spectrum because of aliasing. Due to these artifacts, the first four range gates were discarded. Thus, our estimate of the depth of the blowing-snow layer only accounts for layers that exceed a height of 5.4 m. Raw data of both u_{MRR} and SNR can be affected by the artifacts, especially at low heights and with an absent or weak blowing-snow signal. The influence of the artifacts was mostly evident from implausible radial speeds that are either close to zero or 48 m s^{-1}. Thus, u_{MRR} values below 3 m s^{-1} or above 45 m s^{-1} were discarded.

Before averaging the data per 10-min intervals, the SNR was converted from dB units to the dimensionless power ratio. After the averaging, the power ratio was converted back to dB units. The depth of the blowing-snow layer was estimated to be the height up to which (i) the average SNR was larger than −10 dB and (ii) the instantaneous u_{MRR} values were at least partly between the plausibility limits mentioned above. For several points in time, this estimate was validated by visually inspecting the raw and the 10-min mean Doppler spectra (Fig. 1.2).

1.2.3 Simulations

The LES–LSM model is able to capture the effect of turbulent variations in space and time on the interaction between individual drifting/blowing-snow particles and the atmosphere. The simulation set-up aimed at reproducing the steady-state meteorological conditions measured during a 10-min interval. With a height of 6 m, the simulation domain comprised the near-surface atmosphere above a horizontal snow surface with an area of 18 × 18 m^2. The domain contained 96 and 64 grid points along the horizontal and vertical directions, respectively. The grid spacing was uniform in the horizontal directions (0.1875 m) and stretched in the vertical direction (from 0.015 m at the surface to 0.172 m at the upper boundary). The domain size and grid spacing was a trade-off between an acceptable computation time, a high spatial

resolution, and large (horizontal) dimensions that enable the development of large-scale coherent structures (Munters et al., 2016). High spatial and temporal resolutions are required to resolve the motion of drifting/blowing-snow particles in a Lagrangian frame of reference and the thermodynamic interaction with the air. For this reason, a timestep of 5×10^{-5} s was used. A disadvantage of the rather small domain size is the fact that the maximum size of represented turbulence elements is limited and the contribution of larger turbulence elements to the turbulent fluxes is missing in the simulations. This limitation is currently unavoidable because a larger domain size would lead to unacceptably long simulation times.

In the simulations, the flow is driven by a constant large-scale pressure gradient. The turbulent airflow is simulated by solving the Navier–Stokes equations for incompressible flows while the fields of air temperature and specific humidity are computed using advection–diffusion equations. Subgrid-scale turbulent fluxes are taken into account by applying the scale-dependent Lagrangian dynamic model of Bou-Zeid et al. (2005). Snow transport is simulated considering drag and gravitational forces. To improve the computation time, the trajectories and properties of the snow particles are not modeled individually but for groups of identical particles. Within each group, the particles are assumed to have the same trajectory and identical properties such as location, diameter, mass, and temperature. The number of particles in a group can range between 5000 and 250,000 and is determined during aerodynamic or splash entrainment depending on the local surface shear stress or the impact properties of a group of particles, respectively. After reaching a steady state, the total number of particles aloft was approximately 9.16×10^8 and the number of particle groups was approximately 38,500. Aerodynamic entrainment, rebound, and ejection of particles at the surface are simulated through statistical formulas based on conservation principles (Comola and Lehning, 2017; supplement of Sharma et al., 2018).

A summary of the simulation parameters is presented in Table 1.2. Two cases were simulated: a case with significant snow transport named 'Drift' and another case with negligible snow transport named 'NoDrift'. For each case, the simulation was repeated once, using modified values for the upper boundary conditions for humidity and temperature to study the sensitivity of the modeled sublimation. In the following, the four set-ups are referred to as Drift_1, Drift_2, NoDrift_1, and NoDrift_2. The initial particle diameter of entrained particles is taken from a log-normal distribution that results in similar sizes of drifting/blowing-snow particles compared to the SPC measurements (Fig. 1.3). The choice of a log-normal distribution is based on the study of Colbeck (1986), which determined a log-normal size distribution in water-saturated snow. The initial particle temperature is equal to the surface temperature.

The exchange of moisture, heat, and momentum between particles and the atmosphere is represented by source or sink terms in the advection–diffusion and Navier–Stokes equations. To this end, the coupled mass-balance and energy-balance equations for individual snow particles in turbulent flow are solved, neglecting radiative heat transfer (Sharma et al., 2018):

$$\frac{\mathrm{d}m_p}{\mathrm{d}t} = \pi \, D \, d_p \, (\rho_{v,\infty} - \rho_{v,p}(T_p)) \, Sh \,, \tag{1.6}$$

Table 1.2: Important simulation parameters: two cases were simulated (Drift, NoDrift) and for each case, the simulation was repeated with a modified upper boundary condition. For the NoDrift case, the parameters are only specified if they differ from those of the Drift case.

Parameter	Symbol	Units	Drift	NoDrift
Specific heat capacity of ice	c_i	$\mathrm{J\,kg^{-1}\,K^{-1}}$	2035.7	
Specific heat capacity of air	$c_{p,f}$	$\mathrm{J\,kg^{-1}\,K^{-1}}$	1005.0	
Specific heat capacity of vapor	$c_{p,v}$	$\mathrm{J\,kg^{-1}\,K^{-1}}$	1854.2	
Diffusivity of vapor in air	D	$\mathrm{m^2\,s^{-1}}$	1.96×10^{-5}	
Thermal conductivity of air	k	$\mathrm{W\,m^{-1}\,K^{-1}}$	0.023	
Density of ice	ρ_p	$\mathrm{kg\,m^{-3}}$	918.4	
Density of air	ρ	$\mathrm{kg\,m^{-3}}$	1.18	
Mean initial particle diameter	$\bar{d}_p$	μm	260	
Standard deviation of initial particle diameter	$\sigma(d_p)$	μm	130	
Large-scale pressure-gradient force	F_x	$\mathrm{m\,s^{-2}}$	0.068	0.0019
Momentum roughness length	z_0	m	10^{-4}	
Temperature roughness length	z_{0T}	m	5×10^{-5}	10^{-4}
Humidity roughness length	z_{0q}	m	5×10^{-5}	1.2×10^{-4}
Surface temperature	T_s	°C	−5.63	−2.53
Surface specific humidity	q_s	$\mathrm{g\,kg^{-1}}$	2.613	3.361
Temperature gradient at upper boundary	$\mathrm{d}T\ (\mathrm{d}z)^{-1}$	$\mathrm{K\,m^{-1}}$	12.57	−5.76[c], 0[d]
Specific humidity gradient at upper boundary	$\mathrm{d}q\ (\mathrm{d}z)^{-1}$	$\mathrm{g\,kg^{-1}\,m^{-1}}$	−1.4[a], −3.5[b]	−2.280[c], −0.608[d]

[a] Drift_1
[b] Drift_2
[c] NoDrift_1
[d] NoDrift_2

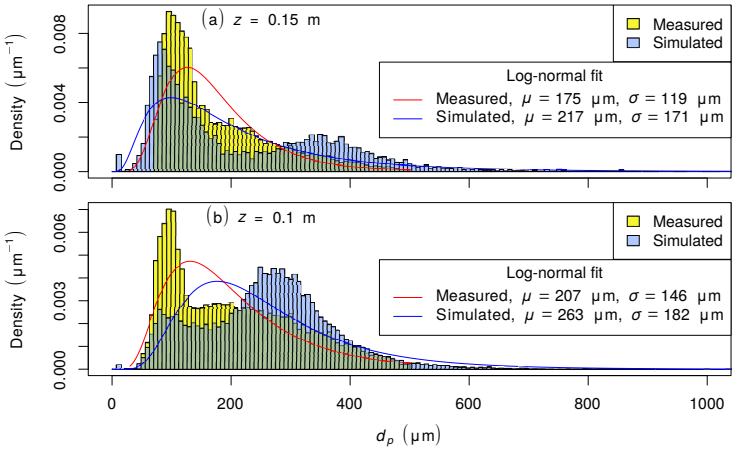

Figure 1.3: Particle size distributions for the Drift_1 simulation set-up and SPC measurements at the S17 site on 11 January 2019, 00:40 to 00:50 UTC: probability density as a function of particle diameter (d_p) at a height of (a) 0.15 m and (b) 0.1 m. The legend specifies the mean (μ) and the standard deviation (σ) of d_p for a log-normal fit based on maximum-likelihood estimation.

$$c_i m_p \frac{\mathrm{d}T_p}{\mathrm{d}t} = L \frac{\mathrm{d}m_p}{\mathrm{d}t} + \pi\, k\, d_p\, (T_{a,\infty} - T_p)\, Nu\,, \tag{1.7}$$

where m_p (kg), d_p (m), and T_p (K) are the mass, diameter, and temperature of a spherical snow particle, respectively; $\rho_{v,\infty}$ (kg m^{-3}) and $T_{a,\infty}$ (K) are the temperature and vapor density of the surrounding air, respectively; $\rho_{v,p}$ (kg m^{-3}) is the vapor density at the particle surface; t (s) is time; Nu and Sh are the dimensionless Nusselt and Sherwood numbers, respectively; and the remaining parameters are included and explained in Table 1.2. In contrast to the widely used formula of Thorpe and Mason (1966), Eqs. 1.6 and 1.7 account for the temperature difference between the particles and the air. This effect is important for an accurate simulation of the moisture exchange, especially for particles in saltation due to their short residence time in the atmosphere (Sharma et al., 2018).

Periodic boundary conditions are required in the horizontal directions because of a Fourier-based pseudo-spectral approach for computing horizontal gradients (Albertson and Parlange, 1999). The lower boundary conditions include constant values for temperature and specific humidity based on the measured average surface temperature and the assumption of saturation at the surface (Table 1.2). As a result, the surface LE and H values are given by the subgrid-scale fluxes at the lower boundary, which are calculated by applying the MOST parameterization to the layer between the surface and the next higher grid level (0.0075 m). The surface shear stress is computed in a similar way. In these computations, the same roughness lengths for momentum, temperature, and humidity are used as in the calculation of the measured MOST-based fluxes (Table 1.2). To achieve steady-state humidity and temperature profiles, constant non-zero gradients of humidity and temperature were prescribed as an

upper boundary condition. These gradients resulted in moisture and heat transport through the upper boundary by means of subgrid-scale fluxes while the resolved fluxes were zero due to the condition of zero vertical velocity component at the upper boundary. Therefore, unrealistically strong temperature and humidity gradients were needed at the upper boundary. In an ideal simulation set-up, the domain height would be larger and would correspond to the boundary-layer height. This was not possible due to long simulation times. Nevertheless, the analysis focuses on the lowest 2 m of the domain, which is sufficiently far from the upper boundary to achieve realistic conditions. A few values for the humidity and temperature gradients at the upper boundary were tested until the resulting quasi-stationary profiles agreed with the average in situ measurements.

The initial conditions included linear profiles for temperature and specific humidity and a logarithmic profile for the wind speed. Each simulation covered a period of 850 s. During the first 25 s of the simulations, a stationary turbulent flow developed while snow transport was disabled. Subsequently, snow transport was allowed and in the Drift simulations, the horizontal mass flux reached a steady state after a total of 250 s. At the same time, the vertical profiles of temperature and specific humidity approximately reached a steady state. The subsequent 600 s of the simulations were compared with the measurements.

The simulation data was post-processed to obtain the fluxes LE and H as a function of height. Due to mass and heat conservation, these fluxes are equal to the mean cumulative exchange of latent and sensible heat between the snow (surface and airborne particles) and the air in steady-state conditions:

$$LE(z) = \frac{1}{N_i} \sum_{i=1}^{N_i} \left[LE(0) - \frac{1}{A} \sum_{p=1}^{N_p(z)} \left(L n_p \frac{\mathrm{d}m_p}{\mathrm{d}t} \right) \right] , \tag{1.8}$$

$$H(z) = \frac{1}{N_i} \sum_{i=1}^{N_i} \left[H(0) + \frac{1}{A} \sum_{p=1}^{N_p(z)} \left(n_p \left(S_{h1} + S_{h2} \right) \right) \right] , \tag{1.9}$$

where N_i is the number of output times during the steady-state period, $LE(0)$ (W m^{-2}) and $H(0)$ (W m^{-2}) are the respective surface fluxes (i.e., the fluxes at a height of 0 m corresponding to the surface of the snowpack), N_p is the number of particle groups below height z, n_p is the number of particles within group p, A (m^2) is the area of a horizontal cross-section of the domain, and S_{h1} (W) is the sensible-heat source resulting from convective heat transfer between a particle and the air:

$$S_{h1} = -\pi \, k \, d_p \, (T_{a,\infty} - T_p) \, Nu \, , \tag{1.10}$$

where k is the thermal conductivity of air (W m^{-1} K^{-1}). The variable S_{h2} (W) is the sensible-heat source resulting from the temperature change of the vapor exchanged between the particle and the air:

$$S_{h2} = \frac{\mathrm{d}m_p}{\mathrm{d}t}\, c_{p,v}\, (T_{a,\infty} - T_p)\,, \tag{1.11}$$

where $c_{p,v}$ (J kg^{-1} K^{-1}) is the specific heat capacity of vapor.

For the height of the EC measurements (1.9 m), *LE* and *H* were additionally calculated from the simulation data using the EC method. More precisely, the sum of the resolved flux, F_{res} (W m^{-2}), and the parameterized subgrid-scale flux, F_{SGS} (W m^{-2}), was computed as

$$F = F_{res} + F_{SGS}\,, \tag{1.12}$$

where F (W m^{-2}) represents either *LE* or *H* and F_{res} is based on the covariance $\overline{w'\rho_v'}$ or $\overline{w'T'}$ (Eq. 1.1). Here, F was averaged horizontally over all grid nodes at the considered height, and F_{SGS} only accounts for 1.5% to 1.8% of the magnitude of F.

1.3 Results and Discussion

1.3.1 Discrepancy Between the Measurement Techniques

From 10 to 13 January 2019, a strong storm with a 10-min averaged wind speed of up to 23 m s^{-1} at a height of 1 m occurred at the S17 site (Fig. 1.4a). During an initial period with increasing wind speeds, the radial velocity component measured by the MRR was beyond the plausibility limits and was discarded (Fig. 1.4b). This observation is consistent with low *SNR* values for the MRR signal, indicating that blowing snow did not exceed the minimum detection height of 5.4 m until 11 January 2019, 06:30 UTC (Fig. 1.4c). However, the SPCs measured drifting snow during that initial period with a maximum horizontal mass flux of 38 kg m^{-2} min^{-1} and 19 kg m^{-2} min^{-1} at a height of 0.1 m and 0.15 m, respectively (Fig. 1.4d). Periods in which at least one of the SPCs indicated drifting snow are highlighted by the grey shading in Fig. 1.4 using a noise threshold of 0.005 kg m^{-2} min^{-1}. As of 11 January, 00:00 UTC, spikes were removed from the data of the ultrasonic anemometer, suggesting that the blowing-snow layer extended up to a height of 1.9 m or more (Fig. 1.4e).

At a height of 1 m, relative humidity with respect to ice was initially 87% and showed an increasing trend before reaching 100% in the late morning of 11 January 2019 (Fig. 1.4f). During the first three hours of the investigation period both the EC method and the MOST parameterization yield a value of *LE* close to zero, while the drifting-snow mass flux was very low (Fig. 1.4d and 1.5a). Subsequently, the EC method indicates an increasing value of *LE* of up to 65 W m^{-2}, coinciding with an increasing trend in the drifting-snow mass flux. Thus, the increase in relative humidity may be largely explained by sublimation of drifting and blowing snow. The maximum sublimation rate was reached before the near-surface air became saturated. For the MOST-based estimate, the sublimation rate remains much lower, with a maximum value of 21 W m^{-2}, three times lower than the EC-based value. Initially, the

snow surface was cooler than the air, indicating a statically stable stratification (Fig. 1.5b). After the drifting-snow mass flux reached high values on 11 January 2019, 00:00 UTC, the surface temperature increased more rapidly than the air temperature, resulting in an approximately isothermal temperature profile during the rest of the storm event. The strong surface heating may be explained by a combination of strong turbulent mixing, incoming solar radiation, enhanced downward longwave radiation due to drifting snow, and, potentially, the release of

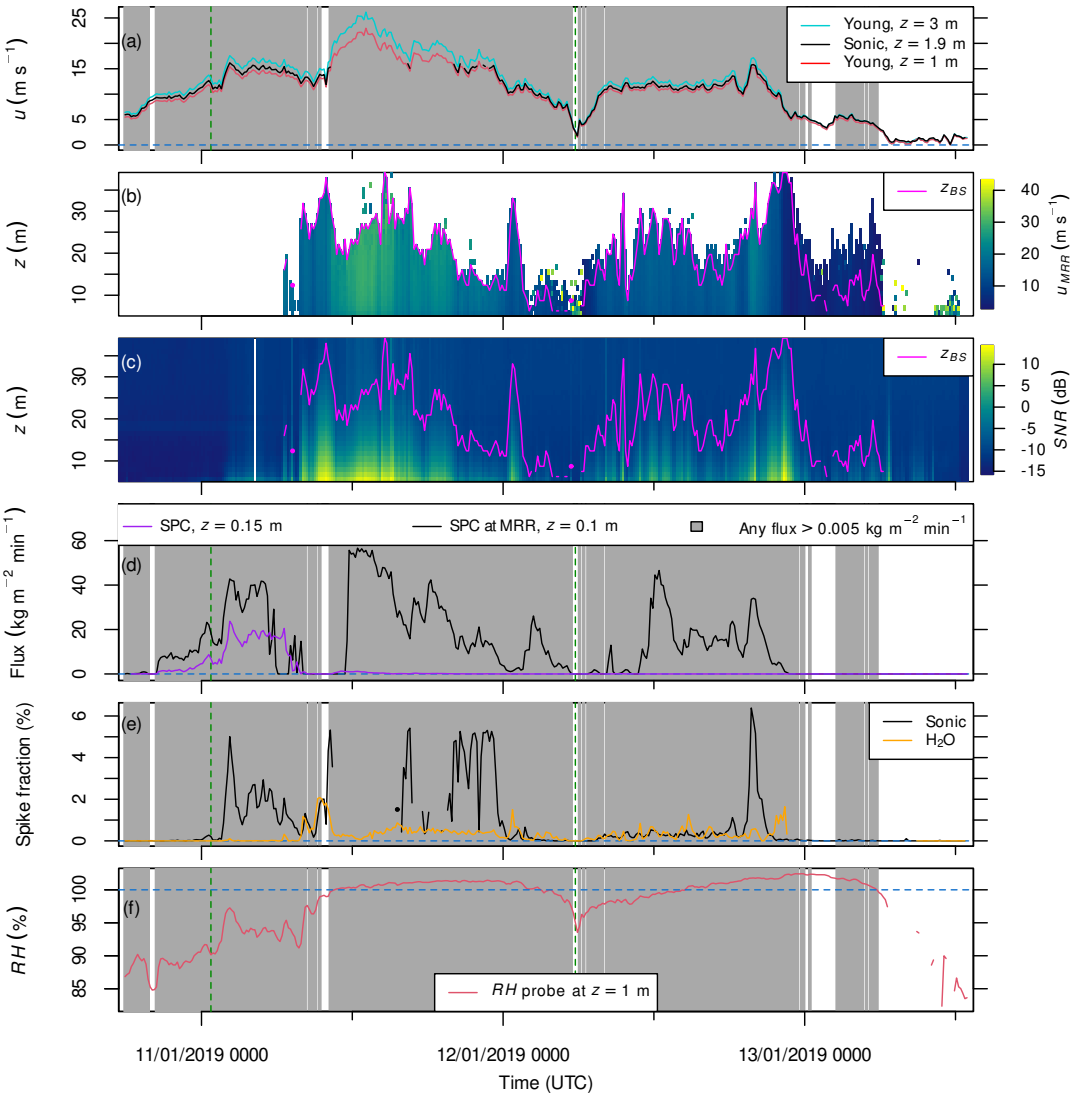

Figure 1.4: Measurements at the S17 site from 10 to 13 January 2019: 10-min averages of (a) wind speed; (b) horizontal blowing-snow speed (u_{MRR}) as a function of height (z), where z_{BS} is the depth of the blowing-snow layer; (c) signal-to-noise ratio for the MRR; (d) horizontal flux of drifting and blowing snow based on the SPCs (grey-shaded in all panels if noise is exceeded); (e) fraction of removed spikes in the EC data; (f) relative humidity with respect to ice. The dashed green lines highlight two example situations, which are compared with simulations in Fig. 1.6 and B.4.

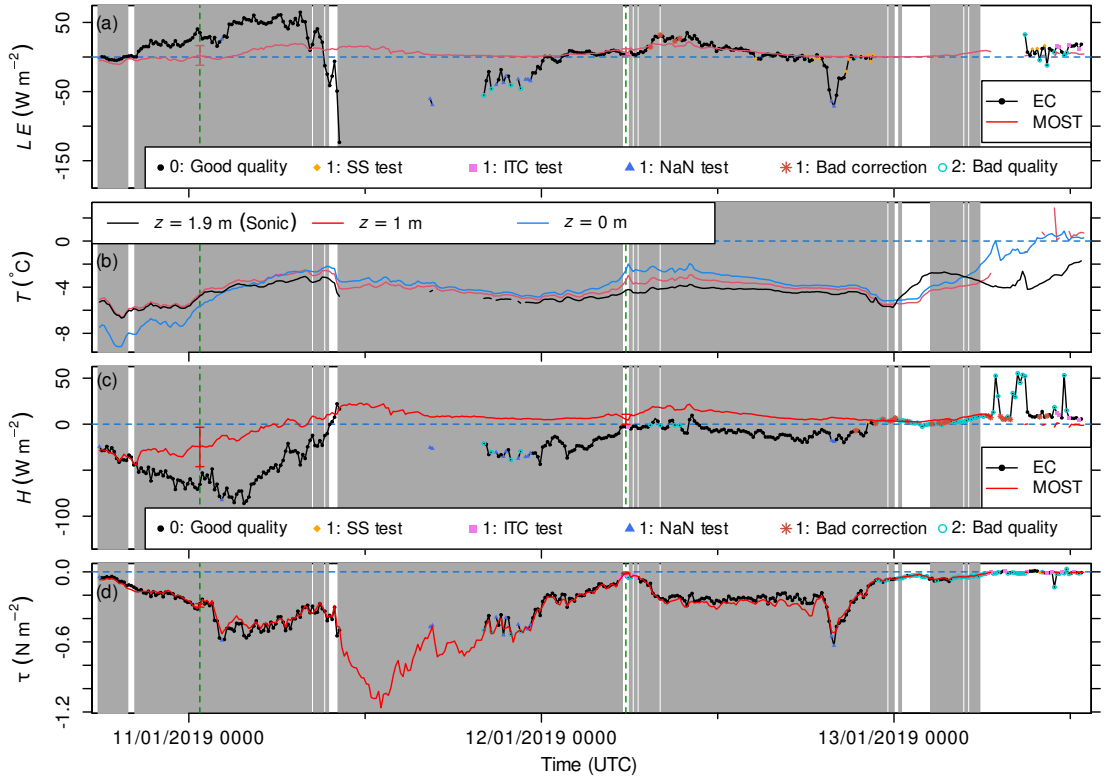

Figure 1.5: (a) Latent heat flux for the EC method and the MOST parameterization with quality-control flags and reasons for an intermediate quality, e.g., tests on steady-state (SS) and developed turbulence (or integral turbulence characteristic, ITC); (b) air and surface temperatures; (c) sensible heat flux; and (d) momentum flux. Instrument-induced standard uncertainties of MOST-based fluxes are shown for two example situations (dashed green), which are compared with simulations in Fig. 1.6 and B.4. The grey shading indicates blowing snow as in Fig. 1.4.

latent heat through vapor deposition at the surface (Yamanouchi and Kawaguchi, 1985; Palm et al., 2018).

When the maximum sublimation rate was reached, the MRR device began to detect a blowing-snow layer with a depth varying between 12 m and 39 m during the subsequent 18 h, which represents the most intense phase of the storm (Fig. 1.4b, c). During this phase, the SPC at the micrometeorological station measured a mass flux close to zero while the SPC at the MRR site measured high mass fluxes apart from the beginning of the phase (Fig. 1.4d). In the field, it was observed that drifting-snow particles can form a thin ice layer on the optical windows of the SPCs, especially in warm conditions. This problem likely explains the very low mass fluxes measured by one or both SPCs while blowing snow was evident from the MRR data and from spikes in the EC data (Fig. 1.4b–e). At the MRR site, the ice layer was manually removed from the SPC windows from time to time but this could not be performed at the micrometeorological station because of its remoteness under such conditions. Apart

from this problem, very intense drifting-snow events can result in a saturation of the SPC measurements, i.e., an individual detection of particles is not possible because the particle concentration or velocity is too high.

During the most intense phase of the storm, relative humidity reached a value of 100% at a height of 1 m and the EC method yielded a downward *LE*, suggesting considerable vapor deposition below the measurement height of 1.9 m (Fig. 1.4f and 1.5a). After measuring a minimum *LE* of $-120\ \mathrm{W\,m^{-2}}$, the EC method failed during the highest wind speeds ($> 15\ \mathrm{m\,s^{-1}}$) due to data gaps and many artifacts. When the wind speed decreased again, the EC-based *LE* values still indicate considerable vapor deposition with values increasing gradually from $-70\ \mathrm{W\,m^{-2}}$ to $0\ \mathrm{W\,m^{-2}}$. For a few data points, the quality-control tests indicate an intermediate or bad quality, mainly due to a large fraction of missing data. Because the depth of the blowing-snow layer was much higher than the sensor heights for the in situ measurements, it is expected that the vapor deposition in the near-surface atmosphere was offset or outweighed by blowing-snow sublimation in a potentially unsaturated upper part of the blowing-snow layer. In contrast to the EC method, the MOST parameterization does not suggest vapor deposition but a weak upward or zero *LE* flux while the air was saturated (Fig. 1.5a).

In the morning of 12 January 2019, the storm ceased for a short time and neither the MRR, nor the SPCs, nor the spike-removal algorithm indicate drifting snow (Fig. 1.4a–e). At the same time, the relative humidity dropped to 94% (Fig. 1.4f). Subsequently, the wind speed increased again and stayed at $11\ \mathrm{m\,s^{-1}}$ for many hours, resulting in drifting and blowing snow. During this phase, relative humidity slowly increased and reached 100% after a few hours. The EC method and the MOST parameterization indicated similar sublimation rates during this phase. The only exception is a short period around 12 January 2019, 20:00 UTC, when considerable vapor deposition with an absolute magnitude of up to $70\ \mathrm{W\,m^{-2}}$ was measured by the EC method while the MOST-based estimate is approximately zero. This mismatch coincides with peaks in the wind speed ($15\ \mathrm{m\,s^{-1}}$), in the depth of the blowing-snow layer (36 m), in the drifting-snow mass flux at a height of 0.1 m ($30\ \mathrm{kg\,m^{-2}\,min^{-1}}$), and in the spike percentage in the sonic data (6%).

Similar to the *LE* flux, the *H* values differed significantly between the measurement methods during most of the time with a considerable amount of drifting and blowing snow (Fig. 1.5c). In contrast, both methods agree well with respect to the momentum flux during the entire investigation period (Fig. 1.5d). The quality-control tests for the EC method suggest that the requirements for steady state and well-developed turbulence are fulfilled most of the time.

The discrepancy between the two estimates for *LE* and *H* indicates that drifting and blowing snow can cause significant errors for at least one of the methods. Uncertainties in the MOST-based estimates mainly arise from (i) instrument uncertainties and (ii) heat and moisture sources or sinks above the surface, violating the assumption of height-constant turbulent fluxes. Here, effect (i) is discussed whereas effect (ii) is discussed later. The relative error

Table 1.3: Instrument-induced uncertainties for some measurements and for the resulting Monin–Obukhov bulk fluxes in a situation with a high wind speed (11 January 2019, 00:40 to 00:50 UTC) and a situation with a low wind speed (12 January 2019 05:40 to 05:50 UTC).

Variable	Units	Standard uncertainty	
		11/01/2019 00:45	12/01/2019 05:45
Air temperature	°C	0.9	0.9
Surface temperature	°C	0.2	0.2
Relative humidity	%	4	6[a]
Wind speed	$m\ s^{-1}$	0.3	0.3
Latent heat flux (bulk)	$W\ m^{-2}$	14	5
Sensible heat flux (bulk)	$W\ m^{-2}$	21	6
Momentum flux (bulk)	$N\ m^{-2}$	0.015	0.003

[a] Increased uncertainty due to a relative humidity > 90%

caused by effect (i) increases with the wind speed because strong turbulent mixing results in relatively small vertical differences in temperature and humidity, compared with their instrument uncertainties. Instrument-induced uncertainties in the fluxes were estimated by means of uncertainty propagation for two example situations with high and low wind speeds, respectively (dashed green lines in Fig. 1.4 and 1.5) (Joint Committee for Guides in Metrology, 2008). This estimation accounts for instrument uncertainties in air and surface temperatures, relative humidity, and wind speed, while uncertainties in other parameters such as roughness length and Obukhov length are assumed to be negligible. For the fluxes *LE* and *H*, the combined standard uncertainties are considerable, mostly due to large uncertainties in air temperature and relative humidity, whereas the momentum flux is little affected by instrument uncertainties (Table 1.3, Fig. 1.5a, c, d). In the example situation with a high wind speed and significant snow transport, the instrument uncertainties only explain approximately half of the difference between the measurement methods for *LE* and *H*, which suggests that other sources of uncertainty are important as well. In the example situation with a low wind speed and without snow transport, the instrument-induced uncertainty in *LE* is larger than the difference between the measurement methods and the instrument-induced uncertainty in *H* accounts for 68% of the difference between the methods.

For the EC method, the largest problems and uncertainties arise from data gaps and spikes in the high-frequency data during periods with very high wind speeds. The choice of the threshold in the spike-removal algorithm remains subjective and an influence of undetected, less obvious spikes cannot be excluded. However, as long as the mass flux of blowing snow is rather weak at the height of the EC instruments, enough valid data records are obtained and the EC method is expected to be more reliable than the MOST parameterization.

1.3.2 Comparing Measurements and Simulations in a Case with Saltation-Dominated Snow Transport

The LES–LSM set-ups named Drift_1 and Drift_2 are used to gain further insights into the example situation on 11 January 2019, 00:40 to 00:50 UTC, indicated by a vertical dashed green line in Fig. 1.4 and 1.5. At that time, both SPCs measured plausible snow mass fluxes of an intermediate magnitude (Fig. 1.4d). The layer of drifting and blowing snow was too shallow to be detected by the MRR (Fig. 1.4b, c). Almost no spikes were detected in the EC data, which suggests that the vast majority of snow particles was transported below the measurement height of 1.9 m (Fig. 1.4e). Thus, the EC measurements are deemed reliable. The main purpose of the simulations was to evaluate whether the simulated sublimation rates are in good agreement with the EC measurements, thereby increasing the confidence in both the measurements and the simulations. Additionally, the simulations are used to investigate the vertical thermodynamic structure of the near-surface atmosphere and to estimate the error of the MOST parameterization without the influence of instrument uncertainties.

The simulations reproduced the measured wind speeds well (Fig. 1.6a). Most of the simulated snow transport occurred in the saltation layer (approximately the lowest 0.1 m) and the simulated horizontal snow mass flux was almost zero above a height of 0.2 m (Fig. 1.6e). Compared with the SPC measurements, the snow mass flux is somewhat underestimated. Possible reasons for this underestimation are shortcomings in the simulation, uncertainties in the SPC height due to spatial and temporal variations in surface elevation, uncertainties in the measured particle numbers, and uncertainties in the assumed particle density and shape. Figure 1.6e only shows an estimate for the uncertainty in the SPC height (dashed vertical bars) because the other uncertainties are difficult to quantify. For example, a non-spherical particle, especially if it is strongly anisotropic, can contribute to an overestimation or underestimation of the mass flux depending on the particle's orientation because the projected area can be larger or smaller than for a spherical particle of the same mass. Whether this effect leads to an overestimation or underestimation of the average mass of many particles, may depend on the shape of the particles.

In the Drift_1 simulation, air temperature, specific humidity, and relative humidity are very close to the values measured at a height of 1 m (Fig. 1.6b–d). In this case, the specific humidity is at a maximum at the height of the first grid node above the surface (0.0075 m) due to drifting-snow sublimation, resulting in a negative value of LE at the surface (-2 W m^{-2}), i.e., vapor deposition (Fig. 1.6c, g). The vertical profiles shown in Fig. 1.6f, g (solid lines) represent the cumulative sensible and latent heat exchange described in Sect. 1.2.3. Sublimation of drifting and blowing snow cause a significant increase in LE with height, at least in the lowest 0.1 m of the domain (Fig. 1.6g). Above, LE = 19 W m^{-2} for the Drift_1 simulation, which is higher than the measured MOST-based flux (2 W m^{-2} $\pm$ 14 W m^{-2}) and lower than the measured EC flux (35 W m^{-2}). Here, the uncertainty of 14 W m^{-2} only accounts for instrument-induced uncertainties of the measured MOST-based flux, whereas the theory-related error is discussed later. The uncertainty of the measured EC flux is not known but rather small because snow

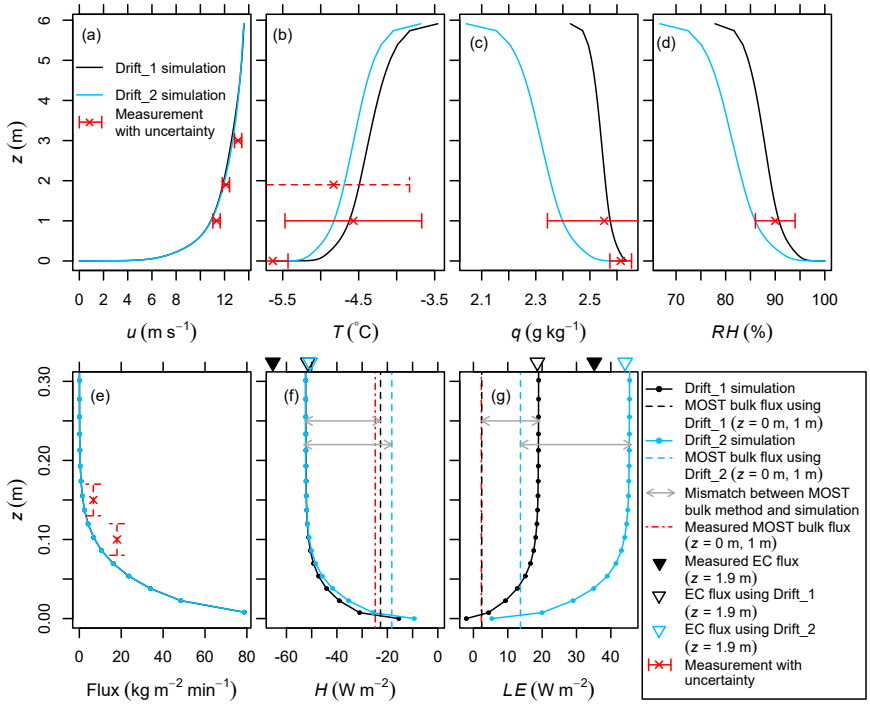

Figure 1.6: Average vertical profiles for a quasi-stationary 10-min period in two LES–LSM set-ups (Drift_1, Drift_2) with a different humidity gradient at the upper boundary: (a) Wind speed, (b) temperature, (c) specific humidity, (d) relative humidity with respect to ice, (e) horizontal snow mass flux, (f) cumulative sensible heat exchange, (g) cumulative latent heat exchange. For comparison, 10-min averaged measurements from the S17 site (11 January 2019, 00:40 to 00:50 UTC) are shown with instrument-specific standard uncertainties (dashed if estimated). Note that (e)–(g) only show the lowest 0.3 m of the profile.

transport was negligible at the sensor height. Additionally, the quality-control tests indicate good data quality and the assumptions about advection are expected to be largely fulfilled due to the almost flat and homogeneous terrain. The simulated H is directed downward with a value of -53 W m^{-2} above a height of 0.1 m and weakens when approaching the surface because of the heat sink associated with drifting-snow sublimation (Fig. 1.6f). The simulated H value is between the measured values and a bit closer to the EC (-65 W m^{-2}) than the MOST-based measurements (-25 ± 21 W m^{-2}).

To crosscheck the theory of the EC method and the consistency of the simulation, the LE and H values based on the simulated covariances and subgrid-scale fluxes at the height of the EC instruments are also shown in Fig. 1.6f, g (open triangles). As expected, these values are very close to the cumulative exchange of latent and sensible heat, respectively. This finding confirms that the theory of the EC method is applicable to conditions of drifting and blowing snow.

The Drift_2 set-up was used to study the sensitivity of LE with respect to a more negative

gradient in specific humidity at the upper domain boundary. Although this condition results in a much lower specific humidity, a lower relative humidity, and slightly lower air temperatures, these quantities are still within the uncertainty range (Fig. 1.6b–d). In the Drift_2 simulation, the surface exhibits the maximum specific humidity and the surface value of *LE* is positive (5 W m^{-2}) (Fig. 1.6c, g). With a value of 46 W m^{-2} above a height of 0.1 m, the *LE* flux is significantly higher than in the Drift_1 simulation and higher than the measured EC flux (Fig. 1.6g). The value of *H* is approximately the same for both simulations (Fig. 1.6f), and is underestimated compared with the EC measurements, which could be due to a potential underestimation of the real air temperature and the snow mass flux.

The model-measurement comparison is further complicated by the small dimensions of the model domain, which limit the size of the turbulence structures. Therefore, the simulations are expected to underestimate the turbulent fluxes present in the field. To better understand this effect, the turbulence cospectrum for the vertical wind velocity component and water-vapor density was computed from time series of the Drift_1 simulation. These time series were sampled at a grid point in the horizontal centre of the domain at the same height and sampling frequency as the EC measurements. In contrast to the field measurements, the simulated time series exhibit wave-like trends that are strongly correlated between the variables (Fig. B.1 in Appendix B). These trends are due to the fact that large-scale coherent structures are artificially locked in their position in the crosswise direction of the mean flow as a result of periodic horizontal boundary conditions and a short domain length (Munters et al., 2016). This effect is evident from streamwise-oriented bands of increased and reduced wind velocity components, air temperatures, specific humidities, etc. in a time-averaged horizontal cross-section of the domain (Fig. B.2). In the simulation, the location of the large-scale coherent structures varies very slowly in the crosswise direction of the mean flow, resulting in an artificial wave-like trend in the time series (Fig. B.3). In the field, the structures are also expected to be present but they change their crosswise location more quickly than in the simulation. Nevertheless, horizontally and temporally averaged quantities in the simulation can still be considered realistic (Munters et al., 2016).

The trend in the simulated time series would strongly influence the turbulence cospectrum at the lowest frequencies, implying that very large turbulence structures contribute much more to the magnitude of *LE* than in the field. Therefore, the trend was removed using a running mean with a time window of 150 s before computing the cospectrum (Fig. B.1). Figure 1.7 compares the cospectrum of the vertical wind velocity component and water-vapor density between the Drift_1 simulation and the field measurements. Although the measured time series does not show a pronounced trend, the same running-mean procedure was applied before computing the cospectrum for the field measurements. For frequencies larger than 0.55 Hz, the spectral density is similar between the simulation results and the field data, indicating a good representation of moisture transport by rather small turbulence structures. However, smaller frequencies between 0.01 Hz and 0.55 Hz are much less pronounced in the simulation compared with the field.

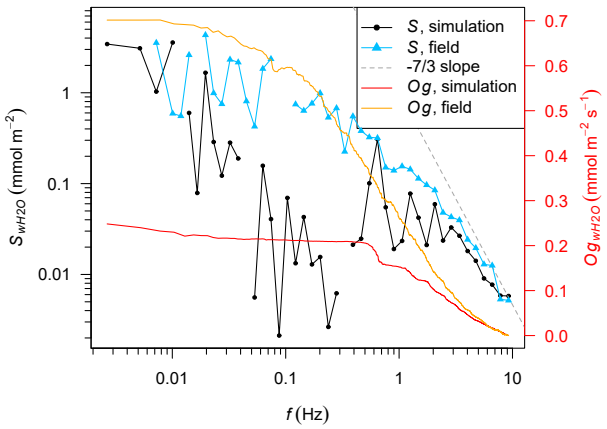

Figure 1.7: Turbulence cospectra of the vertical wind velocity component (w) and molar density of water vapor (H_2O) for the Drift_1 simulation set-up and the field measurements (11 January 2019, 00:41 to 00:48 UTC). Gaps in the bin-averaged spectral density, S, are due to negative values, which cannot be represented on the logarithmic scale. The dashed grey line shows the slope of S that is typical for the inertial subrange ($S_{wH_2O} \propto f^{-7/3}$). The ogive, Og, is the integral of spectral density between the considered frequency, f, and the Nyquist frequency (10 Hz). The plot is based on time series with 2^{13} records, from which a trend was removed. The simulated time series were sampled at a grid point with the same height and at the same frequency as in the field.

Figure 1.7 also shows the ogive, which is the integral of the cospectrum between the considered frequency and the Nyquist frequency. In other words, the ogive shows the cumulative contribution of the frequencies to the covariance of the time series. It is important to note that the measured covariance corresponds to the sublimation rate whereas the covariance from one grid point of the simulation domain does not. The reason for the latter is the artificial locking of large-scale coherent structures, resulting in significant vertical advection at a single grid point although the horizontal average of vertical advection is negligible in the Drift simulations. Due to the same effect, the covariance at a single grid point may differ from the horizontally averaged covariance. Nevertheless, the effect of the limited domain size on the shape of the ogive is expected to be independent from the choice of the sampling point.

For the field, the ogive strongly increases with decreasing frequency from 10 Hz to 0.03 Hz. Consequently, turbulence structures with a wide range in size contribute to the latent heat flux. In contrast, the ogive for the simulation is almost constant for frequencies below 0.55 Hz, indicating that the contribution of this frequency range to the latent heat flux is missing in the simulation. Using Taylor's frozen-turbulence hypothesis, a frequency of $f = 0.55$ Hz can be translated into a length scale of a turbulence structure of

$$d = \frac{\bar{u}}{f} = 22 \text{ m}\,, \tag{1.13}$$

where $\bar{u} = 12.1$ m s^{-1}. This length scale is approximately equal to the domain length (18 m).

Therefore, turbulent transport associated with larger length scales or smaller frequencies is underestimated in the simulations. At $f = 0.55$ Hz, the ogive for the measurements attains 53% of its maximum, suggesting that the conditions to be reproduced may result in a latent heat flux that is roughly twice as large as suggested by the Drift_1 and Drift_2 simulations. This effect is another possible reason for the fact that the latent and sensible heat fluxes in the Drift_1 simulation have lower absolute magnitudes than those based on the EC measurements. Although a larger model domain is desirable, the computational effort makes it currently impossible because the high spatial and temporal resolutions need to be maintained to properly represent saltation dynamics. Given these considerations, the high sensitivity of the simulated *LE* values to the upper boundary condition for humidity, and the measurement uncertainties, the simulated *LE* and *H* values are in reasonable agreement with the EC measurements.

Apart from that, the simulations demonstrate that the overall latent and sensible heat exchange can be strongly dominated by the contribution of transported snow particles while the surface exchange accounts for a rather small fraction (−11% to 12% for *LE* and 18% to 29% for *H* in the analyzed situation, Fig. 1.6f, g). Similar to the results of Wang et al. (2019), sublimation of drifting and blowing snow is strongest in the air layer of the first grid nodes above the surface (lowest 0.015 m) despite a high relative humidity of 97.1% and 95.6% for the Drift_1 and Drift_2 set-ups, respectively.

1.3.3 Theory-Related Error in the Monin–Obukhov Bulk Parameterization

By applying the MOST parameterization to the simulated humidity and temperature differences between the surface and a height of 1 m and comparing it with the simulated turbulent fluxes, the theory-related error of the MOST-based measurements can be estimated without an influence of instrument uncertainties. For the Drift_1 and Drift_2 set-ups, the simulation-based Monin–Obukhov bulk flux underestimates the simulated *LE* values by 17 W m^{-2} and 32 W m^{-2} , respectively, corresponding to high relative errors of 87% and 70% (grey arrows in Fig. 1.6g). For *H*, the mismatch between the simulation-based Monin–Obukhov bulk flux and the simulated flux is 30 W m^{-2} and 35 W m^{-2} based on the Drift_1 and Drift_2 set-ups, respectively, corresponding to relative errors of 57% and 66% (Fig. 1.6f).

If these mismatches are only due to the theory-related error of the MOST parameterization, they would only exist in conditions of drifting and blowing snow. This hypothesis was tested using the NoDrift simulation set-ups, which reproduced the field conditions observed at the S17 site on 12 January between 05:40 UTC and 05:50 UTC. During this period, the average wind speed was 2.8 m s^{-1} at a height of 1.9 m and the measured snow mass fluxes were below the noise threshold (< 0.005 kg m^{-2} min^{-1}). In the corresponding simulations, drifting snow was still enabled but few particles are transported and their effect on the turbulent fluxes is negligible. Average vertical profiles for the NoDrift set-ups and a comparison with the field measurements are presented in Fig. B.4 in Appendix B. The simulated *LE* values are 8.1 W m^{-2} and 2.0 W m^{-2} for the NoDrift_1 and NoDrift_2 set-ups, respectively. The

MOST-based estimates computed from the simulated humidity and temperature differences between the surface and a height of 1 m underestimate this flux by 16% and 20%, respectively. For the sensible heat flux, a similar underestimation of 15% is found for the NoDrift_1 set-up. In the NoDrift_2 simulation, a difference in the sensible heat fluxes is not expected due to an isothermal temperature profile.

The NoDrift simulations show that the theory-related error of the MOST parameterization associated with snow transport is not the only cause for the mismatch between the simulation-based Monin–Obukhov bulk flux and the simulated flux. Another cause may be uncertainties in the simulation. However, the relative underestimation of the fluxes by the MOST parameterization is significantly larger for the Drift set-ups than the NoDrift set-ups. Therefore, a large part of this underestimation can be attributed to the fact that the assumption of height-constant turbulent fluxes is violated in the lowest 0.1 m of the atmosphere due to drifting snow (theory-related error in the MOST parameterization). The moisture sources and heat sinks associated with sublimation of drifting and blowing snow modify the relationship between the temperature and moisture gradients and the turbulent flux, at least in the layer of drifting and blowing snow. For both *LE* and *H*, the sum of the theory-related error and the instrument-induced uncertainty is large enough to explain the difference between the MOST-based and the EC measurements in the investigated case.

In principle, the theory-related error should not occur if MOST was applied to a constant-flux layer above the layer of drifting and blowing snow, i.e., if turbulent fluxes were measured using the profile method. However, Barral et al. (2014) showed that this method is highly sensitive to instrument uncertainties in high wind speeds due to small vertical gradients at typical measurement heights.

Additionally, the LES–LSM results reveal that the MOST parametrization is not a good estimate for surface fluxes during snow-transport events. As expected, the simulation-based Monin–Obukhov bulk estimates are significantly higher than the simulated surface fluxes (Fig. 1.6f, g): the surface *LE* values are overestimated by 217% and 156% based on the Drift_1 and Drift_2 set-ups, respectively, while the absolute magnitudes of the surface *H* are overestimated by respectively 47% and 95%. The analysis confirms the expectation that the MOST parameterization significantly overestimates the surface fluxes and underestimates the overall latent and sensible heat exchange in typical conditions of drifting and blowing snow. This finding suggests that previous studies such as Thiery et al. (2012) overestimated annual surface sublimation by using MOST-based measurements in both the presence and absence of drifting and blowing snow.

1.4 Conclusions

The present study aimed at better understanding the effect of drifting and blowing snow on the reliability of turbulent-flux estimations, especially *LE*, measured using the MOST parameterization or the EC method. Three days of comprehensive measurements from

the S17 site, Antarctica, were discussed and a 10-min interval with saltation-dominated snow transport was reproduced by the LES–LSM model. For the MOST parameterization, the instrument-induced uncertainties of the fluxes *LE* and *H* were quantified using error propagation and the theory-related errors were estimated from the simulation output. The findings verify the hypothesis that the MOST parameterization can be affected by a significant theory-related error in conditions of drifting and blowing snow because the false assumption of height-constant fluxes results in an underestimation of the total latent and sensible heat exchange (surface and drifting/blowing snow) and in an overestimation of the absolute surface fluxes. This error may severely affect estimates of the surface energy and mass balance in experimental and modeling studies employing the MOST parameterization. While the error can be large for instantaneous fluxes, the effect on monthly or yearly averages remains to be explored because an underestimation of both upward and downward fluxes reduces the effect on the average flux. In contrast to the *LE* and *H* fluxes, the momentum flux measured by the Monin–Obukhov bulk method remains in good agreement with the EC measurements in conditions of drifting and blowing snow. To measure *LE* and *H* fluxes, the EC method is preferable over the MOST parameterization as long as intense blowing-snow fluxes do not reach the sensor height and result in data gaps. In the case of a shallow layer of drifting and blowing snow, the *LE* and *H* fluxes based on the EC measurements are of the same order of magnitude as the simulated ones although the simulated *LE* values are sensitive with respect to the upper boundary condition for specific humidity. To improve future model-measurement comparisons, a more accurate sensor for air temperature and relative humidity should be used, which would help to constrain the range of possible upper boundary conditions and simulated fluxes. The plausibility of the EC method is indirectly supported by the fact that the difference between the measurement methods is entirely explained by the errors of the MOST parameterization in the case study with a shallow layer of drifting and blowing snow. However, if blowing snow extends up to the sensor height, it remains unclear whether the removal of spikes from the EC raw data is complete and prevents significant uncertainties. A reliable determination of the moisture exchange between the snow and the atmosphere is not only important for quantifying the surface mass balance but also for understanding changes in the isotopic composition of surface snow. Isotopic fractionation associated with strong sublimation and vapor deposition in a layer of drifting and blowing snow is expected to change the abundance of stable water isotopes in the snow particles and the surface snow. Future studies could investigate a potential effect of these processes on the isotopic signature of ice cores and temperature reconstructions.

Open Research

The measurement and simulation data is published in the EnviDat repository at https://www.doi.org/10.16904/envidat.237 (Sigmund et al., 2021).

2 Parameterizing Snow Sublimation in Conditions of Drifting and Blowing Snow

This chapter corresponds to the draft of an article to be submitted to *Journal of Geophysical Research: Atmospheres* with the following author list and title:

Sigmund, A., Melo, D. B., and Lehning, M.: Parameterizing Snow Sublimation in Conditions of Drifting and Blowing Snow.

To improve the readability of this thesis, we sometimes replace citations of the article presented in Chapter 1 by direct references of the respective sections. AS co-designed the simulations, performed the data analysis, and wrote the draft of the article.

Key Points

- A good representation of sublimation feedbacks requires a prognostic calculation of humidity and temperature close to the surface.
- An empirical correction term in the formula of Thorpe and Mason improves the parameterization near the surface in near-saturated conditions.
- The mass and number mixing ratios of drifting/blowing snow are difficult to parameterize as current saltation schemes are inaccurate.

Abstract

Snow transport favors strong sublimation and may therefore have an important effect on the surface mass balance of polar and high-mountain regions. Recently, small-scale models such as large-eddy simulation (LES) with Lagrangian snow particles have improved the understanding of snow transport processes and revealed shortcomings in the parameterizations of large-scale models. This study leverages LES simulations to assess and improve current parameterizations of sublimation and snow transport. Measurements from the S17 site, East Antarctica, are used to define realistic model parameters and boundary conditions and verify

the plausibility of the simulations. Various parameterization options are tested in a simple one-dimensional model inspired by the large-scale model CRYOWRF. When parameterizing the moisture and heat fluxes for given mixing ratios of drifting and blowing snow, three improvements lead to a good agreement with the LES simulations: (a) At least one grid level in the saltation layer, (b) prognostic profiles of near-surface humidity and temperature, and (c) a correction term in the sublimation formula of Thorpe and Mason. The correction term accounts empirically for transient particle temperatures in the lowest 0.3 m of the atmosphere but may only be valid for a limited range of weather conditions. When parameterized, the mixing ratios of blowing snow are generally overestimated due to discretization errors and an underestimated saltation layer height. Although this overestimation can be mitigated with stretched grid levels and increased particle diameters at the saltation layer height, a more accurate parameterization of the saltation layer would benefit large-scale assessments of snow transport effects.

Plain Language Summary

In snow-covered regions, strong winds often lift snow particles from the surface and cause drifting and blowing snow events, typically associated with intense sublimation. Although the process understanding has recently improved due to small-scale models, it is still challenging to model sublimation for large areas and assess its relevance for mass changes of snow covers and ice sheets. In this study, insights from small-scale simulations of turbulence and snow transport are used to assess and improve the parameterization approach of a large-scale model. The simulation parameters and boundary conditions are based on measurements from an Antarctic site. When parameterizing the sublimation rate for given mixing ratios of drifting and blowing snow, a good agreement with the small-scale simulations is achieved after improving the representation of humidity, air temperature, and particle temperatures close to the snow surface. The parameterization of the particle mixing ratios remains challenging although a substantial overestimation of the mixing ratios can be avoided by using stretched grid levels with a high resolution near the surface and assuming increased particle diameters at the lower boundary. Further work is needed to analyze the impact of the proposed improvements on large-scale assessments of drifting and blowing snow effects.

2.1 Introduction

Quantifying the surface mass balance of regions covered by snow and ice is important for assessing changes in the water storage of ice sheets, mountain glaciers, and snow covers. These changes influence, for example, the sea level rise, water availability in rivers and ecosystems, and winter tourism in mountains. While in-situ measurements can provide accurate information at specific sites, models play a critical role in estimating the surface mass balance on large spatial and temporal scales, including projections for the future. For example, large-scale models such as MAR, RACMO, and CRYOWRF can simulate atmospheric and surface

processes for the entire ice sheet of Antarctica using a horizontal grid spacing of approximately 30 km (Agosta et al., 2019; Hofer et al., 2021; Van Wessem et al., 2018; Van Dalum et al., 2022; Sharma et al., 2023). When modelling the Greenland ice sheet or a part of Antarctica, smaller horizontal grid spacings of approximately 5 to 11 km are feasible (Noël et al., 2018; Amory et al., 2021; Le Toumelin et al., 2021).

One of the critical challenges in large-scale models is the representation of drifting and blowing snow and the associated sublimation or vapor deposition. It is difficult to simulate snow transport as its magnitude depends on the interaction between the wind field and the local topography and on variable properties of surface snow such as grain diameter and interparticle cohesion (Melo et al., 2022). Sublimation of drifting and blowing snow is additionally driven by the vertical profiles of air temperature and specific humidity, which are difficult to resolve close to the surface due to the computational effort and thermodynamic feedback effects of sublimation. In recent MAR simulations, the lowest atmospheric grid level is situated at 2 m above the surface (Hofer et al., 2021). The RACMO and CRYOWRF models typically place the lowest level for general atmospheric processes at a height of $\mathcal{O}$(10 m) while additional levels for snow transport processes are located closer to the surface (Lenaerts et al., 2012; Sharma et al., 2023). For the Antarctic Ice Sheet, estimates of sublimation of drifting and blowing snow range from approximately 100 Gt yr^{-1} in the RACMO and CRYOWRF models to 393 ± 196 Gt yr^{-1} in an assessment based on satellite remote sensing of deep blowing snow layers and reanalysis data (Van Wessem et al., 2018; Gerber et al., 2023; Palm et al., 2017). These values suggest that sublimation of drifting and blowing snow is a relevant but highly uncertain term in the surface mass balance of Antarctica.

To model snow transport and sublimation over high-alpine terrain, a high horizontal resolution is required. Therefore, simulations of an entire winter season in the Alps have only been performed for small domains of the size of a catchment. Depending on the model used, sublimation of drifting and blowing snow has been estimated to correspond on average to 0.1%–4.1% of the precipitation in a winter season for areas in the Swiss and German Alps (Strasser et al., 2008; Bernhardt et al., 2012; Groot Zwaaftink et al., 2013). The simulations suggest that sublimation of drifting and blowing snow plays an important role at mountain crests but has a minor impact on the regional surface mass balance in the Alps. However, the simulations simplify important aspects such as the wind field and particle size distribution of drifting and blowing snow. Over the last decade, atmospheric models with a more advanced treatment of snow transport and short time steps of $\mathcal{O}$(1 s) or $\mathcal{O}$(1 min) have been developed but these models have only been applied to single events of snow transport in high-alpine areas and the validation of simulated sublimation rates remains challenging (Vionnet et al., 2014; Sharma et al., 2023).

Drifting snow processes in the saltation layer are particularly simplified in the above-mentioned models. In this layer, sublimation is either neglected or highly parameterized for a single vertical level using the same approach as at higher levels. Sublimation of drifting and blowing snow is calculated by integrating the formula of Thorpe and Mason (1966) over the particle size

distribution, assuming spherical snow particles. This principle is used in all state-of-the-art large-scale models although different assumptions for particle density, size distribution, and ventilation effects are used (Sharma et al., 2023; Amory et al., 2021; Lin et al., 1983; Lenaerts et al., 2012; Déry and Yau, 1999). The formula of Thorpe and Mason (1966), henceforth called TM formula, assumes that the exchanges of latent and sensible heat between a particle and the atmosphere balance each other such that the particle temperature is stationary. While this assumption is reasonable for particles in suspension, it can lead to significant errors in the saltation layer where most of the particles do not stay long enough in the atmosphere to reach a thermal equilibrium (Sharma et al., 2018). This problem was revealed by large-eddy simulations coupled to a Lagrangian stochastic model for snow transport (LES-LSM).

Small-scale models such as LES-LSM are able to resolve the turbulent exchange of moisture and heat between individual particles of drifting/blowing snow and the atmosphere without assuming a stationary particle temperature. However, these models require a long computation time, limiting the domain dimensions and simulation period to values of $\mathcal{O}$(10 m) and $\mathcal{O}$(10 min), respectively (Sharma et al., 2018; Wang et al., 2019; Sigmund et al., 2022). LES-LSM simulations have demonstrated, that most of the sublimation of drifting and blowing snow can take place in the saltation layer despite high values of relative humidity, at least for rather shallow layers of snow transport. As snow saltation occurs very frequently, it may strongly contribute to the overall moisture exchange between the snow and atmosphere. Even if the saltation layer becomes oversaturated for deep blowing snow layers, it may play an important role because the high particle concentration close to the surface facilitates strong vapor deposition.

Therefore, the error of sublimation rates simulated in large-scale models needs to be assessed, especially in the saltation layer. This assessment is challenging because measurements of the moisture flux suffer from increased uncertainties in conditions of snow transport and cannot distinguish between flux contributions from the surface, saltation layer, and suspension layer (Sigmund et al., 2022). As an alternative to measurements, accurate small-scale models can serve as a reference and help to improve the parameterizations used in large-scale models. The goals of this study are to (a) compare LES-LSM simulations and measurements at the S17 site, coastal East Antarctica, with respect to fluxes of water vapor, sensible heat, and snow particles in various humidity and temperature conditions; (b) compare the LES-LSM simulations with a simple one-dimensional (1D) model, resembling the large-scale model CRYOWRF in terms of the snow transport and sublimation parameterizations; and (c) propose improvements in these parameterizations, mainly concerning the interactions between the near-surface specific humidity, air temperature, and sublimation of drifting and blowing snow. We also illustrate errors and sensitivities of the parameterized particle mixing ratios although major improvements in this regard are beyond the scope of this paper.

2.2 Methods and Data

2.2.1 Measurements in Antarctica

We use in-situ measurements from a field campaign at the S17 site (69°01'28"S, 40°05'14"E, 600 m a.s.l.) near Syowa Station, East Antarctica, in austral summer 2018/2019. The site is permanently snow-covered and located in nearly flat and homogeneous terrain. Details on the site, instrumentation, and data processing are described in Chapter 1 and in the published data set (Sigmund et al., 2021). Here, we use the measured surface temperature, air temperature and relative humidity at a height of $z = 1$ m above the snow surface, wind speed at heights of 1, 1.9, and 3 m, latent and sensible heat fluxes from an eddy-covariance (EC) system at $z = 1.9$ m, and horizontal snow mass fluxes and particle number size distributions from two snow particle counters (SPCs) at $z = 0.1$ m and $z = 0.15$ m.

We focus on three 10-min intervals during a strong snow transport event. The intervals beginning at 11 January 2019 00:40 UTC, 11 January 2019 21:40 UTC, and 12 January 2019 11:00 UTC are referred to as Cases 1, 3, and 2, respectively. Local time at the S17 site corresponds to UTC + 3 h. The three cases cover various conditions with wind speeds between 13.1 and 16.4 m s^{-1}, relative humidity values between 90% and 100 %, air temperatures between −4.6 and −3.4 °C, and EC-based latent heat fluxes between −28 and +35 W m^{-2} (Fig. C.1 of Appendix C). The cases were selected considering the following criteria: (a) In all cases, EC fluxes with a good data quality must be available, which excludes some hours with the highest wind speeds; (b) Case 1 is part of the initial phase of the event because in this phase, both SPCs measure plausible and considerable snow mass fluxes and the relative humidity is rather low; (c) Cases 2 and 3 refer to situations with a considerable snow mass flux (at least for one of the SPCs) and a relative humidity of approximately 100% while the EC method suggests sublimation (positive flux) in Case 2 and vapor deposition (negative flux) in Case 3.

2.2.2 Large-Eddy Simulations with Lagrangian Particles

The LES-LSM simulations solve the Navier-Stokes equations for incompressible flows and advection-diffusion equations for air temperature and specific humidity (Albertson and Parlange, 1999). Snow transport is represented by Lagrangian particles, which are entrained from the surface into the flow due to aerodynamic lift or particle splash (Comola and Lehning, 2017; Sharma et al., 2018; Melo et al., 2022). To save computation time, each Lagrangian particle represents a group of snow particles with the same properties such as location, diameter, and temperature. In the simulations performed, the average number of snow particles represented by a Lagrangian particle is approximately 54000. The model assumes the snow particles to have a spherical shape and the same density as ice (918.4 kg m^{-3}).

When particles are entrained, their diameter is taken from a log-normal distribution, which is motivated by Colbeck (1986). While moving through the atmosphere, the particles of drifting and blowing snow gradually change their size due to the vapor exchange with the atmosphere

while mechanical fragmentation of the particles is neglected. The simulated and measured particle diameters at heights of 0.1 and 0.15 m agree to a satisfactory extent (Sect. C.1 and Fig. C.2 of Appendix C). When particles hit the surface, the splash process is modelled considering momentum and energy conservation and assuming a typical cohesion energy of 10^{-10} J for surface snow (Comola and Lehning, 2017). The particles of drifting and blowing snow interact with the surrounding atmosphere by exchanging momentum, heat, and water vapor. These exchanges depend on the local differences in velocity, temperature and vapor density between each particle and the air (Eqs. 1.6, 1.7, and 1.10 in Chapter 1, Sect. C.2 in Appendix C). The temperature of each particle is initially equal to the surface temperature and then modelled explicitly considering the particle energy balance with terms for sensible and latent heat exchanges while neglecting radiation fluxes. When the diameters of particles reach a value below 10 μm, the model stops accounting for the momentum, heat and vapor exchanges of these particles; we neglect the small remaining mass of these particles and remove them from the data set during post-processing.

The lower boundary of the model domain is a flat and homogeneous snow surface with a constant temperature. The fluxes of latent and sensible heat at the lower boundary, hereafter called surface fluxes, are computed using common bulk parameterizations for neutral stratification and considering the difference in temperature or specific humidity between the surface and the next higher model level at $z = 0.0075$ m (Eqs. 1.2 and 1.3 in Chapter 1). The assumption of neutral stratification is appropriate here because of the proximity to the surface and the fact that roughness elements at the surface are not resolved. The quantities at $z = 0.0075$ m are horizontally smoothed using a spectral cutoff filter before inserting them in the bulk parameterizations because we use instantaneous values although these parameterizations have been developed for averaged quantities. To compute the surface fluxes, we use an aerodynamic roughness length of $z_0 = 10^{-4}$ m, derived from the measured EC-based friction velocity in neutral conditions. The thermal and humidity roughness lengths are parameterized as functions of z_0 and the imposed friction velocity according to Andreas (1987). At the top of the domain, we define Neumann-type boundary conditions for temperature and humidity by testing several values until the simulated steady state agrees satisfactorily with the measured air temperature and humidity at $z = 1$ m. Unrealistically strong temperature and humidity gradients are needed at the upper boundary where the vertical wind velocity component is set to zero and the vertical transport of vapor and heat is solely represented by the subgrid-scale fluxes. Nevertheless, this approach leads to realistic temperature and humidity profiles in the lower half of the domain.

Four simulations were performed to reproduce the three cases observed at the S17 site. The simulations are named according to the case. To represent Case 3, we performed two simulations (Case 3a and Case 3b), which differ in the upper boundary condition for temperature and humidity and therefore in the direction of the latent and sensible heat fluxes. Both simulations are plausible as Case 3a achieves a better agreement with the measured air temperature and specific humidity while Case 3b is consistent with the direction of the measured EC fluxes. Important parameters of the LES-LSM simulations are specified in Table C.1 in Appendix C.

The simulation approach corresponds to that described in more detail in Sect. 1.2.3 of Chapter 1 apart from the following modifications. We increased the domain size (now 38.4 × 19.2 × 18.3 m^3 for stream-wise × cross-wise × vertical dimensions) to represent a larger range of eddy sizes, contributing significantly to the turbulent fluxes. To maintain acceptable computation times, the parallelization of the software was improved and two other modifications were implemented: (a) The horizontal grid spacing was increased from 0.1 m to 0.3 m while maintaining the stretched vertical grid spacing, yielding a total of 128 × 64 × 192 grid points; and (b) the time step for the particle dynamics was increased, now amounting to the four-fold time step used for the fluid dynamics. The fluid time step remained unchanged ($\Delta t = 5 \times 10^{-5}$ s), except in Case 1 where a slightly higher value ($\Delta t = 6 \times 10^{-5}$ s) still guaranteed numerical stability.

As expected, the larger model domain leads to latent and sensible heat fluxes with a higher absolute magnitude (5% and 10% higher, respectively, in Case 1), compared with the smaller domain in Chapter 1. A model-measurement comparison of turbulence cospectra and ogives shows that the increased domain size allows us to represent the range of frequencies or eddy length scales that are responsible for 71% and 74% of the measured latent and sensible heat fluxes in the field, respectively (Sect. C.3 and Fig. C.3 of Appendix C). An even larger domain would be necessary to account for the largest eddies involved but further improvements in this regard are currently not feasible due to the computational limitations. We also checked the sensitivity of the simulation with respect to the increased horizontal grid spacing and particle time step, at least in a small domain. These sensitivity tests only showed minor changes in the rates of snow transport and sublimation, compared to the previous model set-up.

Each simulation begins with an initial period of 25 s, in which steady-state turbulence develops before snow transport is allowed to develop. The final steady state is approached after a total time of approximately 250 s. For Case 1, the simulation continues until a total time of $t = 850$ s. The results suggest that an averaging interval of 400 s is sufficient to characterize the steady state. Therefore, the simulations of Cases 2, 3a, and 3b already end at $t = 650$ s. For the analysis, we compute vertical profiles of simulated quantities by averaging temporally and horizontally the data of the last 400 s of each simulation.

2.2.3 Existing Parameterizations in the CRYOWRF Model

Inspired by the snow transport scheme of the CRYOWRF model, we developed a simple 1D model, which can be compared more easily to the LES-LSM simulations. Before describing the 1D model, we summarize the existing parameterization approach. The snow transport scheme of the CRYOWRF model is a modified version of the scheme implemented in the Meso-NH/Crocus model (Vionnet et al., 2014; Sharma et al., 2023). Like in other large-scale models, general atmospheric processes are computed on a coarse-resolution mesh, which does not resolve the lowest few meters above the surface. The snow transport scheme adds a fine-resolution mesh between the surface and the next higher level of the coarse-resolution mesh

to better capture the strong vertical gradients of the particle concentration near the surface. The lowest prognostic level of the fine-resolution mesh is at $z = 0.5$ m in the CRYOWRF model. Currently, the mass and number mixing ratios of blowing snow are the only variables solved prognostically on the fine-resolution mesh while other variables such as air temperature, specific humidity, and the turbulent diffusion coefficient are determined diagnostically on this mesh. The diagnostic vertical profiles are based on the Monin-Obukhov bulk formulae or, in the case of the diffusion coefficient, on linear interpolation. The Monin-Obukhov bulk formulae are also used to compute the surface fluxes, considering the differences in wind speed, humidity, and temperature between the surface and the first level of the coarse-resolution mesh.

Sublimation of blowing snow is calculated at each level of the fine-resolution and coarse-resolution meshes. This calculation is based on the integral of the TM formula over the particle size distribution. The model assumes that the particles are spherical and their diameters follow a gamma distribution with a prescribed shape parameter of $\alpha = 3$. Under these assumptions, the exact size distribution can be deduced from the mass and number mixing ratios of drifting and blowing snow. The total sublimation of blowing snow in the fine-resolution mesh exerts a feedback effect on the specific humidity and temperature at the first level of the coarse mesh. The effect on temperature can be expressed as a sensible heat sink (source), which is equal to the latent heat source (sink) caused by sublimation of (deposition on) blowing snow. This equivalence is rooted in the assumption of the TM formula that the energy balance of each particle is solely determined by a balance between the latent and sensible heat transfers, implying a stationary particle temperature.

The mass and number mixing ratios of blowing snow are computed using advection-diffusion equations including a sink or source term for sublimation or vapor deposition. The lower boundary conditions for the mass and number mixing ratios are specified at the top of the saltation layer estimated as (Pomeroy and Male, 1992)

$$h_{salt} = 0.084\ u_*^{1.27}\,, \tag{2.1}$$

where u_* (m s^{-1}) is friction velocity. To estimate these boundary conditions, the CRYOWRF model uses the parameterization of the saltation transport rate of Sørensen (2004) in the modified version of Vionnet et al. (2014) and assumes an exponential profile of the mass mixing ratio below h_{salt} according to Nishimura and Hunt (2000). Further details on the snow transport scheme of the CRYOWRF model can be found in Sharma et al. (2023).

An important shortcoming of the parameterization approach is the fact that the model neglects the part of sublimation of drifting and blowing snow taking place below the lowest grid layer of the fine-resolution mesh, that is, approximately below $z = 0.3$ m. Another shortcoming is associated with an error of the Monin-Obukhov bulk formulae in conditions of snow transport because the assumption of height-constant fluxes is no longer valid (Chapter 1). This error is expected to increase with the vertical distance considered in the bulk formulae, corresponding

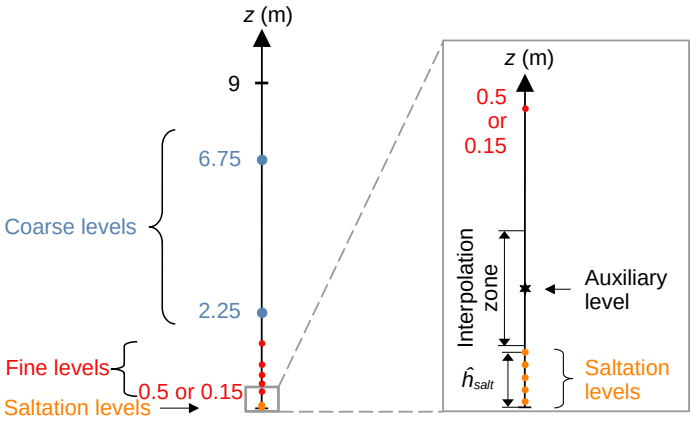

Figure 2.1: Schematic illustration of the vertical levels in the 1D model. In most model set-ups, the lowest fine level is placed at a height of $z = 0.15$ m above the snow surface and the height of the uppermost saltation level, $\hat{h}_{salt}$, corresponds to the rounded outcome of Eq. 2.1.

to the height of the first level of the coarse-resolution mesh.

2.2.4 One-Dimensional Model

The 1D model builds on the parameterizations of the CRYOWRF model and aims to reproduce the steady state of each LES-LSM simulation. The evolution of specific humidity, temperature, and sublimation is computed as a function of time and height in a domain from the snow surface to $z = 9$ m. The domain height is approximately half of that in the LES-LSM simulations because this choice allows us to define realistic upper boundary conditions for specific humidity and temperature, which are consistent with the LES-LSM simulations. These boundary conditions are of Dirichlet type and correspond to the average specific humidity and temperature at $z = 9$ m in the LES-LSM simulations (Table C.2 of Appendix C). At greater heights, the LES-LSM-based profiles deviate from the expected logarithmic shape due to boundary effects (Sect. 2.2.2). The lower boundary conditions for specific humidity and temperature are identical to those in the LES-LSM simulations.

The 1D model contains two levels of the coarse-resolution mesh (Fig. 2.1). The lower coarse level is situated at $z = 2.25$ m. The levels of the fine-resolution mesh are placed at lower heights, compared to the CRYOWRF model, to better represent strong near-surface gradients. In most set-ups of the 1D model, the fine-resolution mesh comprises stretched grid levels with equal spacing on a logarithmic scale ($z = 0.15, 0.23, 0.35, 0.54, 0.83, 1.27, 1.96$ m). In a sensitivity analysis, we use another model set-up, in which the fine levels are equally spaced ($z = 0.5$, 0.86, 1.21, 1.57, 1.92 m) like in a typical CRYOWRF set-up. For the simulated conditions, the LES-LSM model suggests that almost all the sublimation of drifting and blowing snow occurs in the lowest 0.2 m of the atmosphere. Therefore, a good representation of this layer is crucial and we improve the parameterization by adding either one or a few levels in the saltation layer. When using one saltation level only, this level is placed at $z = 0.0075$ m. Otherwise,

further saltation levels are situated above with a spacing of 0.015 m, corresponding to the near-surface spacing in the LES-LSM simulations. Unless modified in sensitivity tests, the uppermost saltation level is the level that follows this spacing and is closest to the outcome of Equation 2.1.

The 1D model assumes a constant air density of 1.18 kg m^{-3} like the LES-LSM simulations. In most model set-ups, u_* is set to the same value that is imposed in the corresponding LES-LSM simulation. Only in a sensitivity analysis, u_* is computed using the Monin-Obukhov bulk formula with prescribed values for the aerodynamic roughness length and the wind speed at the lowest coarse level. At the coarse levels, specific humidity and temperature are solved prognostically considering turbulent diffusion and particle-air interactions. The respective equations are similar to those in Bintanja (2001a) and explained in Sect. C.4. At the fine and saltation levels, we test two options for computing specific humidity and temperature: (a) diagnostic profiles based on the Monin-Obukhov bulk formulae like in the CRYOWRF model and (b) prognostic profiles based on the same equations used at the coarse levels. To initialize specific humidity and temperature, we use the steady-state LES-LSM output for the coarse levels and the Monin-Obukhov bulk formulae for the other levels.

The surface fluxes of latent and sensible heat are calculated using the Monin-Obukhov bulk formulae and considering the lowest prognostic temperature and humidity level above the surface (either $z = 2.25$ m or $z = 0.0075$ m). In contrast to the CRYOWRF model, we take into account that the friction velocity is lower close to the surface than at greater heights because drifting and blowing snow extracts momentum from the airflow. In the main analysis, the friction velocity considered in the calculation of the surface fluxes are identical to those obtained at the surface in the LES-LSM simulations. The thermal and humidity roughness lengths are set to the same values as in the LES-LSM simulations. To compute the exchanges of latent and sensible heat between drifting/blowing snow and the atmosphere, the 1D model uses the integrated version of the TM formula (like in the CRYOWRF model), at least at $z > 0.3$ m. Below this height, we test two options: (a) the same TM-based formula, assuming stationary particle temperatures and (b) a modified version of this formula, which accounts for transient particle temperatures. The latter incorporates an empirical function for the temporal change of the temperature of a particle of drifting or blowing snow close to the surface,

$$\frac{\mathrm{d}T_p}{\mathrm{d}t} = \mathrm{sgn}(\Delta T)\left|\frac{\mathrm{d}T_p}{\mathrm{d}t}\right| \tag{2.2}$$

$$\begin{aligned}\frac{\mathrm{d}T_p}{\mathrm{d}t} = \mathrm{sgn}(\Delta T)\,(\,&0.193 + 0.138\widehat{|\Delta T|} - 0.070\widehat{\sqrt{z_p}} + 0.055\widehat{\Delta RH} + 0.045\widehat{\sqrt{d_p}} \\ &+ 0.014\widehat{u_*} - 0.051\widehat{\sqrt{z_p}}\,\widehat{|\Delta T|} + 0.033\widehat{\sqrt{d_p}}\,\widehat{|\Delta T|} - 0.029\widehat{\sqrt{z_p}}\,\widehat{\Delta RH} \\ &+ 0.018\widehat{\sqrt{d_p}}\,\widehat{\Delta RH} + 0.017\widehat{\sqrt{d_p}}\,\widehat{\sqrt{z_p}}\,)\,,\end{aligned} \tag{2.3}$$

where the hat symbol indicates that the respective variable has been standardized by subtracting the mean and dividing by the standard deviation such that the absolute magnitude of each

coefficient reflects the importance of the variable; $\Delta RH = \mathrm{sgn}(\Delta T)(RH_1 - 100\%)$ represents a measure of the undersaturation of the air, where RH_1 is relative humidity at $z = 0.0075$ m (lowest saltation level); $\Delta T = T_1 - T_0$ is the difference between air temperature at $z = 0.0075$ m and surface temperature; T_p is particle temperature, t is time, z_p is the height of the particle above the surface; and d_p is particle diameter. The expression for the absolute magnitude of $\mathrm{d}T_p/\mathrm{d}t$ was derived from the time-averaged LES-LSM results in the lowest 0.3 m above the snow surface using multiple linear regression with weighted least squares. The regression was applied to the absolute magnitude of $\mathrm{d}T_p/\mathrm{d}t$ because the influences of z_p, d_p, and u_* are expected to be independent of the sign of $\mathrm{d}T_p/\mathrm{d}t$. The training data set covers a limited range of values: $|\Delta T| \in [0.08, 0.52]$ K, $u_* \in [0.52,\ 0.86]$ m s^{-1}, $RH_1 \in [96.8,\ 100.0]$ %, $d_p \in [90,\ 700]$ μm, $z_p \in [0,\ 0.3]$ m. For values outside this range, Equation 2.3 may not be accurate. Additionally, this equation is based on the assumption that the vertical gradient of air temperature in combination with thermal inertia of the particle is a more important driver of $\mathrm{d}T_p/\mathrm{d}t$ than the undersaturation of the atmosphere and its effect on the latent heat exchange. Therefore, the sign of the parameterized $\mathrm{d}T_p/\mathrm{d}t$ values is mainly determined by the sign of ΔT although the sign of ΔRH also plays a role. If the atmosphere is strongly undersaturated and the vertical temperature gradient is approximately zero, the sign of some terms in Equation 2.3 such as the term containing u_* may no longer be appropriate. In this case, however, $\mathrm{d}T_p/\mathrm{d}t$ is expected to play a minor role because the sublimation rate of the particle is rather driven by the strong undersaturation than the transient particle temperature (first versus second term in the numerator of Eq. C.7 in Appendix C). Details about the regression and the complete formula for sublimation of drifting and blowing snow can be found in Sect. C.5.

The grid layer containing the uppermost saltation level requires a special treatment in the sublimation calculations because the grid spacing increases abruptly at this height. We divide this grid layer in a lower part and an upper part. The lower part has a thickness of 0.015 m and is characterized by the quantities modelled at the uppermost saltation level. The upper part is called interpolation zone as it contains an auxiliary model level in its center where all relevant quantities are interpolated (Fig. 2.1). At this auxiliary level, air temperature and specific humidity are computed assuming logarithmic functions of height,

$$x = a\ \ln(z) + b\,, \tag{2.4}$$

where x is air temperature or specific humidity and the coefficients a and b are constrained by the requirement that the function is consistent with the x values at the two neighboring levels. Measurements and model calculations reported in Gordon et al. (2009) suggest that the mixing ratio of drifting and blowing snow follows an exponential profile in the saltation layer and a power law profile in the suspension layer. These profiles are in line with the LES-LSM results, which indicate a transition between both profiles at approximately $z = 0.13$ m to $z = 0.2$ m, depending on the friction velocity and particle size distribution. As the lowest fine level is placed at $z = 0.15$ m in the main analysis, the mass and number mixing ratios of drifting and blowing snow are interpolated at the auxiliary level assuming an exponential profile between

the two neighboring levels,

$$x_{bs} = a \exp(-b\ z)\,, \tag{2.5}$$

where x_{bs} is the mass or number mixing ratio of drifting and blowing snow and a and b are coefficients. The shape parameter of the particle size distribution is estimated at the auxiliary level using linear interpolation. We compute the particle-air interactions at the uppermost saltation level using a weighted average of the source terms for the lower and upper part of the grid layer,

$$S = \frac{\Delta z_1\ S_1 + \Delta z_2\ S_2}{\Delta z_1 + \Delta z_2}\,, \tag{2.6}$$

where S_1 and S_2 are the source terms for temperature or humidity at the uppermost saltation level and auxiliary level, respectively, and Δz_1 (m) and Δz_2 (m) are the thicknesses of the lower and upper parts of the layer, respectively.

We distinguish two configurations of the 1D model. In the first configuration, the mixing ratios of drifting and blowing snow are prescribed consistently with the steady-state LES-LSM output. The second configuration uses additional parameterizations to compute the mixing ratios and size distribution of blowing snow in a similar way as in the CRYOWRF model.

Configuration With Prescribed Mixing Ratios of Drifting and Blowing Snow

To focus on sublimation errors due to inaccurate temperature and humidity values and the assumptions of the TM formula, we prescribe the mass mixing ratio of drifting and blowing snow, mean particle diameter, and shape parameter of the particle size distribution at each vertical level, using the LES-LSM data. The shape parameter is derived by fitting a gamma distribution to the LES-LSM data, using maximum likelihood estimation. From the aforementioned variables, we infer the number mixing ratio of drifting and blowing snow, which is approximately equal to that in the LES-LSM data; small deviations exist if the LES-LSM-based size distribution is poorly approximated by a gamma distribution.

In this configuration, different set-ups of the 1D model are named according to the proposed improvements of the sublimation parameterization. In Table 2.1, we assign a label to each improvement. A combination of these labels constitutes the name of a model set-up. For example, set-up ABC includes all improvements concerning the vertical discretization, near-surface temperature and humidity, and particle temperature.

Configuration With Parameterized Mixing Ratios of Drifting or Blowing Snow

In the model configuration with parameterized mixing ratios of drifting or blowing snow, three different set-ups are used to disentangle different sources of error (Table 2.2). In the *suspension* set-up, we only parameterize the mixing ratios at the fine and coarse levels whereas the *transport* set-up parameterizes additionally the mixing ratios at the saltation levels. The *default* setup is associated with the highest degree of parameterization because the friction

Table 2.1: Proposed improvements of the sublimation parameterization of the CRYOWRF model in conditions of snow transport.

Label	Feature	Existing	Improvement
Ã	Near-surface discretization	First level at $z = 0.5$ m	One saltation level, first fine level at $z = 0.15$ m
A	Near-surface discretization	First level at $z = 0.5$ m	A few saltation levels, first fine level at $z = 0.15$ m
B	T and q at fine (and saltation) levels[a]	Diagnostic profiles (MOST[b])	Prognostic profiles
C	Assumption about particle temperature	Stationary (based on TM[c])	Transient for $z \leq 0.3$ m, stationary for $z > 0.3$ m

[a] T is temperature and q is specific humidity; [b] Monin–Obukhov similarity theory; [c] Thorpe and Mason (1966).

Table 2.2: Set-ups of the 1D model in the configuration with parameterized mixing ratios of drifting or blowing snow.

Feature	Suspension set-up	Transport set-up	Default set-up
q_{bs}, N_{bs}, and $\overline{d}_p$ at fine and coarse levels[a]	Parameterized	Parameterized	Parameterized
Discretization of sedimentation term	Various options (Eqs. 2.7, 2.8, 2.10)	Semi-forward[b]	Semi-forward[b]
q_{bs} at saltation levels	As in LES-LSM	Parameterized	Parameterized
Shape parameter[c] (α)	Fitted to LES-LSM output or $\alpha = 3$	$\alpha = 3$	$\alpha = 3$
Height of uppermost saltation level	Estimated from LES-LSM output or Eq. 2.1	Eq. 2.1	Eq. 2.1
$\overline{d}_p$ at saltation levels	As in LES-LSM or linear increase[d]	Linear increase[d]	Linear increase[d]
Friction velocity	As imposed in LES-LSM	As imposed in LES-LSM	Parameterized
Aerodynamic roughness length	Not used	Not used	2×10^{-3} m
Thermal and humidity roughness lengths	As in LES-LSM	As in LES-LSM	2×10^{-3} m
Sublimation-related improvements	ABC[e]	ABC[e]	ABC[e]

[a] q_{bs} and N_{bs} are mass mixing ratio and number mixing ratio of blowing snow, respectively, and $\overline{d}_p$ is mean particle diameter; [b] Eq. 2.10; [c] refers to the gamma distribution of particle diameter; [d] linear increase with height; [e] as defined in Table 2.1.

velocity is not prescribed directly as in the other set-ups but estimated from the prescribed wind speed and roughness lengths. In this case, the wind speed equals the mean value simulated by the LES-LSM model at $z = 2.25$ m (Table C.2 in Appendix C). The roughness lengths are set to the default value of the CRYOWRF model (0.002 m), which is 20 times higher than the aerodynamic roughness length in the LES-LSM simulations. Although snow transport increases the effective roughness length (Raupach, 1991), the friction velocity is still overestimated in the default set-up.

In all three set-ups, the 1D model solves prognostic equations for the number and mass mixing ratios of blowing snow at the fine and coarse levels. We consider turbulent diffusion, sedimentation, and sublimation or vapor deposition as in the CRYOWRF model but neglect horizontal advection. In the CRYOWRF model, these equations are solved using a semi-implicit numerical method because larger time steps are needed, compared to the 1D model. The current CRYOWRF version discretizes the sedimentation term using the forward finite difference,

$$\frac{\partial}{\partial z}(x_{bs}\, V) = \frac{x_{bs,i+1}\, V_{i+1} - x_{bs,i}\, V_i}{z_{i+0.5} - z_{i-0.5}}\,, \tag{2.7}$$

where the mass-weighted or number-weighted terminal fall velocity, V (m s^{-1}), is expressed explicitly as a function of the particle size distribution and the subscripts i and $i+1$ refer to the model level of interest and the next higher level, respectively. We refer to this discretization method as the *forward* option. To compute the particle size distribution in the 1D model, the shape parameter of the gamma distribution is either determined from a fit to the LES-LSM data at each model level or set to $\alpha = 3$. In a sensitivity test on the influence of the vertical resolution, we set the height of the lowest fine level to 0.5 m as in the CRYOWRF model; the resulting method is called the low-resolution forward option.

Additionally, we test the *central* option using the central finite difference,

$$\frac{\partial}{\partial z}(x_{bs}\, V) = \frac{x_{bs,i+0.5}\, V_{i+0.5} - x_{bs,i-0.5}\, V_{i-0.5}}{z_{i+0.5} - z_{i-0.5}}\,, \tag{2.8}$$

where the mass and number mixing ratios of blowing snow have to be interpolated at the midpoints between the model levels. This interpolation assumes an exponential profile between consecutive model levels if the midpoint is situated below $z = 0.2$ m, which is the case for the lowest midpoint under consideration (Eq. 2.5). At greater heights ($z \geq 0.2$ m), this interpolation is based on a power law profile between consecutive levels,

$$x_{bs} = a\, z^{-b}\,, \tag{2.9}$$

where a and b are coefficients. The central option is more accurate than the forward option but the former cannot be applied to the semi-implicit solver required in the CRYOWRF model because the mixing ratios need to be known to perform the interpolation. The 1D model uses an explicit solver, which avoids this problem but requires a small time step of 0.002 s to achieve

numerical stability. We test another option,

$$\frac{\partial}{\partial z}(x_{bs}\ V) = \frac{x_{bs,i+1}\ V_i - x_{bs,i}\ V_{i-1}}{z_{i+0.5} - z_{i-0.5}}\ . \tag{2.10}$$

which we call the *semi-forward* option because the concept of the forward finite difference is applied to the mixing ratios while the concept of the backward finite difference is applied to the terminal fall velocities. This option can be applied to the semi-implicit solver. Other discretization options are not presented as they do not perform satisfactorily.

At the saltation levels, the mass mixing ratios of drifting snow are taken from the LES-LSM output (suspension set-up) or parameterized diagnostically (transport and default set-ups, Sect. C.4 of Appendix C). The number mixing ratio of drifting snow is derived using a prescribed mean particle diameter, which is taken from the LES-LSM output at each saltation level or assumed to increase linearly from 200 μm at the lowest saltation level to a maximum at the uppermost saltation level. After testing a few values for this maximum, we choose a value leading to a good agreement between the LES-LSM-based mixing ratios and parameterized mixing ratios in the suspension layer (390 μm, 250 μm, 300 μm, and 300 μm in Cases 1, 2, 3a, and 3b, respectively). The mean particle diameter at the uppermost saltation level influences the terminal fall velocity and number mixing ratio of the snow particles and therefore the sedimentation flux at the lower boundary of the suspension parameterization.

In the LES-LSM simulations, the mean particle diameter decreases strongly with height at around z = 0.15 m, which is in line with measurements and reflects the transition from saltation to suspension (Gordon and Taylor, 2009). At the same height, the standard deviation of the particle diameter reaches its maximum and a bi-modal particle size distribution is seen in the LES-LSM simulations (Fig. C.2b,c). It is likely that the small particles belonging to the first mode are transported in suspension while the large particles comprising the second mode are transported in saltation. Therefore, the height of the maximum standard deviation of the diameter in the LES-LSM data is a suitable estimate for the interface between the saltation and suspension layers. This estimate of h_{salt} is 3 to 5 times higher than the outcome of Eq. 2.1 and used in sensitivity tests with the 1D model. If h_{salt} is situated above the lowest fine level (z = 0.15 m), the fine mesh begins at the next higher level. Different versions of the suspension set-up are named Xh-Yd-Zα, where (X, Y, Z) $\in$ {L, P} indicate whether the saltation layer height (here h), the mean particle diameter at the saltation levels (here d), and the shape parameter of the particle size distribution (α) are based on the LES-LSM data (L) or simple parameterizations (P).

In saltation parameterizations, the vertically integrated saltation mass flux depends on the surface friction velocity, which is approximated by the friction velocity of the fluid threshold or impact threshold, i.e., the minimum value at which saltation is initiated or sustained, respectively (e.g., Kok et al., 2012). Additionally, the horizontal particle speed in the saltation layer is typically expressed as a function of the threshold friction velocity (Sect. C.4). In the 1D model, we set the threshold friction velocity to the surface friction velocity obtained in the

LES-LSM simulations instead of estimating it from assumptions on the snow properties. This setting leads to higher mass and number mixing ratios at h_{salt}, compared to the LES-LSM simulations. To understand whether this difference is rather due to the slopes or vertically integrated values of the profiles of mass mixing ratio, we test two versions of the transport set-up. The first version uses a complete saltation parameterization based on the prescribed surface friction velocity and is named u_{*0}-Transport. The second version prescribes the vertically integrated mass mixing ratio of drifting snow while parameterizing the slope of the profile according to Nishimura and Hunt (2000) and is termed C_{salt}-Transport. For this version, the integrated mass mixing ratio is estimated from the LES-LSM results by fitting an exponential profile to the mass mixing ratios between heights of 0.01 and 0.15 m and integrating the profile from $z = 0$ to $z = \infty$.

The upper boundary conditions for the mass and number mixing ratios of blowing snow are of Dirichlet type and defined at $z = 11.25$ m, corresponding to the model level just above the 1D domain. These boundary conditions are taken from the LES-LSM output. The initial mixing ratios of blowing snow are set to zero in the 1D domain. After 40 s or less, the mixing ratios reach stationary values. In all set-ups with parameterized mixing ratios of drifting and blowing snow, the vapor and heat fluxes are computed using all improvements listed in Table 2.1 (ABC option). We analyze the steady-state results obtained at the end of the simulated 100-s period.

2.3 Results and Discussion

2.3.1 Comparison Between Large-Eddy Simulations and Measurements

The LES-LSM simulations aim to represent realistic conditions including plausible fluxes of snow transport, latent heat, and sensible heat. In all four simulated cases, the wind speed, temperature, and humidity conditions agree well with the in-situ measurements although large instrument uncertainties for air temperature and relative humidity complicate the comparison (Fig. 2.2a–d). In the simulations of Cases 2 and 3, specific humidity changes monotonically with height whereas in the Case 1 simulation, specific humidity exhibits a maximum at the first model level above the snow surface (Fig. 2.2c). This maximum is related to the fact that relative humidity is rather low in Case 1 ($RH = 90\%$ at $z = 1$ m), favoring strong sublimation of drifting and blowing snow.

Figure 2.2e presents the horizontal mass flux of snow transport in a semi-logarithmic plot. The nearly straight lines in the lowest 0.2 m of the atmosphere indicate that the mass flux decreases exponentially with height close to the surface, which is typical for the saltation layer (Sugiura et al., 1998; Sato et al., 2001; Nishimura and Nemoto, 2005). In Case 1, the simulation underestimates the measured mass fluxes by a factor of 2.2 and 2.9 at $z = 0.1$ m and $z = 0.15$ m, respectively, but the slope of the exponential decrease is similar for the simulation and SPC measurements. However, this validation of the snow transport flux is strongly influenced by uncertainties in the sensor height, which is difficult to determine due to

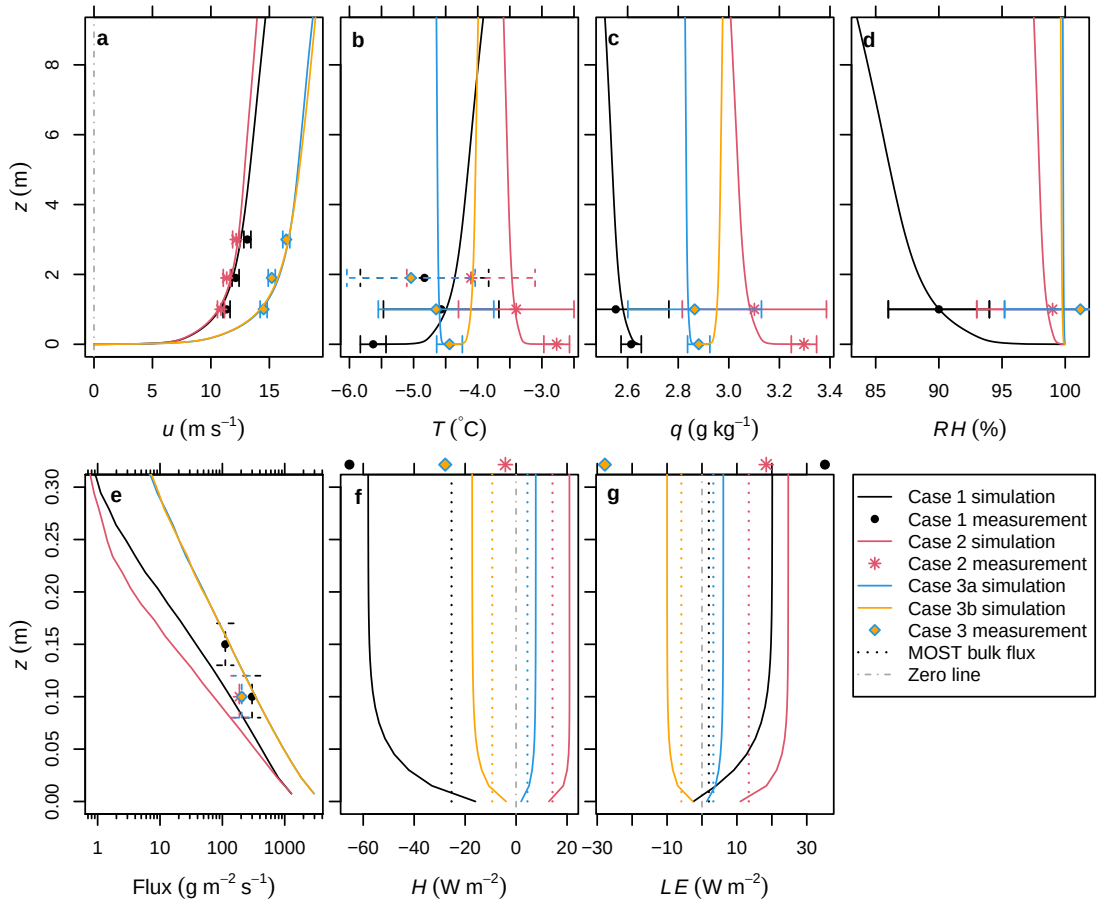

Figure 2.2: Measured and simulated quantities as a function of height (z) in the lowest 9 m (a–d) or 0.3 m (e–g) of the atmosphere: (a) Wind speed, (b) temperature, (c) specific humidity, (d) relative humidity with respect to ice, (e) horizontal snow mass flux, (f) cumulative sensible heat exchange, (g) cumulative latent heat exchange. We show 10-min averaged measurements with instrument-specific standard uncertainties (dashed if estimated) for three cases with snow transport at S17, Antarctica. For the snow mass flux, the uncertainty is not known but uncertainties of the sensor height are indicated; data of the upper sensor is only presented for Case 1 due to artifacts in Cases 2 and 3. The LES-LSM simulation data are horizontally and temporally averaged and characterize a steady state. For comparison, we show simple estimates of the sensible and latent heat fluxes based on Monin–Obukhov similarity theory (MOST, dotted lines) using the simulated vertical differences between heights of 0 and 1 m.

the surface roughness. For Cases 2 and 3, we only show the measurements from the lower SPC sensor in the figure because the upper SPC sensor measured zero or negligible mass fluxes for many hours, likely due to an obstructed laser path (Sigmund et al., 2022). In Case 2, the simulation underestimates the measured mass flux, similarly to Case 1. On the contrary, the simulations of Cases 3a and 3b overestimate the measured mass flux by a factor of 1.7. This overestimation can be partly explained by an overestimation of the size of the snow particles (Fig. C.2). Another reason for the model-measurement mismatch may be an error in the cohesion energy assumed for surface snow. A lower (moderately higher) cohesion energy is expected to decrease (increase) significantly the mass flux at the height of the SPC sensors (Melo et al., 2022).

Figure 2.2f,g illustrate the sensible and latent heat fluxes; the simulated profiles are computed by vertically cumulating the heat or vapor sources associated with snow transport and beginning with the fluxes at the snow surface. The sensible and latent heat fluxes increase in absolute magnitude with height in the lowest 0.1 m to 0.2 m of the atmosphere. Above this layer, the fluxes stay approximately constant with height because the concentration of blowing snow is very small as indicated by mass fluxes of blowing snow below 50 g m^{-2} s^{-1}. The measured sensible and latent heat fluxes included in the figure are obtained from an eddy-covariance system at $z = 1.9$ m. In Cases 1, 2, and 3b, the sign of the latent heat flux is consistent between the measurements and simulations although the magnitude differs with a ratio of simulated-to-measured latent heat fluxes of 0.4 to 1.3. The simulation of Case 3a yields a latent heat flux with the opposite sign and a significantly lower magnitude, compared to the measurements. The same is true for the sensible heat flux in the same simulation. However, this simulation agrees better with the measured air temperature and specific humidity than the simulation of Case 3b. The measured sensible heat fluxes are reproduced reasonably well by the simulations of Cases 1 and 3b but in the other two cases, the sensible heat fluxes differ clearly in both the sign and absolute magnitude between the measurements and simulations.

In Case 3a, there are three possible explanations for the model-measurement mismatch with respect to the sign of the latent and sensible heat fluxes. First, the measured vertical differences of specific humidity and temperature are clearly smaller than the instrument uncertainties. Therefore, the sign of these vertical differences may be incorrect and the simulation of Case 3b may be more realistic than that of Case 3a. Second, the simulations neglect the influence of radiation fluxes on the energy balance of the particles of drifting and blowing snow, which will cause errors if the radiation balance of the particles differs significantly from zero. Case 3 represents conditions at around midnight when radiative cooling can occur, especially for clear-sky conditions. Although the small daily amplitude of the temperature measurements points to cloudy conditions (Fig. C.1), some influence of radiative cooling cannot be ruled out. This cooling may be stronger for drifting snow than the surface and may lead to minima of air temperature and specific humidity in the saltation layer, potentially reconciling the measured fluxes and vertical differences of temperature and humidity. Third, the eddy-covariance measurements may be affected by artifacts caused by blowing snow or non-stationary conditions. However, this explanation is less likely because

spikes were removed from the high-frequency data and the data quality was good according to quality control tests including the steady-state test of Foken et al. (2004).

Case 2 describes an afternoon situation, in which solar radiation might dominate the radiation balance of the particles of drifting and blowing snow. However, if solar radiation was significant and taken into account in the simulation of Case 2, the latent and sensible heat fluxes would increase and deviate more strongly from the measurements. Therefore, other factors are expected to have a stronger impact on the model-measurement comparison in this case. As demonstrated in Sect. 1.3.2 of Chapter 1, the simulated latent heat flux is sensitive with respect to the specific humidity gradient prescribed at the upper boundary of the domain. Similarly, we expect the simulated sensible heat flux to be sensitive with respect to the temperature gradient at the upper boundary of the domain. By modifying these boundary conditions, it would be possible to achieve a better model-measurement agreement for the latent and sensible heat fluxes while the air temperature and humidity would remain in the uncertainty range of the measurements. Additionally, the accuracy of the latent and sensible heat fluxes depends on the accuracy of the snow mass flux in the simulations. This effect likely plays a role in the Case 1 simulation, in which both the snow mass flux and the latent and sensible heat fluxes are underestimated in absolute magnitude.

Considering the significant uncertainties of the temperature and humidity measurements and model parameters such as interparticle cohesion of surface snow, the agreement between the measured and simulated fluxes of latent and sensible heat is reasonable. In the following, we consider the LES-LSM model as a realistic reference for validating and improving parameterizations of sublimation and snow transport. Although this method is associated with limitations in clear-sky conditions with a significant influence of radiation, it can help to improve sublimation estimates in cloudy conditions when the radiation balance of the snow particles is expected to play a minor role.

The LES-LSM simulations can be used to estimate the theory-related error of the Monin–Obukhov bulk parameterization caused by the assumption of height-constant turbulent fluxes as demonstrated for Case 1 in Sect. 1.3.3 of Chapter 1. The simulations of Cases 2, 3a, and 3b provide additional data to assess this error in other conditions. For this purpose, we consider vertical differences between the surface and $z = 1$ m in the bulk parameterization. In all four cases, this parameterization underestimates the total fluxes of latent and sensible heat in absolute magnitude while overestimating the surface fluxes in absolute magnitude (dotted lines in Fig. 2.2). However, the mismatch between the bulk parameterization and LES-LSM simulations is less pronounced in Cases 2, 3a, and 3b than in Case 1 because of higher relative humidity values and reduced exchanges of latent and sensible heat between drifting/blowing snow and the atmosphere. In Cases 2, 3a, and 3b, the relative error of the bulk parameterization amounts, on average, to 45% and 40% for the fluxes of latent and sensible heat, respectively, while in Case 1, this error amounts to 90% and 57%, respectively. Nevertheless, this analysis confirms that the Monin–Obukhov bulk parameterization is not suitable for calculating the latent and sensible heat fluxes in conditions of snow transport. For this purpose, a more

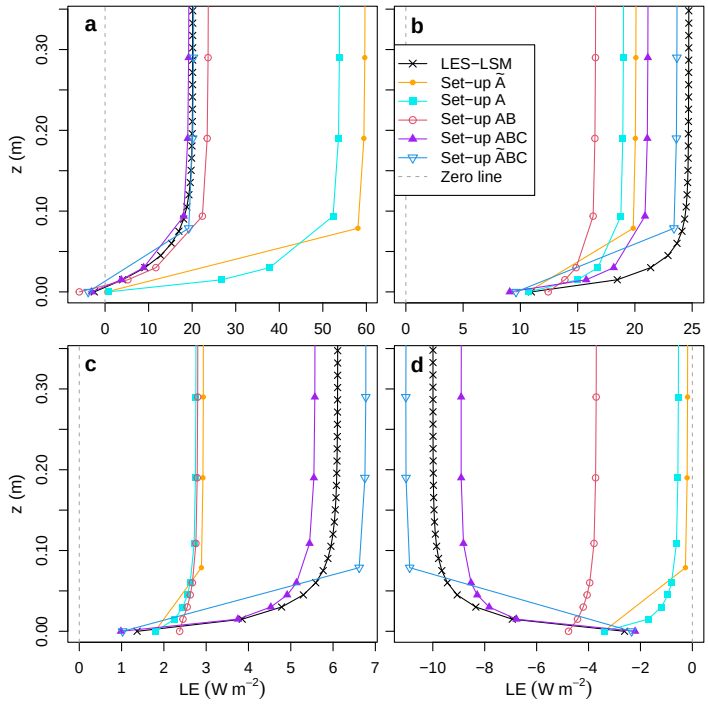

Figure 2.3: Cumulative latent heat exchange (LE) as a function of height (z) in the steady state of the LES-LSM simulations and 1D model set-ups with prescribed mixing ratios of drifting and blowing snow in (a) Case 1, (b) Case 2, (c) Case 3a, and (d) Case 3b. Point markers are drawn at the midpoints between model levels to show the total exchange below the respective height.

sophisticated parameterization approach is necessary.

2.3.2 Performance of the One-Dimensional Model With Prescribed Mixing Ratios of Drifting and Blowing Snow

In the following, we compare the latent and sensible heat fluxes between the 1D model and the LES-LSM simulations to identify the most suitable parameterization set-up with respect to the interactions between humidity, temperature, latent heat exchange and sensible heat exchange. For this purpose, we assess the importance of a small grid spacing in the saltation layer (improvement A), prognostic temperature and specific humidity values at the fine and saltation levels (improvement B), and transient particle temperatures in the lowest 0.3 m of the atmosphere (improvement C). Figure 2.3 gives an overview of the parameterized steady-state profiles of the latent heat flux in each of the four simulated cases. Corresponding profiles of the sensible heat flux are illustrated in Appendix C (Fig. C.8). The primary goal is to reproduce the total fluxes, that is, to achieve a good agreement with the LES-LSM simulations at the top of the presented profiles.

In all four cases, the ÃBC and ABC set-ups of the 1D model perform best while the simplest set-ups, Ã and A, perform poorly. The AB set-up captures the latent heat flux reasonably well in Case 1 (Fig. 2.3a) but clearly underestimates the absolute magnitude of the total latent heat flux in the other cases (Fig. 2.3b–d). The flux contribution of the snow surface is reasonably well reproduced by all set-ups (lowest point in the figures). However, the flux contribution of drifting and blowing snow differs substantially among the set-ups of the 1D model. In Case 3b, the snow particles experience vapor deposition according to the ABC and ÃBC set-ups (latent heat flux decreases with height), which is consistent with the LES-LSM simulation; on the contrary, the other model set-ups lead to sublimation of drifting and blowing snow (latent heat flux increases with height). Similarly, the sign of the sensible heat exchange associated with snow transport differs among the model set-ups in Cases 2 and 3a (Fig. C.8b,c).

In Case 1, the prognostic calculation of temperature and specific humidity at the fine and saltation levels (AB, ÃBC, and ABC set-ups) presents a clear advantage over the diagnostic calculation based on the Monin-Obukhov bulk formulae (Ã and A set-ups). The diagnostic calculation cannot reproduce the non-monotonic profile of specific humidity seen in the LES-LSM simulation of Case 1 (Fig. C.9b). As the model set-ups with the diagnostic option underestimate specific humidity close to the surface in this case, they overestimate significantly the specific humidity difference between the drifting/blowing snow particles and the atmosphere, which scales with the associated latent heat exchange. In Cases 2, 3a, and 3b, the specific humidity and temperature profiles change monotonically with height in the LES-LSM simulations and they are better approximated by diagnostic profiles, compared to Case 1 (Fig. C.9). Therefore, the choice between prognostic and diagnostic profiles only slightly influences the model performance in Cases 2, 3a, and 3b.

In Cases 2, 3a, and 3b, it is crucial to account for transient particle temperatures in order to capture well the magnitude and sign of the flux contribution from drifting and blowing snow. The effect of transient particle temperatures is most visible in these cases because relative humidity is high (> 99% at the saltation levels) and the relative error of the TM formula generally increases when relative humidity approaches 100% (Sharma et al., 2018). Additionally, Cases 3a and 3b are associated with a high friction velocity, which further enhances the error of the TM formula, as demonstrated in the aforementioned study. If the air is almost saturated with vapor, the specific humidity difference between a drifting/blowing snow particle and the atmosphere will be small and rather driven by the temperature difference between the particle and the atmosphere than the relative humidity. According to the TM formula, the sublimation of drifting and blowing snow and its cooling effect will vanish if relative humidity approaches 100% and vapor will only be deposited on the particles if relative humidity exceeds 100%. Yet, if the particles are colder than the air because they originate from a relatively cold snow surface, the saturation specific humidity at the particle temperature can be lower than the specific humidity of unsaturated air, which implies vapor deposition at relative humidity values slightly below 100%. This relationship explains why vapor deposition in Case 3b is only reproduced by the ÃBC and ABC set-ups (Fig. 2.3d).

The sensible heat exchange between drifting/blowing snow and the atmosphere is driven by the temperature difference between the particles and the atmosphere. The TM formula assumes that the thermal energy required for sublimation (released by deposition) is supplied by (transferred to) the air. Consequently, the air will always be cooled by particles experiencing sublimation in the Ã, A, and AB set-ups. However, if transient particle temperatures are taken into account, snow transport can have a net warming effect on the atmosphere despite sublimation of drifting and blowing snow, as demonstrated by the ÃBC and ABC set-ups in Cases 2 and 3a (fluxes increase with height in Fig. 2.3b,c and C.8b,c). In these cases, the particles are on average warmer than the air as they are lifted from a relatively warm snow surface; sublimation of drifting and blowing snow still requires energy and cools the particles but they remain warmer than the air. This fact implies that the energy consumed by sublimation is taken from the heat stored inside the particles, which is supplied by the warm snow surface.

Theoretically, the ABC set-up is expected to perform better than the other set-ups of the 1D model as it includes all proposed improvements. However, this set-up slightly underestimates the total fluxes of latent and sensible heat in absolute magnitude, compared with the LES-LSM results. In Cases 1 and 2, the ÃBC set-up with one saltation level performs best. In the ÃBC set-up, a large part of the flux contribution of drifting and blowing snow happens in the interpolation zone, where the mixing ratios of the particles, air temperature, and specific humidity are interpolated and therefore more uncertain than in the other grid cells. It is likely that an overestimation of the mixing ratios of blowing snow in the interpolation zone compensates for other errors in the ÃBC set-up. We expect three other important error sources in the ÃBC and ABC set-ups: (a) While the LES-LSM simulations consider individual particles and instantaneous, turbulent fields of air temperature, humidity, and wind velocity, the 1D model only considers time-averaged data and assumes that all particles in a grid layer are exposed to the same temperature and humidity conditions; (b) we assume in the derivation of the sublimation formula that the temperature difference between the particles and the atmosphere is small enough to neglect second and higher order terms in a Taylor series (Thorpe and Mason, 1966); (c) we approximate the temporal change of particle temperature using an empirical formula. Additionally, small errors in the 1D model may arise from the assumption of a gamma distribution of the particle diameter, the parameterization of turbulent diffusion of temperature and humidity, and uncertainties of the temperature and humidity values at the upper boundary of the 1D domain. These upper boundary conditions are taken from the LES-LSM output at the middle height of the LES-LSM domain where the temperature and humidity profiles begin to deviate from the expected logarithmic shape due to boundary effects at the top of the domain (Sect. 2.2.2).

To summarize the overall performance of the 1D model, we show in Fig. 2.4 the mean absolute error (MAE) of each set-up with respect to the total latent heat flux (LE) and total sensible heat flux (H), where the four simulated cases are equally weighted. For both fluxes, the lowest MAE values are achieved by the ÃBC set-up (0.8 W m^{-2} and 1.8 W m^{-2} for LE and H, respectively) while the highest MAE values are associated with the Ã set-up (14.3 W m^{-2} and 13.6 W m^{-2} for

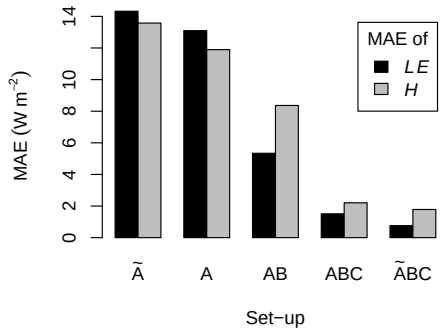

Figure 2.4: Mean absolute error (MAE) of the total latent heat flux (*LE*) and total sensible heat flux (*H*) for the 1D model set-ups with prescribed mixing ratios of drifting and blowing snow. The fluxes in the four LES-LSM simulations are considered as true reference values.

LE and *H*, respectively). The MAE values of the ABC set-up are slightly higher than those of the ÃBC set-up. Nevertheless, both the ÃBC and ABC set-ups represent suitable candidates for a future use in large-scale models because it is not guaranteed that the errors of the ÃBC set-up largely compensate each other in all possible conditions.

It is important to note that the ABC and ÃBC set-ups express the effect of transient particle temperatures using an empirical formula that is based on a limited training data set. Due to the large computational effort of the LES-LSM simulations and a cumbersome process of finding suitable boundary conditions for temperature, humidity, and particle size distribution, the same data set is used here to evaluate the performance of the 1D model. Therefore, further work is necessary to validate the empirical formula more rigorously using independent data, i.e., further LES-LSM simulations covering other temperature, humidity, and wind conditions. As this study focuses on summertime conditions and the saturation vapor pressure depends non-linearly on air temperature, it is unclear whether the empirical formula is applicable to low temperatures and very strong vertical gradients of temperature, which are typical for the winter season and the Antarctic plateau. Moreover, radiation fluxes and non-spherical shapes of drifting and blowing snow particles may influence the particle temperatures and these effects are not taken into account by the LES-LSM simulations and the empirical formula. Therefore, it remains challenging to realistically represent the effect of transient particle temperatures for a wide range of conditions.

Furthermore, the 1D model is expected to somewhat overestimate the error of the parameterization options because the domain height is small and the temperature and humidity prescribed at the upper boundary are only appropriate as long as the total latent and sensible heat fluxes are similar to those in the LES-LSM simulations. For example, if sublimation is much stronger in the 1D model than in the LES-LSM simulations, the fixed upper boundary condition will to some degree prevent specific humidity from increasing; as a result, the self-limiting feedback effect of sublimation will be underestimated.

The representativeness of the investigated cases is difficult to assess because the weather

conditions vary strongly in space and time. We hypothesize that a non-monotonic profile of specific humidity, as seen in Case 1, will develop if specific humidity only changes slightly with height while strong sublimation of drifting and blowing snow is favored by rather low values of relative humidity, which are related to a temperature increase with height (Fig. 2.2b-d). These conditions persist for several hours in the initial phase of the snow transport event analyzed in this study (Fig. C.1b,c). After this phase, specific humidity changes more strongly with height or the sublimation of drifting and blowing snow is reduced due to saturated conditions. Although the prognostic calculation of near-surface humidity and temperature may only benefit the parameterization in the case of a non-monotonic humidity profile, this option is recommended because sublimation is typically significant in these conditions. The effect of transient particle temperatures will play a relevant role if relative humidity is close to 100%, as seen in Cases 2, 3a, and 3b. Although the sublimation rate tends to decrease with increasing relative humidity, near-saturated conditions can account for a considerable fraction of the time with snow transport. At the D17 site, East Antarctica, saturation has been observed at $z \approx 0.4$ m for approximately one third of the time with snow transport in the year of 2013 (Amory et al., 2021). Measurements at Halley Station on the Brunt Ice Shelf, Antarctica, in austral winter also show frequent near-saturated conditions accompanied by snow transport (Mann et al., 2000). Therefore, the effect of transient particle temperatures may be relevant for large-scale estimates of sublimation.

2.3.3 The Effect of Parameterized Mixing Ratios of Drifting or Blowing Snow

In the following analysis, we use the method of the ABC set-up, henceforth called ABC_ref, and parameterize additionally the mixing ratios of drifting or blowing snow in the 1D model. The goal is to understand differences between the LES-LSM simulations and the 1D model with respect to snow transport and its effect on the latent heat flux. We first assess the suspension parameterization while prescribing the mass mixing ratio of drifting snow at the saltation levels according to the LES-LSM data. Later, we also parameterize the mass mixing ratios at the saltation levels and the friction velocity to understand additional sensitivities.

The Effect of the Suspension Parameterization

Considering a balance between turbulent diffusion and sedimentation, the mass mixing ratio for a given particle diameter is expected to follow a power-law profile, $q_{bs} \propto z^{-\gamma}$, where the exponent γ depends on the particle diameter and friction velocity (e.g., Gordon et al., 2009). As the mean particle diameter decreases strongly with height in the lowest part of the suspension layer, γ is expected to be relatively high in the lowest ~ 0.15 m of the suspension layer and relatively low at greater heights according to the aforementioned article. This relationship is visible in the LES-LSM data shown in Fig. C.10 of Appendix C. In the LES-LSM simulations, both the mass mixing ratio and the mean particle diameter decrease strongly with height between h_{salt} and $z \approx 0.3$ m and less strongly between $z \approx 0.3$ m and $z \approx 5$ m (Fig. C.10a,c). At greater heights, the mass mixing ratio begins again to decrease more strongly with height in

the LES-LSM simulations, which is likely an artifact related to the upper boundary condition for the vertical wind component ($w = 0$), leading to an underestimation of turbulence in the upper part of the LES-LSM domain. The number mixing ratio derived from the LES-LSM data exhibits a similar profile as the mass mixing ratio although the number mixing ratio decreases more slightly with height in the lowest part of the suspension layer due to the changing mean particle diameter (Fig. C.10b). The mean and standard deviation of the particle diameter in the LES-LSM simulations decrease strongly with height in the lowest part of the suspension layer and reach nearly constant values at $z > 1$ m, which is in line with measurements (Nishimura and Nemoto, 2005).

In the 1D model, errors can arise from the relatively low vertical resolution, compared to the LES-LSM simulations. This fact is illustrated with a sensitivity analysis in Appendix C (Sect. C.6, Fig. C.10). Our results confirm the finding of Vionnet et al. (2014) that a high vertical resolution is necessary in the lowest part of the suspension layer to avoid a significant overestimation of the mixing ratios of blowing snow. Therefore, the fine levels of the 1D model are stretched and the lowest fine level is placed at $z = 0.15$ m. The current grid spacing of this set-up represents a reasonable compromise between computational efficiency and accuracy. The same grid spacing between the fine levels could be used in a typical CRYOWRF simulation without increasing the number of fine levels. If the sedimentation flux is discretized using central finite differences (central option), the blowing snow profiles of the LES-LSM simulations are generally best reproduced by the 1D model. As the central option cannot be applied to the semi-implicit solver required in the CRYOWRF model (Sect. 2.2.4), the semi-forward option is used in the remaining analysis. With this option, the 1D model can achieve number mixing ratios of blowing snow similar to those in the LES-LSM simulations although the mass mixing ratios are somewhat overestimated.

Figure 2.5 illustrates the effects of h_{salt}, mean particle diameter at h_{salt}, and shape parameter of the size distribution on the suspension parameterization in Cases 1 and 2. Corresponding plots for Cases 3a and 3b are presented in Appendix C (Fig. C.11). The Lh-Ld-Lα set-up of the 1D model is characterized by the lowest degree of parameterization as it prescribes the above-mentioned parameters in accordance with the LES-LSM data. If h_{salt} is parameterized using Eq. 2.1 as in the CRYOWRF model while the other two parameters are taken from the LES-LSM data (Ph-Ld-Lα set-up), both the mass mixing ratios and number mixing ratios of blowing snow are clearly overestimated in the suspension layer, compared to the LES-LSM simulations and the Lh-Ld-Lα set-up (Figs. 2.5a,b,e,f and C.11a,b,e,f). The clear overestimation is related to the fact that h_{salt} is placed at a small height of 0.0375 to 0.0675 m, depending on the friction velocity of the considered case. As the distance between h_{salt} and the next higher model level is larger in the Ph-Ld-Lα set-up than in the Lh-Ld-Lα set-up, the above-mentioned discretization errors are more critical. Another reason for the overestimation is the fact that the LES-LSM simulations show an exponential profile of the mixing ratios below $z = 0.13$ m to $z = 0.2$ m while the suspension parameterization can only generate mixing ratios close to a power-law profile.

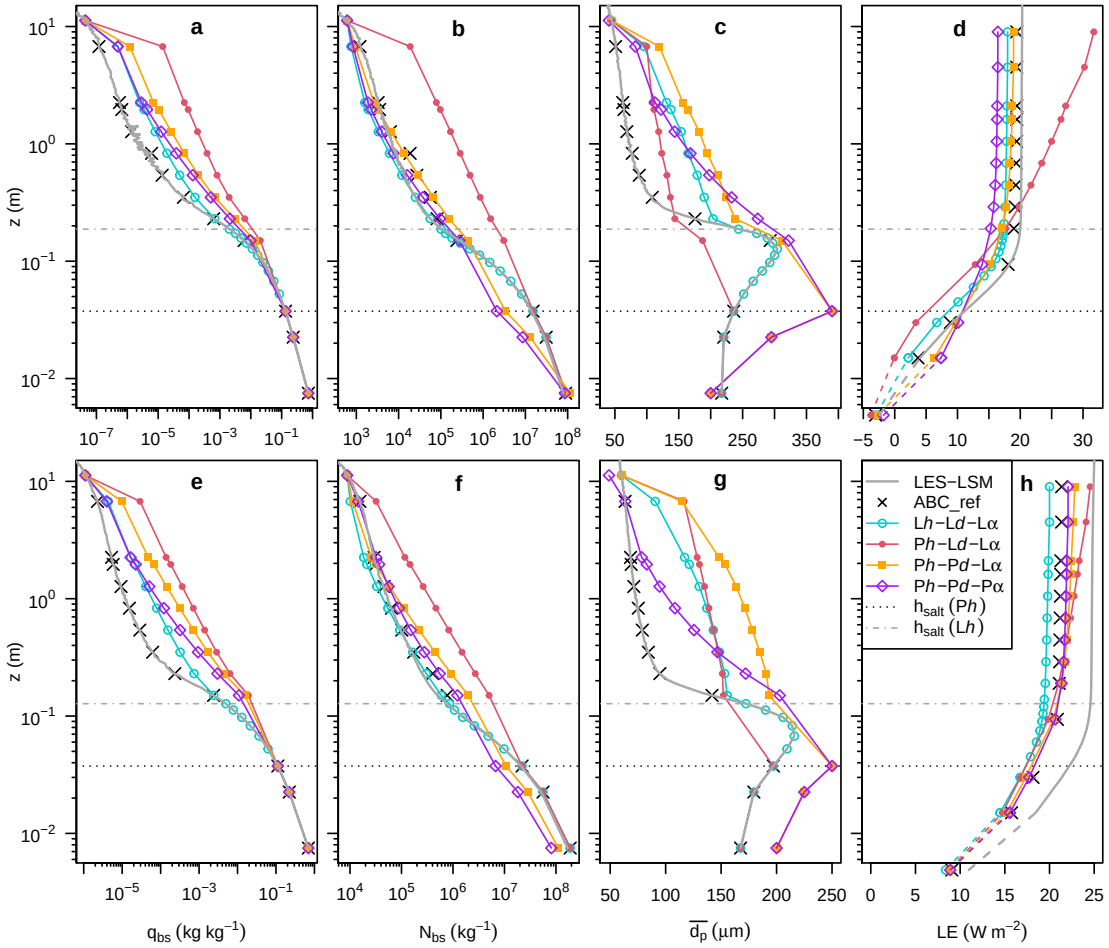

Figure 2.5: The effects of the saltation layer height (h_{salt}), mean particle diameter at h_{salt}, and shape parameter of the size distribution on snow transport and sublimation in the suspension set-up of the 1D model in (a–d) Case 1 and (e–h) Case 2: Steady-state (a,e) mass mixing ratio; (b,f) number mixing ratio; (c,g) mean particle diameter; and (d,h) cumulative latent heat exchange as a function of height (z) near the surface. For comparison, we include the results of the LES-LSM simulations and the reference set-up (ABC_ref), which prescribes the properties of drifting and blowing snow based on the LES-LSM data. The Lh-Ld-Lα set-up prescribes h_{salt} as the height with the highest standard deviation of the diameter in the LES-LSM data (dash-dotted line) while the other set-ups parameterize h_{salt} (dotted line). The markers slightly below panels d and h indicate the latent heat exchange at the snow surface.

These results highlight the need for an accurate parameterization of h_{salt}, describing the saltation-suspension interface as a function of the friction velocity and surface snow properties such as grain size and interparticle cohesion. Yet, this parameterization is currently lacking and its benefit may be limited if the mixing ratio profile in the saltation layer is poorly represented in large-scale models. Therefore, we continue using the underestimated value of h_{salt} and explore the sensitivity of the 1D model with respect to the mean particle diameter assumed at the saltation levels. If the mean diameter is assumed to increase linearly from 200 μm at the lowest saltation level to a relatively high value at h_{salt} (Ph-Pd-Lα set-up), the representation of the mixing ratios can be improved in the suspension layer. In Cases 1 and 2, for example, the mean particle diameter at h_{salt} needs to be 390 and 250 μm, respectively, to obtain mixing ratios close to those in the Lh-Ld-Lα set-up (Figs. 2.5a-c,e-g and C.11a-c,e-g). In particular, the number mixing ratios in the suspension layer are well represented by the Ph-Pd-Lα set-up because the increased mean particle diameter at h_{salt} leads to a reduced number mixing ratio at this height and an increased terminal fall velocity, changing the slope of the mixing ratio profiles in the suspension layer. If the 1D model additionally assumes a height-constant shape parameter of $\alpha = 3$ (Ph-Pd-Pα set-up), the mixing ratios decrease slightly and the mean particle diameter is less strongly overestimated, at least above $z = 0.4$ m, compared to the Ph-Pd-Lα set-up. According to the LES-LSM simulations, the shape parameter increases with height, at least for $z > 0.2$ m, and reaches values of approximately 6 to 23 at $z = 10$ m, which is in line with the literature (Schmidt, 1982; Nishimura and Nemoto, 2005). Nevertheless, the assumption of a constant value of $\alpha = 3$ seems to be a suitable simplification, rather improving than compromising the model performance.

In summary, the results reveal a strong sensitivity of the suspension parameterization with respect to the mean particle diameter at h_{salt}, reflecting the fact that small particles reach more easily great heights than large particles due to the lower terminal fall velocity. This relationship also explains why the LES-LSM simulation of Case 2 yields higher mass mixing ratios of blowing snow at $z > 0.4$ m than the simulation of Case 1 despite a lower friction velocity. In Case 2, a lower mean particle diameter is prescribed at the snow surface and therefore, a larger number of small particles is available and transported to heights above 0.4 m. This finding indicates that the LES-LSM simulations must accurately represent the particle size distribution to obtain realistic mixing ratios in the suspension layer that are representative for the conditions observed in the field. A comparison between measured and simulated particle size distributions at $z = 0.1$ m shows that the LES-LSM simulation of Case 2 reproduces well the measured size distribution while the LES-LSM simulations of the other cases overestimate on average the particle diameters (Fig. C.2). Therefore, we expect the LES-LSM-based mixing ratios of blowing snow to be more realistic in Case 2 than in the other cases. Nevertheless, the LES-LSM simulation of Case 2 seems to underestimate the mixing ratios of drifting and blowing snow because the simulated mass flux is lower than the measured one (Fig. 2.2e).

In Case 2, the Ph-Pd-Pα set-up of the 1D model agrees reasonably well with the LES-LSM simulations if the mean diameter at h_{salt} is set to 250 μm, which is higher than the value

used in the CRYOWRF model (200 μm). Taking additionally into account the lower vertical resolution in a typical CRYOWRF set-up, it is likely that the current CRYOWRF version overestimates the mixing ratios of blowing snow, at least in the conditions found at the S17 site. However, the properties of surface snow and therefore the mean diameter at h_{salt} are expected to vary in space and time. Hence, it remains unclear to which extent blowing snow is currently overrepresented over large areas.

Increased mixing ratios of blowing snow in the suspension layer can substantially influence the latent heat exchange, which is evident in Cases 1 and 2 (Fig. 2.5d,h). For the Ph-Ld-Lα set-up, the total latent heat exchange is substantially higher than for the ABC_ref set-up, especially in Case 1 (32 versus 19 W m^{-2}). Due to high mixing ratios of blowing snow, the Ph-Ld-Lα set-up suggests that a considerable fraction of the total latent heat exchange happens in the layer above z = 0.3 m (38% in Case 1), for which the LES-LSM simulations predict a negligible flux contribution (1.3% in Case 1). The other versions of the suspension set-up yield similar latent heat fluxes as the ABC_ref set-up because the number mixing ratios of drifting and blowing snow are in the same order of magnitude for all of these set-ups. The number mixing ratio influences directly the magnitude of sublimation of drifting and blowing snow while the mass mixing ratio has a smaller, indirect influence through its effect on the parameterized size distribution (Eq. C.23 in Appendix C). Therefore, it is sufficient to accurately represent the number mixing ratio, even if the mass mixing ratio is overestimated by one order of magnitude. In Cases 3a and 3b, the differences between the set-ups in terms of the mixing ratios of blowing snow only have a minor impact on the latent heat exchange (Fig. C.11d,h). This fact is largely explained by the very high relative humidity throughout the 1D domain, limiting the vapor exchange, especially at model levels above z = 0.3 m where the TM formula is used.

The Effects of Parameterizations of Saltation and Friction Velocity

This section compares the transport and default set-ups of the 1D model with the Ph-Pd-Pα version of the suspension set-up and the LES-LSM simulations to examine sensitivities associated with parameterized mass mixing ratios of drifting snow at the saltation levels. The transport and default set-ups adopt the parameter settings of the Ph-Pd-Pα set-up, including an underestimated h_{salt} value. Here, we show vertical profiles for Cases 1 and 2 (Fig. 2.6) while corresponding profiles for Cases 3a and 3b can be found in Appendix C (Fig. C.12).

The u_{*0}-Transport set-up results in a higher mass mixing ratio of drifting snow at h_{salt}, compared to the LES-LSM simulations (Figs. 2.6a,d and C.12a,d). The increased mass mixing ratio at h_{salt} is related to the fact that (a) the vertically integrated mass mixing ratio of drifting snow is higher and (b) the mass mixing ratio decreases more slowly with height, compared to the LES-LSM simulations. Due to the lack of measurements in the lowest few centimeters of the atmosphere, it is difficult to assess whether the LES-LSM simulations or the 1D model represent more accurately the vertically integrated mass mixing ratio of drifting snow at the field site. On one hand, we have more confidence in the LES-LSM simulations because they describe the saltation process in much more detail, compared to the 1D model. On the other

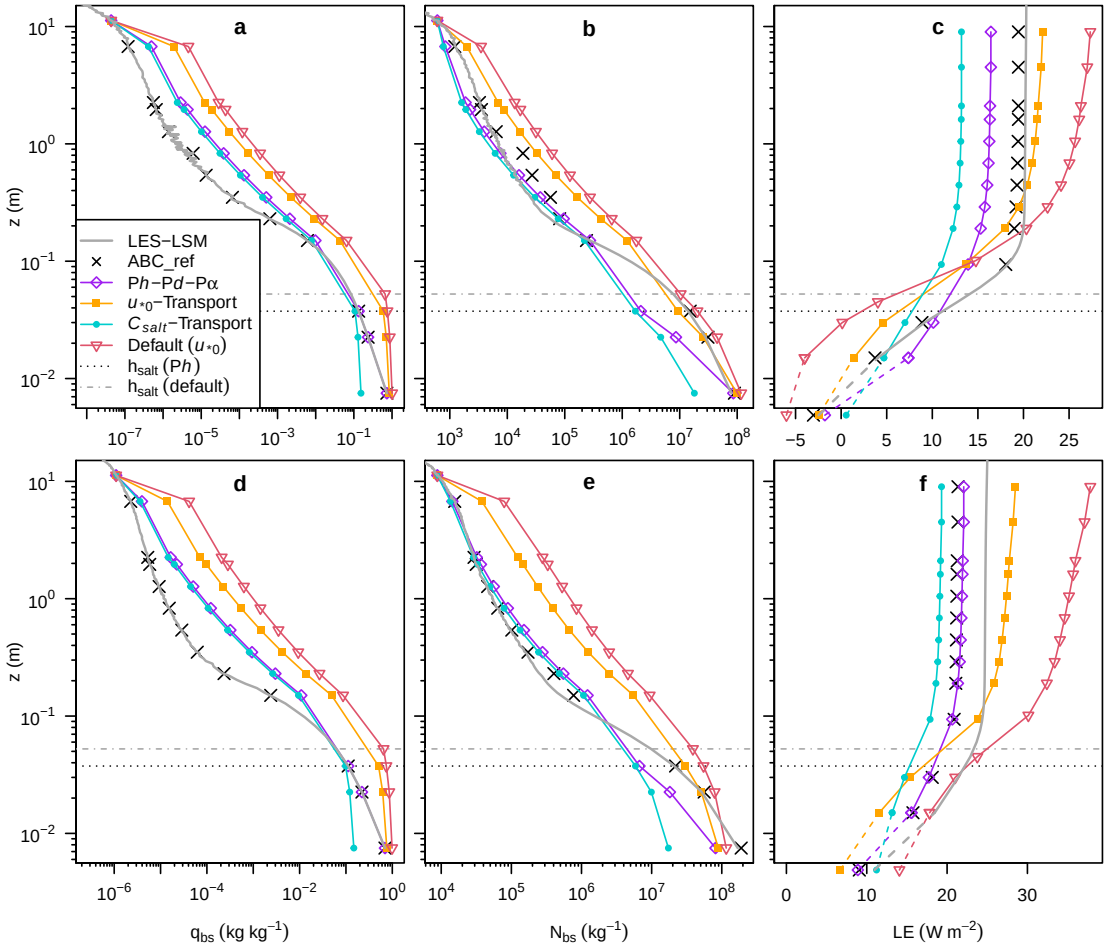

Figure 2.6: The effects of the saltation parameterization and an estimated friction velocity on snow transport and sublimation in the 1D model in (a–c) Case 1 and (d–f) Case 2: Steady-state (a,d) mass mixing ratio, (b,e) number mixing ratio, and (c,f) cumulative latent heat exchange as a function of height (z) close to the surface. For comparison, we show results of the suspension set-up (Ph-Pd-Pα), reference set-up (ABC_ref), and LES-LSM simulations. For the default set-up, the saltation layer height is slightly higher (dash-dotted line) than for the other set-ups (dotted line) due to a higher friction velocity. The markers slightly below panels c and f indicate the latent heat exchange at the snow surface.

hand, some parameters of the LES-LSM simulations such as the cohesion energy of surface snow are difficult to verify and the comparison with the SPC measurements at $z = 0.1$ m and $z = 0.15$ m points to an underestimation of the snow mass flux, at least in Cases 1 and 2 (Fig. 2.2e). Regarding the slope of the mixing ratio profile in the saltation layer, the difference between the LES-LSM simulations and the transport set-up is at least partly explained by the unrealistic assumption of the transport set-up that the horizontal particle speed is constant with height throughout the saltation layer. If the parameterization assumed the particle speed to increase with height, the mixing ratio would decrease more strongly with height for a given mass flux profile.

The saltation parameterization provides the lower boundary condition for the suspension parameterization. Therefore, the u_{*0}-Transport set-up yields higher mixing ratios in the suspension layer with a stronger contribution to the total latent heat fluxes, compared to the Ph-Pd-Pα set-up. In Case 2, for example, these effects lead to a total latent heat flux of 29 W m^{-2} in the u_{*0}-Transport set-up while the Ph-Pd-Pα set-up only yields a flux of 21 W m^{-2}.

If the vertically integrated mass mixing ratio of drifting snow is prescribed according to the LES-LSM results (C_{salt}-Transport set-up), the mixing ratios at h_{salt} and higher levels are almost identical to those for the Ph-Pd-Pα set-up although the slope of the mixing ratio profiles differs at the saltation levels. The difference in this slope affects the abundance and sublimation of drifting snow at the lowest saltation level but has a small impact on the total latent heat exchange because the reduced latent heat exchange at the lowest saltation level is partly compensated by a feedback effect on the surface flux (lowest point in Fig. 2.6c,f and C.12c,f). This finding suggests that the vertically integrated mass mixing ratio of drifting snow is a crucial quantity in the parameterization. On the contrary, the shape of the exponential profile of the mass mixing ratio in the saltation layer is less critical as long as h_{salt} is rather low and close to the height where exponential profiles with different shapes intersect.

Another relevant quantity is the friction velocity, which is directly imposed in the set-ups of the 1D model discussed so far to guarantee that the wind conditions are comparable to the LES-LSM simulations. In the default set-up, however, the friction velocity is estimated, considering a prescribed wind speed. Apart from that, the default set-up uses the same parameter settings as the u_{*0}-Transport set-up. The assumption of a high roughness length of 0.002 m leads to an overestimation of the friction velocity in the default set-up, causing a slightly higher h_{salt} value, a higher value of the vertically integrated mass mixing ratio of drifting snow, and a slightly different slope of the mixing ratio profiles, compared to the u_{*0}-Transport set-up. These differences contribute to an increased total latent heat flux in the default set-up, amounting to 38 W m^{-2} in Case 2. Not only the sublimation of drifting and blowing snow but also the surface sublimation is overestimated in absolute magnitude by the default set-up because the thermal and humidity roughness lengths are higher than in the LES-LSM simulations and the u_{*0}-Transport set-up. The strong latent heat flux in the default set-up is to some degree exaggerated because the specific humidity and temperature at the upper boundary cannot react to the increased flux.

2.4 Conclusions

In this study, latent and sensible heat fluxes were simulated in conditions of snow transport observed at the S17 site, Antarctica. The main goal was to use insights from detailed LES-LSM simulations to propose and assess improvements in the parameterization approach employed by large-scale models, especially the CRYOWRF and Meso-NH/Crocus models. Four LES-LSM simulations were performed and the simulated steady states were found to agree reasonably well with the measurements in terms of the snow mass flux, latent heat lux, and sensible heat flux; yet, some discrepancy was visible, likely due to large uncertainties of the measured air temperature and humidity, uncertain model parameters such as the interparticle cohesion and size distribution of surface snow, and the neglect of radiation fluxes in the simulations. The LES-LSM-based fluxes of latent and sensible heat were dominated by the contribution of drifting and blowing snow in the lowest 0.2 m of the atmosphere while the contribution at greater heights was limited by low mixing ratios of blowing snow. Hence, parameterizations should account for the sublimation of drifting snow in the saltation layer. As demonstrated with a simple 1D model, the parameterization approach of the CRYOWRF model can be modified such that it agrees well with the LES-LSM simulations, at least if the mixing ratios of drifting and blowing snow are known. To obtain realistic results in various humidity and temperature conditions, the parameterization should (a) consider at least one model level in the saltation layer, (b) compute specific humidity and air temperature prognostically at all model levels to take into account the local feedback effects associated with snow transport, and (c) account for transient particle temperatures in the lowest 0.3 m of the atmosphere by applying a modified version of the formula of Thorpe and Mason (1966). Recommendations a and b are expected to improve large-scale simulations even in weather conditions that are not covered in this study. Recommendation c, however, requires an empirical expression of the temporal change of particle temperature, which is based on the LES-LSM results for a limited range of temperature conditions, friction velocities, and relative humidity values in summer. Regarding relative humidity, the training data set covers the most relevant range of values because the effect of transient particle temperatures on sublimation is most important in near-saturated conditions. However, additional LES-LSM simulations with lower air temperatures are needed to assess whether the empirical expression can be generalized and applied to colder conditions. Apart from that, it remains unclear to which extent the radiation balance of drifting and blowing snow influences the particle temperatures and sublimation rate. This effect could be studied in the future by implementing a radiation scheme in the LES-LSM simulations. Furthermore, the parameterization of the mixing ratios of drifting and blowing snow remains challenging. We strongly recommend to use stretched grid levels with a high vertical resolution in the lowest part of the suspension layer to avoid a significant overestimation of the mixing ratios of blowing snow due to discretization errors. Our analysis also reveals shortcomings in current parameterizations of snow saltation, affecting the abundance of blowing snow in the suspension layer and its contribution to the latent and sensible heat fluxes. Major improvements in this regard would be achieved if the saltation layer height and the exponential profile of the mass mixing ratio in the saltation layer were

parameterized more realistically, taking into account the properties of the surface snow. As long as these improvements are lacking, it is advisable to assume an increased mean particle diameter (e.g., 250 μm instead of 200 μm in the CRYOWRF model) at the top of the saltation layer; this modification will reduce the abundance of blowing snow, counteracting the effects of an underestimated height of the saltation layer and discretization errors. Furthermore, the parameterized snow transport is sensitive with respect to the roughness length, which is difficult to estimate for large areas. In large-scale models, it remains to be tested whether the lowest grid level of the snow transport scheme can be placed very close to the surface ($z = 0.0075$ m) because the increased vertical resolution may require a reduced time step to achieve numerical stability. Moreover, it is still unclear whether the improvements of large-scale models proposed in this study will increase or decrease the annual sublimation over the Antarctic Ice Sheet. On one hand, the improvements are expected to reduce the particle mixing ratios in the suspension layer and therefore the sublimation of blowing snow. On the other hand, the improvements favor a stronger contribution of the saltation layer to the moisture exchange, compared to current large-scale models; the saltation layer sometimes experiences net sublimation and at other times net vapor deposition, depending mainly on the undersaturation and the vertical gradient of air temperature. Future simulations with an improved snow transport scheme will shed light on potential implications for large-scale estimates of the surface mass balance in polar regions.

Open Research

The measurement data is stored in the EnviDat repository at https://www.doi.org/10.16904/envidat.237 (Sigmund et al., 2021). The Fortran code of the LES-LSM simulations is maintained in the institutional GitLab repository at https://gitlabext.wsl.ch/atmospheric-models/les-lsm(.) The exact code of the LES-LSM simulations used in this study, the post-processed output of the LES-LSM simulations and 1D model, the R code of the 1D model, and the R code used to post-process and visualize the model results will be published in the EnviDat repository after acceptance.

3 A Case Study on Drivers of the Isotopic Composition of Water Vapor at the Coast of East Antarctica

This chapter corresponds to the postprint version of the article published as

Sigmund, A., Chaar, R., Ebner, P. P., and Lehning, M.: A case study on drivers of the isotopic composition of water vapor at the coast of East Antarctica, *Journal of Geophysical Research: Earth Surface*, 128, e2023JF007062, https://doi.org/10.1029/2023JF007062, 2023,

 AS and RC contributed equally to the work presented in this chapter. AS improved significantly the model originally developed by RC. AS changed the focus of the analysis and rewrote the original version of the article, which had mainly been designed by RC. AS performed all revisions requested by the reviewers of the rewritten article.

Key Points

- Direct air mass advection from the ice sheet leads to strongly depleted vapor isotopic compositions at a ship close to the Mertz glacier.
- Both isotopic distillation due to cloud formation and sublimation of surface snow drive the vapor isotopic composition over the ice sheet.
- Ocean evaporation can quickly overwrite the isotopic signature of air masses shortly before arrival at the ship.

Abstract

Stable water isotopes (SWIs) contain valuable information on the past climate and phase changes in the hydrologic cycle. Recently, vapor measurements in the polar regions have provided new insights into the effects of snow-related and atmospheric processes on SWIs. The purpose of this study is to elucidate the drivers of the particularly depleted vapor isotopic composition measured on a ship close to the East Antarctic coast during the Antarctic

Circumnavigation Expedition in 2017. Reanalysis data and backward trajectories are used to model the isotopic composition of air parcels arriving in the atmospheric boundary layer (ABL) above the ship. A simple model is developed to account for moisture exchanges with the snow surface. The model generally reproduces the observed trend with strongly depleted vapor δ^{18}O values in the middle of the 6-day study period. This depletion is caused by direct air mass advection from the ice sheet where the vapor is more depleted in heavy SWIs due to distillation during cloud formation. The time spent by the air masses in the marine ABL shortly before arrival at the ship is crucial as ocean evaporation typically leads to an abrupt change in the isotopic signature. Snow sublimation is another important driver when the isotopic composition of the sublimation flux differs substantially from that of the advected air mass, e.g., marine air arriving at the coast or free-tropospheric air descending from high altitudes. Despite strong simplifications, our model is a useful and computationally efficient method for understanding SWI dynamics at polar sites.

Plain Language Summary

Stable water isotopes are useful to reconstruct historical temperature conditions from ice cores. This method is possible because phase changes of water alter the isotopic composition. For example, if an air mass cools down, forms clouds, and produces rain or snowfall, the water vapor preferentially loses heavy water molecules. This study aims to explain a remarkable vapor isotopic signal measured on a ship close to the East Antarctic coast during six days in 2017. We model the isotopic composition of air parcels along their pathways to the ship and develop a novel approach to represent moisture exchange with the snow surface. The modeled vapor isotopic composition at the ship reaches a distinct minimum, similar to the measurements, when the air parcels move directly from the ice sheet to the ship. As expected, the vapor isotopic composition is lower over the ice sheet than over the ocean, largely due to cloud formation. However, moisture uptake from the snow surface and from the ocean shortly before arrival at the ship can strongly and abruptly influence the isotopic signature of the air masses. Although our model is not perfect, it helps to improve the interpretation of isotope measurements at polar sites.

3.1 Introduction

Stable water isotopes (SWIs) are widely used as both tracers in the global hydrologic cycle (Koeniger et al., 2010; Elliot, 2014) and as climate proxies in ice cores (Lorius et al., 1979; Grootes et al., 1994; EPICA community members, 2004). The isotopic composition (δ^{18}O or δD) describes the abundance of a heavy water isotopologue ($H_2{}^{18}O$ or $HD^{16}O$) in a water sample, in relation to a standard as defined in Sect. D.1 of Appendix D. The heavy isotopologues contain stronger molecular bonds than the light isotopologue, $H_2{}^{16}O$, which leads to slight differences in the saturation vapor pressure of the isotopologues (e.g., Matsuo and Matsubaya, 1969; Jancso et al., 1970). Therefore, the solid phase is generally more enriched in SWIs than

the liquid phase and, to a stronger degree, than the vapor phase. This effect is known as equilibrium fractionation. Phase changes in natural conditions such as ocean evaporation can additionally be associated with kinetic fractionation, resulting from the fact that the heavy isotopologues have lower molecular diffusivities in air than the light isotopologue (e.g., Jouzel and Merlivat, 1984). Kinetic fractionation will play a relevant role if the phase change occurs at a fast rate. This will be the case if a strong vertical humidity gradient enhances ocean evaporation, which is typical in the cold sector of extratropical cyclones (Thurnherr et al., 2021).

The isotopic compositions of water vapor and snow are affected by several processes, starting from ocean evaporation in the moisture source region (Craig and Gordon, 1965; Merlivat and Jouzel, 1979), transport processes in the atmosphere (Helsen et al., 2006), cloud formation and precipitation (Jouzel and Merlivat, 1984; Ciais and Jouzel, 1994), and postdepositional processes at and below the snow surface (Cuffey and Steig, 1998; Johnsen et al., 2001; Jouzel et al., 2003; Krinner and Werner, 2003; Helsen et al., 2005, 2007). When an air mass experiences more and more cloud formation, the fractionation effects give rise to isotopic distillation of atmospheric vapor. As a result, snowfall and surface snow on the Antarctic Ice Sheet generally become more depleted in heavy SWIs with increasing distance from the coast and elevation (Masson-Delmotte et al., 2008).

Isotopic fractionation also plays an important role in phase changes at the Earth's surface. These phase changes influence air masses transported in the atmospheric boundary layer (ABL) as this layer is typically well mixed by turbulence and thus affected by surface-atmosphere interactions. While the fractionation effects are well understood in the case of ocean evaporation, they are subject of current research in the case of snow sublimation. Traditionally, it was assumed that sublimation occurs layer by layer without fractionation (Friedman et al., 1991; Neumann and Waddington, 2004; Town et al., 2008). More precisely, it was argued that self-diffusion in ice is slow enough such that the snow layer affected by sublimation would transform completely into vapor before being mixed with the snow layer underneath. Consequently, the average isotopic composition of the sublimation flux would equal the initial isotopic composition of the sublimating snow layer. However, recent experimental studies found evidence of fractionation during sublimation. For example, Hughes et al. (2021) sampled near-surface vapor and snow in northeast Greenland with a high temporal resolution on clear-sky summer days and compared the isotope dynamics with sublimation measurements. These observations demonstrated that alternating periods of sublimation and vapor deposition can lead to clear diurnal cycles in the vapor isotopic composition, which are consistent with changes in the snow isotopic composition. Similar diurnal cycles in the vapor isotopic composition were reported for Dome C on the Antarctic plateau and explained by local sublimation and vapor deposition (Casado et al., 2016). These findings are supported by controlled experiments in cold laboratories, showing that snow-vapor exchange at the surface and in the pore space alters the isotopic compositions of snow and vapor (e.g., Sokratov and Golubev, 2009; Ebner et al., 2017). Equilibrium fractionation explains a large part of these SWI dynamics although the measurements indicate some influence of kinetic fractionation

(Casado et al., 2016; Hughes et al., 2021; Wahl et al., 2021).

The influence of kinetic fractionation is often assessed using deuterium excess, also called d-excess and defined as $\delta\mathrm{D} - 8\delta^{18}\mathrm{O}$ (Dansgaard, 1964). This definition is motivated by the fact that most precipitation samples from across the world lie, on average, on a line with a slope of 8 in the δD-δ^{18}O diagram, which agrees approximately with the classic Rayleigh distillation model for an air mass cooling from 20 °C to −20 °C with an initial vapor isotopic composition in equilibrium with ocean water. This model describes condensation assuming equilibrium fractionation and an immediate removal of the liquid or solid water phase. While kinetic fractionation changes the d-excess value, equilibrium fractionation is generally expected to have a negligible effect on this value. However, Dansgaard (1964) notes that the δD-δ^{18}O relationship for a specific precipitation event depends on several parameters, including the initial vapor isotopic composition, initial temperature, and condensation temperature. These dependencies imply that equilibrium fractionation can influence d-excess in certain conditions. For example, the classic Rayleigh distillation model predicts the d-excess of snowfall to increase significantly when reaching very low temperatures and very depleted isotopic compositions, which are typical for the Antarctic plateau (e.g., Touzeau et al., 2016; Dütsch et al., 2017).

The isotopic composition of atmospheric vapor observed at a specific polar site is influenced by weather changes on different time scales. At Thule Air Base, coastal northwest Greenland, Akers et al. (2020) observed a strong seasonal cycle in vapor isotopic composition controlled by shifts in sea-ice extent, which define the distance to marine moisture sources. Synoptic weather events led to variations over multiple days, superimposed on the seasonal cycle. At Syowa station, coastal East Antarctica, Kurita et al. (2016a) also found a strong influence of synoptic weather systems, causing advection of marine or glacial air masses with distinct isotopic signatures. At other coastal polar sites, shifts between these air masses manifest themselves in pronounced diurnal cycles in the vapor isotopic composition, at least in summertime high-pressure periods. An example is Dumont d'Urville, coastal East Antarctica, where strong katabatic winds advect dry air with strongly depleted δ^{18}O values from the interior of the ice sheet during the coldest hours of the day (Bréant et al., 2019). Similar diurnal cycles can be observed at Kangerlussuaq, southwest Greenland, where an ice-free strip of land alternatingly experiences katabatic winds and a see breeze (Kopec et al., 2014).

Apart from measurements, models are an important tool for understanding the dynamics of SWIs in the atmosphere and the driving processes. There are two modeling approaches: (1) Lagrangian models which simulate moist processes and isotopic fractionation along air parcel trajectories (Jouzel and Merlivat, 1984; Ciais and Jouzel, 1994; Helsen et al., 2006; Sinclair et al., 2011; Christner et al., 2017); and (2) Eulerian models, such as general circulation models (GCMs), which consider the temporal change on a fixed three-dimensional grid (e.g., Joussaume et al., 1984; Pfahl et al., 2012). Eulerian models provide a more accurate representation of the spatial variability of the isotopic composition of water vapor across the hydrologic cycle by accounting for the mixing of air masses of different origins and the highly variable

pathways water vapor may take between evaporation and condensation. For example, GCMs are able to satisfactorily reproduce the global and seasonal variations in the isotopic composition of precipitation (Noone and Sturm, 2010; Hoffmann et al., 2000). However, it is more difficult to discern the effect of individual processes on isotopic variability using Eulerian models as these processes can be isolated less easily, compared to the computationally more efficient Lagrangian models (Dütsch et al., 2018). Thurnherr et al. (2021) used a combination of both approaches to better understand vapor isotopic measurements along the ship route of the Antarctic Circumnavigation Expedition (ACE). The output of the Eulerian model $\text{COSMO}_{\text{iso}}$ was analyzed along backward trajectories starting at the position of the ship. This method demonstrated that the cold and warm sectors of extratropical cyclones, associated with evaporation and dew formation, respectively, were important drivers of the vapor isotopic composition over the open ocean.

The ACE campaign also provided insights into meridional SWI variations in the atmospheric boundary layer (ABL) of the Atlantic and the Southern Ocean (Thurnherr et al., 2020b). From November 2016 to April 2017, continuous SWI time series were recorded on the ship as it traveled from Germany via South Africa to Antarctica and back. The vapor was generally more depleted in heavy SWIs with distance from the tropics, reflecting average patterns in temperature and specific humidity and their influence on the fractionation processes.

In the present study, we develop a Lagrangian model to explain the vapor isotopic signal of a specific event during the ACE campaign. We investigate in detail a 6-day period in January 2017, in which the ship stayed close to the Mertz glacier, East Antarctica, and the values of vapor δ^{18}O reached a pronounced minimum. The objectives are to (i) reproduce the δ^{18}O values of water vapor observed at the Mertz glacier using a Lagrangian model with simple isotope dynamics and (ii) better understand the influences of air mass origin and isotopic fractionation during moisture exchange with the Earth's surface and during cloud formation. Our model accounts for equilibrium fractionation but neglects kinetic effects during all phase changes apart from ocean evaporation. As some other models still neglect isotopic fractionation during snow sublimation, we analyze how sensitive the modeled vapor δ^{18}O is with respect to the assumptions that snow sublimation is or is not associated with equilibrium fractionation. Although our model represents some processes less accurately than the $\text{COSMO}_{\text{iso}}$-based modeling framework of Thurnherr et al. (2021), we are able to directly distinguish the effects of individual processes with a lower computational effort. The main novelty of our isotope model is the fact that the isotopic composition of sublimating surface snow is computed by accounting for the history of snowfall and surface-atmosphere exchange. This computation represents the first modeling step, which is performed in an Eulerian frame of reference, considering a multi-layer snowpack. The last aspect is an advantage over the $\text{COSMO}_{\text{iso}}$ model, which treats the snowpack as a single homogeneous layer. As sublimation and vapor deposition affect primarily the uppermost few centimeters of the snowpack and sustained sublimation may uncover deeper snow layers, a realistic description of the isotopic composition of snow may require the approach of a multi-layer snowpack.

3.2 Data and Methods

3.2.1 Water Vapor Measurements at the Mertz Glacier

The ACE expedition involved many research projects in multiple disciplines such as atmospheric chemistry and physics (e.g., Schmale et al., 2019) and oceanography (e.g., Sieber et al., 2019). The vapor isotopic measurements were performed on the ship at heights of approximately 8 m and 13.5 m a.s.l. using PICARRO cavity ring-down laser spectrometers with a high temporal resolution of 1 s (Thurnherr et al., 2020b). Most of the time, the isotopic composition was slightly more depleted at the upper height, compared with the lower height, and a strong correlation was found between both heights. We follow the aforementioned authors and focus on the measurements at the upper height, which are less influenced by sea spray. More details and an overview of the measured time series can be found in the aforementioned article.

The ship track around Antarctica can be divided into three legs (Fig. 3.1). Here, we focus on a small section of leg 2 in the proximity of the outlet of the Mertz glacier, East Antarctica, corresponding to the 6-day period from 27 January to 1 February 2017. This period includes two consecutive days with exceptionally depleted values of δ^{18}O and δD, compared with the remaining time series. The event coincided with low values of specific humidity and high values of d-excess (Fig. 5 in Thurnherr et al., 2020b), typical of continental Antarctic interior air masses (e.g., Bréant et al., 2019).

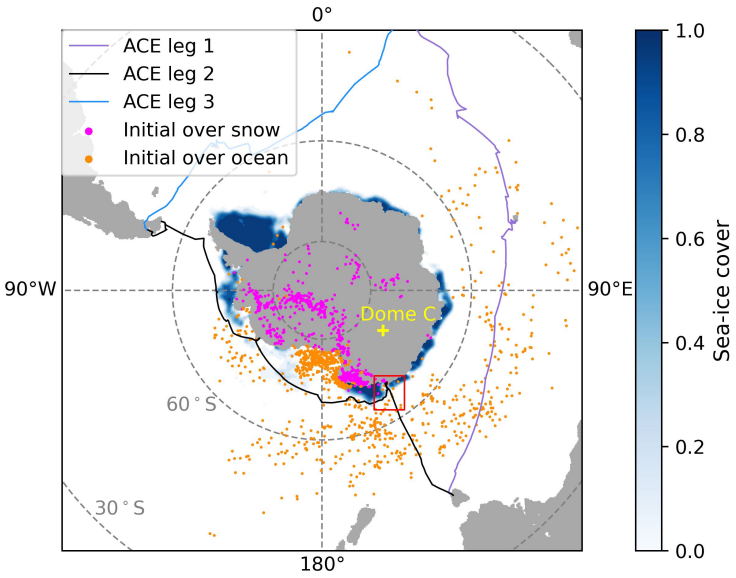

Figure 3.1: Map showing the three legs of the ship track (solid lines) of the Antarctic Circumnavigation Expedition (ACE), average sea-ice cover (blue colors) in the period from 17 January 2017 to 1 February 2017, initial locations of the modeled air parcels (dots), and location of Dome C (yellow cross). The red rectangle highlights the ship track in the study period (close to the Mertz glacier).

3.2.2 Modeling Approach

We developed a model, which considers the most common three SWIs ($H_2{}^{16}O$, $H_2{}^{18}O$, $HD^{16}O$). The model consists of two parts: (i) *Model Sublimation* uses an Eulerian frame of reference to compute the isotopic composition of surface snow, which determines that of the sublimation flux; (ii) *Model Air Parcel* uses a Lagrangian frame of reference to quantify the vapor isotopic composition along air parcel trajectories, considering vapor exchange with the snow or ocean surface and vapor removal due to cloud formation (Fig. 3.2). First, Model Sublimation is run with a spin-up period of approximately six months to allow for the development of realistic snow isotopic compositions. Subsequently, the output of Model Sublimation is used in Model Air Parcel when the air parcel takes up water vapor from the snow surface, that is, when the parcel is located in the ABL and the snow is sublimating. For the phase changes of sublimation, vapor deposition, and condensation, we only consider equilibrium fractionation as a first-order approximation and use temperature-dependent formulas for the fractionation factors from Merlivat and Nief (1967), Majoube (1970), and Majoube (1971). To evaluate the importance of fractionation during sublimation, we compare two simulations, which assume that snow sublimation is associated with equilibrium fractionation (Run E) or not associated with any fractionation (Run N). In both simulations, kinetic fractionation is only taken into account in the process of ocean evaporation by applying the widely-used Craig-Gordon formula in its original form (Craig and Gordon, 1965; Horita et al., 2008).

The next sections explain the input data and main characteristics of the two model parts while further methodological details and equations can be found in Sect. D.1 to D.3 of Appendix D. Important model constants and parameters are listed in Table D.1. For brevity, we refer to the surface water vapor flux as the surface flux from here on. All time information in this paper is given in UTC time while local time at the outlet of the Mertz glacier corresponds to UTC+10 h.

Input Data

The model uses ERA5 reanalysis data produced by the European Centre for Medium-Range Weather Forecasts (ECMWF) with spatial and temporal resolutions of $0.25° \times 0.25°$ and 1 h, respectively (Hersbach et al., 2018). The following variables were retrieved: land-sea mask, mean evaporation rate, air temperature and dew point temperature at 2 m height, surface temperature, atmospheric pressure, snowfall rate, and sea-ice cover. The mean evaporation rate characterizes both ocean evaporation and snow sublimation and is based on the common Monin–Obukhov bulk parameterization, assuming constant roughness lengths on the ice sheet ($z_{0m} = 0.0013$ m, $z_{0T} = z_{0q} = 0.00013$ m) and dynamic roughness lengths for the ocean depending on a wave model (ECMWF, 2016). In addition to the snow surface, drifting and blowing snow particles contribute to the sublimation flux (Chapters 1 and 2) and consequently they may change their isotopic composition. However, drifting and blowing snow is not represented in the ERA5 reanalysis and there is little knowledge about isotopic effects of this process. In the main analysis, we use data for latitudes south of 30° S from July 2016 to February 2017. The first six months serve as a spin-up period to reduce uncertainties arising from the

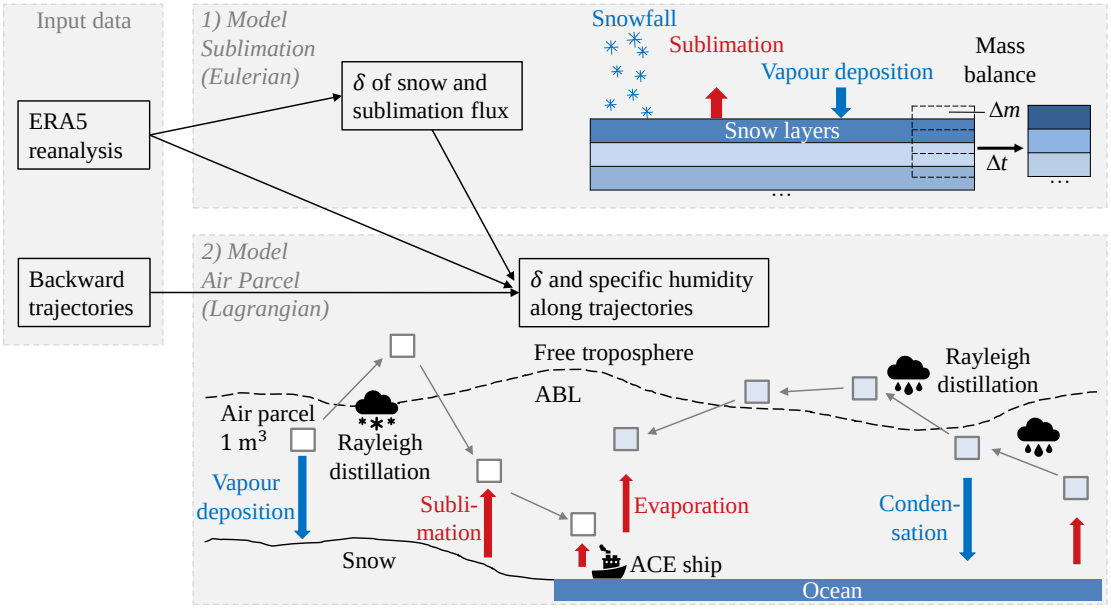

Figure 3.2: Schematic illustration of the modeling approach. The net accumulation of snow mass in one time step (Δt), denoted by Δm, may be positive or negative.

initialization of the snow isotopic composition. For purposes of validation, we compare results of Model Sublimation with isotope measurements at Dome C, East Antarctica, published by Casado et al. (2016, 2018). To this end, ERA5 data for the grid cell including Dome C (75° S, 123.25° E) and the period from January 2013 to January 2016 are used.

Model Air Parcel additionally assimilates 10-day backward air parcel trajectories taken from Thurnherr et al. (2020c). These trajectories were calculated with the Lagrangian analysis tool LAGRANTO (Wernli and Davies, 1997; Sprenger and Wernli, 2015) using the 3D-wind fields from the ECMWF operational analyses. Every hour, a set of trajectories was launched from up to 56 vertical levels between 0 and 500 hPa above sea level along the ACE cruise track. For each trajectory, the time step was 3 h. In this study, the following variables were extracted for trajectories arriving in the ABL above the ship in the period from 27 January to 1 February 2017: air pressure at heights of the air parcel and the ABL, specific humidity, and air temperature.

Model Sublimation

The isotopic composition of the sublimation flux depends on that of the surface snow (e.g., Wahl et al., 2021). The latter is initialized with typical values for snowfall depending on the temperature and then computed prognostically. The effects of snowfall, sublimation, and vapor deposition on the snow isotopic composition are simulated with time in each grid cell, which is considered as snow-covered land (land fraction > 50% and latitude south of 60° S). Model Sublimation uses a time step of 1 h and simulates the period from 1 July 2016 to 1 February 2017 in the main analysis.

The snowfall δ^{18}O is parameterized as a linear function of the daily running mean air temperature because in the literature, this relationship is derived from daily mean values. We apply the same linear function to snowfall over the whole Antarctic continent although different δ^{18}O-temperature slopes have been measured at different sites. In our baseline simulation, the function for snowfall δ^{18}O is taken from Stenni et al. (2016) and characterized by an intermediate slope of 0.45‰ K^{-1}. Sensitivity tests are performed using functions from Landais et al. (2012) and Fujita and Abe (2006) with low and high slopes of 0.35‰ K^{-1} and 0.78‰ K^{-1}, respectively (Sect. D.2, D.4, and D.5 of Appendix D). The δD value of snowfall is always derived using the δD-δ^{18}O relationship of Masson-Delmotte et al. (2008) based on mean isotopic compositions of snow, firn, or ice at many Antarctic sites (Eq. D.10).

The snowpack is modeled as a series of 100 layers, each with the same thickness and a constant density of 350 kg m^{-3}. This density does not account for the natural spatiotemporal variability but represents a typical average value for the uppermost tens of centimeters of the snowpack (e.g., Wever et al., 2022). For the location of Dome C, we tested three values for the snow layer thickness (0.1 cm, 1 cm, and 2 cm) and compared the surface snow δ^{18}O with measurements of Casado et al. (2018). A thickness of 1 cm led to a good agreement and was therefore selected for the remaining analysis (Sect. D.4 and Fig. D.1 of Appendix D). We assume that the snowpack always exists on the Antarctic Ice Sheet, that is, in grid cells south of 60° S with a land fraction greater than 50%. If the snowfall and surface fluxes add or remove snow mass at the surface, a simple mixing mechanism will guarantee that the thickness and mass of the snow layers remain constant. More precisely, a part of each layer is mixed with an adjacent layer to compensate for the mass gain or loss at the surface (Fig. 3.2). We neglect changes in snow density and assume that snow added by snowfall or vapor deposition has the same density as the snowpack. The mixing mechanism is a vastly simplified version of a realistic vapor transport mechanism (Jafari et al., 2020). In reality, the interplay between ventilation, isotope diffusion within the snowpack, and recrystallization can cause a continuous replacement of the interstitial water vapor in the surface snow layer. However, it is still an open question how the combination of these processes can quantitatively change the isotopic compositions of snow and water vapor in the ABL. Therefore, our model is based on the following assumptions: (1) no isotope diffusion within the snow layers; (2) no impact of snow metamorphism on the isotopic profile; (3) fractionation only at the uppermost snow layer because of its direct contact with the atmosphere; and (4) no ventilation within the snow layer.

The deposition flux forms surface hoar with an isotopic composition that depends on the isotopic composition of the atmospheric vapor. Model Sublimation estimates the isotopic composition of the atmospheric vapor as the mean of two hypothetical values, describing two idealized situations. In the first situation, the vapor is formed by local snow sublimation and thus characterized by the isotopic composition of the sublimation flux, which differs between Runs E and N. In the second situation, the vapor originates from a non-local source region and has undergone isotopic distillation. This effect is expressed by assuming the vapor to be in isotopic equilibrium with snowfall. We apply this parametrization regardless of whether snowfall occurs at the location and time of interest or not. The snowfall isotopic composition

is estimated as a simple function of the daily running mean air temperature, as described above.

The highly parametrized estimate of the vapor isotopic composition is only used to compute the effect of a limited amount of vapor deposition in Model Sublimation and to initialize some air parcels in Model Air Parcel. In reality, however, the relative importance of local and non-local vapor origins is expected to vary depending on the weather conditions. Locally sourced vapor is typically abundant in clear-sky conditions in austral summer because solar radiation enhances sublimation by heating the snow surface. On the contrary, surface cooling in austral winter or in the coldest hours of the day can cause vapor deposition although the intensity of this flux is generally lower than that of the sublimation flux. Additionally, marine air intrusions in coastal areas can lead to events of vapor deposition as warm and moist air is cooled by the snow surface. Nevertheless, vapor deposition at the snow surface plays a limited role in our main analysis because the total mass removed from all modeled air parcels due to vapor deposition is 46 times lower than the total mass taken up by all parcels due to snow sublimation. On the contrary, vapor deposition is relevant in a validation and sensitivity study with Model Sublimation at Dome C (Sect. D.4 in Appendix D). This site is located in the interior of the Antarctic Ice Sheet where the particularly cold atmosphere can only take up a small amount of water vapor, limiting sublimation and increasing the relative importance of vapor deposition. The ERA5 data suggests that vapor deposition outweighs sublimation at Dome C with a net surface flux of 2.7 kg m^{-2} yr^{-1} in the years of 2013 to 2015. Figure D.2b shows that, if using Run E, the highly parametrized estimate for vapor $\delta^{18}O$ reproduces the mean value measured by Casado et al. (2016) at Dome C in a 24-d period in austral summer 2014/2015 (mean bias error of −0.2‰) although the temporal variability is strongly underestimated. This comparison suggests that Run E uses a reasonable first-order approximation of the vapor isotopic composition with uncertainties of a few ‰ for $\delta^{18}O$. On the contrary, Run N leads to vapor $\delta^{18}O$ values, which are clearly more enriched than the measurements (mean bias error of 10.8‰).

Model Air Parcel

We consider air parcels with a constant volume of $1 \times 1 \times 1$ m^3, travelling along the trajectories that are located in the ABL when reaching the position of the ship. This criterion is met if the air pressure is higher at the location of the trajectory than at the top of the boundary layer. The pressure at the top of the ABL is taken from the trajectory data set and based on ECMWF operational forecasts. As a result, we select 6 to 24 trajectories per arrival time (13 trajectories on average). The surface of each grid cell is represented by one of four surface types: (i) ice-free ocean if the land fraction is ≤ 50% and the sea-ice cover is ≤ 90%, (ii) snow-covered sea ice if the land fraction is ≤ 50% and the sea-ice cover is higher than 90%, (iii) snow-covered land if the land fraction is higher than 50% and the latitude is south of 60° S, and (iv) snow-free land if the land fraction is higher than 50% and the latitude is north of 60° S.

The somewhat arbitrary threshold for sea ice is rather high (90%) because the ocean water

is typically warmer and contributes more strongly to the surface flux, compared to a snow surface of the same area. On the contrary, the threshold for the land-sea boundary is set to 50% to be consistent with the modeling approach of the ERA5 data set. A more sophisticated treatment of sea ice could theoretically be implemented by dividing the evaporation flux into contributions from the ice-free ocean and snow-covered sea ice. Yet, the relative contributions do not correspond to the fractions of surface area. As any assumption on the relationship between the flux contribution and area fraction would be arbitrary, we choose the simple threshold approach to account for areas with the strongest impact of sea ice.

The air parcels are not always initialized 10 days before arriving at the ship. Instead, the time of initialization equals the first time at which the trajectory is located in the ABL and the following two restrictions are respected: (1) Over the ice-free ocean, evaporation must occur at the time and location of initialization; (2) the air parcels are not allowed to travel through the ABL over snow-free land because there, the isotopic composition of the surface flux is not known. If these restrictions prevent the initialization, the model will select the next possible time, meeting the criteria. Restriction (1) allows us to estimate the initial isotopic composition of the parcel using the Craig-Gordon formula simplified with the global closure assumption (e.g., Dar et al., 2020). Under this assumption, the isotopic composition of atmospheric vapor over the ocean equals that of the evaporation flux.

If the initialization occurs over snow-covered land or sea ice, the isotopic composition of the parcel will be initialized as a function of the isotopic compositions of surface snow and snowfall (same assumption as used in Model Sublimation for atmospheric vapor). It is challenging to model the isotopic composition of snow on top of sea ice, especially because it can be influenced by sea spray (Bonne et al., 2019). Apart from that, Model Sublimation is not applicable to snow-covered sea ice because a spin-up period of several months will not make sense if the sea-ice area changes with time. As a first-order approximation, Model Air Parcel assumes that the isotopic composition of surface snow above sea ice equals that of the nearest grid cell with snow-covered land at any time of the simulation. An overview of the locations of initialization and the position of the ship is given in Fig. 3.1. On average, the air parcels are initialized 5.3 days before arriving at the ship. The specific humidity of the parcel is initially taken from the trajectory data set and then modeled prognostically.

Along the trajectory, the specific humidity and isotopic composition of the parcel can increase or decrease due to the surface flux and decrease due to cloud formation. If the air parcel moves above the ABL, only cloud formation may influence the isotopic composition of the parcel (Fig. 3.2). As soon as the parcel enters the ABL again, the model considers both cloud formation and the surface flux. Assuming a well-mixed ABL with a height-constant vapor density, the moisture flux into or out of the parcel (J_a) due to the surface flux (J) is computed as

$$J_\mathrm{a} = J \frac{d_\mathrm{a}}{d_\mathrm{ABL}} , \tag{3.1}$$

where d_a = 1 m and d_ABL are the depths of the air parcel and ABL, respectively. The specific

humidity in Model Air Parcel agrees approximately with that in the trajectory data set (Fig. D.3 of Appendix D). Considering all data points from the initialization of the air parcels to the arrival at the ship, the specific humidity in Model Air Parcel is characterized by a RMSE of 0.6 g kg^{-1} and a correlation coefficient of $\rho = 0.94$ when compared with the trajectory data set. Comparing only the values at the final position of the air parcels (i.e., at the ship) with the trajectory data set, specific humidity tends to be underestimated with RMSE = 0.9 g kg^{-1} and $\rho = 0.45$.

The isotopic composition of the sublimation flux is taken from Model Sublimation whereas the isotopic composition of the deposition flux is assumed to be in isotopic equilibrium with the air parcel. Consequently, the isotopic composition of the deposition flux can differ between Model Air Parcel and Model Sublimation as the latter uses a simpler estimate based on idealized vapor origins. In the case of vapor deposition, condensation, or ocean evaporation, the isotopic composition of the vapor exchanged between the surface and the air parcel depends and feeds back on the air parcel's isotopic composition (Sect. D.3). To guarantee an accurate feedback, the time step needs to be small enough, especially if the vapor mass taken up or removed from the air parcel is in the same order of magnitude as the vapor mass contained in the parcel. Therefore, the effects of ocean evaporation, condensation, or vapor deposition are computed stepwise by dividing each 3-h time step into 32 subintervals of equal length. This value was justified using an example situation, for which the number of subintervals was continuously increased by a factor of two until the isotopic composition of the parcel at the end of the 3-h step changed by less than 1%. An uncertainty in the order of 1% due to the temporal discretization is acceptable, considering that other model assumptions, for example about the snowfall isotopic composition in Model Sublimation, lead to higher uncertainties.

Cloud formation occurs as soon as the specific humidity of the air parcel exceeds its saturation value. Isotopic fractionation during cloud formation is calculated using the classic Rayleigh distillation model with equilibrium fractionation (Jouzel and Merlivat, 1984; Sinclair et al., 2011). In this model, the cloud water precipitates immediately. In reality, the air is supersaturated in mixed-phase clouds and therefore, kinetic fractionation is expected to occur. Although this kinetic effect may be relevant for reproducing measurements of d-excess (Jouzel and Merlivat, 1984), we neglect this effect because the supersaturation ratio is a poorly constrained parameter and our analysis focuses on the less sensitive $\delta^{18}O$ values. The equilibrium fractionation factors used in the Rayleigh model are computed as in Sinclair et al. (2011), accounting for mixed-phase clouds with a gradual, linear shift from the vapor-liquid to the vapor-ice transition as the air temperature decreases from 0° C to −20° C. Changes in air density along the trajectory influence the vapor mass contained in the parcel as they imply exchange of air with the surrounding atmosphere. The model assumes that this exchange of air does not have a direct effect on the isotopic composition of the parcel.

3.2.3 Data From the COSMOiso Model

Thurnherr et al. (2020a) published regional high-resolution simulations with the isotope-enabled general circulation model COSMOiso, covering parts of the Southern Ocean and Antarctic Ice Sheet during the ACE expedition. We compare vapor isotopic data from one of these simulations with the results of Model Air Parcel. While methodological details of the COMOiso simulation are described by the aforementioned authors and Thurnherr et al. (2021), we summarize the features that are most important for our comparison. The horizontal grid spacing (0.125°) is half of that for the ERA5 data and the model includes 40 vertical levels. Isotopic fractionation during ocean evaporation is modeled using the Craig-Gordon formula with a simple parameterization of the kinetic fractionation factor according to Pfahl and Wernli (2009). The snowpack is represented by a one-layer surface snow model. For snow sublimation, the COSMOiso model considers equilibrium fractionation.

From the COSMOiso simulation called leg2_run1, we extract specific humidity and the specific water vapor contents of $H_2{}^{18}O$ and $HD^{16}O$ at the lowest model level in the grid cell containing the position of the ship. This model level corresponds approximately to the measurement height. The vapor isotopic compositions for the COSMOiso simulation are computed as

$$\delta_\mathrm{i} = \frac{q_\mathrm{i}}{q} - 1 \tag{3.2}$$

and expressed in ‰, where q is specific humidity and q_i is the specific water vapor content of a heavy water isotopologue divided by the isotopic ratio of the Vienna Standard Mean Ocean Water.

3.3 Results and Discussion

As expected, the simulated dynamics of $\delta^{18}O$ and δD are very similar. Therefore, we only present results for $\delta^{18}O$ and briefly discuss d-excess.

3.3.1 Comparison of Modeled and Measured Vapor Isotopic Compositions

Figure 3.3 compares the ensemble averaged vapor $\delta^{18}O$ and d-excess of the air parcels with the measurements on the ship close to the Mertz glacier. We show the baseline simulations using the relationship of Stenni et al. (2016) to parameterize the snowfall isotopic composition in Model Sublimation. For comparison, the figure includes results from the Eulerian model COSMOiso, published by Thurnherr et al. (2020a).

Similar to the measurements, our model predicts vapor $\delta^{18}O$ values at the ship of approximately −15‰ in the beginning and at the end of the investigated 6-day period and a pronounced minimum in the middle of the period. In the simulation considering equilibrium fractionation (Run E), this minimum is more pronounced ($\delta^{18}O = -40$‰), compared to the

simulation neglecting fractionation during snow sublimation (Run N, $\delta^{18}O = -34‰$). Differences between both model runs are mainly visible in the middle of the study period. Overall, both runs achieve a similar agreement with the measurements with root-mean-square errors (RMSE) of 4.4‰ and 4.2‰ and Pearson correlation coefficients of 0.77 and 0.75 for Run E and Run N, respectively.

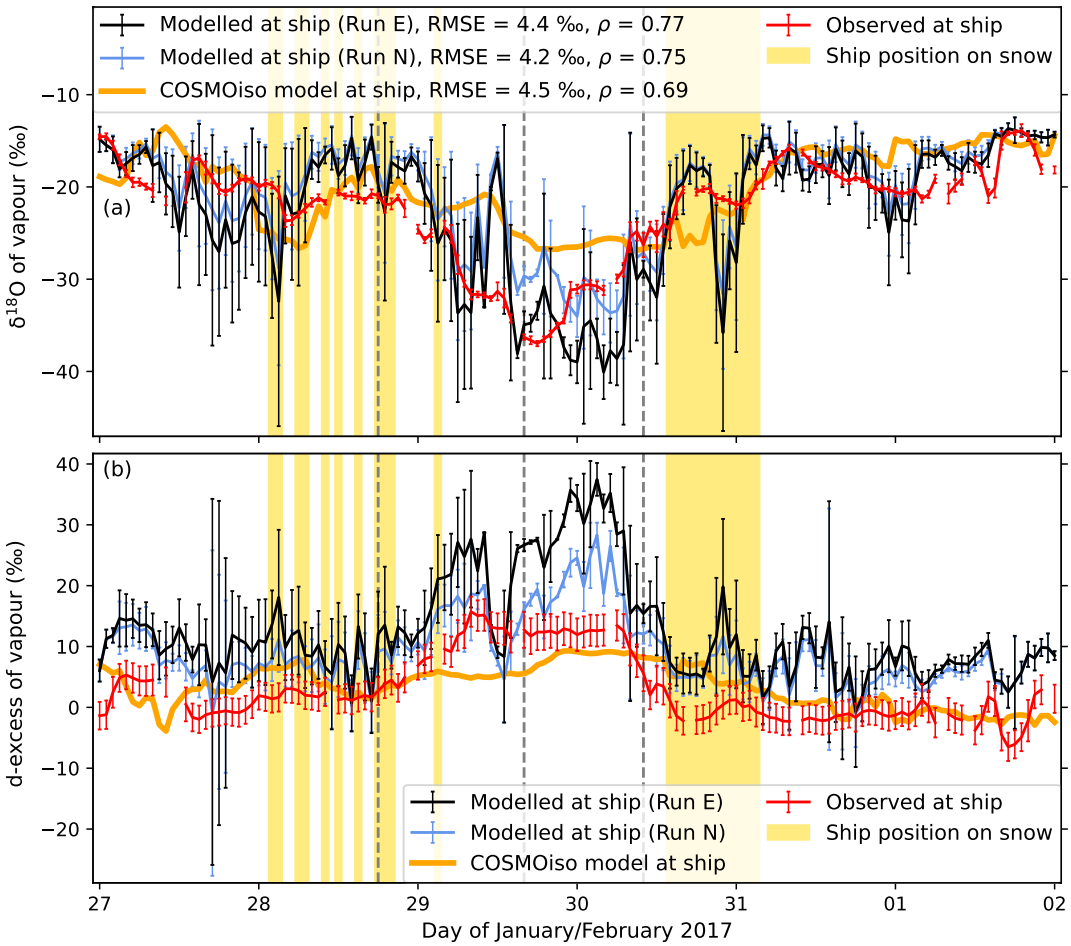

Figure 3.3: Modeled and measured (a) $\delta^{18}O$ and (b) d-excess of atmospheric water vapor at the ship close to the Mertz glacier from 27 January to 1 February 2017. We show the modeled ensemble averages and standard deviations for multiple air parcels in the baseline simulations. The measurements represent 1-h mean values and standard deviations. In the legend, root-mean-square errors (RMSE) and Pearson correlation coefficients (ρ) are specified for the model-measurement comparison. The yellow shading indicates times when the ship was located in a grid cell modeled as snow-covered land; at the other times, the ship was in a grid cell treated as ice-free ocean. The vertical grey dashed lines indicate times analyzed in Fig. 3.5.

In a few short periods, we observe strong deviations of up to ±15‰ between the modeled and measured $\delta^{18}O$ values. Run E predicts clearly too depleted vapor isotopic compositions on 28 January around 03:00 and in the earliest and latest hours of 30 January. On the contrary, the modeled isotopic composition is clearly too enriched on 29 January around 12:00. As will be

shown later, the cases with too depleted isotopic compositions occur at times when the air parcels have experienced a substantial influence of snow sublimation along their trajectories, which is also visible from the noticable difference between Run E and Run N. Therefore, it is likely that the isotopic composition of the surface snow is biased, at least in certain areas. This problem can arise from uncertainties in the δ-temperature relationship for snowfall, applied in Model Sublimation. Figure D.4 and Sect. D.5 of Appendix D show that the lowest δ^{18}O values at the ship are sensitive with respect to the δ-temperature relationship. With the relationships of Fujita and Abe (2006) and Landais et al. (2012), the lowest vapor δ^{18}O values are approximately 5‰ higher and lower, respectively, compared to the baseline simulation. Therefore, the generalization of a site-specific, empirical δ-temperature relationship for snowfall is a strong simplification in the model and contributes to deviations between the model and the measurements. All three δ-temperature relationships tested in this study characterize high-elevation sites on the Antarctic plateau where the temperatures are low and the distillation effect drives the isotopic composition of the snowfall. In coastal areas, however, the snowfall isotopic composition is expected to depend additionally on the humidity conditions in the vapor source region (Touzeau et al., 2016), which is neglected in Model Sublimation. Furthermore, the δ-temperature relationships become more uncertain when applied to temperatures outside the range observed at the high-elevation sites.

Another important source of uncertainty is the simplified representation of sea ice. Air parcels taking up moisture from the surface of grid cells with a sea ice cover below the applied threshold of 90% only experience the effect of ocean evaporation in the model while in reality, a part of the moisture uptake is caused by sublimation of snow or ice with a depleted isotopic composition, compared to the liquid ocean water. Additionally, the isotopic composition of sublimating snow on top of sea ice may be influenced by sea spray, which is neglected in the model.

Moreover, the coarse spatial resolution may contribute substantially to the model-measurement deviations as the coastline is not accurately represented. The model may overestimate or underestimate the time spent by the air parcels in the marine ABL shortly before arriving at the ship, depending on whether the ship is located in a grid cell treated as ice-free ocean or snow surface (yellow shading in Fig. 3.3). If an air parcel with a strongly depleted δ^{18}O value reaches the coast and takes up moisture from the ice-free ocean, the isotopic signature of the parcel can change abruptly as the evaporation flux is much more enriched in heavy SWIs than the air parcel. This effect is particularly strong due to kinetic fractionation, which is driven by the vertical gradients of the water isotopologues above the ocean surface. For an air mass with a very depleted δ^{18}O value, the abundance of the heavy isotopologue will decrease strongly with height above the ocean surface, which enhances the evaporation of the heavy isotopologue. In extreme cases, this kinetic effect can outweigh the effect of equilibrium fractionation such that the evaporation flux can be more enriched in SWIs than the ice-free ocean (Eq. D.13). As the air parcel spends more time in the ABL over the ice-free ocean, the parcel's isotopic composition becomes more similar to that of the ocean and the kinetic effect is generally less pronounced than before.

Further sources of uncertainty with probably minor impacts on the vapor δ^{18}O values may be (i) a bias in the initial isotopic composition of air parcels over the ocean due to the global closure assumption or a bias in the surface water δ^{18}O; (ii) the neglect of kinetic fractionation during cloud formation; (iii) the neglect of mixing of air masses with different isotopic compositions, e.g., at weather fronts; (iv) uncertainties of the ABL height provided with the trajectory data set, influencing the modeled time period and magnitude of moisture exchange between the air parcels and the surface; and (v) the simple assumption that the vapor mass exchanged between the atmosphere and the surface is homogeneously distributed between the surface and the ABL height (Eq. 3.1). This last assumption neglects the fact that, even in a perfectly mixed ABL, an air parcel located close to the surface would take up slightly more mass of vapor from the evaporation or sublimation flux than a parcel at a greater height because the air density decreases with height. The assumption of a perfectly mixed ABL could be implemented more rigorously by considering the mass ratio instead of the thickness ratio for the air parcel and the ABL in Eq. 3.1. Yet, this choice only has a minor effect on our analysis as the ABL height is generally small (780 m on average). Additionally, the air in the ABL is not always perfectly mixed, especially in a stable ABL.

Although there are some hours with a large model-measurement mismatch, Model Air Parcel is able to reproduce the general trend and timing of the vapor depletion event on 29 and 30 January 2017. This depletion event is less visible in the δ^{18}O time series extracted from the COSMOiso simulation, which predicts a minimum δ^{18}O that is 10‰ more enriched, compared to the measurements (Fig. 3.3a). This mismatch may be related to the fact that the snowpack is represented as a single layer with vertically homogeneous isotopic compositions in the COSMOiso model. As demonstrated with a sensitivity analysis for Model Sublimation (Sect. D.4, Fig. D.1), the seasonal and shorter-term variability of the snow isotopic composition decreases significantly with increasing thickness of the considered snow layers.

The measured d-excess of water vapor at the ship is mostly close to zero in the first two and last two days of the study period and exhibits higher values of approximately 13‰ in the middle of the period when the most depleted isotopic compositions are reached (Fig. 3.3b). Our model generally overestimates the measured d-excess values, especially for Run E in the middle of the study period (maximum d-excess: 37‰). Some disagreement between the modeled and measured d-excess is expected, given the poor representation of kinetic fractionation. Future work could improve the model by parameterizing kinetic fractionation during cloud formation using the semi-empirical approach of Jouzel and Merlivat (1984). Additionally, the d-excess of snowfall in Model Sublimation is uncertain because it is based on the δD-δ^{18}O relationship derived by Masson-Delmotte et al. (2008) from a variety of samples including snowfall, snow pits, firn cores, and ice cores, which may partly be influenced by postdepositional processes such as sublimation. Compared to our model, the COSMOiso model performs better in reproducing the measured d-excess although the maximum d-excess is slightly underestimated by the COSMOiso simulation (Fig. 3.3b). Due to the limitations of our model with respect to d-excess, the remaining analysis focuses on the δ^{18}O signal.

3.3.2 Drivers of the Vapor Isotopic Composition

Previous studies at other coastal polar sites have found distinct isotopic signatures for air masses advected from the ocean and those advected from the ice sheet (e.g., Kopec et al., 2014; Kurita et al., 2016a,b; Bréant et al., 2019). Therefore, it is a plausible hypothesis that shifts between such air masses largely explain the observed isotope dynamics close to the Mertz glacier. The more depleted isotopic composition and higher d-excess of vapor over the ice sheet is generally thought to result from the distillation effect of cloud formation with contributions from both equilibrium and kinetic fractionation (Jouzel and Merlivat, 1984; Masson-Delmotte et al., 2008; Kurita et al., 2016a). However, the sublimation and deposition fluxes including isotopic fractionation also influence the variability of the vapor isotopic signal. As the ocean is often a strong vapor source, the distance between the ship and the ice sheet or sea ice may play an important role. In the marine boundary layer, a strong vertical humidity gradient, typically associated with cold air advection over a relatively warm ocean surface, leads to strong evaporation with enhanced kinetic fractionation. This effect can cause differences of several ‰ in the vapor δ^{18}O between cold and warm sectors of extratropical cyclones but it is unlikely to explain a large decrease of more than 10‰ (Thurnherr et al., 2021). We now investigate which of the aforementioned drivers play a dominant role in our case study.

On the first day and during most of the last two days of the study period, the ship moved towards and away from the ice sheet, respectively (Fig. 3.1). Due to a longer distance to the ice sheet, it is likely that recent ocean evaporation caused the relatively enriched vapor δ^{18}O at this time. From 28 January 2017, 02:00, to 31 January 2017, 06:00, the ship stayed in close proximity to the ice sheet. In this phase, the δ^{18}O remained relatively enriched for one day and then dropped to very depleted values. The fact that only the most depleted δ^{18}O values and the highest d-excess values in the time series are sensitive with respect to assumptions in Model Sublimation (Figs. 3.3 and D.4) is consistent with the hypothesis that processes over the ocean drove the vapor isotopic composition in the first and last two days of the period while processes over the Antarctic Ice Sheet influenced the isotopic signature in the middle of the period.

Moreover, the rather small differences between Runs E and N demonstrate that isotopic fractionation during snow sublimation can only explain a small part of the minimum in the δ^{18}O time series. Regarding d-excess, the difference between Runs E and N shows that equilibrium fractionation during sublimation influences the modeled d-excess. This influence is caused by the fact that the δD-δ^{18}O slope associated with equilibrium fractionation amounts to a value lower than 8 at very depleted isotopic compositions and low temperatures (e.g., Touzeau et al., 2016; Dütsch et al., 2017). For the same reason, the modeled d-excess is also influenced by other processes such as vapor deposition and cloud formation, which are represented assuming equilibrium fractionation. Consequently, the increased d-excess values in the middle of the study period do not necessarily reflect an influence of kinetic fractionation.

The initial isotopic composition of the air parcels can influence the model results, especially if the time between initialization and arrival at the ship is short. Air parcels initialized over the ocean start their trajectories with fairly uniform δ^{18}O values between approximately −17‰ and −11‰ (Fig. 3.4a). These initial values are similar to the final isotopic composition modeled at the ship during the first two and last two days of the investigation period, suggesting that ocean evaporation is an important driver. As expected, air parcels initialized over snow have more variable and more depleted initial δ^{18}O values than those initialized over ocean. Interestingly, there are almost always some air parcels that are initialized over snow and the range of their initial δ^{18}O values remains similar throughout the period (approximately −70‰ to −40‰ in Run E). However, when the most depleted δ^{18}O values are observed at the ship, almost all air parcels are initialized over snow. This fact supports the hypothesis that the air masses originate from the interior of the ice sheet at this time.

To assess the importance of different moisture exchange processes along the trajectories, we show in Fig. 3.4b the ensemble-averaged relative contribution of specific processes to the total absolute exchange of moisture mass between an air parcel and the surrounding. Moisture uptake from the ocean is relevant throughout the study period and often represents the process with the strongest contribution to the total moisture exchange. The contribution of moisture uptake from snow surfaces is variable in time and becomes highest when the modeled vapor isotopic composition at the ship is most depleted and sometimes significantly more depleted than the measured values (Figs. 3.3a and 3.4b). In most of these cases, moisture uptake from the snow surface contributes more than any other process to the total moisture exchange. Moisture removal due to cloud formation is a relevant process for most of the time but plays a minor role in the middle of the study period when sublimation is the dominating process. Overall, the contribution of cloud formation to the total moisture exchange correlates strongly with the travel time of the air parcels, that is, the time between initialization and arrival at the ship (Fig. 3.4b,c). This correlation reflects the fact that a longer travel time increases the probability for air mass lifting and cooling. Vapor removal due to the surface flux generally represents the smallest term in the moisture budget with a relative contribution of no more than 5%.

Although the parcels experience little cloud formation in the middle of the period, the distillation effect of cloud formation may still be responsible for the very depleted δ^{18}O values as this effect influences indirectly the initial isotopic composition of air parcels, which begin their trajectory over the interior of the ice sheet. More precisely, the initial isotopic composition of a parcel over snow depends on the snowfall isotopic composition, which decreases with lower air temperatures, reflecting more isotopic distillation due to a larger temperature difference between the ocean (typical vapor source) and the air parcel.

In the middle of the study period, the air parcels spend very little time in the ABL over the ice-free ocean (at times only in the last time step) while they spend more time in the ABL over snow-covered land or sea ice (Fig. 3.4c). Overall, Figs. 3.3 and 3.4 show that the air masses with the most depleted δ^{18}O values and the highest d-excess values originate from the ice

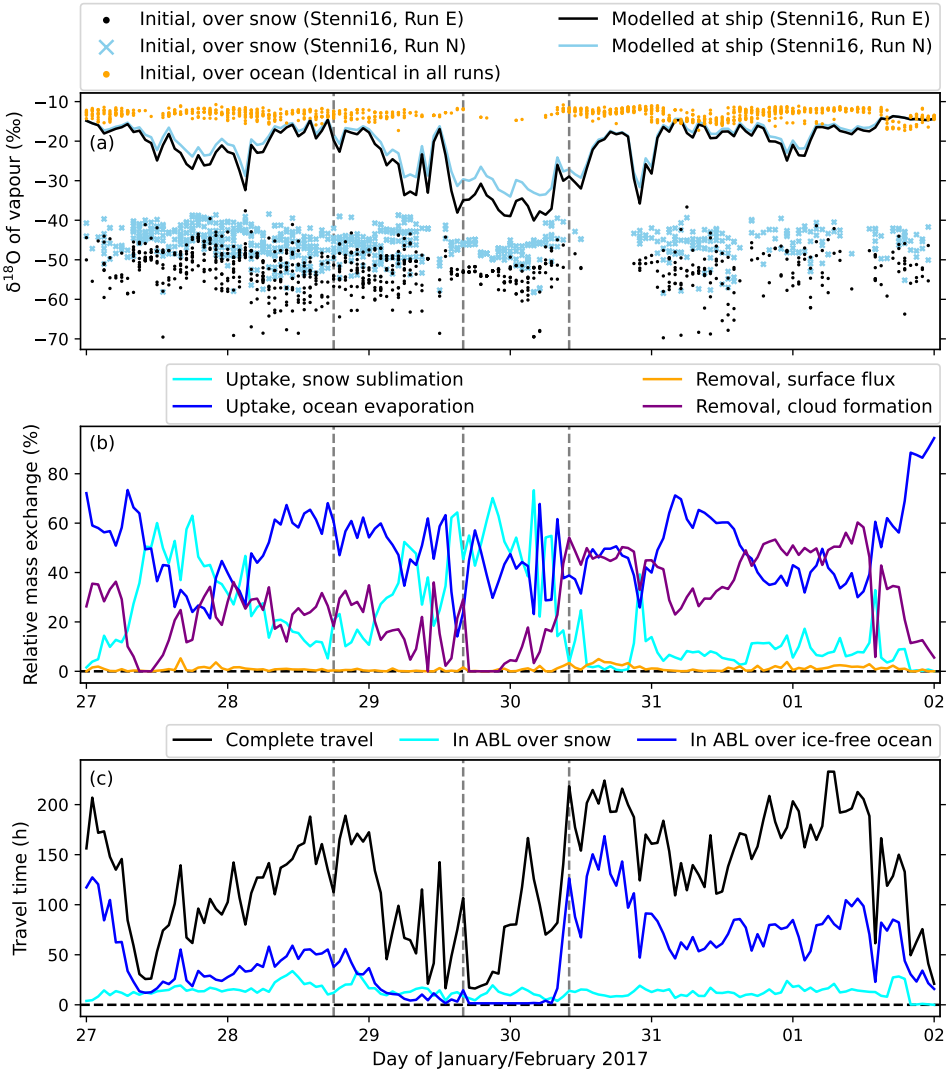

Figure 3.4: (a) Comparison between initial δ^{18}O of individual air parcels and ensemble-averaged final δ^{18}O at the ship; (b) Ensemble average of the relative exchange of moisture mass between an air parcel and the surrounding due to different processes between initialization and arrival at the ship; the sum of the displayed values is 100% at each time; (c) Average travel time of the air parcels and average times spent in the boundary layer (ABL) over snow-covered land or sea ice and the ABL over the ice-free ocean. The vertical grey dashed lines indicate times analyzed in Fig. 3.5.

sheet and their isotopic signature is influenced by snow sublimation. This isotopic signature seems to only reach the ship if the air masses spend little time in the ABL over the ice-free ocean shortly before their arrival such that ocean evaporation cannot overwrite the signature.

To better understand which drivers act in which sections of the air parcel trajectories, we illustrate the δ^{18}O values along indivual trajectories in space and time for three different arrival times in Fig. 3.5. The arrival times include situations with relatively enriched and

depleted δ^{18}O values while the ship is close to the ice sheet, the ensemble averaged travel time of the air parcels is at least 4 days, and the modeled vapor δ^{18}O only deviates slightly from the measured one. Figures 3.5a,b show a situation leading to relatively enriched δ^{18}O values at the ship. In this case, the air parcels travel some distance in the ABL over the ice-free ocean parallel to the Antarctic coast before moving in the ABL over a snow-covered area in the last 10 h of their travel. Almost half of the air parcels are initialized over the ice sheet and exhibit strongly depleted δ^{18}O values around −52‰ until they enter the ABL over the ice-free ocean. Due to ocean evaporation, the δ^{18}O of the air parcels quickly increases and reaches values comparable to those of parcels initialized over the ocean.

Figures 3.5c,d refer to a situation with one of the most depleted δ^{18}O values measured at the ship. Four of seven air parcels are initialized over the ice sheet and take a direct and short route to the ship where they only take up moisture from the ice-free ocean in the last time step. Their final δ^{18}O values are similar to those of the other three parcels that are initialized over the ocean and travel over the interior of the ice sheet before taking the same final route as the parcels initialized over snow. While the parcels are lifted over the ice sheet and above the ABL, their isotopic composition becomes increasingly depleted due to the distillation effect of cloud formation and reaches extreme δ^{18}O values of approximately −60‰ to −75‰. After reaching these extreme values, the air parcels maintain their isotopic composition for approximately four days because cloud formation stops as soon as the parcels begin to descend and the surface flux does not affect the free troposphere above the ABL. Only towards the end of the trajectories as the parcels move over the escarpment zone of the ice sheet, they enter the ABL over snow. At this time, approximately 20 h before the arrival at the ship, snow sublimation adds vapor with a relatively enriched δ^{18}O value to the parcels (Fig. 3.5d). The sublimation flux in the escarpment zone is relatively enriched in heavy SWIs compared to the air parcels because their isotopic composition was shaped at higher and colder levels over the interior of the ice sheet. Additionally, the parcel isotopic composition is particularly sensitive with respect to moisture uptake after most of the initial vapor mass was removed from parcels due to cloud formation. As a consequence, the moisture uptake in the escarpment zone increases the isotopic composition of the parcels abruptly. This increase caused by sublimation is similarly strong as another increase in the last time step, when the parcels reach the ice-free ocean and take up moisture from the water surface.

The situation shown in Figs. 3.5e,f leads to an intermediate δ^{18}O at the ship. All air parcels start their trajectories over the ocean and finally travel over the coastal zone of the ice sheet. Already over the ocean, cloud formation and condensation at the surface begin to decrease the δ^{18}O of the parcels. As soon as the parcels reach the ice sheet, their δ^{18}O continues to decrease because snow sublimation adds vapor with a more depleted δ^{18}O value to the air parcels. In this situation, the sublimation flux is more depleted in heavy SWIs compared to the parcels because the latter carry the isotopic signature of processes over the ocean.

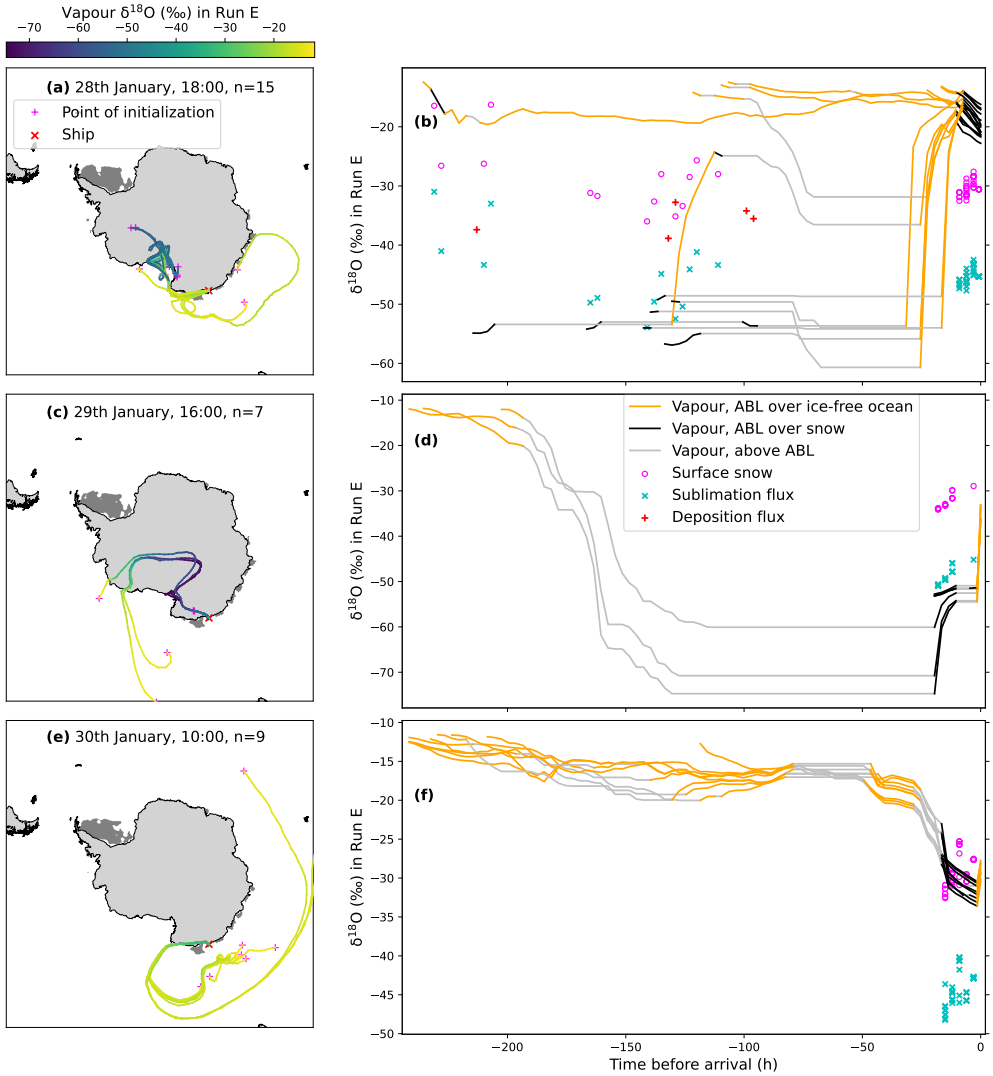

Figure 3.5: Vapor δ^{18}O along air parcel trajectories in the baseline simulation of Run E for three different times of arrival at the ship (grey dashed lines in Figs. 3.3 and 3.4). Each of the three cases is illustrated with a map (a, c, e) and δ^{18}O-time diagram (b, d, f). The number of trajectories is denoted by n and areas treated as snow-covered sea ice are colored darkgrey in the maps. The surface snow and sublimation flux are only shown in b, d, and f when sublimation affects the air parcel. Trajectories arriving at the ship at a lower height are plotted on top of others.

3.4 Conclusions

We developed a Lagrangian isotope model with the aim to reproduce and explain the vapor δ^{18}O time series measured on the ACE ship close to the Mertz glacier in a 6-day period in austral summer 2017. The vapor mass and isotopic composition of air parcels was modeled along trajectories between an initial location in the ABL and the final location in the ABL at the ship. While isotope effects of cloud formation and ocean evaporation were represented

with common approaches (classic Rayleigh distillation model and Craig-Gordon formula, respectively), the effect of snow sublimation was estimated using a novel approach, considering changes of the isotopic composition in a multi-layer snowpack due to snowfall, sublimation, and vapor deposition.

Similar to the measured values, the modeled vapor δ^{18}O at the ship reaches a pronounced minimum value of −40‰ in the middle of the study period. The RMSE of the baseline simulation amounts to 4.4‰, which is reasonable considering the model limitations such as the generalization of a site-specific δ^{18}O-temperature relationship for snowfall and the strongly simplified representation of snow on top of sea ice. Our analysis confirms the hypothesis that the relatively enriched δ^{18}O values are associated with air masses advected from the ocean whereas the strongly depleted δ^{18}O values are caused by direct advection of air masses from the Antarctic Ice Sheet. This result is consistent with similar observations at other coastal polar sites in the literature. As expected, cloud formation leads to very depleted vapor isotopic compositions over the ice sheet. Snow sublimation can also significantly modify the isotopic composition of the air parcels depending on their origin. For example, air parcels originating from high levels over the interior of the ice sheet may carry a strongly depleted isotopic signature to the escarpment zone of the ice sheet and then experience an abrupt and strong enrichment in heavy SWIs due to a relatively enriched sublimation flux. The model run considering equilibrium fractionation during snow sublimation leads to a more pronounced minimum in the vapor isotopic composition at the ship, compared with the model run neglecting fractionation during sublimation. Although the latter model run agrees slightly better with the measured isotopic composition at the ship, snow sublimation may still be associated with fractionation as the model-measurement agreement is also influenced by the other model uncertainties. A critical factor for the vapor δ^{18}O at the ship is the time that the air parcels spend in the marine ABL shortly before arriving at the ship because ocean evaporation can quickly overwrite their isotopic signature.

Our modeling approach could be adapted for a study similar to Helsen et al. (2006) to simulate the vertical isotope profile in snow pits using backward trajectories for events of snow accumulation at an Antarctic site and deriving the isotopic composition of local snowfall from that of the air parcels. In contrast to the model of Helsen et al. (2006), our model accounts for the postdepositional effects of snow sublimation and vapor deposition. However, further improvements in our model such as the parameterization of kinetic fractionation during cloud formation and snow-atmosphere exchange as well as a more sophisticated vapor transport mechanism in the snowpack may be important for this purpose. Moreover, the deposition of drifting and blowing snow can contribute to snow accumulation and influence the isotopic composition of surface snow. To understand the latter effect, fundamental research is needed as the isotopic composition of drifting and blowing snow particles may be altered by sublimation, which has not been studied so far.

Open Research

Model results were generated using Copernicus Climate Change Service information [2021] available at https://doi.org/10.24381/cds.adbb2d47 (Hersbach et al., 2018). The air parcel trajectories were downloaded from https://doi.org/10.5281/zenodo.4031705 (Thurnherr et al., 2020c). The calibrated isotope maesurements from the ACE campaign were downloaded from https://doi.org/10.5281/zenodo.3250790 (Thurnherr and Aemisegger, 2020). Simulation data of the COSMOiso model were downloaded from https://doi.org/10.3929/ethz-b-000445744 under the CC BY 4.0 license available at https://creativecommons.org/licenses/by/4.0/ (Thurnherr et al., 2020a). Validation data from the Dome C site containing δ^{18}O of surface snow and atmospheric vapor were retrieved from https://doi.org/10.5194/tc-12-1745-2018-supplement and https://doi.org/10.5194/acp-16-8521-2016-supplement, respectively (Casado et al., 2016, 2018). The python programming code and the main model output including the data shown in the figures are available at https://doi.org/10.16904/envidat.417 (Sigmund et al., 2023). The figures were made with Matplotlib version 3.5.1, available under the Matplotlib license at https://matplotlib.org/(.)

General Conclusions

In this work, we analyzed in-situ measurements, LES-LSM simulations, and a simple 1D model of sublimation and snow transport to assess the reliability of sublimation measurements in conditions of snow transport and propose improvements in the parameterizations of sublimation and snow transport of large-scale models. Additionally, we compared vapor isotopic measurements with a simple Lagrangian isotope model to better understand the influence of surface sublimation and other drivers on the vapor isotopic composition observed at a coastal polar site.

The analysis demonstrates that measurements based on the Monin–Obukhov bulk parameterization underestimate significantly the total fluxes of moisture and heat in conditions of snow transport because of the assumption of height-constant turbulent fluxes between the surface and a certain measurement height, e.g., $z = 1$ m. If this measurement height was reduced, the flux divergence between the considered heights would be smaller and therefore the above-mentioned theory-related error of the Monin–Obukhov bulk parameterization would decrease; yet, the sensitivity with respect to instrument uncertainties would increase, making this measurement approach unsuitable. The theory-related error leads to an underestimation of both sublimation and vapor deposition. Therefore, this error is expected to be less pronounced for fluxes averaged over large temporal and spatial scales, compared to instantaneous fluxes at a specific site. Nevertheless, averaged fluxes based on the Monin–Obukhov bulk parameterization should still be interpreted with care because sublimation generally outweighs vapor deposition on large scales and similarly, the respective theory-related errors may not balance each other.

Eddy-covariance measurements can capture the total sublimation below the sensor height as long as there is little blowing snow or snowfall at the sensor height and spikes are removed from the high-frequency data. To minimize the effect of artifacts caused by blowing snow, it is recommended to install the eddy-covariance sensors at a greater height, compared to the set-up used for this study. A greater sensor height would reduce the number of artifacts, most notably spikes, because the concentration of blowing snow particles generally decreases strongly with height. The more spikes are contained in the high-frequency data, the more careful should the eddy-covariance fluxes be interpreted because an influence of undetected artifacts cannot be excluded.

In models, the Monin–Obukhov bulk parameterization is currently the only reasonable method to compute the surface fluxes. To minimize the theory-related error of this parameterization in conditions of snow transport, the lowest model level with prognostic temperature and humidity values should be close to the snow surface. Regarding the sublimation of drifting and blowing snow, it is important that the parameterizations of large-scale models represent the thermodynamic conditions close to the surface as accurate as possible. Similar to current parameterizations of the mixing ratio of blowing snow, specific humidity and temperature should be solved prognostically using a surface scheme with a high vertical resolution in the lowest few meters of the atmosphere. As demonstrated for four situations, it is possible to parameterize the effect of transient particle temperatures on sublimation in the lowest 0.3 m of the atmosphere by introducing an empirical term in the formula of Thorpe and Mason (1966), leading to a significantly better agreement with the LES-LSM simulations, at least in near-saturated conditions. Since the empirical term is based on data for a few situations at a single site close to the Antarctic coast in summer, we will risk introducing errors in large-scale simulations if we apply this empirical term to the whole Antarctic Ice Sheet and all seasons. Therefore, further LES-LSM simulations are needed to validate the empirical term outside a narrow range of rather warm temperatures and moderate friction velocities and potentially improve the term. Additionally, the effect of radiation fluxes on the empirical term and on the sublimation of drifting and blowing snow in general remains to be explored. While the radiation fluxes may largely balance each other in cloudy conditions or dense and deep blowing snow layers, radiation may have a relevant effect on shallow blowing snow layers in clear-sky conditions.

Regarding snow transport, the 1D model shows that current parameterizations of the mixing ratio of blowing snow are sensitive with respect to (a) the vertical resolution in the lowest part of the suspension layer and (b) poorly constrained parameters such as the height of the saltation layer, mean particle diameter at this height, and roughness length. Although these parameters can be reasonably well defined for specific sites and periods by means of measurements, it is challenging to estimate the parameters for large areas. Choices concerning the above-mentioned parameters influence significantly the abundance of blowing snow and the total sublimation rate, at least if the blowing snow layer is not saturated with respect to water vapor. In the CRYOWRF and Meso-NH/Crocus models, the saltation layer height seems to be underestimated. On one hand, this underestimation has the advantage that the mass and number mixing ratios of drifting snow at the saltation layer height are not sensitive with respect to an incorrect slope of the vertical profile of the mixing ratios in the saltation layer. On the other hand, the underestimated saltation layer height contributes to an overestimation of the mixing ratios of blowing snow in the suspension layer. The LES-LSM model can be used in the future to develop improved parameterizations of the height of the saltation layer and the exponential profile of the mass mixing ratio of drifting snow in this layer. Some progress in this regard is shown in Melo et al. (2023) and may help to better define the lower boundary condition for snow suspension in large-scale models. As long as these improvements of the saltation parameterization are missing, the effect of the underestimated height of the saltation

layer can be counteracted by increasing the mean particle diameter at this height. Regarding the roughness length, the available measurement data is not sufficient to characterize the spatio-temporal variability and it remains unclear whether current large-scale models use an appropriate average value to define this parameter.

The results of this thesis show that the LES-LSM model is a powerful tool, providing detailed insights in the vertical profiles of particle-turbulence interactions, which are only partly accessible with measurements. Nevertheless, the LES-LSM simulations performed in this study are associated with two important limitations and some potential for future improvements. First, the radiation fluxes are neglected in the energy balance of drifting and blowing snow particles. This shortcoming could be addressed in the future by implementing a radiation scheme in the LES-LSM simulations and comparing the results with radiation measurements at different heights in blowing snow conditions. With this improvement, the LES-LSM simulations may be able to reproduce the sign of the measured latent and sensible heat fluxes for a larger range of conditions. Second, the computational effort limits the domain size and prevents us from representing the influence of the largest eddies contributing to the turbulent moisture flux. We were able to increase the domain size and represent a large range of eddy sizes by improving the computational efficiency of the software but further improvements in this regard would be possible if the parallelization strategy was changed more fundamentally. With a greater height of the LES domain, it would also be possible to define the upper boundary conditions of the 1D model at a greater height, which would allow the parameterized specific humidity and temperature to react more realistically to changes of the moisture and heat fluxes as a result of certain parameterization options.

Despite some limitations, the findings of this thesis will contribute to improving large-scale assessments of snow sublimation and surface mass balance in snow-covered environments. It is planned to implement the proposed improvements of the sublimation parameterization in the CRYOWRF model to study implications for the surface mass balance of the Antarctic Ice Sheet in recent years. Comparisons between CRYOWRF simulations with nested domains and eddy-covariance measurements of sublimation will play an important role in assessing the reliability of the simulations. For this purpose, suitable measurement data have been acquired at Princess Elisabeth Station and Davis Station, East Antarctica, in all seasons of recent years.

The proposed improvements of large-scale simulations are expected to reduce on average the contribution of the suspension layer to the moisture flux while increasing the contribution of the saltation layer. For the CRYOWRF model, the improvement due to prognostic humidity profiles very close to the surface is expected to reduce the contribution of the snow surface to the moisture flux because the theory-related error of the Monin-Obukhov bulk parameterization is mitigated. The net effect of the aforementioned changes is difficult to estimate a priori and remains to be explored. Apart from that, the technical feasibility of the proposed improvements remains to be shown. The additional computational effort of computing humidity and temperature prognostically in the lowest few meters of the atmosphere is likely acceptable because similar calculations for the mass and number mixing ratios of blowing

snow only account for a minor fraction of the model runtime (Sharma et al., 2023). However, the increased vertical resolution with the lowest saltation level at a height of 0.0075 m may require a reduced time step to achieve numerical stability.

Regarding stable water isotopes, our simple Lagrangian model underlines the conclusion of previous studies that the vapor isotopic composition at coastal polar sites is strongly driven by shifts between air masses recently influenced by ocean evaporation and air masses advected from the interior of the ice sheet. The latter air masses are strongly depleted in the heavy isotopologues because of the distillation effect of cloud formation. Two novel insights in the isotope dynamics of atmospheric vapor were gained. First, air masses carrying a strongly depleted isotopic composition from the ice sheet to the marine boundary layer typically lose their isotopic signature within few hours due to a sudden and strong enrichment under the influence of ocean evaporation. Second, surface snow sublimation can significantly modify the isotopic composition of air masses, especially for marine air intrusions over the ice sheet or air masses descending from the free-troposphere to the boundary layer. Therefore, both Lagrangian and Eulerian isotope models should carefully represent the isotopic compositions of the surface snow and sublimation flux.

While our Lagrangian isotope model successfully reproduces the general evolution of the measured vapor δ^{18}O values in the study period, there are temporarily strong deviations between the model and measurements. These deviations are likely related to the simplified representation of the (a) snowfall isotopic composition, (b) areas covered by sea ice, (c) isotopic composition of sea-ice surfaces, and (d) the uncertainties associated with the exact origin of an air mass, which is modeled by multiple air parcel trajectories. As general circulation models can better represent features a to c, it would be interesting to perform a similar analysis using an isotope-enabled general circulation model after improving and validating the calculation of the isotopic composition of surface snow in this model.

Moreover, current isotope models may underestimate the effect of sublimation on the vapor isotopic composition because kinetic fractionation in the sublimation process and the influence of sublimation of drifting and blowing snow are currently not well understood and therefore typically neglected. While we focused on modeling the effect of the origin of air masses, it is necessary to perform in-situ measurements near the snow surface or laboratory experiments to develop a better process understanding with respect to kinetic fractionation and snow transport effects. If the process understanding improves in the future, it may eventually be possible to represent isotope dynamics in LES-LSM or CRYOWRF simulations and develop a more comprehensive understanding of the effects of snow-atmosphere exchange on the vapor and snow isotopic composition.

A Processing of Eddy-Covariance Data

The initial steps of the post-processing of the EC data aimed at removing artifacts from the high-frequency data and a bias in the water-vapor density (Fig. A.1). Diagnostic flags and values from the ultrasonic anemometer and the gas analyzer were only recorded in aggregated form for each 30-s interval. If the fraction of flags indicating a malfunction of the ultrasonic anemometer is > 33.3% in the 30-s interval under consideration, the whole interval is discarded in the anemometer data. This threshold is a trade-off between data quality and availability. Because a large number of problematic flags is associated with a large number of spikes in the time series, the remaining artifacts were likely removed later by the spike-removal procedure. The water-vapor density was discarded during the 30-s interval if more than 1% of the records were flagged with a malfunction of the gas analyzer (which was not frequent) or the mean automatic gain control (AGC) value exceeded 60%, indicating some obstruction of the optical path.

In the next step, lower and upper plausibility limits were applied to the high-frequency records (Table A.1). The upper plausibility limit for water-vapor density was based on the saturation value for the upper plausibility limit for sonic temperature, while additionally accounting for a systematic overestimation of the water-vapor density by the gas analyzer.

This bias was evident from a comparison with low-frequency reference data from a temperature and relative humidity probe. It can be explained by an instrument drift because a zero calibration of the gas analyzer had not been performed for a long time due to the remoteness

Table A.1: Plausibility limits for horizontal (u, v) and vertical (w) wind velocity components, sonic temperature (T_{sonic}), and molar density of water vapor (ρ_{vm})

Type of limit	u ($\mathrm{m\,s^{-1}}$)	v ($\mathrm{m\,s^{-1}}$)	w ($\mathrm{m\,s^{-1}}$)	T_{sonic} (°C)	ρ_{vm} ($\mathrm{mmol\,m^{-3}}$)
Lower	−40	−40	−10	−19	0
Upper	+40	+40	+10	+11	680

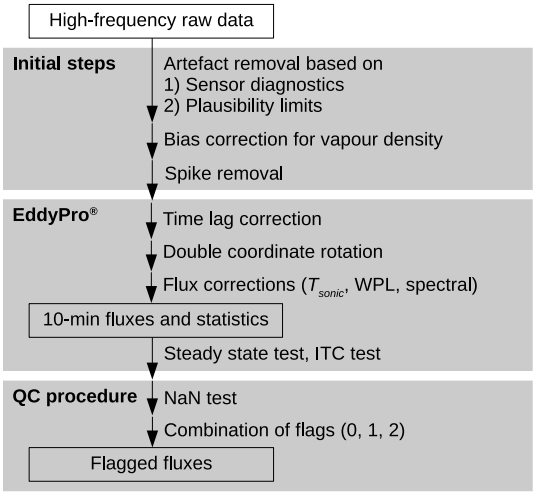

Figure A.1: Processing of EC data including initial steps, the use of the EddyPro® Software, and quality control (QC). The flux corrections account for the difference between sonic temperature (T_{sonic}) and air temperature, for density fluctuations (WPL terms), and for spectral losses at high and low frequencies.

of the site. Due to a nonlinear calibration curve, a constant bias in the raw absorptance leads to a slightly varying bias in the vapor density and affects the calculation of vapor fluctuations and fluxes (Fratini et al., 2014). Similar to Nieberding et al. (2020), a correction procedure adapted from Fratini et al. (2014) was applied after estimating the bias for each 10-min interval from the difference between the median vapor densities of the gas analyzer and the reference sensor. The bias amounted to approximately +40 mmol m^{-3} and the correction reduced the magnitude of LE by 5%.

Spikes in the high-frequency time series were removed using a novel algorithm. In contrast to existing algorithms, it makes use of the observations that (i) the variables measured by the ultrasonic anemometer often exhibit simultaneous spikes and (ii) the vast majority of spikes are single-point spikes. The algorithm builds on the spike criterion of Mauder et al. (2013):

$$|d_i| > \frac{q\,MAD}{0.6745}\,, \tag{A.1}$$

where $|d_i|$ is the absolute difference between an instantaneous value and the 5-min median of a time series, MAD is median absolute deviation, and $q = 7$ is an empirical factor. The denominator in Eq. A.1 relates the MAD with the standard deviation if the instantaneous values reflect a normal distribution. Instead of $|d_i|$, we use a metric for single-point spikes taking the two neighbouring data points into account:

$$\hat{x} = |d_i| - 0.5(|d_{i-1}| + |d_{i+1}|)\,, \tag{A.2}$$

where the spike metric $\hat{x}$ becomes positive and large for single-point spikes. In this calculation, NaN (not a number) values are treated as being equal to the 5-min median. The spike criterion

for the anemometer variables combines the respective spike metrics as follows:

$$\frac{\hat{u}}{MAD(u)} + \frac{\hat{v}}{MAD(v)} + \frac{\hat{w}}{MAD(w)} + \frac{\hat{T}_{sonic}}{MAD(T_{sonic})} > \frac{q_s}{0.6745}\,, \tag{A.3}$$

where u and v are the horizontal wind velocity components, w is the vertical wind velocity component, T_{sonic} is sonic temperature, and $q_s = 6$ is an empirical factor. The advantage of this multivariate spike criterion is the detection of artifacts with a less pronounced deviation from the 5-min median, if visible in several variables.

The gas-analyzer variables (water vapor and carbon dioxide) usually did not exhibit spikes at the same time. Thus, the spike criterion for water-vapor density was only based on the water-vapor spike metric:

$$\frac{\hat{\rho_v}}{MAD(\rho_v)} > \frac{q_s}{0.6745}\,, \tag{A.4}$$

with the same empirical factor of $q_s = 6$. Spikes were replaced by NaN values and the spike removal was iterated until the last iteration increased the total number of spikes by less than 5% or until a maximum of ten iterations was reached.

The EC data were further processed using the EddyPro® Software while allowing for a maximum fraction of missing data of 40% per 10-min interval (LI-COR Biosciences, 2019). Potential time lags between the wind and vapor measurements were corrected by maximizing the cross-covariance. The median time lag was 0.10 s. In 1% of the cases, this method suggested a time lag beyond the plausibility limits of ±1.00 s and a default time lag of 0.15 s was assumed. A double coordinate rotation was applied. Fluctuations were computed using block averaging without detrending. The flux H was corrected for the difference between sonic and air temperature (Van Dijk et al., 2004). The flux LE was corrected for density fluctuations considering the so-called WPL terms (Webb et al., 1980). All turbulent fluxes were corrected for spectral losses at high and low frequencies (Massman, 2000, 2001; Moncrieff et al., 2004). The spectral correction for high frequencies increased the LE, H, and τ values on average by 6.7%, 1.1%, and 0.9%, respectively. The quality-control procedure is described in Sect. 1.2.2.

B Supplementary Material for Chapter 1

B.1 Artificially Locked Large-Scale Coherent Structures in the Simulation

To compare a turbulence cospectrum between the large-eddy simulations coupled with a Lagrangian stochastic model (LES–LSM) and the field measurements, high-frequency time series were extracted from a certain grid point of the simulation domain. This grid point is located at approximately the same height as the eddy-covariance (EC) sensors in the field and at the horizontal centre of the domain. The time series extracted from the Drift_1 simulation exhibit wave-like trends (Fig. B.1), which are not visible in the field measurements.

The trends can be explained by the small domain length (18 m) and the periodic horizontal boundary conditions, leading to an artificial locking of large-scale coherent structures (Munters et al., 2016). These strucures are characterized by streamwise-elongated streaks with a high wind speed, which are flanked by similar streaks with a low wind speed (Fang and Porté-Agel, 2015). Due to the limited domain length, the structures cannot freely meander but they are largely locked in their position in the y direction perpendicular to the mean flow. This effect is evident from streamwise-oriented bands of increased and reduced wind velocity components, air temperatures, specific humidities, etc., in time-averaged horizontal cross-sections of the domain (Fig. B.2). Another important consequence is the fact that the 10-min averaged vertical wind velocity component can differ significantly from zero at individual grid points although the horizontal average is zero (Fig. B.2b).

Fig. B.3 shows the time–width cross-sections for the profile indicated by the dashed red line in Fig. B.2. As the variability of the flow properties is small along the streamwise direction, the time–width cross-sections are nearly independent of the streamwise location (not shown). The data shown in Fig. B.3 has a temporal resolution of 5 s and demonstrates that flow structures with a relatively high streamwise velocity component are associated with a negative vertical velocity component, a relatively high temperature and a relatively low specific humidity. The location of these structures on the y-axis varies slowly with time, causing artificial wave-like

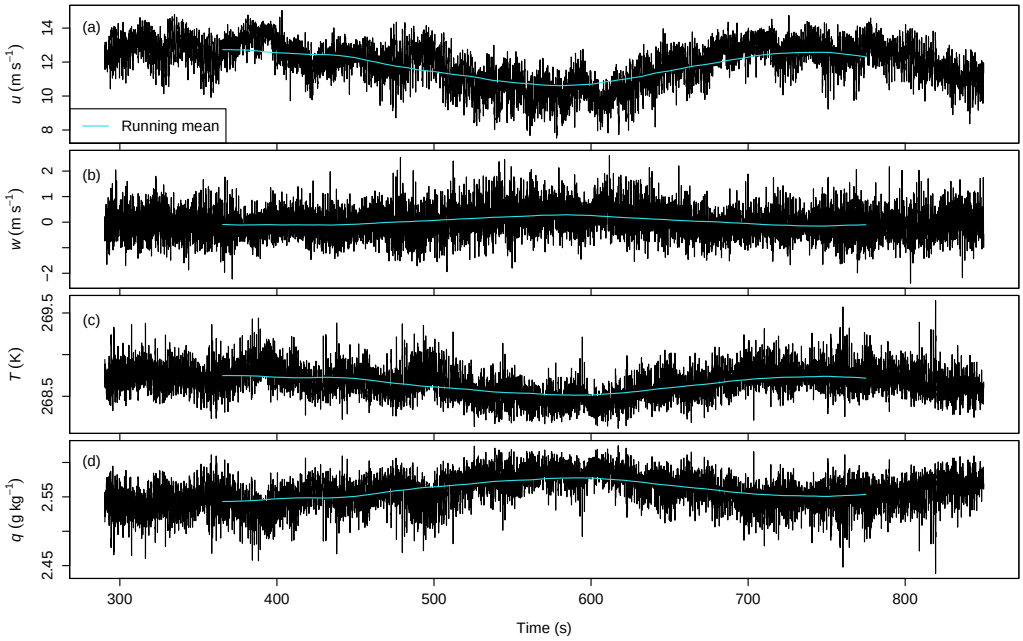

Figure B.1: Simulated time series sampled at a frequency of 20 Hz at a grid point with a height of 1.97 m in the centre of the domain during the quasi-stationary period of the Drift_1 simulation set-up: (a) wind velocity component (u) along the direction of the mean flow, (b) vertical wind velocity component (w), (c) air temperature (T), and (d) specific humidity (q). The running mean is based on a time window of 150 s and shown for the period, on which the turbulence cospectrum in Fig. 1.7 of Chapter 1 is based.

trends at the sampling location for the high-frequency time series.

B.2 Simulated Vertical Profiles in a Case with Negligible Snow Transport

The NoDrift simulation set-ups aimed at reproducing the conditions with low wind speeds measured at the S17 site on 12 January 2019 between 05:40 UTC and 05:50 UTC. At that time, the snow particle counters measured mass fluxes of drifting snow below the noise threshold (< 0.005 kg m^{-2} min^{-1}). Despite the low wind speed in the NoDrift set-ups (2.4 m s^{-1} at a height of 1 m, Fig. B.4a), a small amount of drifting snow is simulated very close to the surface (Fig. B.4e). At the first grid level above the surface, the horizontal mass flux of drifting snow is three orders of magnitude lower than in the simulations with significant snow transport (Drift_1, Drift_2). At the heights of the snow particle counters, the mass flux is negligible and in agreement with the measurements.

In the NoDrift_1 simulation, air temperature, specific humidity and relative humidity are very close to the measured values at a height of 1 m (Fig. B.4b–d). The NoDrift_2 set-up is used to study the sensitivity of the sensible and latent heat fluxes with respect to modified upper

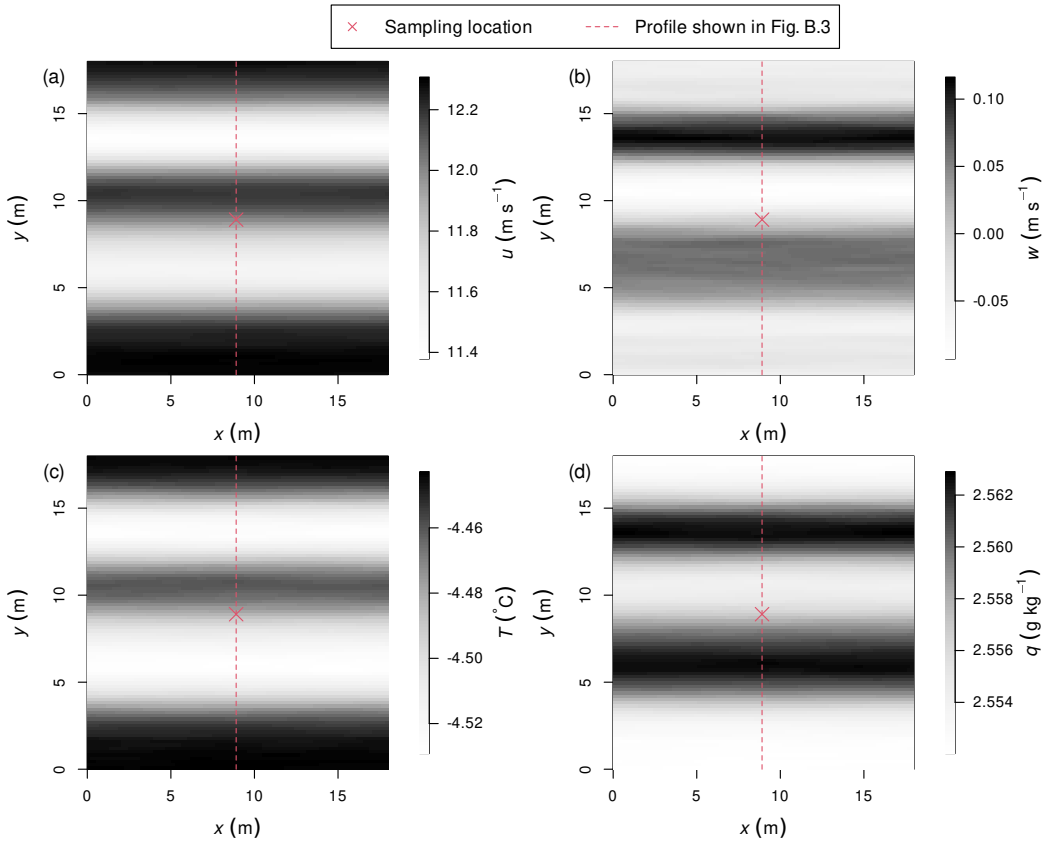

Figure B.2: Time-averaged horizontal cross-sections of (a) the wind velocity component (u) along the direction of the mean flow (x), (b) the vertical wind velocity component (w), (c) the air temperature (T), and (d) the specific humidity (q) at a height of 1.97 m above the surface for the 10-min quasi-stationary period of the Drift_1 simulation set-up. In the centre of the cross-sections, the time series of Fig. B.1 were sampled. The red dashed line indicates the profile, for which the temporal evolution is shown in Fig. B.3.

boundary conditions that result in maximum values for air temperature and specific humidity within the uncertainty range of the measurements. Fig. B.4f, g show that the exchange of sensible and latent heat is almost entirely achieved by the surface fluxes while the contribution from the small amount of drifting snow is negligible. The simulated sensible heat flux (H) is 6.6 W m^{-2} and 0.0 W m^{-2} for the NoDrift_1 and NoDrift_2 set-ups, respectively. These values are close to the measured H value of 5.1 ± 6 W m^{-2} based on the bulk parametrization of the Monin–Obukhov similarity theory (MOST) while the EC measurements suggest a slightly negative H value (-3.0 W m^{-2}). The simulated latent heat flux (LE) is 8.3 W m^{-2} and 2.0 W m^{-2} for the NoDrift_1 and NoDrift_2 set-ups, respectively. Both the MOST-based measurements (6.5 ± 5 W m^{-2}) and the EC measurements (4.0 W m^{-2}) yielded a LE value between the simulated ones.

The simulation-based Monin–Obukhov bulk fluxes are a bit lower than the simulated LE and

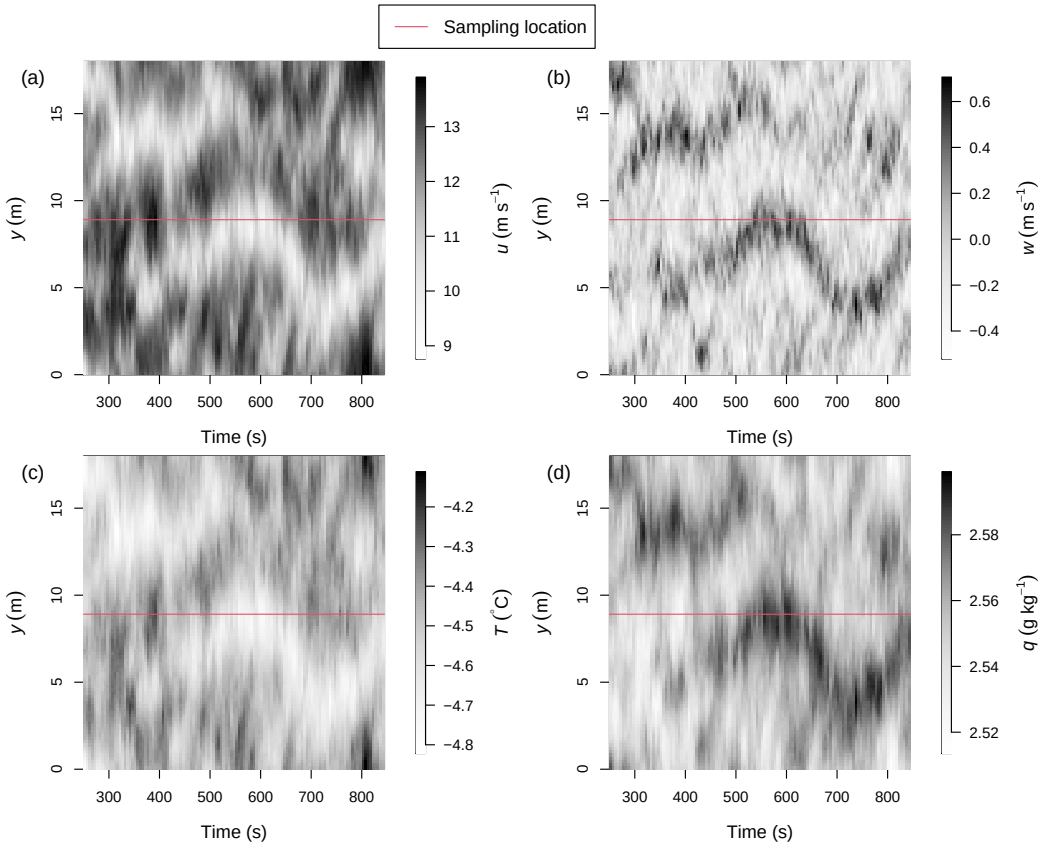

Figure B.3: Time-width cross-section for the 10-min quasi-stationary period of the Drift_1 simulation set-up: (a) wind velocity component (u) along the direction of the mean flow, (b) vertical wind velocity component (w), (c) air temperature (T), and (d) specific humidity (q). The variability along the width of the domain (y) is shown for the middle position on the length axis ($x = 8.91$ m) at a height of 1.97 m, as indicated by the dashed line in Fig. B.2. The plot is based on 5-s average values. The solid red line highlights the sampling location for the time series of Fig. B.1.

H values. Nevertheless, the aggreement is substantially better than for the simulations with significant snow transport. The simulation-based EC fluxes agree well with the simulated LE and H values in the NoDrift_2 set-up but not in the NoDrift_1 set-up. This finding can be explained by the following effect of the artificial locking of large-scale coherent structures. As the 10-min averaged vertical wind velocity component differs from zero at individual grid points, only a part of the vertical transport of heat and moisture is represented by the turbulent flux while the other part results from vertical advection, at least at indivual grid points. In the NoDrift_1 simulation, the horizontally averaged vertical advection of heat and moisture is in the same order of magnitude as the simulation-based EC flux. Therefore, the simulation-based EC fluxes roughly account for half of the exchange of sensible and latent heat (Fig. B.4f, g) in the NoDrift_1 set-up.

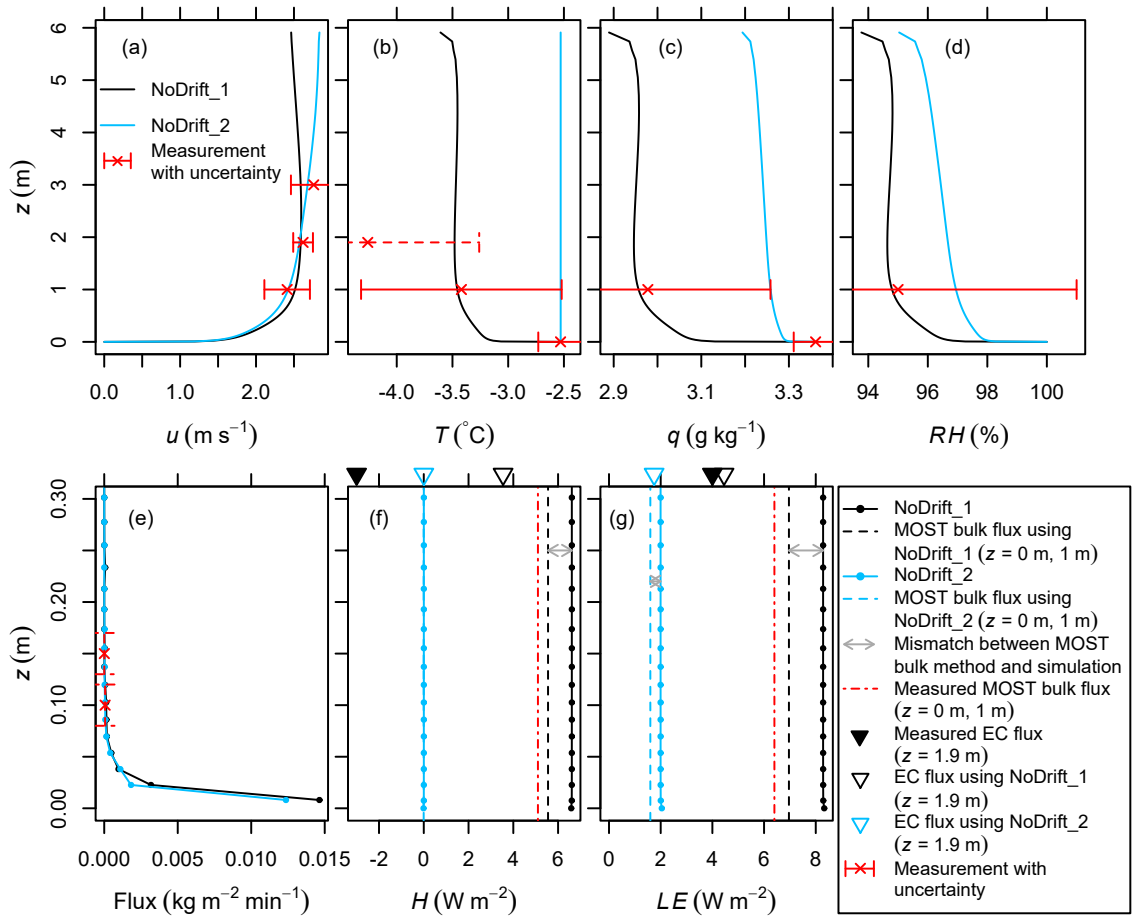

Figure B.4: Average vertical profiles for a quasi-stationary 10-min period in two LES–LSM set-ups (NoDrift_1, NoDrift_2) with different temperature and humidity gradients at the upper boundary: (a) wind speed, (b) temperature, (c) specific humidity, (d) relative humidity with respect to ice, (e) horizontal snow mass flux, (f) cumulative sensible heat exchange, (g) cumulative latent heat exchange. For comparison, 10-min averaged measurements based on the EC method and the MOST parametrization are shown for the S17 site (12 January 2019, 05:40 to 05:50 UTC), including instrument-specific standard uncertainties (dashed if estimated). Note that (e)–(g) only show the lowest 0.3 m of the profile.

C Supplementary Material for Chapter 2

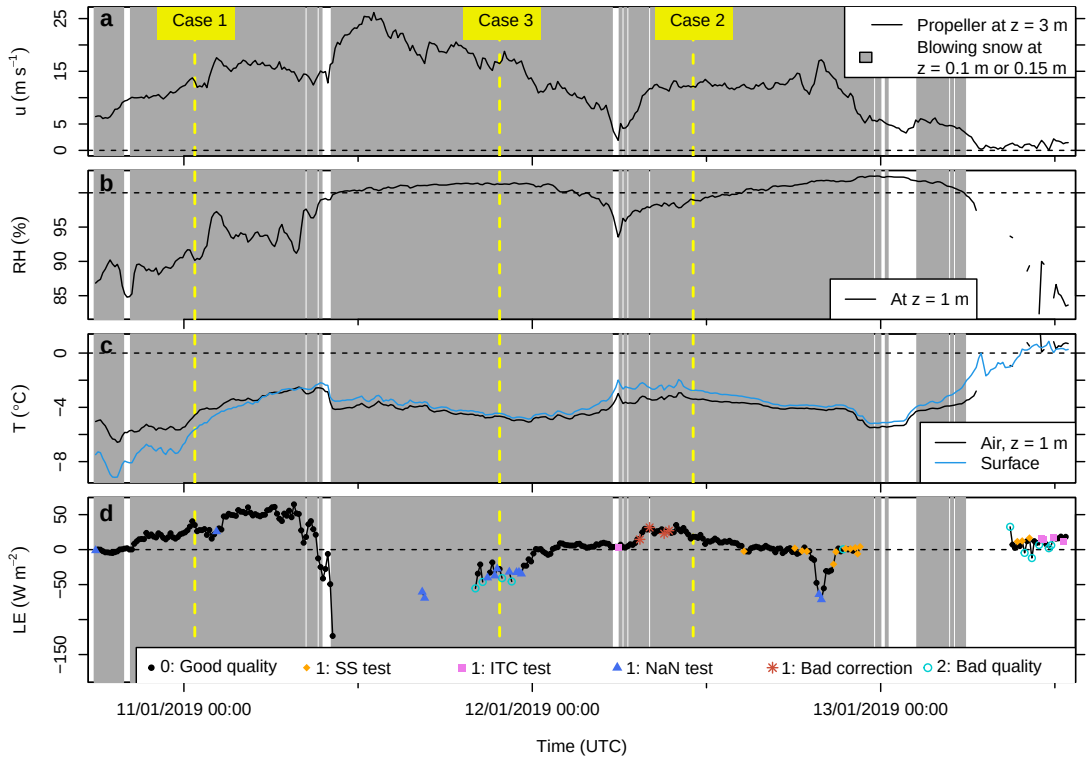

Figure C.1: Measurements at S17, East Antarctica, from 10th to 13th January 2019: 10-min averages of (a) wind speed, (b) relative humidity with respect to ice, (c) air and surface temperatures, and (d) latent heat flux based on the eddy-covariance technique. The dashed vertical lines highlight the three cases modelled in this study. The grey shading indicates times at which at least one of the two snow particle counters at heights of 0.1 m and 0.15 m detected drifting and blowing snow. Quality-control flags shown in (d) are based on the tests on steady state (SS test) and well-developed turbulence (ITC test) described by Foken et al. (2004) and a test on missing data described in Sect. 1.2.2 of Chapter 1. Data gaps in panel d correspond to intervals with many artifacts, leading to a fraction of missing high-frequency records of ≥ 40%.

Table C.1: Important parameters in the LES-LSM simulations. The imposed friction velocity is computed as $u_* = \sqrt{P\,L_z}$, where P (m s^{-2}) is the imposed large-scale pressure gradient force and L_z (m) is domain height. Cases 3a and 3b refer to two separate simulations with different upper boundary conditions for humidity and temperature.

Parameter	Symbol	Units	Case 1	Case 2	Case 3
Imposed friction velocity	u_*	m s^{-1}	0.605	0.568	0.795
Air density	ρ	kg m^{-3}	1.18	1.18	1.18
Mean initial particle diameter	$\bar{d}_p$	μm	260	200	200
Standard deviation of initial particle diameter	$\sigma(d_p)$	μm	130	100	100
Cohesion energy of a particle at the surface	ϕ_s	J	10^{-10}	10^{-10}	10^{-10}
Aerodynamic roughness length	z_0	m	10^{-4}	10^{-4}	10^{-4}
Thermal roughness length	z_{0H}	m	5×10^{-5}	5×10^{-5}	3×10^{-5}
Humidity roughness length	z_{0Q}	m	5×10^{-5}	6×10^{-5}	4×10^{-5}
Surface temperature	T_0	°C	−5.63	−2.77	−4.44
Surface specific humidity	q_0	g kg^{-1}	2.613	3.297	2.880
Temperature gradient at upper boundary	$\mathrm{d}T\ (\mathrm{d}z)^{-1}$	K m^{-1}	11.9	−3.3	-0.9^a, 2.2^b
Specific humidity gradient at upper boundary	$\mathrm{d}q\ (\mathrm{d}z)^{-1}$	g kg^{-1} m^{-1}	−1.32	−1.47	-0.25^a, 0.41^b

[a] Case 3a.
[b] Case 3b.

C.1 Measured and Simulated Particle Size Distributions

Figure C.2 compares the number size distributions of drifting and blowing snow particles measured and simulated at heights of $z = 0.1$ m and $z = 0.15$ m above the snow surface in the three cases highlighted in the time series of Fig. C.1. In Cases 2 and 3, the distributions are only shown for $z = 0.1$ m because the upper snow particle counter (SPC) either detected no particles or an extremely small number of particles, likely due to an obstructed laser path (Sect. 1.3.1 of Chapter 1). For the simulated distribution, we consider all particles in a 5-mm thick layer at the height of the SPC in the last 400 s of each LES-LSM simulation. As large-scale models typically assume the particle diameter to follow a gamma distribution, Fig. C.2 also shows gamma distributions fitted to the data using maximum-likelihood estimation.

The simulated size distribution depends on the prescribed log-normal distribution for the particle diameter at the snow surface. The mean and standard deviation of the diameters at the surface are prescribed as $\bar{d}_p = 260$ μm and $\sigma = 130$ μm in Case 1 and $\bar{d}_p = 200$ μm and $\sigma = 100$ μm in Cases 2 and 3. Additionally, the range of initial diameters is restricted to the interval from 50 to 2000 μm.

In Case 1, the LES-LSM simulation tends to overestimate the particle sizes at both $z = 0.1$ m and $z = 0.15$ m, compared with the measurements (Fig. C.2a,b). This overestimation seems to be related to the model sensitivity with respect to the horizontal grid spacing because a similar simulation shown in Fig. 1.3 of Chapter 1 achieves a better agreement with the measured size distribution although the simulation set-ups only differ in the domain size and horizontal grid spacing. With the current simulation set-up, the agreement with the measured particle sizes could be improved by reducing the prescribed mean and standard deviation of the initial particle diameter. However, the current agreement is sufficient for the purpose of this study because the simulated conditions are still realistic in the sense that they can occur at other locations or times with slightly different surface snow characteristics. Additionally, other model limitations may introduce similar uncertainties. For example, the model does not account for the fact that the particle size distribution at the snow surface may change with time due to fragmentation of drifting snow. Another important limitation is the neglect of eddies larger than the model domain (Sect. C.3). Moreover, the simulations suggest that the mean particle diameter depends strongly on height in the lowest 0.3 m of the atmosphere. Therefore, uncertainties in the measurement height of the SPCs further complicate the assessment of the simulated particle sizes.

In Case 2, the simulated size distribution is closest to the measured one, compared with the other cases, although the mean and standard deviation of the distribution are slightly overestimated (Fig. C.2c). In particular, the large amount of small particles with a diameter around 100 μm is better represented and large particles are less strongly overrepresented, compared to the other simulations. This feature is related to the assumption of a rather low spatial variability of the wind velocity in the shallow layer between the surface and the next higher grid level, as discussed in Sect. 2.2.2 of Chapter 2. The simulations of Cases 3a and 3b

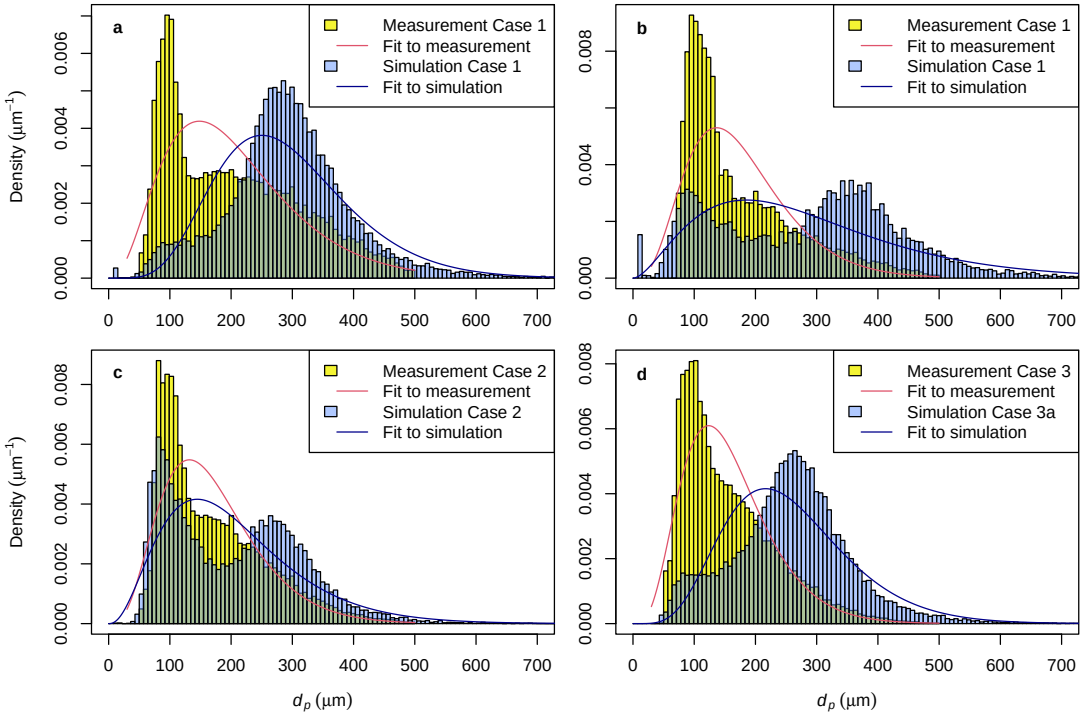

Figure C.2: Particle number size distributions based on measurements of snow particle counters and LES-LSM simulations: Probability density as a function of particle diameter (d_p) in (a) Case 1 at a height of $z = 0.1$ m, (b) Case 1 at $z = 0.15$ m, (c) Case 2 at $z = 0.1$ m, (d) Case 3a at $z = 0.1$ m. The lines show gamma distributions fitted using maximum likelihood estimation.

only differ in the temperature and humidity conditions and yield almost identical particle size distributions. Therefore, Fig. C.2d only shows results for the simulation of Case 3a. This simulation clearly overestimates the particle sizes at $z = 0.1$ m but is still considered to be representative of similar situations in the field.

C.2 Details on the Moisture and Heat Exchanges in the Large-Eddy Simulations With Lagrangian Particles

After simulating all cases, we noticed a small inconsistency in the model, concerning the particle-flow interaction in the shallow layer between the surface and the next higher grid level. When interpolating the flow properties (wind velocity, temperature, humidity) in this layer to estimate these properties at the location of a particle, the model assumed a logarithmic vertical profile defined by the bulk parameterizations. This profile was computed using local values at the first grid level above the surface while another module of the model used horizontally smoothed values as the bulk parameterizations have been developed for averaged quantities. Therefore, we repeated the simulation of Case 2 considering smoothed quantities in both modules. Although this modification led to a better agreement with the measured particle

size distribution, the simulated steady-state snow transport rate and sublimation rate only changed by 7% and 5%, respectively, which was not enough to justify the computational effort of repeating the other simulations. In the main analysis, the Case 2 simulation refers to the simulation with smoothed quantities in both modules.

C.3 Simulated and Measured Turbulence Cospectra

We use turbulence cospectra to understand the contributions of various eddy sizes to the latent and sensible heat fluxes measured and simulated at a height of 1.9 m above the snow surface in Case 1 (around 11th January 2019, 00:45 UTC). In the LES-LSM simulations, we imitate eddy-covariance measurements by extracting the time series of the vertical wind velocity component, specific humidity, and air temperature from a horizontally centered grid point using the same sampling frequency (20 Hz) as for the measurements. Due to the periodic lateral boundary conditions, large-scale coherent structures are largely locked at their position in the cross-wise direction of the mean flow and meander much more slowly than in reality (Munters et al., 2016; Sigmund et al., 2022). This effect creates an artificial wave-like trend in the time series simulated at a single grid point, which depends on the cross-wise location in the model domain and is not visible in the measurements. Therefore, a model-measurement comparison of the lowest frequencies in the cospectra would only be useful if we averaged several cospectra simulated at several grid points with different cross-wise locations. However, the respective data was only outputted for a single grid point. We therefore remove the wave-like trend calculated as running mean with a time window of 150 s and focus on frequencies larger than approximately 150^{-1} Hz ≈ 0.007 Hz in the cospectra. The measured time series is treated in the same way by applying the same running mean procedure.

The resulting cospectra and ogives for the vertical transport of water vapor and heat are shown in Fig. C.3. The cospectra of the simulation are similar to those of the measurements for frequencies > 0.25 Hz (small eddies) but tend to underestimate those of the measurements for frequencies < 0.25 Hz (large eddies). The ogives of the simulation exhibit a noticeable kink at a frequency of 0.25 Hz, illustrating that higher frequencies contribute strongly to the simulated vapor and heat fluxes while lower frequencies are almost absent in the simulation. This kink is not visible in the ogives of the measurements. Similar ogives have been presented in Fig. 1.7 of Chapter 1 for a smaller model domain with approximately half of the length and one-third of the height used here. In this previous study, the kink in the ogive occurred at a higher frequency (0.55 Hz) than in our current study and was explained by the fact that frequencies associated with eddies larger than the domain cannot be represented in the simulation. This interpretation also applies to our current simulation. The frequency at the kink ($f = 0.25$ Hz) translates into an eddy length scale of $d = \bar{u}\, f^{-1} = 48$ m according to Taylor's frozen-turbulence hypothesis, where $\bar{u} = 11.9$ m s^{-1} is the mean wind speed. This length scale corresponds approximately to the length of the longest diagonal line in the domain (47 m).

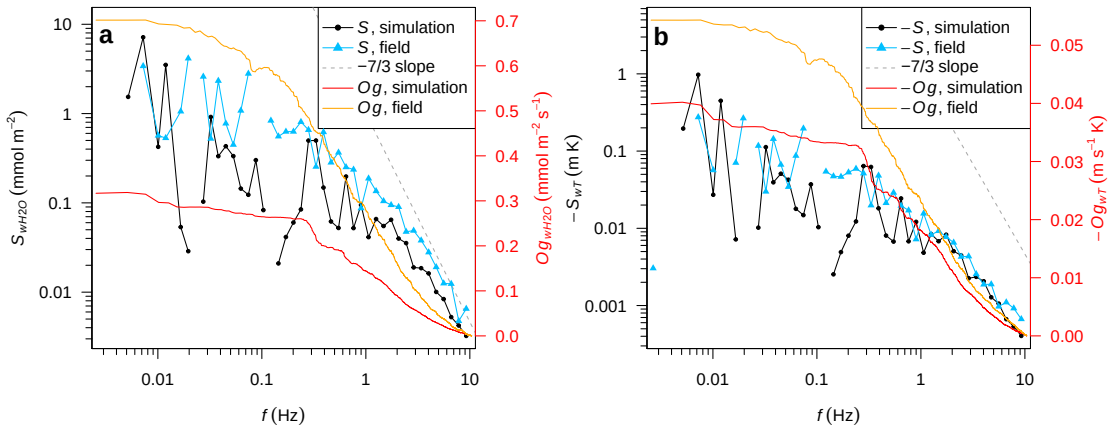

Figure C.3: Turbulence cospectra and ogives for the Case-1 simulation and field measurements (11th January 2019, 00:41 to 00:48 UTC) with respect to (a) the vertical wind velocity component (w) and molar density of water vapor (H_2O) and (b) w and air temperature (T). Negative values of the bin-averaged spectral density (S) cannot be displayed on a logarithmic scale and appear as gaps. In the inertial subrange, S is expected to be parallel to the dashed grey line ($S \propto f^{-7/3}$). The ogive (Og) represents the integral of spectral density between a certain frequency (f) and the Nyquist frequency (10 Hz). The plot is based on time series with 2^{13} records, from which the trends were removed. The simulated records were sampled at a single grid point at the same height and frequency as the measured records.

C.4 Details on the Methods of the One-Dimensional Model

The 1D prognostic equation for air temperature or specific humidity is

$$\frac{\mathrm{d}x}{\mathrm{d}t} = -\frac{\mathrm{d}\overline{w'x'}}{\mathrm{d}z} + S \tag{C.1}$$

$$= K\frac{\mathrm{d}^2x}{\mathrm{d}z^2} + S\,, \tag{C.2}$$

where x is either mean air temperature, T (K), or mean specific humidity, q (kg kg^{-1}); $\overline{w'x'}$ (K m s^{-1} or kg kg^{-1} s^{-1}) is the turbulent flux of temperature or humidity; t (s) is time; z (m) is height; and S is either the source term for air temperature, S_T (K s^{-1}), or that for water vapor, S_v (kg kg^{-1} s^{-1}), caused by drifting and blowing snow. The turbulent diffusion coefficient K (m^2 s^{-1}) is evaluated at the midpoints between the vertical levels and expressed using the common mixing length parameterization for the surface layer with neutral stratification,

$$K = \kappa\, z\, u_{*z} \tag{C.3}$$

where $\kappa = 0.4$ is the dimensionless von Kármán constant and u_{*z} is the friction velocity (m s^{-1}) at height z (m). The profile of u_{*z} is computed using the analytical expression of Raupach

Table C.2: Upper boundary conditions and wind forcing in the 1D model: friction velocity (u_*) and surface friction velocity (u_{*0}), which are imposed in all set-ups apart from the default set-up; horizontal wind speed (u), which is only used in the default set-up; air temperature (T_a); specific humidity (q); and mass and number mixing ratios of blowing snow (q_{bs} and N_{bs}, respectively), which are only used in set-ups with parameterized mixing ratios of drifting or blowing snow.

Parameter	Unit	Height z (m)	Case 1	Case 2	Case 3a	Case 3b
u_*	m s^{-1}	$z \to \infty$	0.605	0.568	0.795	0.795
u_{*0}	m s^{-1}	0.00	0.327	0.330	0.298	0.295
u	m s^{-1}	2.25	12.1	12.0	16.1	16.1
T_a	°C	9.00	−3.93	−3.59	−4.64	−4.00
q	g kg^{-1}	9.00	2.51	3.01	2.83	2.98
q_{bs}	10^{-6} kg kg^{-1}	11.25	0.044	1.100	1.985	1.953
N_{bs}	kg^{-1}	11.25	606	8797	11036	11253

(1991) to account for reduced values in the saltation layer,

$$u_{*z} = u_* \left(1 - (1 - \frac{u_{*0}}{u_*}) \exp\left\{-\frac{z}{h_{salt}}\right\}\right), \tag{C.4}$$

where u_* (m s^{-1}) is the imposed friction velocity, which is approached by u_{*z} with increasing height; u_{*0} (m s^{-1}) is the surface friction velocity, which is prescribed according to the LES-LSM output (Table C.2); and h_{salt} (m) is the height of the saltation layer.

When parameterizing the mixing ratios and size distribution of drifting and blowing snow, the 1D model largely follows the approach of the CRYOWRF model. At the fine and coarse model levels, we solve prognostic equations for the mass and number mixing ratios of blowing snow, as described in Sharma et al. (2023). The 1D model assumes horizontal homogeneity and therefore neglects the term for horizontal advection. At the saltation levels, the mass and number mixing ratios of drifting snow are computed diagnostically. More precisely, the mass mixing ratios are estimated using the parameterization of the transport rate for saltation of Sørensen (2004) in the modified version of Vionnet et al. (2014) and assuming the mass mixing ratio to follow an exponential profile in the saltation layer (Nishimura and Hunt, 2000; Vionnet et al., 2014),

$$q_{salt}(z) = \frac{1}{\rho} C_{salt} \frac{\lambda_{salt} g}{{u_*}^2} \exp\{-\frac{\lambda_{salt} z g}{{u_*}^2}\}, \tag{C.5}$$

where q_{salt} (kg kg^{-1}) is the mass mixing ratio of drifting snow at the saltation levels, λ_{salt} = 0.45 is the dimensionless decay coefficient and C_{salt} (kg m^{-2}) is the vertically integrated concentration of drifting snow,

$$C_{salt} = \frac{Q_{salt}}{u_p}, \tag{C.6}$$

where Q_{salt} (kg m^{-1} s^{-1}) is the transport rate for saltation and $u_p = 2.8 u_{*,t}$ (m s^{-1}) is the

horizontal particle speed, which is expressed as in Pomeroy and Gray (1990) with $u_{*,t}$ (m s^{-1}) being the impact threshold friction velocity, which is set to the LES-LSM-based surface friction velocity. To derive the number mixing ratio of drifting snow at the saltation levels, we prescribe the mean particle diameter in accordance with the LES-LSM output at each level or assume that the mean diameter increases linearly from 200 μm at the lowest level to a higher value at h_{salt}.

C.5 Modified Parameterization of Mass and Heat Exchange Between Drifting/Blowing Snow and Air

In the following, we derive the parameterization for sublimation of drifting and blowing snow that accounts for transient particle temperatures and is used by the 1D model in the lowest 0.3 m of the atmosphere. The derivation begins with Eqs. 1.6 and 1.7 in Chapter 1 for the mass exchange and energy balance of a single spherical snow particle in a turbulent flow. In contrast to Thorpe and Mason (1966), Eq. 1.7 does not assume a stationary particle temperature and includes a term for the change of heat stored inside the particle. Following the other calculation steps of Thorpe and Mason (1966), we combine Eqs. 1.6 and 1.7 and arrive at the formula

$$\frac{\mathrm{d}m_p}{\mathrm{d}t} = \frac{2\pi r\sigma + \Omega\, Nu^{-1}\, c_i\, m_p\, \mathrm{d}T_p/\mathrm{d}t}{\Omega\, L\, Nu^{-1} + (D\, \rho_s\, Sh)^{-1}}\,, \tag{C.7}$$

where r (m) is the radius of the snow particle, $\sigma = \rho_{v,\infty}/\rho_s - 1$ is the dimensionless undersaturation of the air, ρ_s is the saturation vapor density at the temperature of the air, and the term Ω (W m^{-1}) represents the expression

$$\Omega = \frac{1}{kT}\left(\frac{LM}{RT} - 1\right), \tag{C.8}$$

where $M = 18.02 \times 10^{-3}$ kg mol^{-1} is the molar mass of water and $R = 8.314$ J mol^{-1} K^{-1} is the universal gas constant. If the particle temperature is stationary, Eq. C.7 reduces to the formula of Thorpe and Mason (1966). Similarly, this formula has been modified by Schmidt (1972) and Liston and Sturm (1998) to include a term for absorption of shortwave radiation. We neglect the radiative energy exchange of the snow particle because radiation measurements are not available at the study site. Additionally, the radiation effects are expected to play a minor role in cloudy conditions.

The main novelty of our sublimation formula is the empirical expression of $\mathrm{d}T_p/\mathrm{d}t$ for particles of drifting and blowing snow, presented in Eq. 2.3 in Chapter 2. This expression was derived from the LES-LSM data, which includes explicitly modelled particle temperatures. The change in particle temperature reflects the net effect of all energy exchange processes experienced by a particle. For a particle with a typical ballistic trajectory, $\mathrm{d}T_p/\mathrm{d}t$ is expected to depend on (i) the mean vertical difference in air temperature, ΔT, driving the temperature difference between the particle and air and consequently the sensible heat exchange; (ii) the particle

diameter, d_p, because the volume increases more strongly with the diameter than the surface area, leading to a higher thermal inertia for larger particles; (iii) the height above the surface, z, which is related to the residence time in the atmosphere and therefore the available period for approaching a thermal equilibrium; (iv) the mean relative humidity, RH, influencing the latent heat exchange; and (v) the friction velocity, u_*, influencing the velocity differences between the particle and airflow and consequently the efficiency of the sensible and latent heat exchanges. The effect of the friction velocity is expected to be height-dependent because the particle and wind velocities are typically independent of the friction velocity in the lowest 0.01 m of the atmosphere while they increase with friction velocity at greater heights (Melo et al., 2022).

We parameterize $\mathrm{d}T_p/\mathrm{d}t$ by estimating its sign from the sign of the vertical temperature difference and expressing its absolute magnitude as a function of the five aforementioned variables. Before performing a multiple linear regression, the variables ΔT, RH, z, and d_p are transformed into $|\Delta T| = |T_1 - T_0|$, $\Delta RH = \mathrm{sgn}(\Delta T)(RH_1 - 100\%)$, $\sqrt{z}$, and $\sqrt{d_p}$, respectively, where the subscripts 0 and 1 refer to the surface and the lowest saltation level at $z = 0.0075$ m, respectively. At these heights, temperature and humidity will always be available in the 1D model if there is snow transport. The regression is performed with time-averaged and bin-averaged $\mathrm{d}T_p/\mathrm{d}t$ values, considering the lowest 0.3 m of the atmosphere with 20 height bins (0.015 m each) and 70 particle diameter bins (10 μm each) ranging from 90 to 700 μm. Ideally, we would aim to parameterize $\mathrm{d}T_p/\mathrm{d}t$ in a deeper layer because the LES-LSM simulations suggest that the latent and sensible heat exchanges between the particles and the atmosphere only balance each other at heights above $z = 1.0$ m (Fig. C.4). Consequently, transient particle temperatures are expected in the lowest 1 m of the atmosphere. However, a regression attempt considering the lowest 1 m did not yield satisfactory results, likely due to non-linear relationships between the variables. As a compromise, our regression focuses on the lowest 0.3 m of the atmosphere, where $\mathrm{d}T_p/\mathrm{d}t$ can be approximated by a multi-linear function and the error of the TM formula is largest.

For the regression, we only use the diameter range from 90 to 700 μm because this range is responsible for almost the entire latent heat exchange for typical size distributions. To account for the fact that the lowest centimeters contribute most to the moisture and heat exchanges in the LES-LSM simulations, we use weighted least squares; the weights decrease linearly from a value of 1000 for the lowest height bin to a value of 1 for $z = 0.3$ m. In a first regression attempt, we encountered singularity problems, i.e., some interaction terms were excluded because they depended linearly on other terms since variables such as $|\Delta T|$ and ΔRH only varied among four values, characterizing the four simulated cases. To avoid these problems, we double the number of data points by computing 200-s averages instead of 400-s averages. To estimate the friction velocity, we assume that the mean wind speed is well approximated by a logarithmic vertical profile for heights from 1 m to 9 m, where small concentrations of blowing snow and the upper boundary conditions have negligible effects on the shape of the wind profile. Under

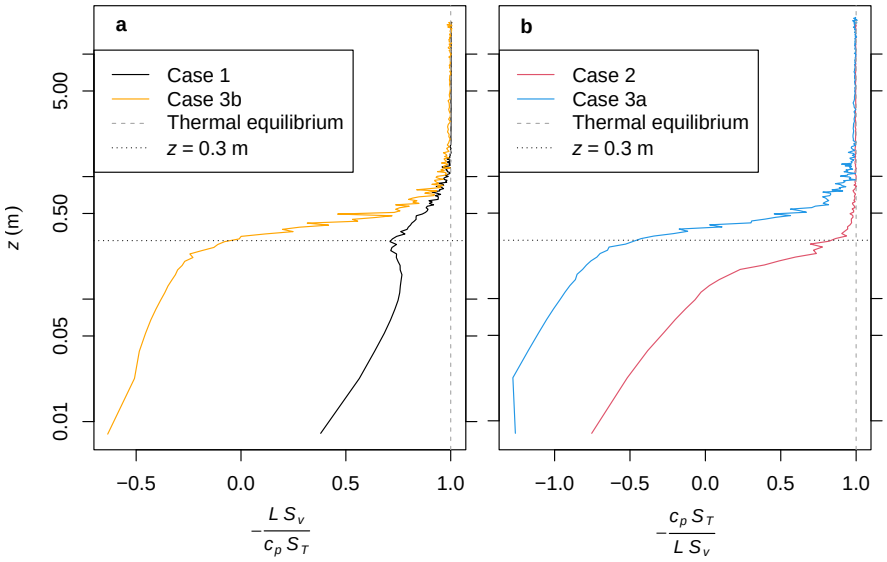

Figure C.4: Dimensionless negative ratio of (a) latent heat exchange, $L\,S_v$ (W kg^{-1}), to sensible heat exchange, $c_p\,S_T$ (W kg^{-1}), or (b) vice versa between drifting/blowing snow and the atmosphere as a function of height, z, in the four LES-LSM simulations. Deviations from a ratio of one indicate transient particle temperatures and the unsuitability of the formula of Thorpe and Mason (1966). Note the logarithmic height axis.

these assumptions, the friction velocity is

$$u_* = \frac{\kappa}{a}\,, \tag{C.9}$$

where a is the slope of a linear regression line fitted to the 200-s mean wind speeds (u) at $z = 1$ m, 2 m, ..., 9 m in a u–$ln(z)$ plot. This calculation yields u_* values similar to the imposed friction velocities specified in Table 1.2.

The regression model includes some interaction terms with two variables. These interaction terms are selected using the best subset approach, which identifies the regression model with the lowest residual sum of squares for each model size (number of terms) (Miller, 2002). Increasing the number of interaction terms from 1 to 5 reduces clearly the weighted mean squared residual while adding further interaction terms leads to a negligible reduction (Figure C.5a). The Akaike information criterion (Akaike, 1998) decreases similarly with the number of interaction terms, suggesting an improvement of the model, especially from one to five interaction terms. We also take into account a cross-validation procedure, in which we fit the best model of each size three times, each time excluding Case 2, 3a, or 3b from the training data and using the excluded case for validation. Case 1 is not used for validation because the other cases do not contain sufficient information to satisfactorily predict the results of Case 1 with any of the tested models. The model with five interaction terms achieves the lowest weighted mean squared residual in the cross-validation procedure, which supports our choice of five interaction terms (Figure C.5b).

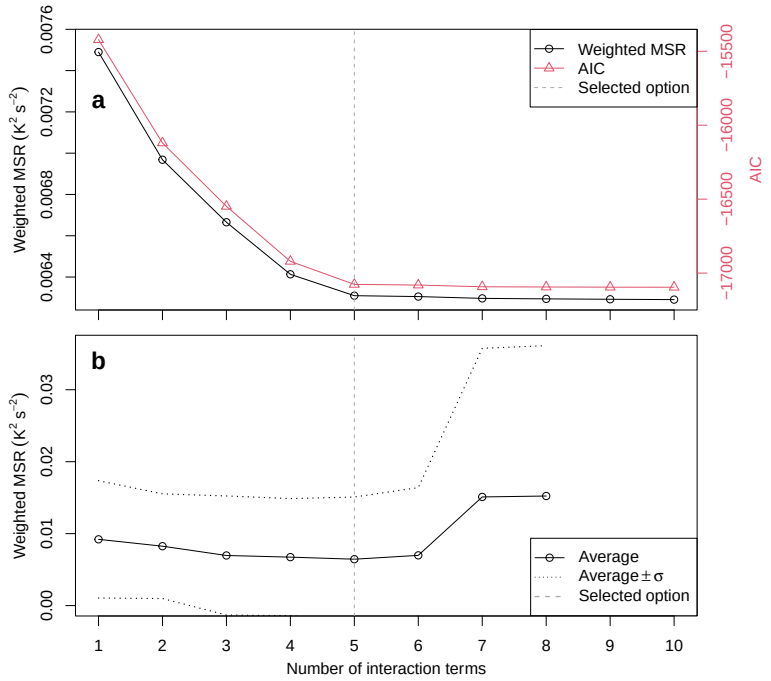

Figure C.5: Best subset selection of linear regression models for the absolute temporal change of particle temperature: (a) Weighted mean squared residual (MSR) and Akaike information criterion (AIC) when using all four simulated cases as training data and (b) weighted MSR in a cross-validation procedure using Case 2, 3a, or 3b as validation data and the other three cases as training data. The standard deviation of the weighted MSR (σ) corresponds to the distance between the solid and dotted lines. In b, the MSR cannot be determined for 9 or 10 interaction terms because of rank deficiency.

The Pearson correlation coefficient between the $|\mathrm{d}T_p/\mathrm{d}t|$ values used for the regression and those predicted by the regression model amounts to 0.68. Figures C.6 and C.7 visualize the performance of the regression model as a function of particle diameter and height. The LES-LSM-based $|\mathrm{d}T_p/\mathrm{d}t|$ values are generally well approximated by the regression model, especially for intermediate particle diameters (250 to 500 μm). For smaller diameters, the regression model cannot capture the non-linear relationship between $|\mathrm{d}T_p/\mathrm{d}t|$, diameter and height but is still close to the LES-LSM data in the lowest height bin at $z = 0.0075$ m. The lowest height bin is particularly relevant for the total vapor and heat exchanges because it is characterized by the highest particle number concentration. At the next higher levels, only particles at the lower tail of the number size distribution are poorly described by the regression model, which has a limited effect on the total vapor and heat exchanges because the surface area of a particle is expected to scale with its contribution to the vapor and heat exchanges. For particle diameters larger than ~200 μm and heights greater than ~0.15 m, the LES-LSM results of Cases 1 and 2 show very variable $|\mathrm{d}T_p/\mathrm{d}t|$ values with strong deviations from zero. This variability is likely related to the fact that only few large particles reach heights above 0.15 m and the high number of snow particles represented by one Lagrangian particle reduces the

robustness of averaged data for certain diameter and height bins.

To obtain a sublimation parameterization for all particles at a specific model level, we perform an integration with respect to the particle diameter (Sharma et al., 2023),

$$S_v = -\int_0^\infty \frac{\mathrm{d}m_p}{\mathrm{d}t}\, N_{bs}\, f_n(d_p)\, \mathrm{d}d_p\,, \tag{C.10}$$

where S_v (kg kg^{-1} s^{-1}) is the vapor source due to sublimation of drifting and blowing snow, N_{bs} is the particle number mixing ratio (kg^{-3}), and $f_n(d_p)$ (m^{-1}) is the probability density function for the particle number size distribution, which is represented by a gamma distribution (Sharma et al., 2023),

$$f_n(d_p) = \frac{\lambda^\alpha\ {d_p}^{\alpha-1}\ \exp\{-d_p\lambda\}}{\Gamma(\alpha)}\,, \tag{C.11}$$

where α (dimensionless) and λ (m^{-1}) are the shape and inverse-scale parameters, respectively, and $\Gamma(\alpha)$ (dimensionless) is the gamma function. Although $\mathrm{d}m_p/\mathrm{d}t$ depends on the regression model for $\mathrm{d}T_p/\mathrm{d}t$, which may not be valid for diameters outside the range from 90 to 700 μm, Eq. C.10 considers the entire range of diameters because typical size distributions lead to a negligible contribution of very small or very large particles to the entire sublimation.

Before integrating, we rearrange Eq. C.7, insert the regression model for $\mathrm{d}T_p/\mathrm{d}t$, and assume that $Nu = Sh$:

$$\frac{\mathrm{d}m_p}{\mathrm{d}t} = \frac{\pi\ d_p\ \sigma\ Sh + \Omega\ c_i\ \rho_i\ \frac{1}{6}\pi {d_p}^3\ (\beta_1 + \beta_2\ \sqrt{d_p})}{\Omega\ L + (D\ \rho_s)^{-1}}\,. \tag{C.12}$$

Here, $\rho_i = 918.4$ kg m^{-3} is the density of the snow particle represented by the density of ice and β_1 (K s^{-1}) and β_2 (K m$^{-0.5}$ s^{-1}) are terms in the regression model,

$$\begin{aligned}\beta_1 &= \mathrm{sgn}(\Delta T)\ (\ 0.108 + 0.836|\Delta T| - 0.569\sqrt{z_p} + 0.046\Delta RH + 0.133 u_* \\ &\quad -2.23\sqrt{z_p}|\Delta T| -\ 0.164\sqrt{z_p}\Delta RH\ ), \qquad \text{(C.13)}\\ \beta_2 &= \mathrm{sgn}(\Delta T)\ (\ -10.1 + 39.2|\Delta T| + 2.75\Delta RH + 28.5\sqrt{z_p}\ )\,, \qquad \text{(C.14)}\end{aligned}$$

where ΔT, z_p, u_*, and d_p are expressed in SI base units and ΔRH is given in %. Equations C.13 and C.14 are consistent with Eq. 2.3 in Chapter 2 although the coefficients differ because here, the input variables are not standardized. The Sherwood number is expressed like in the CRYOWRF model (Sharma et al., 2023),

$$Sh = 2\ (0.78 + 0.308 Re^{1/2} Sc^{1/3}) \tag{C.15}$$

where Sc is the dimensionless Schmidt number and Re is the dimensionless particle Reynolds number expressed as (Mitchell, 1996; Sharma et al., 2023)

$$Re = a_m\ \phi^{b_m}\ {d_p}^{3b_m}\,, \tag{C.16}$$

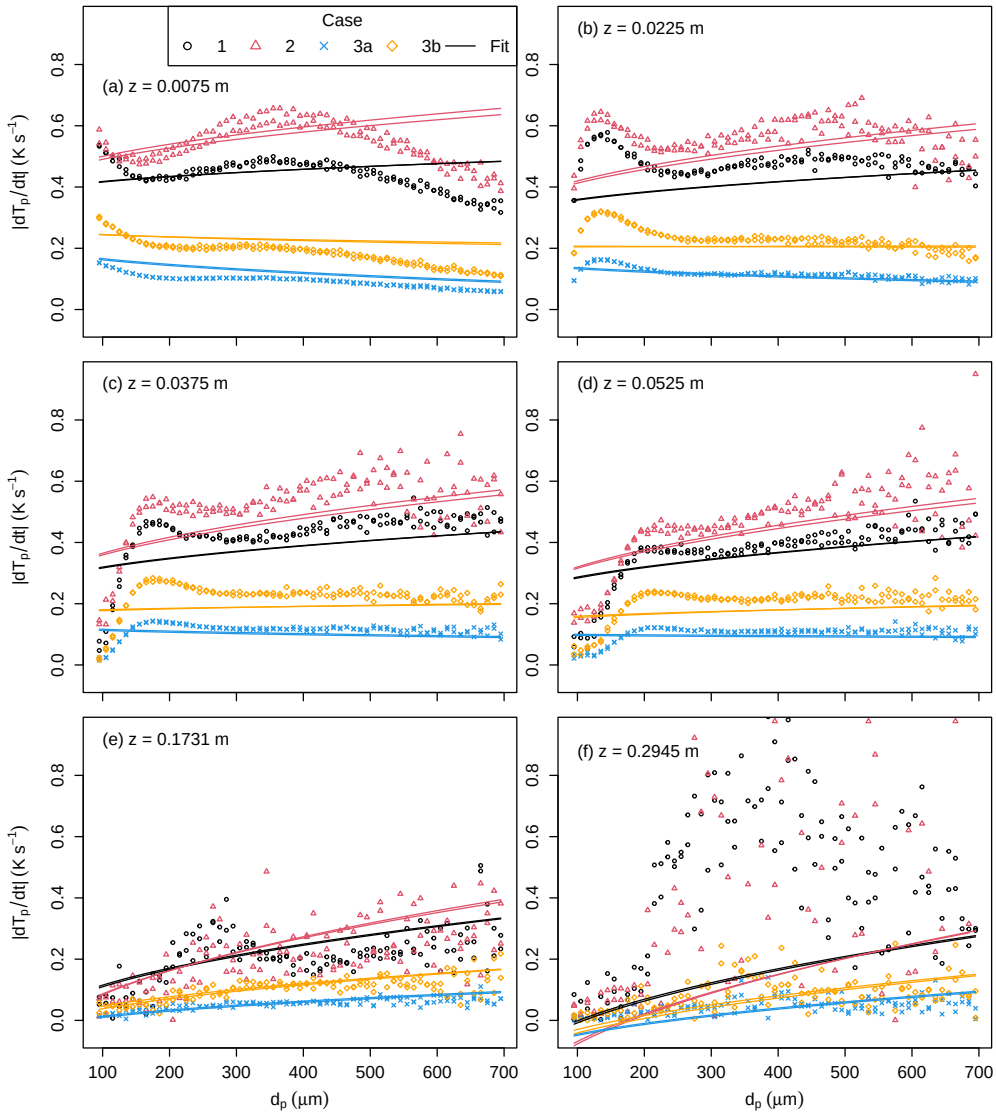

Figure C.6: Bin-averaged absolute temporal change of the temperature of drifting and blowing snow particles ($|\mathrm{d}T_p/\mathrm{d}t|$) as a function of particle diameter (d_p) from 90 to 700 μm for height (z) bins centered at (a) 0.0075, (b) 0.0225, (c) 0.0375, (d) 0.0525, (e) 0.1731, (f) 0.2945 m. Each point marks an average over a 200-s period in one of the four LES-LSM simulations while the lines represent the regression model. In panel f, 21 data points are not visible because of exceptionally high $|\mathrm{d}T_p/\mathrm{d}t|$ values.

where ϕ (m^{-3}) represents the term

$$\phi = \frac{4}{3}\frac{\rho\,(\rho_i - \rho)\,g}{\eta^2} \tag{C.17}$$

with η (kg m^{-1} s^{-1}) being dynamic viscosity of air and g (m s^{-2}) being acceleration of gravity. In Eq. C.16, a_m and b_m are coefficients computed as functions of the dimensionless mean

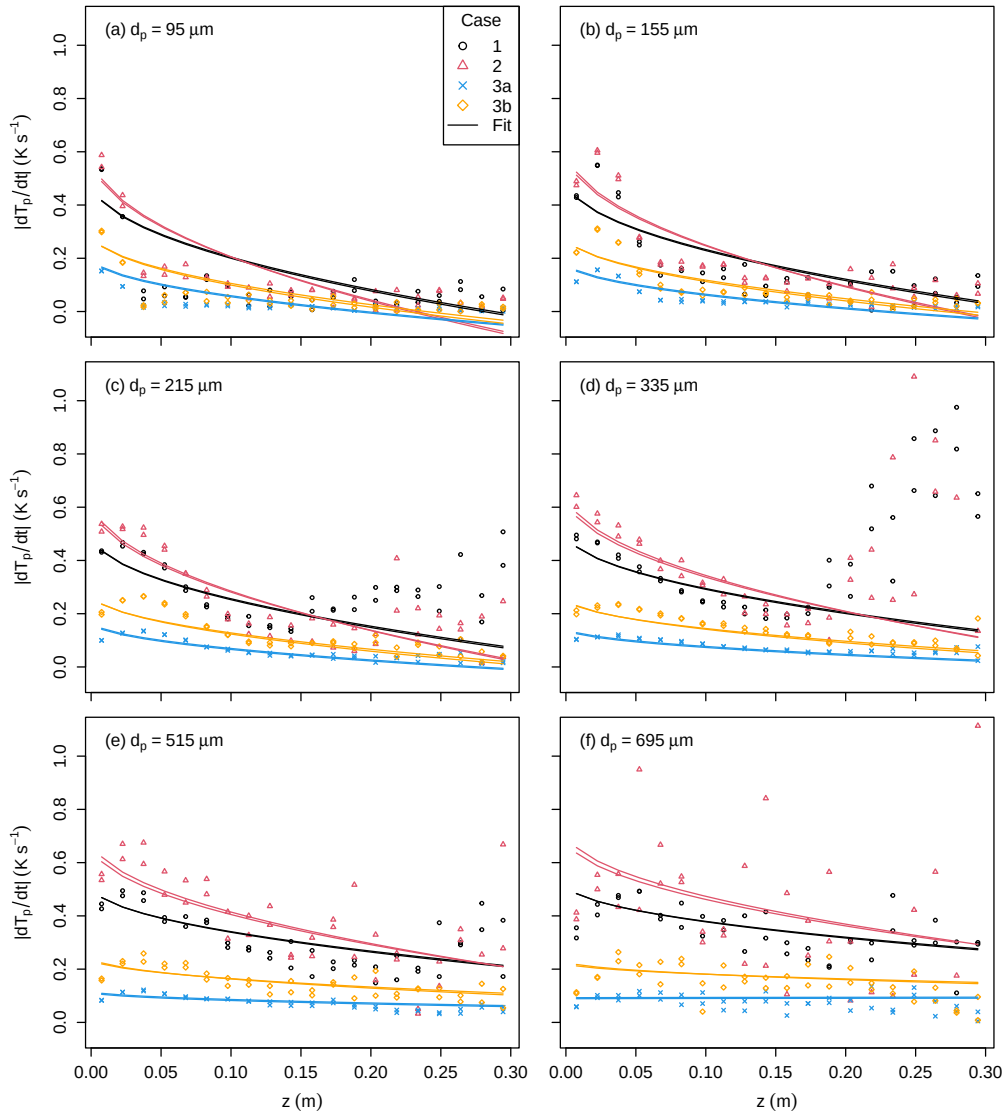

Figure C.7: Bin-averaged absolute temporal change of the temperature of drifting and blowing snow particles ($|\mathrm{d}T_p/\mathrm{d}t|$) as a function of height (z) for particle diameter (d_p) bins centered at (a) 95, (b) 155, (c) 215, (d) 335, (e) 515, (f) 695 μm. Each point marks an average over a 200-s period in one of the four LES-LSM simulations while the lines represent the regression model. In panel d, one data point is not visible because of an exceptionally high $|\mathrm{d}T_p/\mathrm{d}t|$ value.

best number, $\overline{X}$, like in the CRYOWRF model,

$$a_m = \frac{0.25 \times 5.83^2 \, (Y-1)^2}{\overline{X}^{b_m}}, \tag{C.18}$$

$$b_m = \begin{cases} 0.5 \times 0.1519 \sqrt{\overline{X}} \, [(Y-1) \, Y]^{-1} & \text{if } (Y-1) \, Y \geq 10^{-12}, \\ 1 & \text{if } (Y-1) \, Y < 10^{-12}, \end{cases} \tag{C.19}$$

with

$$Y = \sqrt{1 + 0.1519\sqrt{\overline{X}}}\,, \tag{C.20}$$

$$\overline{X} = \phi\,\frac{\Gamma(\alpha+3)}{\Gamma(\alpha)}\,\frac{1}{\lambda^3}\,. \tag{C.21}$$

Inserting Eqs. C.15 and C.16 in Eq. C.12 and substituting $B_1 = \pi[\Omega\ L + (D\ \rho_s)^{-1}]^{-1}$ and $B_2 = 0.308 Sc^{1/3} {a_m}^{0.5} \phi^{0.5 b_m}$, we obtain

$$\frac{\mathrm{d}m_p}{\mathrm{d}t} = B_1\left[2\ d_p\ \sigma\ (0.78 + B_2\ {d_p}^{1.5 b_m}) + \Omega\ c_i\ \rho_i\ \frac{1}{6}\ {d_p}^3\ \left(\beta_1 + \beta_2\sqrt{d_p}\right)\right]. \tag{C.22}$$

Inserting Eqs. C.11 and C.22 in Eq. C.10 and using the relationships $\int_0^\infty {d_p}^{\alpha-1} \exp\{-d_p\lambda\}\,\mathrm{d}d_p = \Gamma(\alpha)\ \lambda^{-\alpha}$ and $\Gamma(\alpha+1) = \alpha\ \Gamma(\alpha)$, we arrive at the sublimation formula,

$$\begin{aligned} S_v &= -B_1 N_{bs}\left[2\sigma\alpha\left(\frac{0.78}{\lambda} + \frac{B_2\ \Gamma(\alpha + 1.5 b_m + 1)}{\lambda^{1.5 b_m + 1}\ \Gamma(\alpha+1)}\right)\right. \\ &\quad \left. + \Omega\ c_i\ \rho_i\ \frac{1}{6}\ \frac{\beta_1 \lambda^{0.5}\Gamma(\alpha+3) + \beta_2\Gamma(\alpha+3.5)}{\lambda^{3.5}\Gamma(\alpha)}\right]. \end{aligned} \tag{C.23}$$

If stationary particle temperatures are assumed, i.e., if $\beta_1 = \beta_2 = 0$, Eq. C.23 reduces to the sublimation formula used in the current CRYOWRF version and at levels above $z = 0.3$ m in the 1D model.

In the model configuration with parameterized mixing ratios of drifting or blowing snow, the vapor exchange influences the abundance of blowing snow. The source/sink term for the mass mixing ratio of blowing snow, S_q (kg kg^{-1}), corresponds to the negative vapor source/sink term,

$$S_q = -S_v\,, \tag{C.24}$$

while the source/sink term for the number mixing ratio of blowing snow, S_N (kg^{-1}), is estimated using the concept of Morrison and Grabowski (2008):

$$S_N = S_q\ \frac{N_{bs}}{q_{bs}}\,, \tag{C.25}$$

where q_{bs} (kg kg^{-1}) is the mass mixing ratio of blowing snow.

The sensible heat exchange between drifting/blowing snow and the atmosphere is derived using the same integration approach as in Eq. C.10,

$$S_T = -\frac{1}{c_p}\int_0^\infty \left.\frac{\mathrm{d}Q}{\mathrm{d}t}\right|_{conv} N_{bs}\ f_n(d_p)\ \mathrm{d}d_p\,, \tag{C.26}$$

where S_T (K s^{-1}) is the source term for air temperature and $\mathrm{d}Q/\mathrm{d}t|_{conv}$ is the sensible heat

exchange between a particle and the atmosphere. Considering the particle energy balance (Eq. 1.7 in Chapter 1), we can write

$$\begin{aligned} S_T &= -\frac{1}{c_p}\left(\int_0^\infty c_i m_p \frac{\mathrm{d}T_p}{\mathrm{d}t}\, N_{bs}\, f_n(d_p)\, \mathrm{d}d_p - \int_0^\infty L \frac{\mathrm{d}m_p}{\mathrm{d}t}\, N_{bs}\, f_n(d_p)\, \mathrm{d}d_p\right) \\ &= -\frac{1}{c_p}\left(N_{bs}\, c_i\, \rho_i\, \frac{1}{6}\, \pi\, \frac{\beta_1 \lambda^{0.5}\Gamma(\alpha+3) + \beta_2 \Gamma(\alpha+3.5)}{\lambda^{3.5}\Gamma(\alpha)} + L\, S_v\right). \end{aligned} \tag{C.27}$$

Again, the formula currently used in the CRYOWRF model is obtained if $\beta_1 = \beta_2 = 0$.

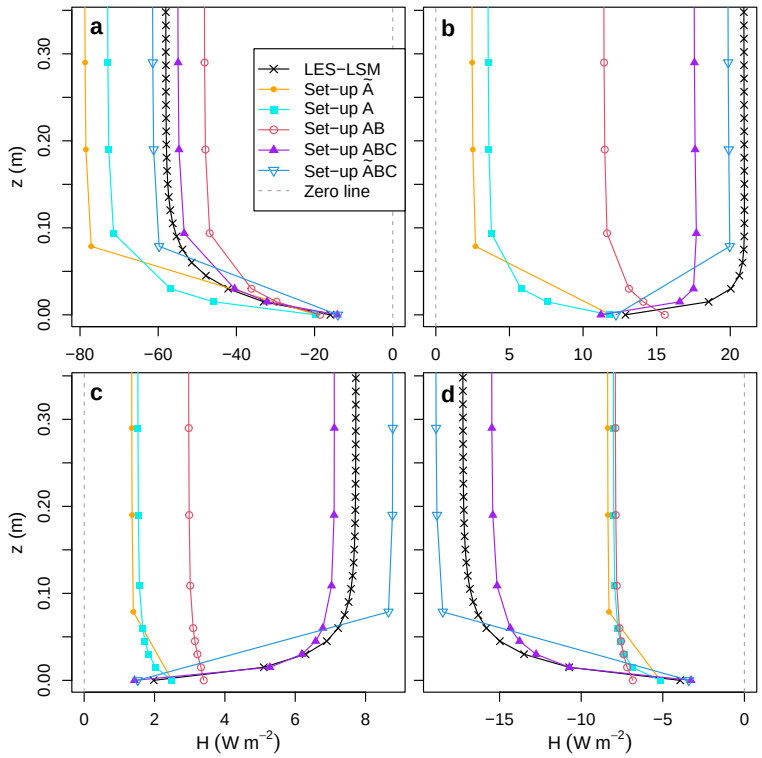

Figure C.8: Cumulative sensible heat exchange (H) as a function of height (z) in the steady state of the LES-LSM simulations and 1D model set-ups with prescribed mixing ratios of drifting and blowing snow in (a) Case 1, (b) Case 2, (c) Case 3a, and (d) Case 3b. Point markers are drawn at the midpoints between model levels to show the total exchange below the respective height.

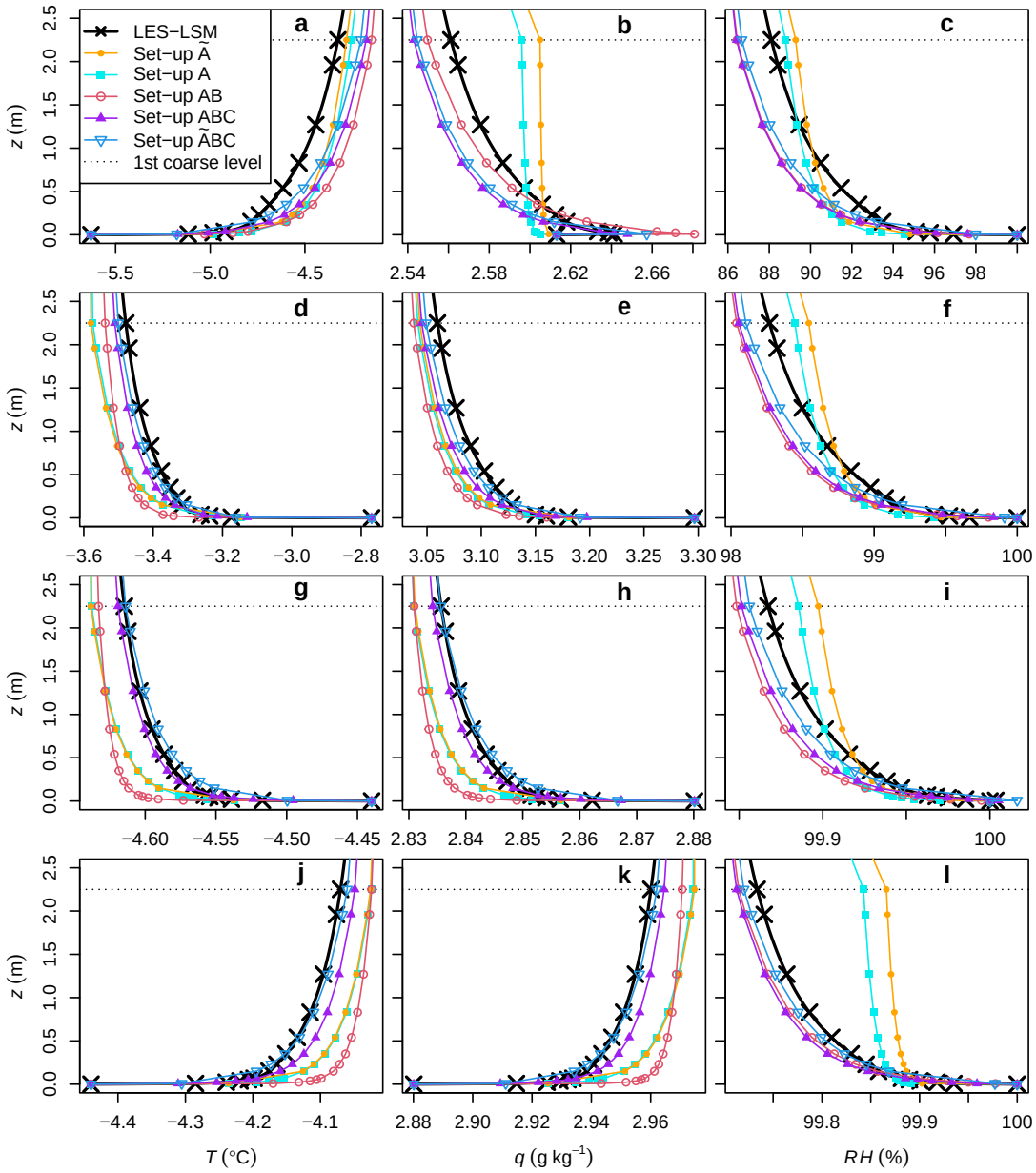

Figure C.9: Steady-state profiles of temperature (T), specific humidity (q), and relative humidity with respect to ice (RH) up to a height of $z = 2.25$ m for the LES-LSM simulations and the 1D model set-ups with prescribed mixing ratios of drifting and blowing snow in (a–c) Case 1, (d–f) Case 2, (g–i) Case 3a, and (j–l) Case 3b. Point markers are drawn at the levels of the 1D model.

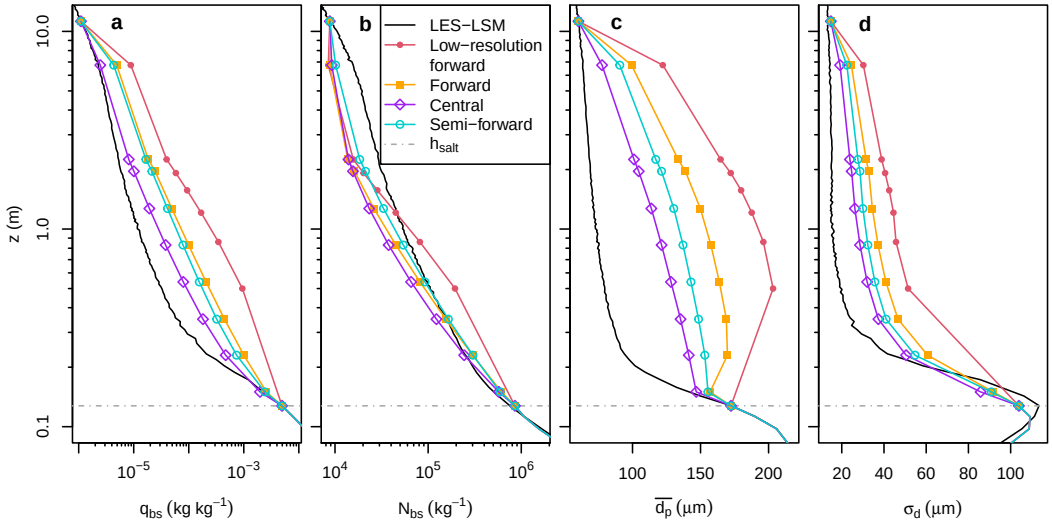

Figure C.10: The effect of discretization options on blowing snow properties in the Lh-Ld-Lα version of the suspension set-up of the 1D model in Case 2: Steady-state (a) mass mixing ratio, (b) number mixing ratio, (c) mean particle diameter, and (d) standard deviation of the particle diameter as a function of height (z). Point markers are drawn at the height of the saltation layer and higher model levels. For comparison, we include the results of the LES-LSM simulation.

C.6 Discretization Errors of Parameterized Mixing Ratios of Blowing Snow

We choose Case 2 as an example to illustrate parameterization errors associated with the vertical resolution and the discretization of the sedimentation flux because the measured particle size distribution is best reproduced in this case. In the other cases, the blowing snow profiles are qualitatively similar. Figure C.10 compares the mixing ratios and diameters of blowing snow particles between the LES-LSM simulations and the Lh-Ld-Lα version of the suspension set-up of the 1D model. The effect of other factors on this comparison is small because the parameter settings of the Lh-Ld-Lα set-up are prescribed consistently with the LES-LSM data in terms of h_{salt}, the mean particle diameter at h_{salt}, and the shape parameter of the size distribution.

The mass mixing ratio is best reproduced by the 1D model if the sedimentation flux is discretized using the central finite difference and a high vertical resolution (central option). Nevertheless, this option leads to some overestimation of the mass mixing ratio and some underestimation of the number mixing ratio in the suspension layer, compared to the LES-LSM simulations. As a result, the mean particle diameter is somewhat overestimated (Fig. C.10c). Interestingly, all discretization options poorly reproduce the strong decrease of the mean particle diameter with height between h_{salt} and $z = 0.3$ m. Even with the central option, the mean particle diameter deviates clearly from the profile obtained with the LES-LSM simulation above the lowest fine level ($z = 0.15$ m). This deviation can be attributed to an insufficient

vertical resolution or the fact that the assumed gamma distribution poorly approximates the bi-modal particle size distribution seen in the LES-LSM results at heights around h_{salt} (Fig. C.2). Furthermore, the agreement between the central option and the LES-LSM results may be influenced by (a) uncertainties of the h_{salt} parameter, which is difficult to define due to a gradual transition from saltation to suspension, (b) an underestimation of the mixing ratios at the upper boundary (z = 11.25 m) due to an underestimation of turbulence in the upper part of the LES-LSM domain (Sect. 2.3.3), and (d) uncertainties of the turbulent diffusion coefficient for blowing snow, which is assumed to equal that for momentum and heat in the 1D model. In the literature, there is no consensus on whether blowing snow and other particles are associated with a lower or higher turbulent diffusion coefficient, compared to momentum and heat (e.g., Déry et al., 1998; Vionnet et al., 2014).

Currently, the CRYOWRF model applies the low-resolution forward option, which evaluates the sedimentation flux at slightly too great heights and places the first fine level at z = 0.5 m. Figure C.10 demonstrates that this option overestimates significantly the mass mixing ratios, mean particle diameter, and standard deviation of the diameter. Using the forward option with a higher vertical resolution improves the representation of blowing snow. If the concept of the backward finite difference is applied to the terminal fall velocity (semi-forward option), the performance of the 1D model improves further, albeit only slightly. With this option, the number mixing ratios are close to those of the LES-LSM simulation but the mass mixing ratios are overestimated by a factor of approximately seven at several model levels.

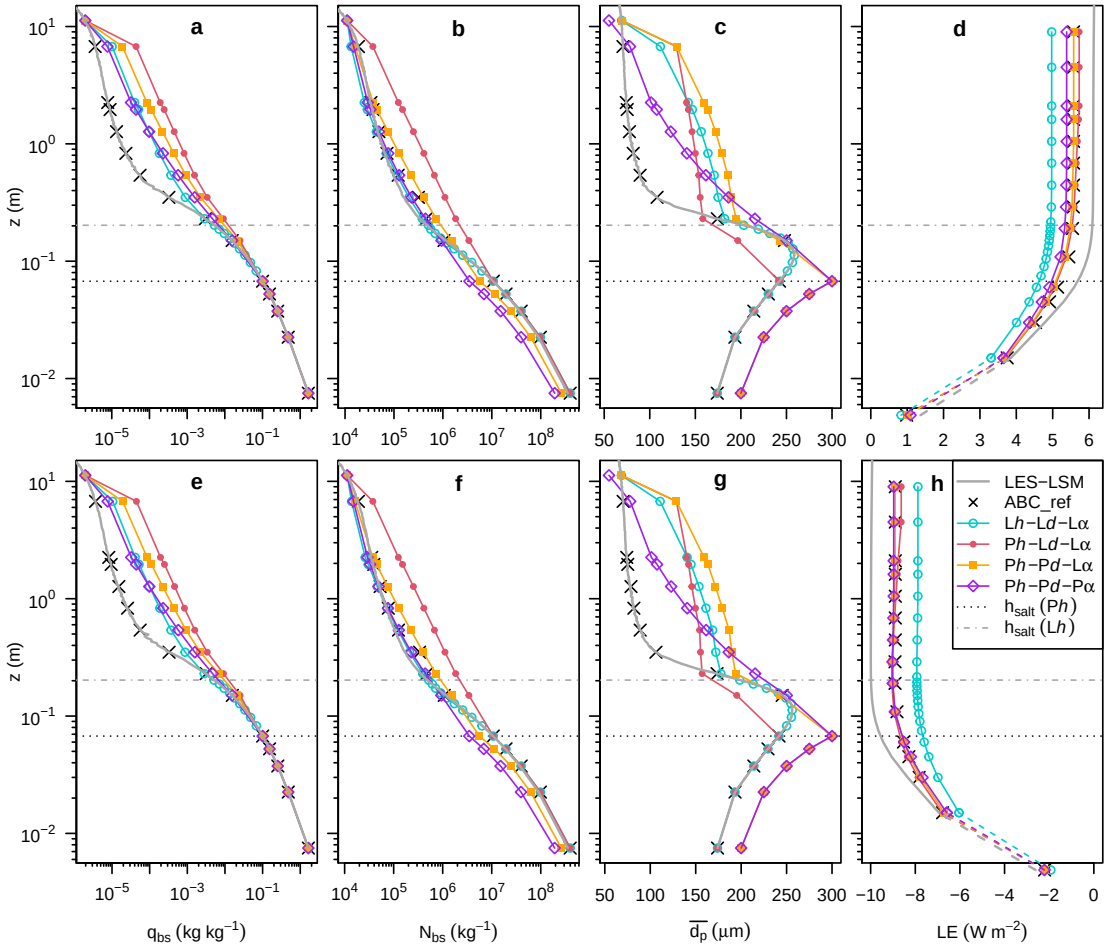

Figure C.11: Properties of drifting and blowing snow and latent heat exchange in the suspension set-up of the 1D model in (a–d) Case 3a and (e–h) Case 3b with the same presentation as in Fig. 2.5 of Chapter 2.

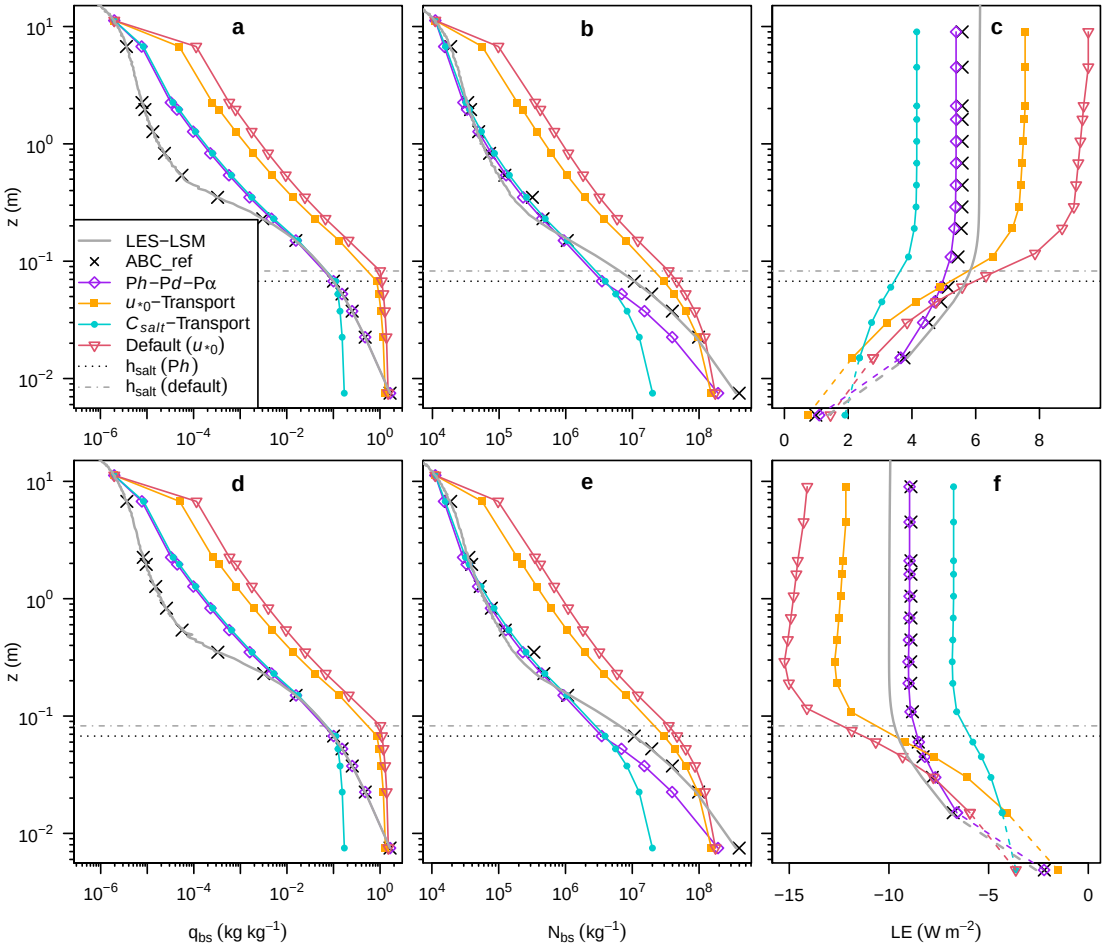

Figure C.12: Mixing ratios of drifting and blowing snow and latent heat exchange in the transport and default set-ups of the 1D model in (a–d) Case 3a and (e–h) Case 3b with the same presentation as in Fig. 2.6 of Chapter 2.

D Supplementary Material for Chapter 3

D.1 Basic Equations for Stable Water Isotopes

The isotopic composition (δ_i) throughout this manuscript is formulated in delta notation and given in ‰ (Craig, 1961):

$$\delta_i = \frac{R_i}{R_{i,VSMOW}} - 1 \,. \tag{D.1}$$

Here, the subscript i refers to a heavy water isotopologue ($H_2{}^{18}O$ or $HD^{16}O$), R_i is the abundance ratio of heavy to light water isotopologues and $R_{i,VSMOW}$ is the reference isotopic ratio of the Vienna Standard Mean Ocean Water (VSMOW) listed in Table D.1 together with other constants and parameters.

The isotopic ratio can be expressed as

$$R_i = \frac{m_i}{m_{H_2{}^{16}O}} \frac{M_{H_2{}^{16}O}}{M_i} \,, \tag{D.2}$$

where $m_{H_2{}^{16}O}$ is the mass of the light isotopologue in a water sample, m_i is the mass of a heavy isotopologue ($H_2{}^{18}O$ or $HD^{16}O$), and $M_{H_2{}^{16}O}$ and M_i are the respective molecular masses.

For given values of $R_{H_2{}^{18}O}$, $R_{HD^{16}O}$, and the total mass of a water sample ($m_{tot} = m_{H_2{}^{16}O} + m_{H_2{}^{18}O} + m_{HD^{16}O}$), the masses of the individual isotopologues are known, e.g.:

$$m_{H_2{}^{18}O} = m_{tot} \left(1 + \frac{M_{H_2{}^{16}O} + R_{HD^{16}O}\, M_{HD^{16}O}}{R_{H_2{}^{18}O}\, M_{H_2{}^{18}O}} \right)^{-1} \,. \tag{D.3}$$

The equilibrium fractionation factor (α_{X-V}) is defined as

$$\alpha_{X-V} = \frac{R_X}{R_V} > 1 \,, \tag{D.4}$$

where the subscript X refers to the solid (S) or liquid (L) phase and the subscript V refers to

Table D.1: Important simulation constants and parameters.

Quantity	Symbol	Value	Unit
Molar mass for $H_2{}^{16}O$	$M_{H_2{}^{16}O}$	0.018	kg mol^{-1}
Molar mass for $H_2{}^{18}O$	$M_{H_2{}^{18}O}$	0.020	kg mol^{-1}
Molar mass for $HD^{16}O$	$M_{HD^{16}O}$	0.019	kg mol^{-1}
Isotopic ratio for VSMOW	$R_{H_2{}^{18}O}$	2.0052×10^{-3}	–
Isotopic ratio for VSMOW	$R_{HD^{16}O}$	1.5595×10^{-4}	–
Ratio of molecular diffusivities	$D_{H_2{}^{18}O}/D_{H_2{}^{16}O}$	0.9727[a]	–
Ratio of molecular diffusivities	$D_{HD^{16}O}/D_{H_2{}^{16}O}$	0.9757[a]	–
Latent heat of evaporation	L_e	2.5×10^6	J kg^{-1}
Number of snow layers	n_{max}	100	–
Snow layer thickness	SLT	0.01[b]	m
Snow density	ρ_s	350	kg m^{-3}
Air parcel volume	V	$1 \times 1 \times 1$	m^3

[a] Merlivat (1978)
[b] Refers to the baseline simulation; other values of 0.001 m and 0.02 m are used in sensitivity tests

the vapor phase. These factors are computed as a function of surface temperature, which is taken from the ERA5 reanalysis data. The α_{S-V} factors for $H_2{}^{18}O$ and $HD^{16}O$ are calculated according to Majoube (1970) and Merlivat and Nief (1967), respectively. For α_{L-V}, the formulas of Majoube (1971) are used.

D.2 Details of Model Sublimation

The isotopic composition of the sublimation flux is computed from that of the surface snow, either assuming equilibrium fractionation (Run E, Eq. D.4) or neglecting fractionation (Run N). To simulate changes in the isotopic composition of surface snow with time, Model Sublimation parameterizes the mass of each water isotopologue in snowfall and in the surface vapor flux. The model neglects liquid precipitation on the ice sheet, i.e., rain-on-snow events, which are rare in Antarctica. To represent the case of vapor deposition, Model Sublimation estimates the isotopic ratio of the atmospheric vapor ($R_{i,V}$) as

$$R_{i,V} = \begin{cases} 0.5 \left(\frac{R_{i,snow}}{\alpha_{S-V}(T)} + \frac{R_{i,p}}{\alpha_{S-V}(\overline{T}_a)} \right) & \text{in Run E,} \\ 0.5 \left(R_{i,snow} + \frac{R_{i,p}}{\alpha_{S-V}(\overline{T}_a)} \right) & \text{in Run N,} \end{cases} \tag{D.5}$$

where T is surface temperature, $\overline{T}_a$ (K) is the daily running mean air temperature at a height of 2 m, and $R_{i,snow}$ and $R_{i,p}$ are the isotopic ratios of surface snow and potential snowfall, respectively. Assuming equilibrium fractionation and multiplying Eq. D.5 with $\alpha_{S-V}(T)$ yields

the isotopic ratio of the deposition flux ($R_{\mathrm{i,flx}}$):

$$R_{\mathrm{i,flx}} = \begin{cases} 0.5 \left(R_{\mathrm{i,snow}} + \frac{\alpha_{\mathrm{S-V}}(T)}{\alpha_{\mathrm{S-V}}(\overline{T}_{\mathrm{a}})} R_{\mathrm{i,p}} \right) & \text{in Run E,} \\ 0.5 \left(\alpha_{\mathrm{S-V}}(T)\ R_{\mathrm{i,snow}} + \frac{\alpha_{\mathrm{S-V}}(T)}{\alpha_{\mathrm{S-V}}(\overline{T}_{\mathrm{a}})} R_{\mathrm{i,p}} \right) & \text{in Run N,} \end{cases} \tag{D.6}$$

In the baseline simulation, the isotopic composition of snowfall is parameterized using the empirical function of Stenni et al. (2016), henceforth referred to as Stenni16:

$$\delta^{18}\mathrm{O} = 0.45 \left(\overline{T}_{\mathrm{a}} - 273.15 \right) - 31.21 \ . \tag{D.7}$$

This function represents a linear fit to local measurement data from Dome C, averaged over daily intervals, where the air temperatures span the broad range from −80 °C to −20 °C. Although Masson-Delmotte et al. (2008) derived δ_{i}-temperature relationships from a data set with many Antarctic sites, these relationships are not suitable for our purpose because they are based on yearly averages and a variety of snow samples including ice cores, firn cores, snow pits, and precipitation. In a sensitivity study, we perform simulations with other local δ^{18}O-temperature relationships for snowfall, namely those for Vostok from Landais et al. (2012), henceforth Landais12,

$$\delta^{18}\mathrm{O} = 0.35 \left(\overline{T}_{\mathrm{a}} - 273.15 \right) - 40 \ , \tag{D.8}$$

and for Dome Fuji from Fujita and Abe (2006), henceforth FA06,

$$\delta^{18}\mathrm{O} = 0.78 \left(\overline{T}_{\mathrm{a}} - 273.15 \right) - 18.4 \ . \tag{D.9}$$

Equations D.8 and D.9 are based on data in the temperature range from −76 °C to −44 °C and from −76 °C to −28 °C, respectively. For all of these options, δD of the snowfall is derived using the δD-δ^{18}O relationship from Masson-Delmotte et al. (2008),

$$\delta\mathrm{D} = (7.75\ \delta^{18}\mathrm{O}) - 4.93 \ . \tag{D.10}$$

We initialize Model Sublimation by assuming that a large quantity of snowfall has just occurred. Hence, for a particular location, the initial isotopic composition of all snow layers is the same. In the surface snow layer, the mass balance for each water isotopologue is

$$m_{\mathrm{i}}|_t^1 = m_{\mathrm{i}}|_{t-1}^1 + m_{\mathrm{i,p}}\big|_t + m_{\mathrm{i,flx}}\big|_t \begin{cases} -f\ m_{\mathrm{i}}|_{t-1}^1 & \text{if } \Delta m|_t \geq 0 \ , \\ +f\ m_{\mathrm{i}}|_{t-1}^2 & \text{if } \Delta m|_t < 0 \ , \end{cases} \tag{D.11}$$

where, $m_{\mathrm{i}}|_t^1$ and $m_{\mathrm{i}}|_{t-1}^1$ are the masses of a specific water isotopologue (i) in the surface snow layer at time step t and the previous time step $(t-1)$, respectively; $m_{\mathrm{i,p}}\big|_t$ is the mass added by precipitation; $m_{\mathrm{i,flx}}\big|_t$ is the mass added or removed (positive or negative sign, respectively) by the surface flux; $m_{\mathrm{i}}|_{t-1}^2$ is the mass of the water isotopologue in the layer below the surface snow layer; and f is the absolute ratio between the net mass gain or loss at the surface ($\Delta m|_t$)

and the total mass of the snow layer. For layers below the surface snow layer ($n > 1$), the balance equation becomes

$$m_\mathrm{i}|_t^n = m_\mathrm{i}|_{t-1}^n - f\ m_\mathrm{i}|_{t-1}^n + \begin{cases} f\ m_\mathrm{i}|_{t-1}^{n-1} & \text{if } \Delta m|_t \geq 0\,, \\ f\ m_\mathrm{i}|_{t-1}^{n+1} & \text{if } \Delta m|_t < 0\,, \end{cases} \tag{D.12}$$

where n is the number of the layer. For the lowest layer ($n = 100$), the term $m_\mathrm{i}|_{t-1}^{n+1}$ is not known and assumed to be equal to $m_\mathrm{i}|_{t-1}^{n}$.

D.3 Details of Model Air Parcel

For each air parcel, we consider time intervals of 3 h centered around data points from the trajectory data set. Due to these centered intervals, the first and the last interval are only 1.5 h long. For each interval, we use ERA5 reanalysis data for the closest grid cell and the hour beginning at the center of the air parcel interval. The only exception is the last interval, for which we use ERA5 data in the hour ending at the center of the interval, i.e., in the last hour before the parcel arrives at the ship.

During ocean evaporation, equilibrium and kinetic fractionation are modeled using the Craig-Gordon formula (e.g. Horita et al., 2008),

$$\delta_\mathrm{E} = \frac{\alpha_{\mathrm{L-V}}^{-1}\,\delta_\mathrm{L} - h_\mathrm{s}\,\delta_\mathrm{A} - (\varepsilon* + \varepsilon_\mathrm{k})}{1 - h_\mathrm{s} + 10^{-3}\,\varepsilon_\mathrm{k}}\,, \tag{D.13}$$

where the isotopic composition of ocean water (δ_L) is set to $\delta^{18}\mathrm{O} = -0.5$‰ or $\delta\mathrm{D} = -1.7$‰, which is typical for surface water in the Southern Ocean (LeGrande and Schmidt, 2006; Bonne et al., 2019); δ_E and δ_A are the isotopic compositions of the evaporation flux and the air parcel, respectively; h_s is the ratio of ambient vapor pressure (here evaluated at a height of 2 m) and saturation vapor pressure at the surface; and $\varepsilon* = (1 - \alpha_{\mathrm{L-V}}^{-1})10^3 > 0$ and $\varepsilon_\mathrm{k} = (1 - \alpha_\mathrm{k}^{-1})10^3 > 0$ are functions of the equilibrium ($\alpha_{\mathrm{L-V}}$) and kinetic (α_k) fractionation factors, respectively. The expression for ε_k is parameterized as

$$\varepsilon_\mathrm{k} = (1 - h_\mathrm{s})\,\theta \left[1 - \left(\frac{D_\mathrm{i}}{D}\right)^n\right] 10^3\,, \tag{D.14}$$

where the ratio of diffusion coefficients for the heavy and light water isotopologues (D_i/D) is taken from Merlivat (1978). For the exponent, a value of $n = 0.5$ is assumed, which is typical for open water bodies in natural conditions (Gat et al., 2001). The term θ is approximated with a value of $\theta = 1$, which is appropriate if h_s and δ_A are evaluated in the lower part of the boundary layer, where they are directly influenced by evaporation (Gat et al., 1996). If h_s approaches a value of 1, Eq. D.13 will yield a δ_E value approaching ± infinity depending on δ_A. At the same time, propagated errors in δ_E will approach infinity (Kumar and Nachiappan, 1999). To avoid implausible isotopic compositions, δ_E is limited to minimum and maximum values of −1000‰ and +10000‰, respectively, corresponding to isotopic ratios of zero and

approximately 11 times the VSMOW values, respectively.

To initialize air parcels over the ocean, Eq. D.13 is simplified using the global closure assumption. Taking into account Eq. D.1, this simplification yields (e.g. Dar et al., 2020)

$$R_{\mathrm{E}} = \frac{\alpha_{\mathrm{k}} R_{\mathrm{L}}}{\alpha_{\mathrm{L-V}}(1 - h_{\mathrm{s}} + \alpha_{\mathrm{k}} h_{\mathrm{s}})} \,, \tag{D.15}$$

where R_{E} and R_{L} are the isotopic ratios of the evaporation flux and the ocean, respectively. Air parcels which are initialized over snow, begin their journey with isotopic ratios according to Eq. D.5.

While the volume of the air parcel (V) stays constant, its mass (m_{A}) changes according to the ideal gas law,

$$m_{\mathrm{A}} = \frac{p\, V}{R_{\mathrm{d}}\, T_{\mathrm{v}}} \,, \tag{D.16}$$

where p is air pressure, R_{d} is the specific gas constant of dry air, and T_{v} is virtual temperature. If the specific humidity of the parcel exceeds its saturation value, the model will account for cloud formation and precipitation by reducing the vapor mass to reach the saturation specific humidity. The effect of this phase change and mass removal on the isotopic composition of the parcel is computed using the classic Rayleigh distillation model in its integrated form (Sinclair et al., 2011),

$$\delta_{\mathrm{i},2} = (1 + \delta_{\mathrm{i},1}) \left(\frac{q_2}{q_1} \right)^{\hat{\alpha}_{\mathrm{X-V}} - 1} - 1 \,, \tag{D.17}$$

where $\delta_{\mathrm{i},1}$ and q_1 are, respectively, the isotopic composition and specific humidity of the parcel after accounting for surface exchange and before accounting for cloud formation, $\delta_{\mathrm{i},2}$ and q_2 are, respectively, the isotopic composition and specific humidity of the parcel after accounting for cloud formation, and $\hat{\alpha}_{\mathrm{X-V}}$ is a weighted average of the equilibrium fractionation factors for the liquid-vapor and solid-vapor transitions, considering a cloud ice fraction that increases linearly from 0 to 1 in the temperature range from 0° C to −20° C.

D.4 Model-Measurement Comparison for the Location of Dome C

In this section, we analyze the sensitivity of Model Sublimation with respect to the settings for snow layer thickness (SLT) and snowfall isotopic composition. In addition to these settings, the fractionation assumption for snow sublimation is varied, that is, we either assume equilibrium fractionation (Run E) or neglect fractionation (Run N) during sublimation. The model is run for the location of Dome C, in the period from January 2013 to January 2016 and the results are compared with isotope measurements for surface snow and atmospheric water vapor, published by Casado et al. (2016, 2018).

With increasing values of SLT, the modeled isotopic composition of surface snow responds more slowly to the surface flux and snowfall (Fig. D.1). Using a SLT value of 1 cm or 2 cm, the model reproduces well the measured seasonal cycle in surface snow δ^{18}O, especially in

Run E. For a lower value of SLT = 0.1 cm, the seasonal amplitude is overestimated and the seasonal maxima and minima are attained slightly too early. For SLT values of 1 cm and 2 cm, the root-mean-square error (RMSE) with respect to the measurements is identical (2.4‰ for Run E). However, the seasonal amplitude is better captured with SLT = 1 cm and hence, we use this value in the remaining analysis. The sensitivity with respect to SLT is similar to the sensitivity with respect to snow density as both parameters determine the mass contained in each snow layer. Changing the snow density by a certain factor has the same effect on the modeled isotopic composition as changing SLT by the same factor.

On short time scales, the measured δ^{18}O of surface snow varies more strongly than the simulated one, partly because the sampling location changes slightly with time and the small-scale spatial variability is not represented in the simulations (Casado et al., 2018). In Run N, the surface snow is generally enriched in the heavy isotopologues, compared to Run E. For SLT = 1 cm, the difference between the model runs amounts up to 2.6‰. This difference can only result from a different representation of the sublimation and deposition fluxes (Sect. D.2, Eq. 6). At Dome C, vapor deposition dominates, on average, over sublimation according to the ERA5 data; sublimation is only significant from November to February. Therefore, the more enriched surface snow in Run N, compared to Run E, is explained by the fact that the deposition flux is more enriched in heavy isotopologues in Run N.

So far, we have used the snowfall δ-temperature relationship of Stenni16 because it was derived from measurements at Dome C. Figure D.2a shows how the surface snow δ^{18}O at Dome C changes when applying snowfall δ-temperature relationships from other Antarctic sites (Equations D.8 and D.9). This sensitivity test allows us to estimate uncertainties arising from the generalization of a site-specific snowfall δ-temperature relationship. As expected, the relationship of FA06 with a high δ^{18}O-temperature slope leads to an increased seasonal amplitude in the surface snow δ^{18}O. In austral summer, the agreement with the measurements is still reasonable while in austral winter, the surface snow δ^{18}O is clearly too depleted. Overall, the RMSE of the surface snow δ^{18}O is 3.9‰ for the relationship of FA06 in Run E, which is 1.6 times higher than for the relationship of Stenni16 in Run E. Using the relationship of Landais12, the modeled δ^{18}O of the surface snow is systematically too depleted while the seasonal amplitude is only slightly reduced compared to the relationship of Stenni16. The systematic difference is due to a low intercept value in the δ-temperature relationship of Landais12, leading to the highest RMSE of approximately 5‰ in Run E.

Figure D.2b compares the estimated isotopic composition of atmospheric water vapor with measurements at Dome C available in a 24-d period in December 2014 and January 2015 (grey shading in Fig. D.2a). It is important to note that this figure is only based on the simple parameterization used in Model Sublimation without considering air parcel trajectories. The comparison with the measurements allows us to assess potential uncertainties in this parameterization, affecting the isotopic composition of the deposition flux in Model Sublimation and the initialization of the air parcel δ^{18}O over snow in Model Air Parcel.

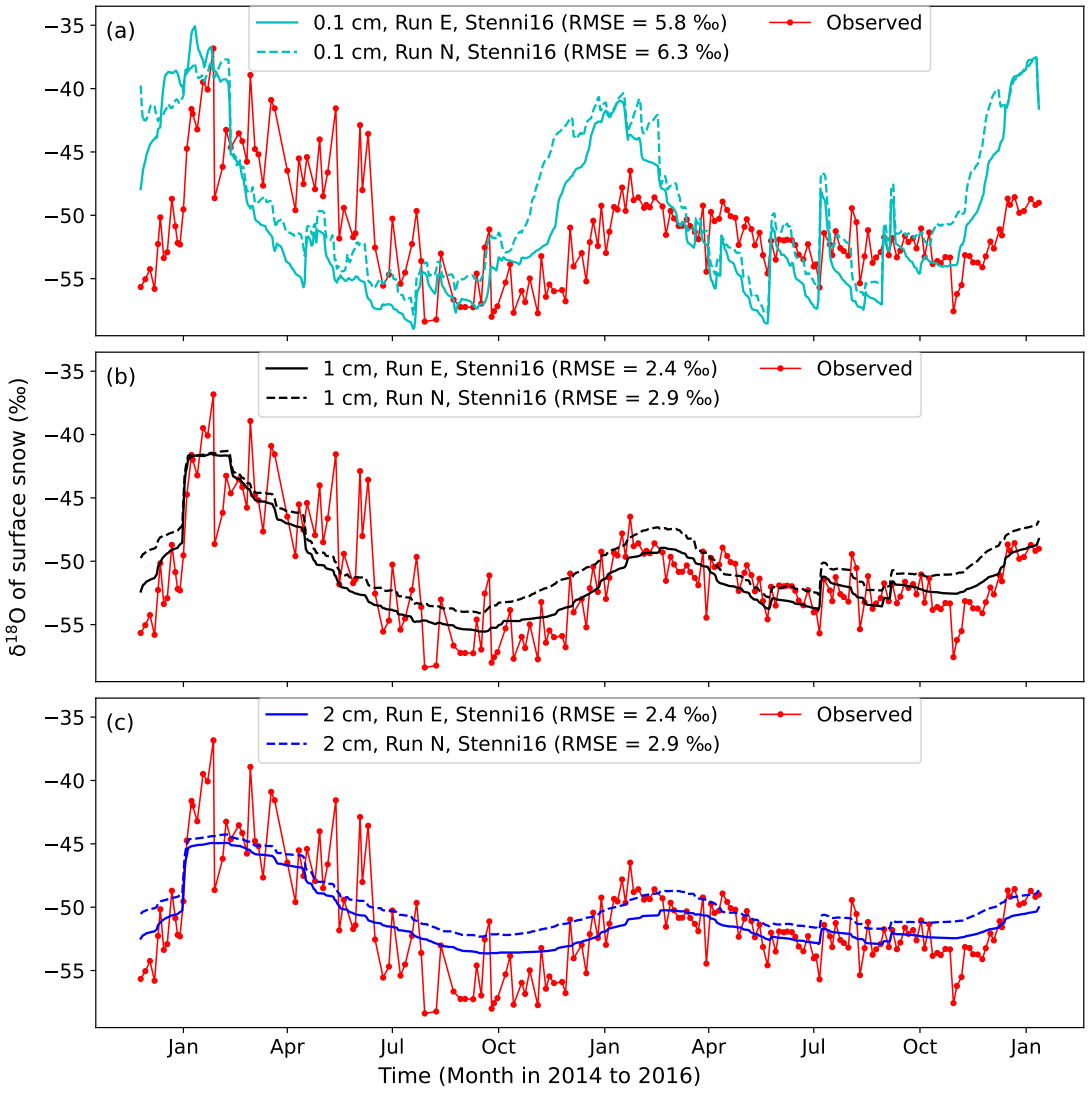

Figure D.1: Sensitivity of the modeled δ^{18}O of surface snow at Dome C with respect to snow layer thickness for values of (a) 0.1 cm, (b) 1 cm, and (c) 2 cm in Run E (solid lines) and Run N (dashed lines) from November 2013 to January 2016. Daily averages are compared with observed samples taken approximately every four days as described in Casado et al. (2018); respective root-mean-square errors are shown in the legend. For this figure, the snowfall $\delta-$temperature relationship of Stenni et al. (2016) is used.

With the snowfall δ-temperature relationships of Stenni16 and FA06, the estimated vapor δ^{18}O values are very similar and, in Run E, close to the measured mean value for the whole period. For the relationship of Stenni16 and Run E, the vapor δ^{18}O is characterized by a mean bias error (MBE) of −0.2‰. For the same model run, the RMSE is 3.7‰ because our simple estimate of the vapor δ^{18}O strongly underestimates the measured diurnal variations. Using the snowfall δ-temperature relationship of Landais12 in Run E, the vapor δ^{18}O values are generally too depleted at Dome C with a MBE of −4.9‰ and a RMSE of 6.2‰. In Run N, the atmospheric

vapor is clearly too enriched in heavy isotopologues for all snowfall δ-temperature relationship. These findings suggests that Run E is more realistic than Run N and the initial air parcel δ^{18}O over snow may be under- or overestimated by several ‰ depending on where and when the air parcel is initialized.

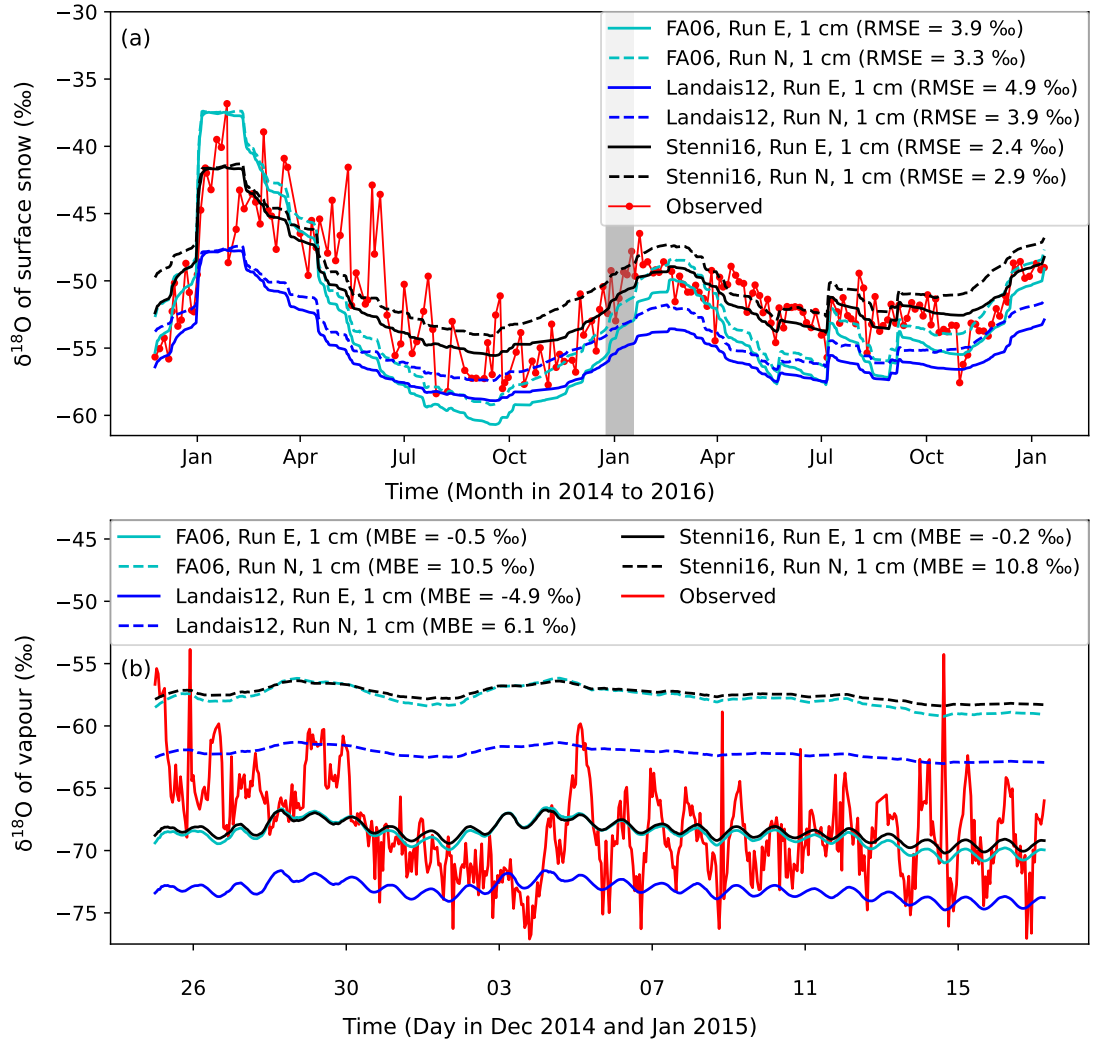

Figure D.2: Sensitivity of the modeled δ^{18}O of (a) surface snow and (b) atmospheric water vapor at Dome C with respect to the assumed $\delta-$temperature relationship for snowfall in Run E (solid lines) and Run N (dashed lines) of Model Sublimation. In all cases, a snow layer thickness of 1 cm is used. Panel (a) compares hourly averages with observed samples taken approximately every four days as described in Casado et al. (2018). Panel (b) shows hourly values for vapor in the grey-shaded period and the measurements represent running mean values as described in Casado et al. (2016). The legend specifies the root-mean-square error (RMSE) or mean bias error (MBE) for the model-measurement comparison.

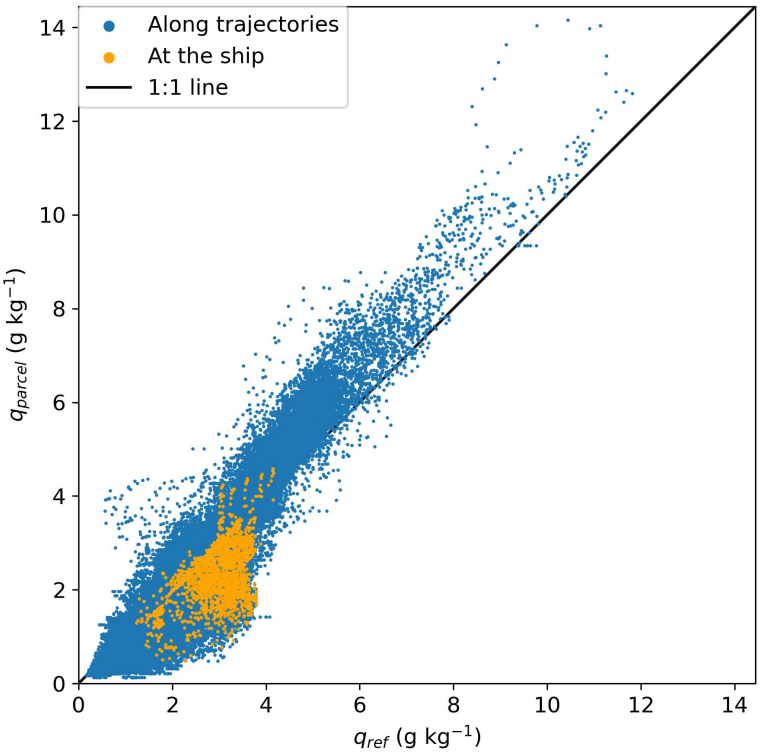

Figure D.3: Comparison of the specific humidity between Model Air Parcel (q_{parcel}) and the trajectory data set (q_{ref}), which is based on operational analyses of the European Centre for Medium-Range Weather Forcasts.

D.5 Sensitivity of the Isotopic Composition of the Air Parcels With Respect to That of Snowfall

It is important to note that changing the snowfall isotopic composition in Model Sublimation does not affect the isotopic composition of the air parcels during cloud formation. The isotopic composition of snowfall is only used to estimate that of surface snow, which determines that of the sublimation flux and influences the initial isotopic composition of the air parcels. Figure D.4 shows how the modeled δ^{18}O at the ship changes when assuming different snowfall δ-temperature relationships in Run E (Equations D.7 to D.9). Differences in the δ^{18}O time series are most pronounced in the middle of the study period, suggesting that many air parcels are initialized over snow or influenced by sublimation at this time. While the snowfall δ-temperature relationship of Stenni16 (baseline simulation) leads to a minimum of −40‰ in the vapor δ^{18}O time series, the relationship of FA06 leads to a less pronounced minimum of −34‰. On the contrary, the snowfall δ-temperature relationship of Landais12 leads to the most pronounced δ^{18}O minimum of −45‰. The best agreement with the measurements is obtained with the relationship of FA06 (RMSE = 4.2‰, Pearson correlation coefficient $\rho = 0.77$) although the agreement is only slightly better than for the baseline simulation (RMSE = 4.4‰, $\rho = 0.77$). For the relationship of Landais12, the deviations from the measurements are, on average, largest but still reasonable (RMSE = 5.6‰, $\rho = 0.77$). Although the parameterized snowfall δ^{18}O is an important source of uncertainty in our model, the associated sensitivity of the vapor δ^{18}O is small enough to draw useful conclusions about the dominant processes driving the isotopic signal.

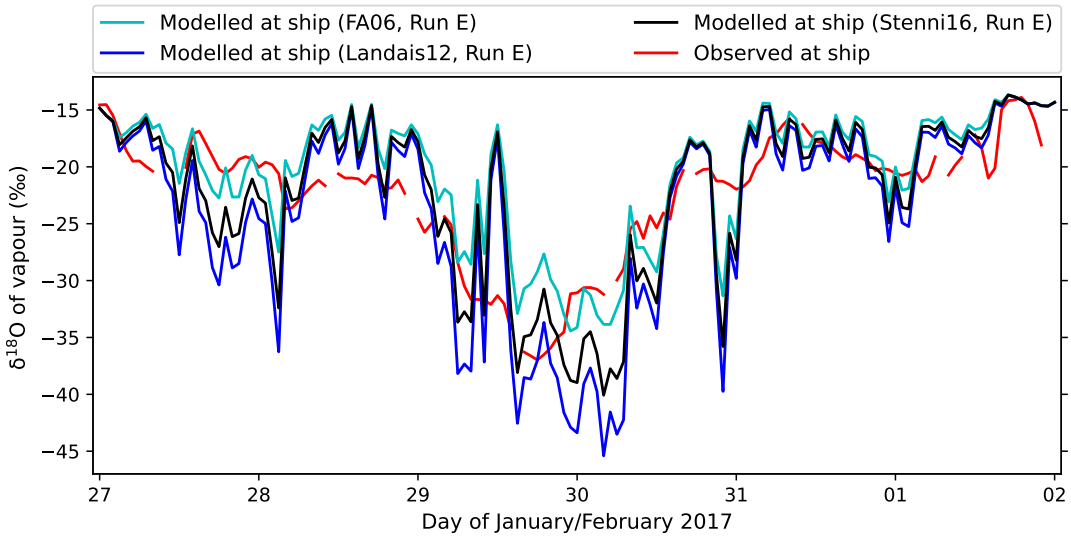

Figure D.4: Effect of different snowfall δ-temperature relationships assumed in Model Sublimation on the modeled δ^{18}O of atmospheric water vapor at the ship in Run E. Modeled ensemble averages are compared with measured 1-h averages.

Bibliography

Aemisegger, F., Trachsel, J., Sadowski, Y., Eichler, A., Lehning, M., Avak, S., and Schneebeli, M.: Fingerprints of Frontal Passages and Post-Depositional Effects in the Stable Water Isotope Signal of Seasonal Alpine Snow, Journal of Geophysical Research: Atmospheres, 127, e2022JD037 469, URL https://doi.org/10.1029/2022JD037469, 2022.

Agosta, C., Amory, C., Kittel, C., Orsi, A., Favier, V., Gallée, H., van den Broeke, M. R., Lenaerts, J. T. M., van Wessem, J. M., van de Berg, W. J., and Fettweis, X.: Estimation of the Antarctic surface mass balance using the regional climate model MAR (1979–2015) and identification of dominant processes, The Cryosphere, 13, 281–296, URL https://doi.org/10.5194/tc-13-281-2019, 2019.

Akaike, H.: Information Theory and an Extension of the Maximum Likelihood Principle, in: Selected Papers of Hirotugu Akaike, edited by Parzen, E., Tanabe, K., and Kitagawa, G., pp. 199–213, Springer, New York, URL https://doi.org/10.1007/978-1-4612-1694-0_15, 1998.

Akers, P. D., Kopec, B. G., Mattingly, K. S., Klein, E. S., Causey, D., and Welker, J. M.: Baffin Bay sea ice extent and synoptic moisture transport drive water vapor isotope (δ^{18}O, δ^{2}H, and deuterium excess) variability in coastal northwest Greenland, Atmospheric Chemistry and Physics, 20, 13 929–13 955, URL https://doi.org/10.5194/acp-20-13929-2020, 2020.

Albertson, J. D. and Parlange, M. B.: Natural integration of scalar fluxes from complex terrain, Advances in Water Resources, 23, 239–252, URL https://doi.org/10.1016/S0309-1708(99)00011-1, 1999.

Amory, C., Kittel, C., Le Toumelin, L., Agosta, C., Delhasse, A., Favier, V., and Fettweis, X.: Performance of MAR (v3.11) in simulating the drifting-snow climate and surface mass balance of Adélie Land, East Antarctica, Geoscientific Model Development, 14, 3487–3510, URL https://doi.org/10.5194/gmd-14-3487-2021, 2021.

Andreas, E. L.: A theory for the scalar roughness and the scalar transfer coefficients over snow and sea ice, Boundary-Layer Meteorology, 38, 159–184, URL https://doi.org/10.1007/BF00121562, 1987.

Andreas, E. L., Persson, P. O. G., Grachev, A. A., Jordan, R. E., Horst, T. W., Guest, P. S., and Fairall, C. W.: Parameterizing Turbulent Exchange over Sea Ice in Winter, Journal of Hydrometeorology, 11, 87–104, URL https://doi.org/10.1175/2009JHM1102.1, 2010.

Barral, H., Genthon, C., Trouvilliez, A., Brun, C., and Amory, C.: Blowing snow in coastal Adélie Land, Antarctica: three atmospheric-moisture issues, The Cryosphere, 8, 1905–1919, URL https://doi.org/10.5194/tc-8-1905-2014, 2014.

Beria, H., Larsen, J. R., Ceperley, N. C., Michelon, A., Vennemann, T., and Schaefli, B.: Understanding snow hydrological processes through the lens of stable water isotopes, Wiley Interdisciplinary Reviews: Water, 5, e1311, URL https://doi.org/10.1002/wat2.1311, 2018.

Bernhardt, M., Schulz, K., Liston, G. E., and Zängl, G.: The influence of lateral snow redistribution processes on snow melt and sublimation in alpine regions, Journal of Hydrology, 424-425, 196–206, URL http://www.doi.org/10.1016/j.jhydrol.2012.01.001, 2012.

Bintanja, R.: Snowdrift Sublimation in a Katabatic Wind Region of the Antarctic Ice Sheet, Journal of Applied Meteorology and Climatology, 40, 1952–1966, URL https://doi.org/10.1175/1520-0450(2001)040<1952:SSIAKW>2.0.CO;2, 2001a.

Bintanja, R.: Modelling snowdrift sublimation and its effect on the moisture budget of the atmospheric boundary layer, Tellus A: Dynamic Meteorology and Oceanography, 53, 215–232, URL https://doi.org/10.3402/tellusa.v53i2.12189, 2001b.

Bonne, J.-L., Behrens, M., Meyer, H., Kipfstuhl, S., Rabe, B., Schönicke, L., Steen-Larsen, H. C., and Werner, M.: Resolving the controls of water vapour isotopes in the Atlantic sector, Nature Communications, 10, 1632, URL https://doi.org/10.1038/s41467-019-09242-6, 2019.

Bou-Zeid, E., Meneveau, C., and Parlange, M.: A scale-dependent Lagrangian dynamic model for large eddy simulation of complex turbulent flows, Physics of Fluids, 17:025105, URL http://www.doi.org/10.1063/1.1839152, 2005.

Box, J. E. and Steffen, K.: Sublimation on the Greenland Ice Sheet from automated weather station observations, Journal of Geophysical Research: Atmospheres, 106, 33 965–33 981, URL https://doi.org/10.1029/2001JD900219, 2001.

Bréant, C., Dos Santos, C. L., Agosta, C., Casado, M., Fourré, E., Goursaud, S., Masson-Delmotte, V., Favier, V., Cattani, O., Prié, F., et al.: Coastal water vapor isotopic composition driven by katabatic wind variability in summer at Dumont d'Urville, coastal East Antarctica, Earth and Planetary Science Letters, 514, 37–47, URL https://www.doi.org/10.1016/j.epsl.2019.03.004, 2019.

Businger, J. A., Wyngaard, J. C., Izumi, Y., and Bradley, E. F.: Flux-Profile Relationships in the Atmospheric Surface Layer, Journal of the Atmospheric Sciences, 28, 181–189, URL https://doi.org/10.1175/1520-0469(1971)028<0181:FPRITA>2.0.CO;2, 1971.

Campbell Scientific: CSAT3 Three Dimensional Sonic Anemometer: Instruction Manual, https://s.campbellsci.com/documents/us/manuals/csat3.pdf. Last access: 30 June 2020, 2017.

Casado, M., Landais, A., Masson-Delmotte, V., Genthon, C., Kerstel, E., Kassi, S., Arnaud, L., Picard, G., Prie, F., Cattani, O., Steen-Larsen, H.-C., Vignon, E., and Cermak, P.: Continuous measurements of isotopic composition of water vapour on the East Antarctic Plateau, Atmospheric Chemistry and Physics, 16, 8521–8538, URL https://www.doi.org/10.5194/acp-16-8521-2016, 2016.

Casado, M., Landais, A., Picard, G., Münch, T., Laepple, T., Stenni, B., Dreossi, G., Ekaykin, A., Arnaud, L., Genthon, C., et al.: Archival processes of the water stable isotope signal in East Antarctic ice cores, The Cryosphere, 12, 1745–1766, URL https://doi.org/10.5194/tc-12-1745-2018, 2018.

Christner, E., Kohler, M., and Schneider, M.: The influence of snow sublimation and meltwater evaporation on δD of water vapor in the atmospheric boundary layer of central Europe., Atmospheric Chemistry and Physics, 17, URL https://doi.org/10.5194/acp-17-1207-2017, 2017.

Ciais, P. and Jouzel, J.: Deuterium and oxygen 18 in precipitation: Isotopic model, including mixed cloud processes, Journal of Geophysical Research: Atmospheres, 99, 16 793–16 803, URL https://doi.org/10.1029/94JD00412, 1994.

Colbeck, S.: Statistics of coarsening in water-saturated snow, Acta Metallurgica, 34, 347–352, URL https://doi.org/10.1016/0001-6160(86)90070-2, 1986.

Comola, F. and Lehning, M.: Energy- and momentum-conserving model of splash entrainment in sand and snow saltation, Geophysical Research Letters, 44, 1601–1609, URL https://doi.org/10.1002/2016GL071822, 2017.

Craig, H.: Standard for reporting concentrations of deuterium and oxygen-18 in natural waters, Science, 133, 1833–1834, 1961.

Craig, H. and Gordon, L. I.: Deuterium and oxygen 18 variations in the Ocean and the Marine Atmosphere, in: Stable Isotopes in Oceanographic Studies and Paleotemperatures, edited by Tongiorgi, E., pp. 9–130, Consiglio nazionale delle richerche, Laboratorio de geologia nucleare Pisa, Spoleto, 1965.

Cuffey, K. M. and Steig, E. J.: Isotopic diffusion in polar firn: implications for interpretation of seasonal climate parameters in ice-core records, with emphasis on central Greenland, Journal of Glaciology, 44, 273–284, URL https://doi.org/10.3189/S0022143000002616, 1998.

Dansgaard, W.: Stable isotopes in precipitation, Tellus, 16, 436–468, URL https://www.doi.org/10.3402/tellusa.v16i4.8993, 1964.

Dar, S. S., Ghosh, P., Swaraj, A., and Kumar, A.: Craig–Gordon model validation using stable isotope ratios in water vapor over the Southern Ocean, Atmospheric Chemistry and Physics, 20, 11 435–11 449, URL https://doi.org/10.5194/acp-20-11435-2020, 2020.

Dütsch, M., Pfahl, S., Meyer, M., and Wernli, H.: Lagrangian process attribution of isotopic variations in near-surface water vapour in a 30-year regional climate simulation over Europe, Atmospheric Chemistry and Physics, 18, 1653–1669, URL http://doi.org/10.5194/acp-18-1653-2018, 2018.

Déry, S. J. and Yau, M. K.: A Bulk Blowing Snow Model, Boundary-Layer Meteorology, 93, 237–251, URL https://doi.org/10.1023/A:1002065615856, 1999.

Déry, S. J., Taylor, P. A., and Xiao, J.: The Thermodynamic Effects of Sublimating, Blowing Snow in the Atmospheric Boundary Layer, Boundary-Layer Meteorology, 89, 251–283, URL http://doi.org/10.1023/A:1001712111718, 1998.

Dütsch, M., Pfahl, S., and Sodemann, H.: The Impact of Nonequilibrium and Equilibrium Fractionation on Two Different Deuterium Excess Definitions, Journal of Geophysical Research: Atmospheres, 122, 12,732–12,746, URL http://doi.org/10.1002/2017JD027085, 2017.

Ebner, P. P., Steen-Larsen, H. C., Stenni, B., Schneebeli, M., and Steinfeld, A.: Experimental observation of transient δ^{18}O interaction between snow and advective airflow under various temperature gradient conditions, The Cryosphere, 11, 1733–1743, URL https://www.doi.org/10.5194/tc-11-1733-2017, 2017.

ECMWF: IFS documentation CY41R2 – Part IV: Physical processes, no. 4 in IFS Documentation, URL https://doi.org/10.21957/tr5rv27xu, 2016.

Elliot, T.: Environmental Tracers, Water, 6, 3264–3269, URL http://doi.org/10.3390/w6113264, 2014.

EPICA community members: Eight glacial cycles from an Antarctic ice core, Nature, 429, 623–628, URL http://doi.org/10.1038/nature02599, 2004.

Fang, J. and Porté-Agel, F.: Large-Eddy Simulation of Very-Large-Scale Motions in the Neutrally Stratified Atmospheric Boundary Layer, Boundary-Layer Meteorology, 155, 397–416, URL https://doi.org/10.1007/s10546-015-0006-z, 2015.

Foken, T., Göckede, M., Mauder, M., Mahrt, L., Amiro, B., and Munger, W.: Post-field quality control, in: Handbook of Micrometeorology: A guide for surface flux measurments, edited by Lee, X., Massman, W., and Law, B., pp. 81–108, Kluwer Academic, Dordrecht, 2004.

Fratini, G., McDermitt, D. K., and Papale, D.: Eddy-covariance flux errors due to biases in gas concentration measurements: origins, quantification and correction, Biogeosciences, 11, 1037–1051, URL https://www.doi.org/10.5194/bg-11-1037-2014, 2014.

Friedman, I., Benson, C., and Gleason, J.: Isotopic changes during snow metamorphism, in: Stable Isotope Geochemistry: A Tribute to Samuel Epstein, edited by Taylor, H., O'Neil, J., and Kaplan, I., pp. 211–221, Geochemical Society, 1991.

Fujita, K. and Abe, O.: Stable isotopes in daily precipitation at Dome Fuji, East Antarctica, Geophysical Research Letters, 33, URL http://doi.org/10.1029/2006GL026936, 2006.

Gat, J. R., Shemesh, A., Tziperman, E., Hecht, A., Georgopoulos, D., and Basturk, O.: The stable isotope composition of waters of the eastern Mediterranean Sea, Journal of Geophysical Research: Oceans, 101, 6441–6451, URL http://doi.org/10.1029/95JC02829, 1996.

Gat, J. R., Mook, W. G., and Meijer, H.: Environmental isotopes in the hydrological cycle: Principles and Applications, Technical Documents in Hydrology, 2, 2001.

Gerber, F., Sharma, V., and Lehning, M.: CRYOWRF—Model Evaluation and the Effect of Blowing Snow on the Antarctic Surface Mass Balance, Journal of Geophysical Research: Atmospheres, 128, e2022JD037 744, URL http://doi.org/10.1029/2022JD037744, 2023.

Gordon, M. and Taylor, P. A.: Measurements of blowing snow, Part I: Particle shape, size distribution, velocity, and number flux at Churchill, Manitoba, Canada, Cold Regions Science and Technology, 55, 63–74, URL http://doi.org/10.1016/j.coldregions.2008.05.001, 2009.

Gordon, M., Savelyev, S., and Taylor, P. A.: Measurements of blowing snow, part II: Mass and number density profiles and saltation height at Franklin Bay, NWT, Canada, Cold Regions Science and Technology, 55, 75–85, URL http://doi.org/10.1016/j.coldregions.2008.07.001, 2009.

Grazioli, J., Madeleine, J.-B., Gallée, H., Forbes, R. M., Genthon, C., Krinner, G., and Berne, A.: Katabatic winds diminish precipitation contribution to the Antarctic ice mass balance, Proceedings of the National Academy of Sciences, 114, 10 858–10 863, URL http://doi.org/10.1073/pnas.1707633114, 2017.

Groot Zwaaftink, C. D., Mott, R., and Lehning, M.: Seasonal simulation of drifting snow sublimation in Alpine terrain, Water Resources Research, 49, 1581–1590, URL http://www.doi.org/10.1002/wrcr.20137, 2013.

Grootes, P., Steig, E., and Stuiver, M.: Taylor Ice Dome study 1993-1994: An ice core to bedrock, Antarctic Journal of the United States, 29, 79–81, 1994.

Helsen, M., Van de Wal, R., Van den Broeke, M., As, D. v., Meijer, H., and Reijmer, C.: Oxygen isotope variability in snow from western Dronning Maud Land, Antarctica and its relation to temperature, Tellus B: Chemical and Physical Meteorology, 57, 423–435, URL https://doi.org/10.1111/j.1600-0889.2005.00162.x, 2005.

Helsen, M., Van de Wal, R., Van den Broeke, M., Masson-Delmotte, V., Meijer, H., Scheele, M., and Werner, M.: Modeling the isotopic composition of Antarctic snow using backward trajectories: Simulation of snow pit records, Journal of Geophysical Research: Atmospheres, 111, URL https://doi.org/10.1029/2005JD006524, 2006.

Helsen, M., Van de Wal, R., and Van den Broeke, M.: The isotopic composition of present-day Antarctic snow in a Lagrangian atmospheric simulation, Journal of Climate, 20, 739–756, URL https://doi.org/10.1175/JCLI4027.1, 2007.

Hersbach, H., Bell, B., Berrisford, P., Biavati, G., Horányi, A., Muñoz Sabater, J., Nicolas, J., Peubey, C., Radu, R., Rozum, I., et al.: ERA5 hourly data on single levels from 1979 to present. Copernicus Climate Change Service (C3S) Climate Data Store (CDS)., URL https://www.doi.org/10.24381/cds.bd0915c6, Accessed on 15-10-2021, [Dataset], 2018.

Hofer, S., Amory, C., Kittel, C., Carlsen, T., Le Toumelin, L., and Storelvmo, T.: The Contribution of Drifting Snow to Cloud Properties and the Atmospheric Radiative Budget Over Antarctica, Geophysical Research Letters, 48, URL https://doi.org/10.1029/2021GL094967, 2021.

Hoffmann, G., Jouzel, J., and Masson, V.: Stable water isotopes in atmospheric general circulation models, Hydrological Processes, 14, 1385–1406, URL https://doi.org/10.1002/1099-1085(20000615)14:8<1385::AID-HYP989>3.0.CO;2-1, 2000.

Högström, U.: Non-dimensional wind and temperature profiles in the atmospheric surface layer: A re-evaluation, Boundary-Layer Meteorology, 42, 55–78, URL https://doi.org/10.1007/BF00119875, 1988.

Horita, J., Rozanski, K., and Cohen, S.: Isotope effects in the evaporation of water: A status report of the Craig–Gordon model, Isotopes in Environmental and Health Studies, 44, 23–49, URL https://doi.org/10.1080/10256010801887174, 2008.

Hughes, A. G., Wahl, S., Jones, T. R., Zuhr, A., Hörhold, M., White, J. W. C., and Steen-Larsen, H. C.: The role of sublimation as a driver of climate signals in the water isotope content of surface snow: Laboratory and field experimental results, The Cryosphere, 15, 4949–4974, URL https://doi.org/10.5194/tc-15-4949-2021, 2021.

Jafari, M., Gouttevin, I., Couttet, M., Wever, N., Michel, A., Sharma, V., Rossmann, L., Maass, N., Nicolaus, M., and Lehning, M.: The Impact of Diffusive Water Vapor Transport on Snow Profiles in Deep and Shallow Snow Covers and on Sea Ice, Frontiers in Earth Science, 8, 249, URL https://www.doi.org/10.3389/feart.2020.00249, 2020.

Jancso, G., Pupezin, J., and Van Hook, W.: Vapour Pressure of $H_2{}^{18}O$ Ice (I) (-17° C to 0° C) and $H_2{}^{18}O$ Water (0° C to 16° C), Nature, 225, 723, URL https://doi.org/10.1038/225723a0, 1970.

Johnsen, S. J., Dahl-Jensen, D., Gundestrup, N., Steffensen, J. P., Clausen, H. B., Miller, H., Masson-Delmotte, V., Sveinbjörnsdottir, A. E., and White, J.: Oxygen isotope and palaeotemperature records from six Greenland ice-core stations: Camp Century, Dye-3, GRIP, GISP2, Renland and NorthGRIP, Journal of Quaternary Science: Published for the Quaternary Research Association, 16, 299–307, URL https://doi.org/10.1002/jqs.622, 2001.

Joint Committee for Guides in Metrology: Evaluation of measurement data – Guide to the expression of uncertainty in measurement, https://www.bipm.org/utils/common/documents/jcgm/JCGM_100_2008_E.pdf. Last access: 30 August 2020, 2008.

Joussaume, S., Sadourny, R., and Jouzel, J.: A general circulation model of water isotope cycles in the atmosphere, Nature, 311, 24–29, URL https://doi.org/10.1038/311024a0, 1984.

Jouzel, J. and Merlivat, L.: Deuterium and oxygen 18 in precipitation: Modeling of the isotopic effects during snow formation, Journal of Geophysical Research: Atmospheres, 89, 11 749–11 757, URL https://doi.org/10.1029/JD089iD07p11749, 1984.

Jouzel, J., Vimeux, F., Caillon, N., Delaygue, G., Hoffmann, G., Masson-Delmotte, V., and Parrenin, F.: Magnitude of isotope/temperature scaling for interpretation of central Antarctic ice cores, Journal of Geophysical Research: Atmospheres, 108, URL https://doi.org/10.1029/2002JD002677, 2003.

King, J. C. and Anderson, P. S.: Heat and water vapour fluxes and scalar roughness lengths over an Antarctic ice shelf, Boundary-Layer Meteorology, 69, 101–121, URL https://doi.org/10.1007/BF00713297, 1994.

King, J. C., Anderson, P. S., and Mann, G.: The seasonal cycle of sublimation at Halley, Antarctica, Journal of Glaciology, 47, 1–8, URL https://doi.org/10.3189/172756501781832548, 2001.

Koeniger, P., Leibundgut, C., Link, T., and Marshall, J. D.: Stable isotopes applied as water tracers in column and field studies, Organic Geochemistry, 41, 31–40, URL https://doi.org/10.1016/j.orggeochem.2009.07.006, 2010.

Kok, J. F., Parteli, E. J. R., Michaels, T. I., and Karam, D. B.: The physics of wind-blown sand and dust, Reports on Progress in Physics, 75, 106 901, URL https://doi.org/10.1088/0034-4885/75/10/106901, 2012.

Kopec, B., Lauder, A., Posmentier, E., and Feng, X.: The diel cycle of water vapor in west Greenland, Journal of Geophysical Research, 119, 9386–9399, URL https://doi.org/10.1002/2014JD021859, 2014.

Krinner, G. and Werner, M.: Impact of precipitation seasonality changes on isotopic signals in polar ice cores: A multi-model analysis, Earth and Planetary Science Letters, 216, 525–538, URL https://doi.org/10.1016/S0012-821X(03)00550-8, 2003.

Kumar, B. and Nachiappan, R. P.: On the sensitivity of Craig and Gordon Model for the estimation of the isotopic composition of lake evaporates, Water Resources Research, 35, 1689–1691, URL https://doi.org/10.1029/1999WR900011, 1999.

Kurita, N., Hirasawa, N., Koga, S., Matsushita, J., Steen-Larsen, H. C., Masson-Delmotte, V., and Fujiyoshi, Y.: Identification of Air Masses Responsible for Warm Events on the East Antarctic Coast, SOLA, 12, 307–313, URL https://doi.org/10.2151/sola.2016-060, 2016a.

Kurita, N., Hirasawa, N., Koga, S., Matsushita, J., Steen-Larsen, H. C., Masson-Delmotte, V., and Fujiyoshi, Y.: Influence of large-scale atmospheric circulation on marine air intrusion toward the East Antarctic coast, Geophysical Research Letters, 43, 9298–9305, URL https://doi.org/10.1002/2016GL070246, 2016b.

Landais, A., Ekaykin, A., Barkan, E., Winkler, R., and Luz, B.: Seasonal variations of ^{17}O-excess and d-excess in snow precipitation at Vostok station, East Antarctica, Journal of Glaciology, 58, 725–733, URL https://doi.org/10.3189/2012JoG11J237, 2012.

Le Toumelin, L., Amory, C., Favier, V., Kittel, C., Hofer, S., Fettweis, X., Gallée, H., and Kayetha, V.: Sensitivity of the surface energy budget to drifting snow assimulated by MAR in coastal Adelie Land, Antarctica, The Cryosphere, 15, 3595–3614, URL https://doi.org/10.5194/tc-2020-329, 2021.

LeGrande, A. N. and Schmidt, G. A.: Global gridded data set of the oxygen isotopic composition in seawater, Geophysical Research Letters, 33, L12 604, URL https://doi.org/10.1029/2006GL026011, 2006.

Lenaerts, J. T. M., van den Broeke, M. R., Déry, S. J., van Meijgaard, E., van de Berg, W. J., Palm, S. P., and Sanz Rodrigo, J.: Modeling drifting snow in Antarctica with a regional climate model: 1. Methods and model evaluation, Journal of Geophysical Research: Atmospheres, 117, URL https://doi.org/10.1029/2011JD016145, 2012.

Leuning, R., Zegelin, S. J., Jones, K., Keith, H., and Hughes, D.: Measurement of horizontal and vertical advection of CO_2 within a forest canopy, Agricultural and Forest Meteorology, 148, 1777–1797, URL https://doi.org/10.1016/j.agrformet.2008.06.006, 2008.

LI-COR: LI-7500 CO_2/ H_2O Analyzer: Instruction Manual, https://www.licor.com/documents/ij79q7adnx7ozr1r1yil. Last access: 11 October 2020, 2004.

LI-COR Biosciences: Eddy Covariance Software, https://www.licor.com/env/products/eddy_covariance/software.html. Last access: 4 November 2019, 2019.

Lin, Y.-L., Farley, R. D., and Orville, H. D.: Bulk Parameterization of the Snow Field in a Cloud Model, Journal of Applied Meteorology and Climate, 22, 1065–1092, URL https://doi.org/10.1175/1520-0450(1983)022<1065:BPOTSF>2.0.CO;2, 1983.

Liston, G. E. and Sturm, M.: A snow-transport model for complex terrain, Journal of Glaciology, 44, 498–516, URL https://doi.org/10.3189/S0022143000002021, 1998.

Liu, C., Gao, Z., Yang, Q., Han, B., Wang, H., Hao, G., Zhao, J., Yu, L., Wang, L., and Li, Y.: Measurements of turbulence transfer in the near-surface layer over the Antarctic sea-ice surface from April through November in 2016, Annals of Glaciology, 61, 12–23, URL https://www.doi.org/10.1017/aog.2019.48, 2020.

Lorius, C., Merlivat, L., Jouzel, J., and Pourchet, M.: A 30,000-yr isotope climatic record from Antarctic ice, Nature, 280, 644–648, URL https://doi.org/10.1038/280644a0, 1979.

Maahn, M. and Kollias, P.: Improved Micro Rain Radar snow measurements using Doppler spectra post-processing, Atmospheric Measurement Techniques, 5, 2661–2673, URL https://doi.org/10.5194/amt-5-2661-2012, 2012.

Majoube, M.: Fractionation factor of ^{18}O between water vapour and ice, Nature, 226, 1242–1242, URL https://www.doi.org/10.1038/2261242a0, 1970.

Majoube, M.: Fractionnement en oxygène 18 et en deutérium entre l'eau et sa vapeur, Journal de Chimie Physique et de Physico-Chimie Biologique, 68, 1423–1436, URL https://doi.org/10.1051/jcp/1971681423, 1971.

Mann, G. W., Anderson, P. S., and Mobbs, S. D.: Profile measurements of blowing snow at Halley, Antarctica, Journal of Geophysical Research: Atmospheres, 105, 24 491–24 508, URL https://www.doi.org/10.1029/2000JD900247, 2000.

Massman, W.: A simple method for estimating frequency response corrections for eddy covariance systems, Agricultural and Forest Meteorology, 104, 185–198, URL https://doi.org/10.1016/S0168-1923(00)00164-7, 2000.

Massman, W.: Reply to comment by Rannik on "A simple method for estimating frequency response corrections for eddy covariance systems", Agricultural and Forest Meteorology, 107, 247–251, URL https://doi.org/10.1016/S0168-1923(00)00237-9, 2001.

Masson-Delmotte, V., Hou, S., Ekaykin, A., Jouzel, J., Aristarain, A., Bernardo, R. T., Bromwich, D., Cattani, O., Delmotte, M., Falourd, S., Frezzotti, M., Gallée, H., Genoni, L., Isaksson, E., Landais, A., Helsen, M. M., Hoffmann, G., Lopez, J., Morgan, V., Motoyama, H., Noone, D., Oerter, H., Petit, J. R., Royer, A., Uemura, R., Schmidt, G. A., Schlosser, E., Simões, J. C., Steig, E. J., Stenni, B., Stievenard, M., van den Broeke, M. R., van de Wal, R. S. W., van de Berg, W. J., Vimeux, F., and White, J. W. C.: A Review of Antarctic Surface Snow Isotopic Composition: Observations, Atmospheric Circulation, and Isotopic Modeling, Journal of Climate, 21, 3359–3387, URL https://doi.org/10.1175/2007JCLI2139.1, 2008.

Matsuo, S. and Matsubaya, O.: Vapour Pressure of $H_2{}^{18}O$ Ice, Nature, 221, 463–464, URL https://doi.org/10.1038/221463a0, 1969.

Mauder, M., Desjardins, R. L., Pattey, E., and Worth, D.: An Attempt to Close the Daytime Surface Energy Balance Using Spatially-Averaged Flux Measurements, Boundary-Layer Meteorology, 136, 175–191, URL https://doi.org/10.1007/s10546-010-9497-9, 2010.

Mauder, M., Cuntz, M., Drüe, C., Graf, A., Rebmann, C., Schmid, H. P., Schmidt, M., and Steinbrecher, R.: A strategy for quality and uncertainty assessment of long-term eddy-covariance measurements, Agricultural and Forest Meteorology, 169, 122–135, URL https://doi.org/10.1016/j.agrformet.2012.09.006, 2013.

Melo, D. B., Sharma, V., Comola, F., Sigmund, A., and Lehning, M.: Modeling Snow Saltation: The Effect of Grain Size and Interparticle Cohesion, Journal of Geophysical Research: Atmospheres, 127, e2021JD035 260, URL https://doi.org/10.1029/2021JD035260, 2022.

Melo, D. B., Sigmund, A., and Lehning, M.: Understanding snow saltation parameterizations: lessons from theory, experiments and numerical simulations, EGUsphere, 2023, 1–37, URL https://doi.org/10.5194/egusphere-2023-488, preprint, 2023.

Merlivat, L.: Molecular diffusivities of $H_2{}^{16}O$, $HD^{16}O$, and $H_2{}^{18}O$ in gases, The Journal of Chemical Physics, 69, 2864–2871, URL https://doi.org/10.1063/1.436884, 1978.

Merlivat, L. and Jouzel, J.: Global climatic interpretation of the deuterium-oxygen 18 relationship for precipitation, Journal of Geophysical Research: Oceans, 84, 5029–5033, URL https://doi.org/10.1029/JC084iC08p05029, 1979.

Merlivat, L. and Nief, G.: Fractionnement isotopique lors des changements d'état solide-vapeur et liquide-vapeur de l'eau à des températures inférieures à 0°C, Tellus, 19, 122–127, URL https://doi.org/10.1111/j.2153-3490.1967.tb01465.x, 1967.

Miller, A.: Subset Selection in Regression, Monographs on Statistics & Applied Probability, Chapman & Hall/CRC, Boca Raton, 2002.

Mitchell, D. L.: Use of Mass- and Area-Dimensional Power Laws for Determining Precipitation Particle Terminal Velocities, Journal of the Atmospheric Sciences, 53, 1710–1723, URL https://doi.org/10.1175/1520-0469(1996)053<1710:UOMAAD>2.0.CO;2, 1996.

Moncrieff, J., Clement, R., Finnigan, J., and Meyers, T.: Averaging, Detrending, and Filtering of Eddy Covariance Time Series, in: Handbook of Micrometeorology: A guide for surface flux measurments, edited by Lee, X., Massman, W., and Law, B., pp. 7–32, Kluwer Academic, Dordrecht, 2004.

Monin, A. S. and Obukhov, A. M.: Basic laws of turbulent mixing in the surface layer of the atmosphere, Contrib. Geophys. Inst. Acad. Sci. USSR, 24, 163–187, 1954.

Morrison, H. and Grabowski, W. W.: A Novel Approach for Representing Ice Microphysics in Models: Description and Tests Using a Kinematic Framework, Journal of the Atmospheric Sciences, 65, 1528 – 1548, URL https://doi.org/10.1175/2007JAS2491.1, 2008.

Munters, W., Meneveau, C., and Meyers, J.: Shifted periodic boundary conditions for simulations of wall-bounded turbulent flows, Physics of Fluids, 28, 025 112, URL https://doi.org/10.1063/1.4941912, 2016.

Neumann, T. A. and Waddington, E. D.: Effects of firn ventilation on isotopic exchange, Journal of Glaciology, 50, 183–194, URL https://www.doi.org/10.3189/172756504781830150, 2004.

Nieberding, F., Wille, C., Fratini, G., Asmussen, M. O., Wang, Y., Ma, Y., and Sachs, T.: A Long Term (2005–2019) Eddy Covariance Data Set of CO_2 and H_2O Fluxes from the Tibetan Alpine Steppe, Earth System Science Data, 12, 2705–2724, URL https://doi.org/10.5194/essd-12-2705-2020, 2020.

Nishimura, K. and Hunt, J. C. R.: Saltation and incipient suspension above a flat particle bed below a turbulent boundary layer, Journal of Fluid Mechanics, 417, 77–102, URL https://doi.org/10.1017/S0022112000001014, 2000.

Nishimura, K. and Nemoto, M.: Blowing snow at Mizuho station, Antarctica, Philosophical Transactions of the Royal Society A: Mathematical, Physical and Engineering Sciences, 363, 1647–1662, URL https://doi.org/10.1098/rsta.2005.1599, 2005.

Noël, B., van de Berg, W. J., van Wessem, J. M., van Meijgaard, E., van As, D., Lenaerts, J. T. M., Lhermitte, S., Kuipers Munneke, P., Smeets, C. J. P. P., van Ulft, L. H., van de Wal, R. S. W., and van den Broeke, M. R.: Modelling the climate and surface mass balance of polar ice sheets using RACMO2 – Part 1: Greenland (1958–2016), The Cryosphere, 12, 811–831, URL https://doi.org/10.5194/tc-12-811-2018, 2018.

Noone, D. and Sturm, C.: Comprehensive Dynamical Models of Global and Regional Water Isotope Distributions, in: Isoscapes, edited by West, J. B., Bowen, G. J., Dawson, T. E., and Tu, K. P., pp. 195–219, Springer, Dordrecht, URL https://doi.org/10.1007/978-90-481-3354-3_10, 2010.

Palm, S. P., Kayetha, V., Yang, Y., and Pauly, R.: Blowing snow sublimation and transport over Antarctica from 11 years of CALIPSO observations, The Cryosphere, 11, 2555–2569, URL https://doi.org/10.5194/tc-11-2555-2017, 2017.

Palm, S. P., Yang, Y., Kayetha, V., and Nicolas, J. P.: Insight into the Thermodynamic Structure of Blowing-Snow Layers in Antarctica from Dropsonde and *CALIPSO* Measurements, Journal of Applied Meteorology and Climatology, 57, 2733–2748, URL https://doi.org/10.1175/JAMC-D-18-0082.1, 2018.

Park, S.-J., Park, S.-U., and Ho, C.-H.: Roughness Length of Water Vapor over Land Surfaces and Its Influence on Latent Heat Flux, Terrestrial, Atmospheric and Oceanic Sciences, 21, 855, URL https://doi.org/10.3319/TAO.2009.11.13.01(Hy), 2010.

Peters, G., Fischer, B., and Andersson, T.: Rain observations with a vertically looking Micro Rain Radar (MRR), Boreal Environment Research, 7, 353–362, URL https://www.borenv.net/BER/archive/pdfs/ber7/ber7-353.pdf, 2002.

Pfahl, S. and Wernli, H.: Lagrangian simulations of stable isotopes in water vapor: An evaluation of nonequilibrium fractionation in the Craig-Gordon model, Journal of Geophysical Research: Atmospheres, 114, URL https://doi.org/10.1029/2009JD012054, 2009.

Pfahl, S., Wernli, H., and Yoshimura, K.: The isotopic composition of precipitation from a winter storm – a case study with the limited-area model $COSMO_{iso}$, Atmospheric Chemistry and Physics, 12, 1629–1648, URL https://doi.org/10.5194/acp-12-1629-2012, 2012.

Pomeroy, J. and Male, D.: Steady-state suspension of snow, Journal of Hydrology, 136, 275–301, URL https://doi.org/10.1016/0022-1694(92)90015-N, 1992.

Pomeroy, J. W. and Essery, R. L. H.: Turbulent fluxes during blowing snow: field tests of model sublimation predictions, Hydrological Processes, 13, 2963–2975, URL https://doi.org/10.1002/(SICI)1099-1085(19991230)13:18<2963::AID-HYP11>3.0.CO;2-9, 1999.

Pomeroy, J. W. and Gray, D. M.: Saltation of snow, Water Resources Research, 26, 1583–1594, URL https://doi.org/10.1029/WR026i007p01583, 1990.

Raupach, M. R.: Saltation layers, vegetation canopies and roughness lengths, in: Aeolian Grain Transport 1. Acta Mechanica Supplementum, edited by Barndorff-Nielsen, O. E. and Willetts, B. B., vol. 1, pp. 83–96, Springer, Vienna, URL https://doi.org/10.1007/978-3-7091-6706-9_5, 1991.

Reba, M. L., Pomeroy, J., Marks, D., and Link, T. E.: Estimating surface sublimation losses from snowpacks in a mountain catchment using eddy covariance and turbulent transfer calculations, Hydrological Processes, 26, 3699–3711, URL https://doi.org/10.1002/hyp.8372, 2012.

Sato, T., Kosugi, K., and Sato, A.: Saltation-layer structure of drifting snow observed in wind tunnel, Annals of Glaciology, 32, 203–208, URL https://doi.org/10.3189/172756401781819184, 2001.

Schlögl, S., Lehning, M., Nishimura, K., Huwald, H., Cullen, N. J., and Mott, R.: How do Stability Corrections Perform in the Stable Boundary Layer Over Snow?, Boundary-Layer Meteorology, 165, 161–180, URL https://doi.org/10.1007/s10546-017-0262-1, 2017.

Schmale, J., Baccarini, A., Thurnherr, I., Henning, S., Efraim, A., Regayre, L., Bolas, C., Hartmann, M., Welti, A., Lehtipalo, K., Aemisegger, F., Tatzelt, C., Landwehr, S., Modini, R. L., Tummon, F., Johnson, J. S., Harris, N., Schnaiter, M., Toffoli, A., Derkani, M., Bukowiecki, N., Stratmann, F., Dommen, J., Baltensperger, U., Wernli, H., Rosenfeld, D., Gysel-Beer, M., and Carslaw, K. S.: Overview of the Antarctic Circumnavigation Expedition: Study of Preindustrial-like Aerosols and Their Climate Effects (ACE-SPACE), Bulletin of the American Meteorological Society, 100, 2260–2283, URL https://doi.org/10.1175/BAMS-D-18-0187.1, 2019.

Schmidt, R. A.: Sublimation of Wind-transported Snow: A Model, USDA Forest Service research paper RM, Rocky Mountain Forest and Range Experiment Station, Forest Service, U.S. Department of Agriculture, 1972.

Schmidt, R. A.: Vertical profiles of wind speed, snow concentration, and humidity in blowing snow, Boundary-Layer Meteorology, 23, 223–246, URL https://doi.org/10.1007/BF00123299, 1982.

Sharma, V., Comola, F., and Lehning, M.: On the suitability of the Thorpe-Mason model for Calculating Sublimation of Saltating Snow, The Cryosphere, 12, 3499–3509, URL https://doi.org/10.5194/tc-12-3499-2018, 2018.

Sharma, V., Gerber, F., and Lehning, M.: Introducing CRYOWRF v1.0: multiscale atmospheric flow simulations with advanced snow cover modelling, Geoscientific Model Development, 16, 719–749, URL https://doi.org/10.5194/gmd-16-719-2023, 2023.

Sieber, M., Conway, T. M., de Souza, G. F., Hassler, C. S., Ellwood, M. J., and Vance, D.: High-resolution Cd isotope systematics in multiple zones of the Southern Ocean from the Antarctic Circumnavigation Expedition, Earth and Planetary Science Letters, 527, 115 799, URL https://doi.org/10.1016/j.epsl.2019.115799, 2019.

Sigmund, A., Dujardin, J., Comola, F., Sharma, V., Huwald, H., Melo, D. B., and Lehning, M.: Meteorology and snow transport at S17 near Syowa, Antarctica, in austral summer 2018/2019, URL https://doi.org/10.16904/envidat.237, [Dataset], 2021.

Sigmund, A., Dujardin, J., Comola, F., Sharma, V., Huwald, H., Melo, D. B., Hirasawa, N., Nishimura, K., and Lehning, M.: Evidence of Strong Flux Underestimation by Bulk Parametrizations During Drifting and Blowing Snow, Boundary-Layer Meteorology, 182, 119–146, URL https://doi.org/10.1007/s10546-021-00653-x, 2022.

Sigmund, A., Chaar, R., and Lehning, M.: Modeled Isotopic Composition of Water Vapour Along Air Parcel Trajectories in the Antarctic, URL http://doi.org/10.16904/envidat.417, [Dataset], 2023.

Sinclair, K. E., Marshall, S. J., and Moran, T. A.: A Lagrangian approach to modelling stable isotopes in precipitation over mountainous terrain, Hydrological Processes, 25, 2481–2491, URL https://doi.org/10.1002/hyp.7973, 2011.

Smeets, C. J. P. P. and van den Broeke, M. R.: The Parameterisation of Scalar Transfer over Rough Ice, Boundary-Layer Meteorology, 128, 339–355, URL https://www.doi.org/10.1007/s10546-008-9292-z, number: 3, 2008.

Sokratov, S. A. and Golubev, V. N.: Snow isotopic content change by sublimation, Journal of Glaciology, 55, 823–828, URL https://www.doi.org/10.3189/002214309790152456, 2009.

Sprenger, M. and Wernli, H.: The LAGRANTO Lagrangian analysis tool–version 2.0, Geoscientific Model Development, 8, 2569–2586, URL https://www.doi.org/10.5194/gmd-8-2569-2015, 2015.

Stearns, C. R. and Weidner, G. A.: Sensible and Latent Heat Flux Estimates in Antarctica, in: Antarctic Meteorology and Climatology: Studies Based on Automatic Weather Stations, edited by Bromwich, D. H. and Stearns, C. R., pp. 109–138, American Geophysical Union (AGU), Washington, DC, URL https://doi.org/10.1029/AR061p0109, 1993.

Stenni, B., Scarchilli, C., Masson-Delmotte, V., Schlosser, E., Ciardini, V., Dreossi, G., Grigioni, P., Bonazza, M., Cagnati, A., Karlicek, D., et al.: Three-year monitoring of stable isotopes of precipitation at Concordia Station, East Antarctica, The Cryosphere, 10, 2415–2428, URL https://doi.org/10.5194/tc-10-2415-2016, 2016.

Stiperski, I. and Rotach, M. W.: On the Measurement of Turbulence Over Complex Mountainous Terrain, Boundary-Layer Meteorology, 159, 97–121, URL https://doi.org/10.1007/s10546-015-0103-z, 2016.

Strasser, U., Bernhardt, M., Weber, M., Liston, G. E., and Mauser, W.: Is snow sublimation important in the alpine water balance?, The Cryosphere, 2, 53–66, URL https://www.doi.org/10.5194/tc-2-53-2008, 2008.

Stössel, F., Guala, M., Fierz, C., Manes, C., and Lehning, M.: Micrometeorological and morphological observations of surface hoar dynamics on a mountain snow cover, Water Resources Research, 46, URL https://doi.org/10.1029/2009WR008198, 2010.

Sugiura, K., Nishimura, K., Maeno, N., and Kimura, T.: Measurements of snow mass flux and transport rate at different particle diameters in drifting snow, Cold Reg Sci Technol, 27, 83–89, URL https://doi.org/10.1016/S0165-232X(98)00002-0, 1998.

Sørensen, M.: On the rate of aeolian sand transport, Geomorphology, 59, 53–62, URL https://doi.org/10.1016/j.geomorph.2003.09.005, 2004.

The IMBIE team: Mass balance of the Antarctic Ice Sheet from 1992 to 2017, Nature, 558, 219–222, URL https://doi.org/10.1038/s41586-018-0179-y, 2018.

Thiery, W., Gorodetskaya, I. V., Bintanja, R., Van Lipzig, N. P. M., Van den Broeke, M. R., Reijmer, C. H., and Kuipers Munneke, P.: Surface and snowdrift sublimation at Princess Elisabeth station, East Antarctica, The Cryosphere, 6, 841–857, URL https://doi.org/10.5194/tc-6-841-2012, 2012.

Thorpe, A. D. and Mason, B. J.: The evaporation of ice spheres and ice crystals, British Journal of Applied Physics, 17, 541–548, URL https://doi.org/10.1088/0508-3443/17/4/316, 1966.

Thurnherr, I. and Aemisegger, F.: Calibrated data of stable water isotope measurements in water vapour at 13.5 m a.s.l., made in the austral summer of 2016/2017 around the Southern Ocean during the Antarctic Circumnavigation Expedition (ACE)., URL https://doi.org/10.5281/zenodo.3250790, [Dataset], 2020.

Thurnherr, I., Jansing, L., Aemisegger, F., and Wernli, H.: Numerical weather simulations using COSMOiso from December 2016–March 2017 along the ship track of the Antarctic Circumnavigation Expedition, URL https://doi.org/10.3929/ethz-b000445744, [Dataset], 2020a.

Thurnherr, I., Kozachek, A., Graf, P., Weng, Y., Bolshiyanov, D., Landwehr, S., Pfahl, S., Schmale, J., Sodemann, H., Steen-Larsen, H. C., et al.: Meridional and vertical variations of the water vapour isotopic composition in the marine boundary layer over the Atlantic and Southern Ocean, Atmospheric Chemistry and Physics, 20, 5811–5835, URL https://doi.org/10.5194/acp-20-5811-2020, 2020b.

Thurnherr, I., Wernli, H., and Aemisegger, F.: 10-day backward trajectories from ECMWF analysis data along the ship track of the Antarctic Circumnavigation Expedition in austral summer 2016/2017, URL https://doi.org/10.5281/zenodo.4031705, [Dataset], 2020c.

Thurnherr, I., Hartmuth, K., Jansing, L., Gehring, J., Boettcher, M., Gorodetskaya, I., Werner, M., Wernli, H., and Aemisegger, F.: The role of air–sea fluxes for the water vapour isotope signals in the cold and warm sectors of extratropical cyclones over the Southern Ocean, Weather and Climate Dynamics, 2, 331–357, URL https://doi.org/10.5194/wcd-2-331-2021, 2021.

Touzeau, A., Landais, A., Stenni, B., Uemura, R., Fukui, K., Fujita, S., Guilbaud, S., Ekaykin, A., Casado, M., Barkan, E., Luz, B., Magand, O., Teste, G., Le Meur, E., Baroni, M., Savarino, J., Bourgeois, I., and Risi, C.: Acquisition of isotopic composition for surface snow in East Antarctica and the links to climatic parameters, The Cryosphere, 10, 837–852, URL https://doi.org/10.5194/tc-10-837-2016, 2016.

Town, M. S., Warren, S. G., Walden, V. P., and Waddington, E. D.: Effect of atmospheric water vapor on modification of stable isotopes in near-surface snow on ice sheets, Journal of Geophysical Research: Atmospheres, 113, URL https://www.doi.org/10.1029/2008JD009852, 2008.

Van Dalum, C. T., van de Berg, W. J., and van den Broeke, M. R.: Sensitivity of Antarctic surface climate to a new spectral snow albedo and radiative transfer scheme in RACMO2.3p3, The Cryosphere, 16, 1071–1089, URL https://doi.org/10.5194/tc-16-1071-2022, 2022.

Van Dijk, A., Moene, A. F., and De Bruin, H. A. R.: The principles of surface flux physics: theory, practice and description of the ECPACK library, Internal Report 2004/1, Wageningen University, Wageningen, the Netherlands, 2004.

Van Wessem, J. M., van de Berg, W. J., Noël, B. P. Y., van Meijgaard, E., Amory, C., Birnbaum, G., Jakobs, C. L., Krüger, K., Lenaerts, J. T. M., Lhermitte, S., Ligtenberg, S. R. M., Medley, B., Reijmer, C. H., van Tricht, K., Trusel, L. D., van Ulft, L. H., Wouters, B., Wuite, J., and van den Broeke, M. R.: Modelling the climate and surface mass balance of polar ice sheets using RACMO2 – Part 2: Antarctica (1979–2016), The Cryosphere, 12, 1479–1498, URL https://doi.org/10.5194/tc-12-1479-2018, 2018.

Vickers, D. and Mahrt, L.: Quality Control and Flux Sampling Problems for Tower and Aircraft Data, Journal of Atmospheric and Oceanic Technology, 14, 512–526, URL https://doi.org/10.1175/1520-0426(1997)014<0512:QCAFSP>2.0.CO;2, 1997.

Vignon, E., Genthon, C., Barral, H., Amory, C., Picard, G., Gallée, H., Casasanta, G., and Argentini, S.: Momentum- and Heat-Flux Parametrization at Dome C, Antarctica: A Sensitivity Study, Boundary-Layer Meteorology, 162, 341–367, URL https://doi.org/10.1007/s10546-016-0192-3, 2017.

Vionnet, V., Martin, E., Masson, V., Guyomarc'h, G., Naaim-Bouvet, F., Prokop, A., Durand, Y., and Lac, C.: Simulation of wind-induced snow transport and sublimation in alpine terrain using a fully coupled snowpack/atmosphere model, The Cryosphere, 8, 395–415, URL https://doi.org/10.5194/tc-8-395-2014, 2014.

Wahl, S., Steen-Larsen, H. C., Reuder, J., and Hörhold, M.: Quantifying the Stable Water Isotopologue Exchange Between the Snow Surface and Lower Atmosphere by Direct Flux Measurements, Journal of Geophysical Research: Atmospheres, 126, e2020JD034 400, URL https://doi.org/10.1029/2020JD034400, 2021.

Wahl, S., Steen-Larsen, H. C., Hughes, A. G., Dietrich, L. J., Zuhr, A., Behrens, M., Faber, A.-K., and Hörhold, M.: Atmosphere-Snow Exchange Explains Surface Snow Isotope Variability, Geophysical Research Letters, 49, e2022GL099 529, URL https://doi.org/10.1029/2022GL099529, 2022.

Walter, B., Huwald, H., Gehring, J., Bühler, Y., and Lehning, M.: Radar measurements of blowing snow off a mountain ridge, The Cryosphere, 14, 1779–1794, URL https://doi.org/10.5194/tc-14-1779-2020, 2020.

Wang, Z., Huang, N., and Pähtz, T.: The Effect of Turbulence on Drifting Snow Sublimation, Geophys Res Lett, 46, 1–8, URL https://doi.org/10.1029/2019GL083636, 2019.

Webb, E. K., Pearman, G. I., and Leuning, R.: Correction of flux measurements for density effects due to heat and water vapour transfer, Quarterly Journal of the Royal Meteorological Society, 106, 85–100, 1980.

Wernli, B. H. and Davies, H. C.: A Lagrangian-based analysis of extratropical cyclones. I: The method and some applications, Quarterly Journal of the Royal Meteorological Society, 123, 467–489, URL https://www.doi.org/10.1002/qj.49712353811, 1997.

Wever, N., Keenan, E., Amory, C., Lehning, M., Sigmund, A., Huwald, H., and Lenaerts, J. T. M.: Observations and simulations of new snow density in the drifting snow-dominated environment of Antarctica, Journal of Glaciology, pp. 1–18, URL https://doi.org/10.1017/jog.2022.102, 2022.

Wilson, K., Goldstein, A., Falge, E., Aubinet, M., Baldocchi, D., Berbigier, P., Bernhofer, C., Ceulemans, R., Dolman, H., Field, C., Grelle, A., Ibrom, A., Law, B., Kowalski, A., Meyers, T., Moncrieff, J., Monson, R., Oechel, W., Tenhunen, J., Valentini, R., and Verma, S.: Energy balance closure at FLUXNET sites, Agricultural and Forest Meteorology, 113, 223–243, URL https://doi.org/10.1016/S0168-1923(02)00109-0, 2002.

Yamanouchi, T. and Kawaguchi, S.: Effects of drifting snow on surface radiation budget in the katabatic wind zone, Antarctica, Annals of Glaciology, 6, 238–241, URL https://doi.org/10.3189/1985AoG6-1-238-241, 1985.

Armin Sigmund – Curriculum Vitae

Education

2018 – 2023	PhD in Civil and Environmental Engineering, EPFL PhD thesis: Assessing sublimation in conditions of blowing snow and sublimation effects on the isotopic composition of water vapour
2015 – 2018	M.Sc. in Geoecology (Environmental Sciences), University of Bayreuth Master thesis: Proof of concept for real-time air mass discrimination at the Schneefernerhaus, Zugspitze
2012 – 2015	B.Sc. in Geoecology (Environmental Sciences), University of Bayreuth Bachelor thesis: Investigating the near-surface air temperature gradient for cold-air drainage flows on a sloped surface using fiber-optic Distributed Temperature Sensing (DTS)

Peer-reviewed publications

2023	Sigmund, A., Chaar, R., Ebner, P. P., & Lehning, M.: A case study on drivers of the isotopic composition of water vapor at the coast of East Antarctica, Journal of Geophysical Research: Earth Surface, 128, e2023JF007062, https://doi.org/10.1029/2023JF007062
2023	Melo, D. B., Sigmund, A., and Lehning, M.: Understanding snow saltation parameterizations: lessons from theory, experiments and numerical simulations, EGUsphere [preprint], https://doi.org/10.5194/egusphere-2023-488
2022	Wever, N., Keenan, E., Amory, C., Lehning, M., Sigmund, A., Huwald, H., and Lenaerts, J.: Observations and simulations of new snow density in the drifting snow-dominated environment of Antarctica, Journal of Glaciology, 1-18, doi:10.1017/jog.2022.102
2022	Melo, D. B., Sharma, V., Comola, F., Sigmund, A., and Lehning, M.: Modeling snow saltation: The effect of grain size and interparticle cohesion, Journal of Geophysical Research: Atmospheres, 127, e2021JD035260, https://doi.org/10.1029/2021JD035260
2022	Sigmund, A., Dujardin, J., Comola, F., Sharma, V., Melo, D. B., Hirasawa, N., Nishimura, K., and Lehning, M.: Evidence of Strong Flux Underestimation by Bulk Parametrizations During Drifting and Blowing Snow. Boundary-Layer Meteorol 182, 119–146, https://doi.org/10.1007/s10546-021-00653-x
2019	Sigmund, A., Freier, K., Rehm, T., Ries, L., Schunk, C., Menzel, A., and Thomas, C. K.: Multivariate statistical air mass classification for the high-alpine observatory at the Zugspitze Mountain, Germany, Atmos. Chem. Phys., 19, 12477–12494, https://doi.org/10.5194/acp-19-12477-2019
2017	Sigmund, A., Pfister, L., Sayde, C., and Thomas, C. K.: Quantitative analysis of the radiation error for aerial coiled-fiber-optic distributed temperature sensing deployments using reinforcing fabric as support structure, Atmospheric Measurement Techniques, 10, 2149-2162, https://doi.org/10.5194/amt-10-2149-2017
2017	Pfister, L., Sigmund, A., Olesch., J. and Thomas, C. K.: Nocturnal Near-Surface Temperature, but not Flow Dynamics, can be Predicted by Microtopography in a Mid-Range Mountain Valley, Boundary-Layer Meteorology, 165, 333-348, https://doi.org/10.1007/s10546-017-0281-y

Conference presentations

2023 Sigmund, A., Huwald, H., Gerber, F., Dujardin, J., Comola, F., Sharma, V., Melo, D.B., Lehning, M.: Constraining Latent and Sensible Heat Fluxes during Drifting and Blowing Snow Events in Antarctica using in–situ Measurements and Large–Eddy Simulations, 24th Symposium on Boundary Layers and Turbulence, Denver, USA and online, 8–12 January 2023.

2022 Sigmund, A., Sharma, V., Melo, D. B., Comola, F., Dujardin, J., Gerber, F., Huwald, H., and Lehning, M.: Parametrizing drifting snow sublimation in the saltation layer, EGU General Assembly 2022, Vienna, Austria, 23-27 May 2022, EGU22-11853, https://doi.org/10.5194/egusphere-egu22-11853

2022 Sigmund, A., Lehning, M.: Water vapour fluxes above snow in conditions of drifting and blowing snow, CATCH Open Science Workshop, online, 10 May 2022.

2021 Sigmund, A., Melo, D. B., Sharma, V., Huwald, H., Lehning, M.: How important are snow transport and sublimation for the mass balance of Antarctica?, Geneva Cryosphere Hub, UN Climate Change Conference of the Parties (COP26), Geneva, Switzerland, 1-12 November 2021.

2017 Sigmund, A., Freier, K., Rehm, T., Kirchner, M., Mauder, M., Harsch, C., Thomas, C.K.: Toward nowcasting the mixing layer regime at the environmental research station Schneefernerhaus, Zugspitze, VAO symposium, Bolzano, Italy, 28-30 March 2017.

2016 Sigmund, A., Pfister, Lena, Olesch, J., and Thomas, C.K.: Measuring centimeter-resolution air temperature profiles above land and water using fiber-optic Distributed Temperature Sensing, EGU General Assembly, Vienna, Austria, 17-22 April 2016.